

Data-driven patient motion compensation in cardiac positron
emission tomography

by

Spencer Thomas Manwell

A thesis submitted to the Faculty of Graduate and Postdoctoral Affairs in partial
fulfillment of the requirements for the degree of

Doctor of Philosophy

in

Physics

Specialization in Medical Physics

Ottawa-Carleton Institute for Physics

Department of Physics

Carleton University

Ottawa, Ontario

© 2020, Spencer Thomas Manwell

Abstract

Positron emission tomography (PET) is a molecular imaging modality that has been demonstrated to be a powerful, non-invasive, tool for the assessment and diagnosis of cardiac pathologies like coronary artery disease. The accuracy of these clinical examinations for detecting and prognosticating disease can be marred in cases where patient motion is severe. Clinical use of motion tracking/compensation tools, however, is relatively uncommon partly due to the increases in complexity and time of patient setup prior to imaging. The purpose of the work described here was to develop and evaluate new methods of patient motion detection and compensation in the context of cardiac PET imaging studies that are less complex than standard commercial options in the hope of reducing barriers to clinical adoption.

The proposed methods are based on measuring and tracking the motion of a low-activity radioactive marker placed on patients using the positron emission tracking (PeTrack) algorithm. Motion information was employed to compensate and/or correct for either respiratory or whole-body patient motion.

The performance of PeTrack for respiratory tracking and motion compensation was evaluated in a clinical population in comparison with a commonly used commercial optical tracking device. Within a practical comparison framework PeTrack was shown to perform comparably to the commercial system. From this comparison shortcomings of both PeTrack and the commercial system were identified; knowledge of the former can inform future development and improvement.

A method for whole-body patient motion correction (WBMC) in static cardiac perfusion studies using PeTrack was developed. Motion corrected images demonstrated significantly

less blurring of the myocardial walls and improved contrast. Relative perfusion measurements among the clinical data sets were not significantly affected although the extent of patient motion was limited.

The WBMC algorithm was extended for dynamic acquisitions used for quantification of myocardial blood flow. Motion detection and estimation with PeTrack was compared to that of another data-driven motion tracking algorithm within a clinical population. Body motion estimation with PeTrack was more robust than the alternative method. Motion correction using PeTrack demonstrated improvement among various quality indicators of the kinetic modelling used to estimate blood flow.

Acknowledgements

There were many who contributed to this work either directly and indirectly and it is difficult to overstate the importance of each. I will do my best to acknowledge these individuals and organizations here, but I am sure that I will not do so sufficiently. I had the unique experience of being co-supervised by three people. In no particular order, I would like to express my sincere gratitude to Dr. Ran Klein, Dr. Robert deKemp, and Dr. Tong Xu for investing their time and resources into my training during my doctoral studies. Each of these individuals have unique strengths and I am confident that I was able to absorb some of these from each of them. Ran Klein is a spectacular engineer and he never missed an opportunity to impress upon me the value of good design and the importance of automation. Together these concepts lead to the development of things that are, hopefully, as easy as possible to use and to share with others. Whether I was writing computer code, or imagining an experiment, I tried in earnest to incorporate these notions. Robert deKemp showed me the importance of understanding the data within a study and how important findings can be made that are outside of the principle research questions and are often found in the fringe cases of your study. Unless one closely examines all the data points and asks questions regarding their relationships, information will undoubtedly go unnoticed. Tong Xu is a very talented physicist and regularly demonstrated how important it was to consider questions and interpret results from first principles - in the end everything is explainable and one should seek to do so with respect to basic concepts that are well founded. Thank you, all of you, for sharing your gifts with me.

While less directly involved in my work, the people with whom I spent most of my office/study time with also are deserving of my thanks. My peers, my colleagues, my friends, provided useful suggestions, necessary distractions, and companionship beyond the boundaries of study. So, Sarah Cuddy-Walsh, Owen Clarkin, Jennifer Renaud, Hanif Juma, Odai Salman, Chad Hunter, Zahra Ashoori, Robert Miner, Eric Christiansen, Chris Dydula, Ming Liu, Alexandra Bourguoin, Marc Chamberland, Martin Martinov, Nick Majtenyi, Iymad Mansour, and Nathan Murtha, thank you for your friendship, your help, and your encouragement.

Several other staff at researchers at University of Ottawa Heart Institute and Carleton University were also very helpful and supportive during my studies. Dr. R. Glenn Wells, thank you for helpful comments on several presentations that I delivered and also for letting me borrow one your text books – at the time of writing this I still have yet to return it to you. Ms. May Aung, Ms Kimberly Gardner, and Ms. Azmina Merani, are nuclear medicine technologists at UOHI, all of whom were incredibly helpful, friendly, and patient with me when I needed to use the PET scanner console. Thank you all very much for your help, getting to know each of you was my privilege. Ms. Alison Conley, and Ms. Ann Nguyen of UOHI Research Services helped me on many occasions with travel/funding applications, thank you both. Ms. Eva Lacelle and Ms. Temi Gouti both held the incredibly important position of Graduate Student Administrator with the Carleton Physics Department. These two individuals acted as the buffer between anxious graduate students (myself, at least) and the confusing world of university bureaucracy, most importantly both of you helped make sure that I received my funding; thank you very, very much. Several Carleton Physics faculty members involved with advising

graduate students also deserve my thanks; Dr. Heather Logan, Dr. Paul Johns, Dr. Kevin Graham, thank you all very much for your dedication to graduate student success in our department.

I would also like to acknowledge the research funding agencies who not only supported my work, but who help facilitate the provision of financial support for graduate students who, in many cases, sacrifice higher pay in the workforce to pursue their passions and help drive Canadian research. The Government of Ontario, the National Sciences and Engineering Research Council of Canada, the Canadian Institutes of Health research, the Carleton University Faculty of Graduate and Post-Doctoral Affairs, the Ottawa Heart Institute Research Corporation, and the IEEE Nuclear and Plasma Sciences Society, have all contributed to varying degrees to my research and travel funding.

To my parents, thank you for your love and support not only during this degree but during my whole life. I am sure that you have shaped the curiosities I now have about the world which have certainly guide me to path on which I now find myself. You have helped me, and my own young family, with so many things that allowed me to continue to focus on my research – I only hope that I can someday return the kindness.

To my wife and partner, Robyn, it is impossible to express in words the appreciation, admiration, and respect that I have for you. You supported us and made the life that we have built together possible while I underwent this half-decade pursuit. Beyond your love and encouragement, you have given me (us) two beautiful sons who at the current ages of 3 years and 2 weeks, have completely reshaped my life, values, and purpose. I will never fail to recognize and appreciate the personal sacrifices that you have made so that we can have the life we'd hoped for while I spent this time chasing a dream. Thank you.

*To my sons,
Henry and Oliver.*

“I would not be one of those who will foolishly drive a nail into mere lath and plastering; such a deed would keep me awake nights. Give me a hammer, and let me feel for the furring. Do not depend on the putty. Drive a nail home and clinch it so faithfully that you can wake up in the night and think of your work with satisfaction -- a work at which you would not be ashamed...”

This passage, from Henry David Thoreau’s *Walden*, really struck me when I first came upon it. What I took from it was this; whatever it is that you choose to do, do it with all your heart and to the best of your ability.

Contributions

The work described in this thesis represent a detailed summary of my research activities during my doctoral studies. All work was performed under the co-supervision of (in no particular order) Dr. Ran Klein, Dr. Robert deKemp, and Dr. Tong Xu, each of whom provided guidance to me while designing studies, analyzing data, interpreting results and preparing materials for dissemination during presentations or manuscripts. This work represents the most comprehensive application of the Positron Emission Tracking (PeTrack) algorithm to the clinical setting for the purpose of patient motion compensation in cardiac PET imaging. It also represents the first application of PeTrack for to whole-body motion correction in dynamic cardiac PET studies, as well as to cardiac PET studies that used ^{13}N -Ammonia as the radiotracer.

All image reconstructions described in this thesis were performed using research software developed by the manufacturer (GE Healthcare) of the PET scanners at the University of Ottawa Heart Institute. I developed various additions to this package that were necessary to generate gated images from list-mode data. I created utilities that gated dead time and single-event count rate data from the list-mode data files, incorporated respiratory and body-motion triggers from algorithms developed and/or implemented, incorporated spatial transformations to extend the software to permit motion compensation, and extended the DICOM file writing utilities to include fields needed for image viewers to correctly interpret 4D image data sets. Lastly, I extended the software to perform post-reconstruction image registration for estimating patient body motion. Prior to my use of it, the reconstruction software was significantly refactored for ease of use by Dr. Chad Hunter.

I drafted the study protocol which was submitted to the UOHI Ethics Board to attain retrospective access to the clinical data sets described in this thesis. The protocol was additionally reviewed by Dr. Robert deKemp and Ms. Linda Garrard. The protocol was modified by myself and reviewed by Dr. Tong Xu for submission to the Carleton University Ethics Board to attain permission to conduct my research involving human patient data. I collected all clinical data sets used within this thesis following the de-identification and archival measures described in the REB-approved study protocol.

The PeTrack ADROI code used extensively throughout my work was developed by Dr. Marc Chamberland and Dr. Tong Xu. I contributed to this software package by including methods for producing respiratory and body-motion triggers from PeTrack motion traces. I implemented a respiratory trigger detection algorithm had been previously published (described in Chapter 3) and created two methods for body-motion detection (described in Chapter 4 and Chapter 5). I included methods for stochastically sampling list-mode data files to manipulate image noise (described in Chapter 3). Based on the PeTrack ADROI code, I also implemented a previously published data-driven motion tracking algorithm known as the Centroid-of-Distribution (COD) method which modifications that allows the user to limit the list-mode events that are used during tracking (described in Chapter 5). I developed an automated tool to measure myocardial wall thicknesses from PET images as described in Chapter 3 and Appendix A. I also proposed a respiratory trigger quality control framework based on previous work aimed at cardiac (ECG) triggering.

I designed the phantom experiment described in Chapter 4 and fabricated a translatable table with which rigid patient motion was simulated. The experiment was performed by Dr. Robert deKemp, Dr. Tong Xu, Dr. Ran Klein and myself.

I disseminated my research through peer-review publication, conference proceedings, and oral and poster presentations. These are listed below.

Peer-reviewed papers:

1. Spencer Manwell, Ran Klein, Tong Xu, Robert deKemp, “Clinical comparison of the Positron Emission Tracking (PeTrack) algorithm with the Real-Time Position Management System for respiratory gating in cardiac positron emission tomography”, *Medical Physics* 2020; 47(4): 1713-1726, DOI: 10.1002/mp.14052.^{i,151}

Conference proceedings:

1. S. Manwell, R. Klein, R. deKemp, T. Xu, “Whole-body motion correction ¹³N-ammonia myocardial perfusion imaging using positron emission tracking”, 2019 IEEE Nuclear Science Symposium and Medical Imaging Conference (NSS/MIC) Record, Manchester UK, November 2019, pp 1-5, DOI: 10.1109/NSS/MIC42101.2019.9059704^{ii,168}
2. S. Manwell, R. Klein, R. deKemp, T. Xu, “Whole-body motion correction in cardiac PET/CT using Positron Emission Tracking: A phantom validation study”, 2018 IEEE Nuclear Science Symposium and Medical Imaging Conference

ⁱ This publication was modified for inclusion in this thesis and comprises the content of Chapter 3.

ⁱⁱ The poster for this abstract was shown again at the Carleton University Life Sciences Day, Ottawa, ON, May 2018 and awarded 1st place among graduate student posters.

(NSS/MIC) Record, Sydney, AU, October 2018, pp 1-3, DOI:

10.1109/NSSMIC.2018.8824715.^{iii,167}

3. S. Manwell, M. Chamberland, R. Klein, T. Xu, R. deKemp, “Evaluation of the clinical efficacy of the PeTrack motion tracking system for respiratory gating in cardiac PET imaging”, Proc. SPIE 10132, Medical Imaging 2017: Physics of Medical Imaging, 1013251 (9 March 2017), Orlando, FL, 10.1117/12.2255544.¹⁵⁷

Conference abstracts:

1. Spencer Manwell, Ran Klein, Tong Xu, and Robert deKemp, “‘Bad-Breath’ Rejection: quality control metrics for respiratory gating in PET/CT.”, Society of Nuclear Medicine and Molecular Imaging (SNMMI) Annual Meeting, Anaheim, CA, June 2019. Published in J. Nucl. Med. May 1, 2019, vol. 60 no. supplement 1, 1366.
2. Spencer Manwell, Ran Klein, Tong Xu, and Robert deKemp, “Data-driven respiratory gating in cardiac PET/CT using the Positron Emission Tracking Algorithm”, Society of Nuclear Medicine and Molecular Imaging (SNMMI) Annual Meeting, Philadelphia, PA, June 2018. Published in J. Nucl. Med. May 1, 2018, vol. 59 no. supplement 1, 16.
3. Spencer Manwell, Ran Klein, Robert deKemp, Tong Xu, “Patient motion management using the positron emission tracking (PeTrack) algorithm in cardiac

ⁱⁱⁱ This abstract was reformatted abstract as an oral presentation and presented at The Ottawa Hospital Department of Medicine Research Day, Ottawa, ON, May 2019, and awarded Best Graduate Student Scientific Presentation. The original poster was also presented at the Carleton University Life Sciences Day, Ottawa, ON, May 2017 and awarded 2nd place among graduate student posters.

PET without time-of-flight”, Canadian Organization of Medical Physicists 63rd
Annual Scientific Meeting, Ottawa, Canada, July 2017.

Table of Contents

Abstract	i
Acknowledgements	iii
Contributions	vii
Table of Contents.....	xii
List of Tables.....	xvii
List of Illustrations	xix
List of Acronyms.....	xxxv
Chapter 1 Introduction.....	1
1.1 Physics of Nuclear Medicine.....	2
1.1.1 Nuclear Structure, Stability and Radioactive Decay.....	2
1.1.2 Interactions of Radiation with Matter	8
1.2 Positron Emission Tomography	13
1.2.1 Photon Detection with Scintillators	14
1.2.2 PET System Design and Performance	20
1.2.2.1 Spatial Resolution	24
1.2.2.2 Energy Resolution.....	25
1.2.2.3 Timing Resolution.....	25
1.2.2.4 Dead Time and Count Rate Performance.....	25
1.2.2.5 Sensitivity.....	27
1.2.2.6 Performance Characteristics of GE Discovery 690 PET/CT System.....	28
1.2.3 Data Correction for Quantitative PET	29
1.2.3.1 Normalization correction	30
1.2.3.2 Random Coincidence Correction	30
1.2.3.3 Dead Time Correction.....	31

1.2.3.4	Attenuation Correction.....	31
1.2.3.5	Scatter Correction.....	33
1.2.4	Tomographic Image Reconstruction.....	35
1.3	Imaging the Heart with PET.....	40
1.3.1	Anatomy of the Heart and Electrocardiographic Signals.....	40
1.3.2	Myocardial Perfusion Imaging with PET.....	45
1.3.3	Kinetic Tracer Modelling and Estimate of Absolute Myocardial Blood Flow....	51
1.4	Thesis Summary.....	57
Chapter 2	Patient Motion Tracking and Compensation.....	59
2.1	Patient Motions: Respiratory, Cardiac and Body.....	59
2.2	Motion Tracking.....	63
2.2.1	Hardware-Based Tracking.....	65
2.2.2	Data-Driven Tracking.....	68
2.3	Compensation and Correction.....	71
2.3.1	Breath-hold Techniques and Patient Immobilization.....	71
2.3.2	Respiratory and Cardiac Gating.....	73
2.3.3	Motion Correction.....	76
2.4	Positron Emission Tracking (PeTrack).....	80
2.4.1	The Tracking Algorithm.....	80
2.4.2	Motivation for the Use of PeTrack in PET.....	85
Chapter 3	Respiratory Gating in Cardiac Perfusion PET.....	89
3.1	Motivation.....	89
3.2	Methods.....	90
3.2.1	Respiratory-Gated Acquisition.....	90
3.2.2	Patient Population.....	92
3.2.3	Respiratory-Signal Generation.....	93

3.2.4	Respiratory-Gating and Image Reconstruction.....	94
3.2.5	Measurements for Comparison.....	95
3.2.6	Comparing Respiratory Signals and Triggers.....	96
3.2.7	Comparing Image-Based Measurements.....	98
3.2.8	Statistical Methods.....	101
3.3	Results.....	101
3.4	Discussion.....	109
3.4.1	Respiratory Signal and Trigger Measurements.....	110
3.4.2	Quality Control.....	113
3.4.3	Image based motion estimates.....	116
3.4.4	Considerations for PeTrack.....	117
3.4.5	Clinical Use of PeTrack for Respiratory Gating.....	119
3.5	Conclusion.....	121

Chapter 4 Whole-Body Motion Correction in Myocardial Perfusion Imaging with PET/CT 122

4.1	Motivation.....	122
4.2	Methods.....	123
4.2.1	Whole-Body Motion Correction Framework.....	123
4.2.2	Validation Using an Anthropomorphic Torso Phantom.....	127
4.2.3	Application to ¹³ N-Ammonia Perfusion Studies.....	128
4.2.4	Quantitative Measurements.....	129
4.3	Results.....	133
4.3.1	Motion Tracking Validation.....	133
4.3.2	LV Wall Thickness and Blood Pool Volume Comparison.....	137
4.3.3	Effects of Motion Correction on CNR.....	141
4.3.4	Relative Perfusion and Left-Ventricular Volumes.....	144

4.4	Discussion.....	144
4.5	Conclusions	150

Chapter 5 Whole-Body Motion Correction for Absolute Blood Flow

Quantification	151
5.1	Motivation	151
5.2	Methods	152
5.2.1	Centroid of Distribution (COD) Motion Tracking.....	152
5.2.2	Whole-Body Motion Detection	155
5.2.3	Motion Estimation and Correction	158
5.2.4	Clinical Dataset.....	162
5.2.5	Verification of COD Tracking and Image Registration Methods.....	164
5.2.6	Absolute Blood Flow Quantification and Figures of Merit	166
5.3	Results	170
5.3.1	Verification of COD Tracking.....	170
5.3.2	Verification of the Image Registration Method.....	173
5.3.3	Evaluation of the Body-Motion Detection and Estimation Methods.....	174
5.3.4	Sensitivity of Kinetic Modelling Quality Metrics to Motion.....	176
5.3.5	Patient Motion Assessment Among Severe Motion Cases.....	177
5.3.6	Kinetic Modelling Results Among Severe Motion Cases	182
5.4	Discussion.....	187
5.4.1	Motion Estimation with PeTrack.....	188
5.4.2	COD Motion Estimation.....	189
5.4.3	Optimization of Motion Detection.....	192
5.4.4	Motion Estimation Using Image Registration	195
5.4.5	Classification of Cases Which Could Benefit from Motion Correction	197
5.5	Conclusions	199

Chapter 6	Conclusions and Future Work.....	201
6.1	Summary of Findings	201
6.2	Final Thoughts and Suggestions for Future Work.....	203
Appendices	207
Appendix A	Left-Ventricular Wall Segmentation from 1-D Profiles	207
Appendix B	Elastix Image Registration Input Parameters.....	213
References	215

List of Tables

Table 1.1 Selection of physical properties of three inorganic scintillation crystals commonly used in PET systems. Measured values correspond to interactions with 511 keV annihilation photons. These data have been reproduced from Table 2.5 of <i>Physics and Instrumentation in PET</i> by D. L. Bailey, J. S. Karp, and S. Surti. ²²	15
Table 1.2 Performance measurements of the GE Discovery 690 PET system. ²⁷	29
Table 1.3 Physical and practical characteristics of commonly used PET radiotracers for MPI imaging. The references associated with each characteristic are indicated after their names in the first column.....	51
Table 2.1 Five commercial respiratory gating systems are described. Comments about their use, strengths, and weaknesses are also provided. Information about these systems has largely been attained from the following review papers on the topic of motion management in PET imaging: <i>Motion-tracking hardware and advanced applications in PET and PET/CT</i> by V. Bettinardi et al. ⁹⁴ ; and <i>Respiratory Motion in Positron Emission Tomography/Computed Tomography: A Review</i> by S. A. Nehmeh and Y. E. Erdi. ¹⁰⁰	67
Table 3.1 Mean anterior and inferior LV wall widths for each reconstruction method for the entire cohort as well as for the subset of cases with SI motion ≥ 7 mm. Additionally, the mean differences are shown for each paired comparison. Comparisons with statistically significant differences ($p < 0.05$) are written in bold font.....	107
Table 3.2 SI motion measurements for each gated reconstruction method for the cohort as well as for the subset of cases with motion ≥ 7 mm. Additionally, the mean differences	

in SI motion among all paired comparisons are shown. Statistically significant differences ($p < 0.05$) are emphasized with bold font. 108

Table 4.1 LV thicknesses measured for each phantom trial averaged among all 16 segments. Standard deviations (SD) are also provided. Reported p-values correspond to a two-tailed paired Student's *t*-test for each trial compared to the reference measurements – data were paired by segment for these tests. The image label 'MC' indicates motion correction. 139

Table 4.2 LV thicknesses measured for the clinical dataset averaged among all 16 segments. Standard deviations (SD) are also provided. Reported p-values correspond to a two-tailed paired Student's *t*-test for acquisition between non-corrected and corrected images – data were paired by segment for these tests. Patients were labelled with the characters A, B, and C, and the physiologic state of each acquisition is indicated. Patient motion indicators such as the number of triggers and motion frames as well as the maximum displacement magnitudes are also provided 140

Table 4.3 Mean relative myocardial perfusion in the LV among the clinical dataset of this study. Measurements are reported within the LAD, LCX, and RCA territories as well as for the entire LV. The measurements were made from the non-corrected and motion-corrected images. 144

Table 5.1 Summary statistics of proposed motion correction figures of merit for motion-negative ($N_{MN} = 13$) and motion-positive ($N_{MP} = 4$) groups. The relative change in the value from the motion-negative to motion-positive groups are also provided. 176

List of Illustrations

Figure 1.1 Partial decay scheme of ^{82}Rb (rubidium-82) which decays primarily via β^+ decay to produce stable ^{82}Kr (krypton-82). Solid horizontal lines indicate various energy levels of the parent and daughter nuclei, each of which are labelled with their energy levels. Note that the ‘g.s.’ line of ^{82}Rb corresponds to its ground state. The solid and dashed arrows indicate isobaric and isomeric transitions, respectively. Each β^+ transition is labelled with the associated probabilities of occurring, and similarly the γ decay transitions are labelled with their relative likelihoods with respect to the energy level from which they originate. The data in this figure were acquired from the nuclear data publication of the Laboratoire National Henri Bequerel in Gif-sur-Yvette Cedex, France.¹⁴

..... 7

Figure 1.2 Schematic representation of a colinear and non-colinear annihilation of an electron-positron pair. The energy and momentum of the positron, β^+ are indicated as E_+ and \mathbf{p}_+ , respectively in the upper row of the image (“Interaction”). The annihilation photons and their energies are denoted at $\gamma_1, \gamma_2, E_{\gamma_1}$, and E_{γ_2} , respectively in the lower row of the image (“Annihilation”). It is assumed that the electron has zero kinetic energy and momentum..... 11

Figure 1.3 Schematic representation of a full-ring multi-slice PET detector configuration. Cross-sectional views from the front face of the gantry and from the side are shown in sub-figures A, and B, respectively. Each gray rectangle represents a detector. In sub-figure A, the transverse coordinate directions, \mathbf{x} , and \mathbf{y} , are depicted by dashed lines. The transverse origin is shown as a circle at the intersection of the \mathbf{x} and \mathbf{y}

axes. A line of response (LOR), which originates at the position marked by the lightning bolt, subtends an azimuthal angle φ with the positive y axis. A model patient is represented by the blue ellipse. In sub-figure B, the span of axial direction, or z axis, is shown. The same LOR subtends a polar angle θ with the positive z axis. The vector $s(s, u)$ describes the position of the LOR..... 21

Figure 1.4 Arrangement of 64 scintillation crystal elements and 4 PMTs in detector block design. The block quadrants A, B, C, and D correspond to unique PMTs. 22

Figure 1.5 An example oblique projection plane intersecting an eccentric cylindrical object. The sinogram elements of this projection are described by $p = (s, \varphi, u, \theta)$. The transverse and axial components of the projection are shown in left and right drawings, respectively. Individual LORs are depicted as double-headed arrows. The origin of the FOV is marked as O 37

Figure 1.6 An example sinogram and image from a PET acquisition of an anthropomorphic torso phantom. This sinogram corresponds to the set of projections described by (s, φ) with a polar angle $\theta = 0^\circ$ and a fixed u coordinate. A reconstructed transverse image of the phantom is shown on the right and is defined on x and y for a fixed z -coordinate. The most intense feature of the image is the cardiac model which has a horseshoe-like appearance in this perspective. An air-bubble in the cardiac insert caused the void at the highest region of the insert. 40

Figure 1.7 Basic anatomical diagram of the heart containing the four chambers, valves and major veins and arteries. This figure has been reproduced from the public domain clipart repository *WPClipart*. The file was accessed on February 10, 2020..... 42

Figure 1.8 The American Heart Association 17-segment model provides a 2D polar map representation of the left ventricle. The coronary artery territories are indicated with gray shading. The region corresponding to the left-anterior descending (LAD), left-circumflex (LCX) and right coronary (RCA) arteries are shown in white, light gray, and gray, respectively. The outer annulus (segments 1 – 6) corresponds to the basal region, the middle annulus (segments 7 – 12) corresponds to mid region, the inner annulus (segments 13 – 16) corresponds to the apical level of the LV, and the apex (segment 17) is shown at the center. 44

Figure 1.9 Schematic representation of a normal ECG signal. The P, QRS and T waves are indicated along the waveform. So too are the phases of ventricular systole and diastole. The period spanning subsequent R-waves is referred to as the R-R interval. The amplitude of the R-wave makes is easy to detect on ECG signals and serves as an indicator of the start of each cardiac contraction. The waveform shown in this figure was simulated using an open source MATLAB function called *ECG simulation* and was created by R. Karthik. 45

Figure 1.10 One- (A) and Two-Tissue-Compartment (B) model representations of blood flow within the myocardium. In both cases, capillary (Blood) regions and myocardial tissue are coloured as white and gray, respectively. Black arrows indicate the directions of tracer flux across compartmental boundaries, each of which is labelled with its respective rate constant. In the Two-Compartment model the myocardial tissue region is divided into two more specific compartments which are the myocytes and the extracellular space..... 53

Figure 1.11 Example kinetic modelling data from a clinical dataset. The time-activity curve (A) data are shown for the measured blood pool (red), measured myocardium (blue dots), the modelled activity of the myocardium (blue line), and modelled tissue (cyan) activity. The blood pool data have been averaged over a volume of interest in the LV cavity and the myocardium data shown correspond to an average across the entire LV. The polar map (B) depicts the estimated blood flow values in each of the voxels sampled within the myocardium. The mean \pm SD flow value for this case is also indicated. 56

Figure 2.1 Schematic representation of the gating process. Triggers can be derived from physiologic monitoring devices, e.g. ECG or respiratory monitoring systems, as well as based on pre-defined dynamic time frames. In the dynamic acquisition the list-mode data from each reconstructed frame come from contiguous blocks. In the ECG or respiratory gated acquisitions, the data corresponding to each frame are sampled throughout the original data set in a repeating fashion corresponding to the physiologic state of each frame. The ECG signal shown here was produced using an open-source function by Kathrik Raviprakash (2020). 75

Figure 2.2 The adaptive region-of-interest procedure is exemplified in this figure which shows the histogram of LORs with a perpendicular distance 'r' (denoted in this work as dLn, m) from the estimated marker position from a phantom acquisition. The columns with hashed lines indicate the events following the initial ROI and TOF based rejection techniques. The solid black line represents a fit of the combined marker PDF and linear background model. The marker PDF and linear background fits are shown as the dotted and dashed lines, respectively. The solid gray bars indicate the events that remain following subtraction of the linear background fit. In this example the ADROI size was

set as 8 mm. This figure was used with permission from the work of Chamberland, deKemp and Xu.⁹² 84

Figure 3.1 Photograph of the GE Discovery 690 PET/CT scanner used in this work. An anthropomorphic torso phantom is set on the bed and its situated at the level of the CT system the lies near the front face of the scanner. The geometric axes have been annotated using red arrows. The x -axis corresponds to the lateral direction in the photo. The y -axis corresponds to the vertical direction. The z -axis, shown here going to the page, corresponds to the axial direction of the scanner coordinate system..... 91

Figure 3.2 Anterior-inferior activity profiles acquired from the reoriented images of one patient. Image A depicts five 1D profiles that are indicated in the inset vertical long-axis slice image. Image B depicts the average of the five raw profiles as well as the smooth profile which was extracted from the same image volume after convolution with a 3D 7.5 mm FWHM Gaussian smoothing kernel. Image B also depicts the peak and trough locations, which were automatically generated to identify the anterior wall, LV blood pool and inferior wall regions. Note that the inset image corresponds to the smoothed volume. 100

Figure 3.3 Histogram of log-transformed, normalized respiratory rates pooled from RPM and PeTrack gating systems for all 50 acquisitions. The shaded area corresponds to the respiratory cycles that fall within the acceptance criteria determined using the boxplot approach. The limits determined using this method were found to be [38.3, 161.7%] of the patient-specific median respiratory rate after the log-transformation was applied... 102

Figure 3.4 Example respiratory signals and triggers (A) and respiratory rate histogram (B) from a single acquisition. Data are shown for each gating system. Image A shows

high concordance between RPM and PeTrack signals ($\rho = 0.81$, $p < 0.001$) within a randomly selected temporal window of 200 s to 250 s. Additionally, the respiratory triggers generated by each approach are overlaid on their corresponding signals. The number of triggers for each are indicated. Image B shows the respiratory rate histogram for the same case. Respiratory rate acceptance limits are denoted by the vertical dashed lines. The percentage of respiratory cycles identified as outliers is indicated for each gating approach. 104

Figure 3.5 Median respiratory rates (A) and IQR (B) for each gating system for the entire cohort. Mean, ± 1 SD, and individual measurements are represented as solid-red lines, dashed-gray lines, and gray points, respectively. P-values produced from paired *t*-tests are shown in instances where statistically significant differences were observed. 105

Figure 3.6 Respiratory cycle outlier rates for each of the gating systems. Mean, ± 1 SD, and individual measurements are represented as solid-red lines, dashed-gray lines, and gray points, respectively. P-values produced from paired *t*-tests are shown in instances where statistically significant differences were observed. RPMretro had significantly fewer outliers compared to RPM and PT..... 106

Figure 3.7 LV width measurements for both anterior and inferior regions for entire cohort (A) as well as the subset of cases with mean SI LV motion ≥ 7 mm (B). The means, ± 1 SD ranges, and individual measurements for each are indicated by the solid-red lines, dashed-gray lines, and gray points, respectively. Statistically significant p-values, computed from paired *t*-tests, are indicated..... 108

Figure 3.8 SI motion of the LV observed from each gated image series for the entire cohort (A) and the subset of cases with mean motion ≥ 7 mm (B). The mean differences,

± 1 SD ranges, and individual measurements for each are indicated by the solid-red lines, dashed-gray lines, and gray dots, respectively. Statistically significant p-values, computed from paired *t*-tests, are indicated. 109

Figure 3.9 Inter-gate motion comparison for the exemplary case selected for Figure 3.4. On the left, coronal views at end-expiration are shown for comparison from non-gated, PeTrack, RPM, and RPMretro images. Note that the non-gated images were statistically sampled such that they were noise-matched with the gated images. On the right, the superior-inferior displacement of the LV as observed across the six gates using each gating system is plotted: PeTrack in blue squares, RPM in red circles, and RPMretro in gray triangles. Displacements were recorded with respect to the corresponding phase-averaged position. In this example the motion extent observed while gating with PeTrack and RPMretro was substantially larger than that observed with RPM. Note that the images shown here were smoothed with a 10 mm FWHM 3D Gaussian kernel for display purposes. 115

Figure 4.1 An example 1D motion trace is shown from the patient cohort to demonstrate the production of motion triggers after applying the moving mean filter. To simplify the example, only the motion the left-right direction is shown here. The original and filtered traces are depicted by blue and black curves, respectively. The motion triggers are shown as vertical, dashed lines. The motion thresholds are also indicated as the vertical limits of the gray bands which span the domain of the plot. 125

Figure 4.2 A schematic representation of the whole-body motion correction algorithm. Prior to the reconstruction of each motion frame, the AC map was transformed rigidly (3D) based on the mean displacement of the marker during the frame. After

reconstruction, motion frames were spatially aligned using the reversed transformations. After alignment, a single weighted-average image was produced where the weights were determined by the number of coincidence events in each frame. This figure has been reused¹⁶⁸ with some modification with permission; original copyright 978-1-7281-4164-0/19 ©2019 IEEE..... 126

Figure 4.3 Diagram of the radial profile locations cast on the reoriented image volumes for the purpose of making LV thickness measurements. Image A shows a single short-axis slice on which four radial profiles can be seen originating at the LV center and spanning outward across the LV wall. Image B shows a horizontal long-axis image slice depicting the series of short axis slices that were used. The figure is derived from the reference trial reconstruction of the anthropomorphic phantom. A region within the model LV wall can be seen within the apex to be void of activity; this region corresponds to an air-bubble. Note that these profile indicators are only qualitative representations of the profile locations that were actually used for the measurements. 131

Figure 4.4 Phantom motion trace derived from PeTrack algorithm. Images A and B depict the axial and lateral displacements as a function of time during the acquisitions. Traces are shown for each acquisition: reference (blue); axial motion (red); lateral motion (yellow); and diagonal motion (purple). 134

Figure 4.5 Correlation (A) and Bland-Altman (B) plots for the phantom study indicating the agreement of motion measured using PeTrack to that measured in each of the non-corrected (Dynamic) ‘motion-frames’. Measurements for the axial, lateral, and diagonal motion trials are indicated by red, yellow and purple points, respectively. Plot A contains a grey line of identity and a black line of best fit. Only the dominant motion

component was used for each case, e.g. axial motion is considered for the Diagonal case. In plot B, the paired differences between the dynamic image and PeTrack measurements are denoted by ‘ Δ ’..... 134

Figure 4.6 Comparison of marker 3D displacements from PeTrack (PT) and image-based (Img) measurements for the stress acquisition of patient B. Image measurements were made from dynamic reconstructions of the entire acquisition with 1-minute frames. Symbols with error bars indicate the centroid and ± 1 SD limits of the marker in each dimension (RL = right-left, AP = anterior-posterior, IS = inferior-superior) for each of the frames. Note that the standard deviations of the centroids were calculated by using Eq. 3.1. This figure has been reused¹⁶⁸ with permission and was modified from its original version; original copyright 978-1-7281-4164-0/19 ©2019 IEEE..... 136

Figure 4.7 Correlation (A) and Bland-Altman (B) plots comparing PeTrack and image-based marker displacements for all human acquisitions. The PeTrack displacements shown here were averaged over the 1 min duration of each dynamic frame. The paired differences in B were computed as ‘PeTrack - Image’. The Bland-Altman plot shows excellent agreement giving strong evidence for tracking quality with PeTrack in this cohort. 136

Figure 4.8 17-segment polar maps of the model LV of the phantom indicating absolute changes in the thickness compared to the reference image for each motion case before (‘Non-Corrected’: A, C, and E) and after motion correction (‘Corrected’: B, D, and F). All values are in units of millimeters. Graphically, the colour intensity reflects the severity of mismatch between a segment thickness of a trial image with that of the reference. Note that the colour map is identical for all sub-figures..... 138

Figure 4.9 LV blood pool volume measurements for each of the clinical acquisitions. Values from the Non-Corrected and Corrected images are shown in red and yellow, respectively. 141

Figure 4.10 Example short axis images from the four phantom acquisitions. The Reference, Non-Corrected, and Corrected images for each motion case are shown to emphasize the effects of motion correction on this data set. All images are displayed on the same intensity range. This figure has been reused¹⁶⁷ with permission; original copyright 978-1-5386-8495-5/18 ©2018 IEEE. 142

Figure 4.11 CNR bar plots for the phantom (A) and ¹³N-ammonia (B) acquisitions. Reference, non-corrected and motion-corrected data are shown in blue, orange, and yellow, respectively. Note that in sub-figure A, the Reference column is repeated for each of the three motion cases. In sub-figure B, individual patients are indicated by the character labels A, B, and C and the physiological state or rest or stress is also indicated. 143

Figure 4.12 Example images of the stress scans of the clinical data set. Non-corrected and corrected images are shown in the first and second columns, respectively. All images are displayed on a common intensity range. The arrows on the images of Patient C demark the most pronounced intensity change associated with motion correction. This case demonstrated the largest maximum displacements among the clinical data set. 143

Figure 4.13 Effect of radioactive decay between phantom acquisitions on CNR. The signal decay, CNR and acquisition start times are indicated by the solid line, dashed line, and markers, respectively. All data have been normalized to their respective initial value to focus on their relative changes over time. 147

Figure 5.1 Schematic representation of the acceptance/rejection method used to determine the set of LORs used for COD tracking. The volume of interest (VOI) was drawn about the heart (shown in red) as a black rectangle. Two LORs are drawn as dashed arrows originating from the annihilation locations indicated by the lightning bolts. While the true annihilation locations cannot be known, they are indicated here for demonstration purposes. The most-likely annihilation (MLA) points are indicated as empty circles. While both LORs have MLA points within the VOI, the probability of the LOR shown in the upper left is small and is thus rejected. The other, however, likely originated within the LV myocardium and has high probability of being included. 154

Figure 5.2 Example motion detection where the processed trace is depicted along the calculated normal vector. Only the anterior-posterior component of the motion trace is shown. The time domain is split to isolate two body motion triggers (dashed vertical lines) that were identified at 103 s and 238 s. The trigger at 103 s (trigger ‘a’) corresponds to change in position with a relatively steep gradient, whereas the trigger at 238 s (trigger ‘b’) corresponds to a low gradient, steady change in position. The local linear fits at each of the triggers are shown by red dashed lines. The angles between the generalized vectors and the vertical direction are indicated as for each trigger. Note that the length of the arrows is arbitrary as they are scaled automatically to ensure the arrow tips do not cross adjacent arrows. 156

Figure 5.3 Demonstration of the FlowQuant LV sampling method. The spline fit, shown as a solid red curve, and its control points, empty circles, are shown on horizontal long-axis (HLA) and vertical-long axis (VLA) images. The blood sampling volumes of interest are indicated as regions bounded by a solid black border with the labels A

(atrium), B (base), and C (cavity). Dashed lines represent the profiles along which the myocardium is sampled. Note that the apical slices which appear to fan outward are defined by conical surfaces which intersect the myocardium; all other slices are planar short-axis slices. The red dashed line additionally indicates the basal extent of the LV used for myocardial sampling. 168

Figure 5.4 Centroid of Distribution (COD) motion trace (A) derived from the reference phantom acquisition where no motion occurred and the LOR probability cut-off (pCut) was set as 0.0. The components belonging to the right-left, anterior-posterior, and inferior-superior directions of motion are shown as blue, orange, and yellow, respectively. The mean position of each component and the corresponding standard deviation (SD) are plotted as functions of pCut in sub-figures (B) and (C), respectively. 171

Figure 5.5 Inferior-superior motion trace components observed while tracking the phantom motion using COD and PeTrack. The COD traces are shown for $pCut \in [0.1, 0.3, 0.4]$ to simplify the figure. The domain of 100 – 200 s is shown on the right to enhance the differences among the various COD traces. 172

Figure 5.6 Inferior-superior component of the motion traces of PeTrack (gray) and COD (yellow) for the axial motion phantom acquisition. The triggers (t_{bm}) identified for each trace are also shown as dashed lines; they are colour-matched with the trace to which they belong. Due to the limited ability of COD to estimate motion, the trigger corresponding to the first change in position near 60 s was not detected. 174

Figure 5.7 Comparison of PeTrack (PT6D) and COD (CD6D) motion correction when image registration was used to estimate motion. The non-corrected image is shown for

comparison. Both motion corrected images demonstrated reduced blurring compared to the non-corrected image. The PT6D image shows marginally higher contrast in the model LV walls compared to CD6D. Some residual blurring at the lung-liver interface (indicated by arrows) is apparent in the CD6D image..... 175

Figure 5.8 PeTrack (upper plot) and COD (lower plot) motion traces for the D(Stress) acquisition. Right-left, anterior-posterior, and inferior-superior motion trace components are shown as blue, green, and red lines, respectively. Visual assessment indicated a 6 mm translation in the superior direction at 240 s, indicated by point **a**. 177

Figure 5.9 PeTrack (upper plot) and COD (lower plot) motion traces for the H(Rest) acquisition. Right-left, anterior-posterior, and inferior-superior motion trace components are shown as blue, green, and red lines, respectively. Visual assessment indicated a protracted 7 mm translation in the superior direction beginning between 240 and 360 s (indicated by point **a**) and continuing until the end of the acquisition. 179

Figure 5.10 PeTrack (upper plot) and COD (lower plot) motion traces for the H(Stress) acquisition. Right-left, anterior-posterior, and inferior-superior motion trace components are shown as blue, green, and red lines, respectively. Visual assessment indicated a protracted 10 mm translation toward the right which occurred between 180 and 600 s, indicated by point **a**. A counter-clockwise rotation about the inferior-superior axis of the patient around 240 s, indicated by point **b**. A series of clockwise rotations about the inferior-superior axis of the patient began around 480 s (indicated by point **c**) and continued until the end of the acquisition. 180

Figure 5.11 Transverse uptake images of the LV for acquisition H(Stress) for each of the reconstruction methods. These images were averaged from frames 10 – 17 of each

series, which corresponds to 90 – 1200 s of the acquisition. The PT3D image shows the most well resolved representation of the LV with the greatest contrast and uptake uniformity. 181

Figure 5.12 PeTrack (upper plot) and COD (lower plot) motion traces for the I(Stress) acquisition. Right-left, anterior-posterior, and inferior-superior motion trace components are shown as blue, green, and red lines, respectively. Visual assessment indicated a 10 mm translation toward the left which occurred around 360 s, indicated by point **a**. A protracted superior translation of 5 mm was also observed starting after 360 s and continuing until the end of the acquisition, indicated by point **b**..... 182

Figure 5.13 MBF measurements for the severe motion acquisitions. Mean measurements are shown as solid markers with error bars that span ± 1 SD. Minimum and maximum measurements for each reconstruction are indicated as empty markers. Data points corresponding to NMC, PT3D, PT6D, and CD6D reconstructions are shown as blue circles, green squares, red diamonds, and gray triangles, respectively. 183

Figure 5.14 Coefficient of determination (R^2) goodness-of-fit measurements for the myocardial TACs for the severe motion acquisitions. Mean measurements are shown as solid markers with error bars that span ± 1 SD. Minimum and maximum measurements for each reconstruction are indicated as empty markers. Data points corresponding to NMC, PT3D, PT6D, and CD6D reconstructions are shown as blue circles, green squares, red diamonds, and gray triangles, respectively. 184

Figure 5.15 Root-mean-square error ($RMSE_{TAC}$) goodness-of-fit measurements for the myocardial TACs for the severe motion acquisitions. Mean measurements are shown as solid markers with error bars that span ± 1 SD. Minimum and maximum measurements

for each reconstruction are indicated as empty markers. Data points corresponding to NMC, PT3D, PT6D, and CD6D reconstructions are shown as blue circles, green squares, red diamonds, and gray triangles, respectively. 184

Figure 5.16 Voxel-wise MBF precision (FlowSD) measurements for the severe motion acquisitions. Mean measurements are shown as solid markers with error bars that span ± 1 SD. Minimum and maximum measurements for each reconstruction are indicated as empty markers. Data points corresponding to NMC, PT3D, PT6D, and CD6D reconstructions are shown as blue circles, green squares, red diamonds, and gray triangles, respectively. 186

Figure 5.17 Voxel-wise total blood volume precision (TBVSD) measurements for the severe motion acquisitions. Mean measurements are shown as solid markers with error bars that span ± 1 SD. Minimum and maximum measurements for each reconstruction are indicated as empty markers. Data points corresponding to NMC, PT3D, PT6D, and CD6D reconstructions are shown as blue circles, green squares, red diamonds, and gray triangles, respectively. 186

Figure 5.18 LV polar maps depicting coefficient of determination (R^2) values for the myocardium TACs for the NMC and PT3D images for the H(Stress) acquisition. Anatomic labels ‘A’, ‘S’, ‘L’, and ‘P’ correspond to the anterior, septal, lateral, and posterior regions of the LV, respectively. Motion correction with PT3D approach improved R^2 values in the septal and lateral regions of the LV in the presence of severe lateral patient motion. 189

Figure 5.19 Centroid-of-Distribution motion trace for acquisition B(Stress) along each anatomical direction. Right-left, anterior-posterior, and inferior-superior components of

the COD displacement are shown in blue, green, and red, respectively. The body-motion triggers are shown as vertical dashed lines. This case exhibited no apparent motion following visual assessment of the NMC image..... 190

Figure 5.20 Partial PeTrack motion traces for C(Stress) (A) and D(Stress) (B) acquisitions where conspicuous translations were not detected as body motion triggers. Only the component of the trace which exhibited the dominant motion signal is shown here..... 192

List of Acronyms

1D – One dimensional

2D – Two dimensional

3D – Three dimensional

6D – Six dimensional

AC – attenuation correction

ADROI – Adaptive region of interest

AI – Anterior-inferior

AP – Anterior-posterior

APD – Avalanche photodiodes

ASNC – American Society of Nuclear Cardiology

BGO – Bismuth germanate

CAD – Coronary artery disease

CD3D – 3D motion correction with COD

CD6D – 6D motion correction with COD

CFR – Coronary flow reserve

COD – Centroid-of-Distribution

CT – Computed tomography

CTAC - Computed tomography attenuation correction

DICOM – Digital Imaging and Communication in Medicine

ECG – Electrocardiogram

FDG – Fluorodeoxyglucose

FOV – Field-of-view

FWHM – Full-width at half-maximum

HLA – Horizontal-long axis

IQR – Interquartile range

LA – Left atrium

LAD – Left-anterior descending artery

LCX – Left-circumflex artery

LOR – Line of response

LV – Left ventricle

LSO - Lutetium oxyorthosilicate

MAD – Mean absolute difference

MAF – Multiple acquisition frame

MBF - Myocardial blood flow

MC – Motion correction

MFR – Myocardial flow reserve

MLA – Most likely annihilation

MLEM – Maximum likelihood expectation maximization

MPI – Myocardial perfusion imaging

MR – Magnetic resonance

NaI(Tl) – Thallium doped sodium iodide

NMC – Non-motion corrected

OSEM – Ordered subsets expectation maximization

PCA – principal component analysis

PDF – probability density function

PET – Positron emission tomography

PeTrack – Positron emission tracking

PMT – Photomultiplier tube

PT3D – 3D motion correction with PeTrack

PT6D – 6D motion correction with PeTrack

RA – Right atrium

RCA – Right coronary artery

RL – Right-left

RMSE – Root mean square error

ROI – Region of interest

RPM – Real-time Position Management system

RV – Right ventricle

SA – Short axis

SDS – Summed differences score

SI – Superior-inferior

SiPM – Silicon photomultiplier

SL – Septal-lateral

SNMMI – Society of Nuclear Medicine and Molecular Imaging

SPECT – Single photon emission computed tomography

SRS – Summed Rest Score

SS – Sum of squares

SSS – Summed Stress Score

TAC – Time-activity curve

TOF – Time-of-flight

VLA – Vertical-long axis

VOI – Volume of interest

Chapter 1 Introduction

The connections between the fields of physics and medicine are not always intuitive or obvious to many. The advent of diagnostic imaging, for example, is intimately associated with the discovery of x rays in 1895 by the German physicist Wilhelm Röntgen.¹ In his work Röntgen demonstrated a new type of “ray” could be produced through collisions of electrons with metallic targets inside cathode ray tubes. An immediate application of this technology was to peer through the hand of a human subject (his wife) by developing a silhouette of these x rays onto a photographic plate. While diagnostic imaging is now ubiquitous it may be easy to take for granted that these discoveries, and the incredible technological advancement that followed, have given modern societies the ability to ‘look’ inside of the human body without the need to perform invasive surgical procedures. Modern medicine now benefits immensely from x ray and computed tomography (CT) as well as nuclear medicine imaging like single photon emission computed tomography (SPECT) and positron emission tomography (PET).

The work that is presented in this thesis is on the topic of patient motion compensation in PET imaging procedures that are aimed at diagnosing diseases of the heart, like ischemic coronary artery disease. The Chapter 1 reviews fundamental concepts in physics and medicine as a basis upon which the motivation for this work can be explained. Chapter 2 focuses on the problem of patient motion during PET imaging procedures and describes the current state of methods that have been developed to detect and/or compensate for patient motion. Chapters 3, 4 and 5 describe experiments that were performed to develop and evaluate a method of patient motion detection and correction in cardiac PET. In particular, Chapter 3 describes a study aimed at detecting and

compensating for respiratory motion in comparison to a conventional, commercial approach. Chapter 4 describes a proof-of-concept study in which a method of correcting for gross, or whole-body motion was developed and validated. The work of Chapter 4 was then applied to motion correction on dynamic images of the heart, prior to absolute blood flow quantification in cardiac PET studies as is described in Chapter 5. A summary and final thoughts are presented in Chapter 6 to conclude.

1.1 Physics of Nuclear Medicine

The aim of this section is to provide the reader with a review of the basics of radiation physics such that the fundamental principles of emission tomography are understood. The concepts of interest are as follows: atomic nuclei and their properties, nuclear instability and radioactivity, radioactive decay, and interactions of radiation with matter.

1.1.1 Nuclear Structure, Stability and Radioactive Decay

Our current understanding of the basic elements of matter stems from question raised thousands of years ago by Greek philosophers and began to take recognizable form toward the end of the eighteenth century.² The English chemist, John Dalton, postulated that chemical substances were composed of unique discrete elements, or atoms.³ It took nearly one hundred years before experimental evidence suggested that atoms had some internal structure. In 1897, the English physicist J. J. Thomson produced such evidence in the discovery of the electron⁴: a sub-atomic particle that carried with it a negative electric charge. Our model of the basic structure of matter was transformed once more in 1911 when E. Rutherford conducted experiments in his laboratory in Cambridge, UK that provided evidence that suggested the existence of a second atomic constituent: the positively charged nucleus about which electrons orbited.⁵ While the structure and nature

of the atomic nucleus continued to develop into the twentieth century, with, for example, the discovery of protons (by Rutherford in 1919)⁶ and neutrons (by Chadwick in 1932)⁷, scientists had already been directly observing their properties without knowledge of their existence. Around the time of Thomson's discovery of the electron, the nuclear property of radioactivity was observed by Henri Becquerel (1896).⁸ Additionally, Pierre and Marie Curie identified and classified various substances which were radioactive (1898).⁹ It is difficult to overstate the importance of these monumental discoveries which, truly, set the stage for the emergence of new branches of physics, collectively referred to as *modern physics*, which includes quantum, atomic, nuclear, particle, and, to a large extent, medical physics.

It was, perhaps, careless to mention the nuclear property of radioactivity without first describing the concepts of nuclear structure and stability (or instability). As the atom was found to have an inner structure, so too was the nucleus. The primary constituents of the nucleus are called nucleons, which encompass both protons and neutrons. Unique elements are characterized by a specific number of protons within their nucleus – the atomic number (Z). Two nuclei of the same element can differ in the number of neutrons (N) that they contain, these two are referred to as *isotopes*. The sum of the number of protons and neutrons gives the nuclear mass number (A). Nuclei that share the same mass number yet have different values of Z and N are referred to as *isobars*.

A very successful quantum mechanical model of the nucleus, known as the Shell Model¹⁰ describes the structure and arrangement of nucleons within the nucleus. Without some knowledge about the interactions of nucleons with each other it may seem counterintuitive how two (or more) protons, both with a positive charge, could co-exist in

such close proximity and not repel one another due to their electric charge. The explanation is associated with another fundamental force, the strong nuclear force, that exists between nucleons. This force acts only on very short lengths such that if two protons can be brought very close to each other, i.e. if they can be made to overcome the electric repulsion between them, the attractive nuclear force may overcome the electric repulsion and allow the protons to bind.¹¹ While no electric force exists between a neutron and proton, the nuclear force does.

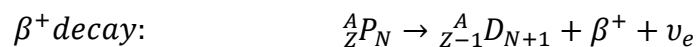
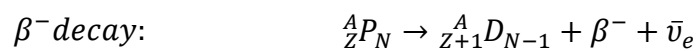
For any system of nucleons, their physical distributions and quantum mechanical properties dictate the energetic state in which they exist. As was mentioned, the competing nuclear and electric forces have significant roles in the physical distribution of the nucleus. Additionally, the quantum mechanical properties of spin, parity, and isospin are associated with available energy state that a nucleus can take. A complete description of the quantum mechanical properties is beyond the scope of this work, but the interested reader is referred to the text *Introductory Nuclear Physics* by K. Krane¹¹ for more information. The binding energy of a nucleus is the amount of energy or work needed to separate its components. It is calculated as the difference in mass-energies between the sum of individual constituents of the atom and that of the whole atom.¹¹ It is, in a sense, a measure of the stability of a particular arrangement of nucleons within the nucleus.

For nuclei with $A < 40$, those that are stable typically exhibit a close agreement between the atomic number and the number of neutrons¹², i.e. $Z \approx N$. For larger nuclei, stability imposes a constraint that $N > Z$. This restriction falls from the fact that the tendency for protons to repel each other increases with Z and more neutrons are required to ensure that the strong force overpowers the Coulomb (electrostatic) force.¹² Nuclei that

do not fall within this stable domain are largely unstable and may undergo a spontaneous transformation characterized by the emission of energy and particles to a more stable configuration. This spontaneous emission by unstable nuclei is referred to as *radioactive decay*.

There are various forms of radioactive decay which can be distinguished by the form of the nucleus before and after a radioactive decay, or the corresponding radiation that is produced during decay. The original radioactive nucleus is referred to as the *parent* and the nucleus that remains after decay is the *daughter*. If the daughter nucleus is also unstable, it too can undergo decay. Some nuclei thus have many steps along their decay path until a stable nucleus is formed. For the purpose of this thesis we are primarily concerned with radioactive decay processes which are isobaric and, to a lesser extent, isomeric.

Isobaric transitions are those where the mass number of the parent is equal to that of the daughter; the numbers of protons and neutrons, however, change in the process. An example of isobaric radioactive decay is the β decay process, of which there are two flavours: β^- decay and β^+ decay. These processes are named by the form of their radioactive emissions, i.e. β particles. β particles are, essentially, electrons that are produced by the decay of an unstable nucleus and can have either a negative or positive electric charge. β^+ and β^- particles are each other's anti-particle. β^+ particles are generally referred to as *positrons*. These processes can be written using the following notation for a nuclear decay, where the parent and daughter nuclei are denoted as P and D , respectively.



In the β^- decay process, compared to the parent, the daughter nucleus has one more proton and one less neutron. The β^- decay process is mediated by the weak force that exists between fundamental particles that are fermions, of which electrons are one example. The emissions of a β^- decay are the β^- particle and an electron anti-neutrino $\bar{\nu}_e$. During the decay process several conservation laws are applicable. Conservation of charge, for example, demands that the total electric charge of the parent equals that of all the decay products and indeed this is upheld as the increase in positive charge within the nucleus is balanced by the negative charge of the β^- particle. The electron anti-neutrino is a particle with negligible mass and no electric charge.¹³ It is, as is an electron, a kind of lepton and the lepton number must also be conserved during the decay.¹⁰ The parent nucleus has a lepton number of zero and it follows that the lepton number (+1) of the β^- particle is cancelled by that of the electron anti-neutrino (-1). Analogous features can also be said of the β^+ decay process noting only that an electron neutrino (lepton number of +1) is produced instead of the anti-neutrino.

It is very common, due to additional quantum mechanical conservation laws, that the daughter nucleus is left in an excited state and must decay via an isomeric transition to its ground state¹⁰. In this type of decay, the parent and daughter have the same nuclear composition, i.e. there is no change in either Z or N . The transition from the excited to ground states is often associated with the emission of electromagnetic radiation, and these photons are referred to as γ -rays. They are distinct from x rays as they originate from the nucleus as opposed to interactions of energetic electrons with an absorbing material (electron interactions are described in more detail in the following section). The energy of the photon is determined by the energy difference between the excited and ground states.

Note that transitions can also occur between excited states. A simplified decay diagram of rubidium-82 (^{82}Rb) is provided in Figure 1.1 to provide an example of these transitions.

Note that only the three most probable β^+ decays are shown although there are numerous other decay mechanisms for this nucleus.

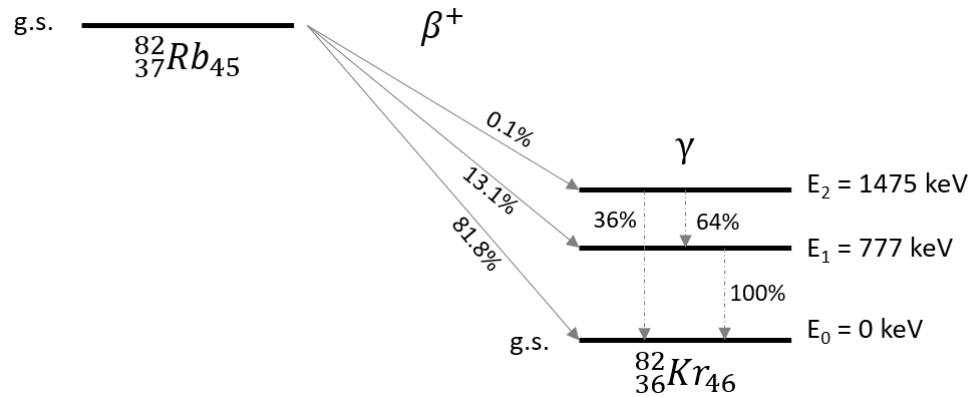


Figure 1.1 Partial decay scheme of ^{82}Rb (rubidium-82) which decays primarily via β^+ decay to produce stable ^{82}Kr (krypton-82). Solid horizontal lines indicate various energy levels of the parent and daughter nuclei, each of which are labelled with their energy levels. Note that the ‘g.s.’ line of ^{82}Rb corresponds to its ground state. The solid and dashed arrows indicate isobaric and isomeric transitions, respectively. Each β^+ transition is labelled with the associated probabilities of occurring, and similarly the γ decay transitions are labelled with their relative likelihoods with respect to the energy level from which they originate. The data in this figure were acquired from the nuclear data publication of the Laboratoire National Henri Bequerel in Gif-sur-Yvette Cedex, France.¹⁴

Radioactive decay is a stochastic process which can be accurately modelled by Poisson statistics. Given a large ensemble of radioactive nuclei it is impossible to predict when any single nucleus will decay. The behaviour of the ensemble, however, can be modelled extremely accurately via a relatively simple relationship which states that the instantaneous rate of change in the number of parent nuclei, N_p , in the ensemble is proportional to the negative of the number of parent nuclei.¹⁵ The proportionality constant is referred to as the *decay constant*, λ , and is representative of the likelihood that

the ensemble of nuclei will decay per unit time. This differential relationship is described below along with its solution (Eq. 0.1 and Eq. 0.2, respectively), where $N_{P,0}$ represents the number of parent nuclei at some reference time $t = 0$. This differential equation and its solution represent a specific case of the more general family of equations known as the Bateman equations which describe decay chains of arbitrary size.¹⁶

$$\frac{dN_p}{dt} = -\lambda N_p \quad \text{Eq. 0.1}$$

$$N_p(t) = N_{P,0}e^{-\lambda t} \quad \text{Eq. 0.2}$$

The *activity* of the ensemble is defined as the rate of disintegrations per unit time and is calculated as the product of $N_p(t)$ with the decay constant. A corollary of the relation described above is that the number of parent nuclei never reaches zero, but rather approaches this limit asymptotically. It is difficult then to know exactly when the radioactive sample has completely decayed. A convenient measure of the longevity of a radioactive sample is its *half-life*, $t_{1/2}$, which is defined as the time required for the activity (and number of parent atoms) of a radioactive sample to decrease by half with respect to its initial value at $t = 0$. It can be expressed in terms of the decay constant as per the following relationship.

$$t_{1/2} = \frac{\ln(2)}{\lambda} \quad \text{Eq. 0.3}$$

1.1.2 Interactions of Radiation with Matter

Within the context of this thesis we are only concerned about the interactions of β -particles and γ -rays as they pass through a medium and so a review of the interaction mechanisms of heavier ions or neutrons is not included in this discussion.

Since β -decays have multiple reaction products the energies of the emitted β -particles are polyenergetic and can be characterized by an energy spectrum which ranges from 0 keV to Q . The value of Q is fixed by the difference in mass energies of the parent nucleus and all the daughter nuclei combined.¹¹ β -particles interact readily with the medium through which they are travelling due to their mass and charge. Upon each interaction they transfer some of their kinetic energy to the medium, slowing them down. β -particles are stopped in a medium once their kinetic energy has been depleted. There are two principal mechanisms for β -particle interactions: collisional or radiative. Collisional interactions occur between β -particles and the atomic electrons of the medium and are described as a Coulomb (electrostatic) scattering process.¹¹ The energy imparted on the medium through collisional interactions leads either to transferring sufficient kinetic energy to orbital electrons to liberate them from the atoms to which they're bound (ionization) or promoting the orbital electrons to a higher energy orbital of the atomic structure (excitation).¹³ Radiative interactions are characterized by the emission of electromagnetic radiation following the rapid change in velocity of the β -particles due to Coulomb interactions with atomic nuclei.¹⁷ These emissions are commonly referred to as *bremssstrahlung* radiation and are the principal mechanism underlying x ray emitting devices. The stopping power, or rate of energy loss per unit distance, of these collisional and radiative interactions was first described by Hans Bethe in 1930 and was shown to depend on the kinetic energy of the β -particle as well as the atomic number of the absorbing material.¹⁸ The collisional interactions typically dominate the energy loss of β -particles except for those with very high kinetic energy and absorbing media with high

atomic number¹¹. The range of a β -particle in an absorbing material thus depends on the combined stopping power of the two interaction types.

Another interaction that is very important to the topic of this thesis, which is unique for positrons, is that of *annihilation*. Annihilation is characterized by the conversion of the mass energy of a positron and an electron to electromagnetic radiation when the two particles combine with each other¹². This type of interaction can occur when any particle meets with its anti-particle. The electromagnetic radiation is emitted in the form of two photons which have equal energy and a relative orientation of 180° with respect to each other (collinear trajectories). The energies and trajectories of the emitted photons are determined by the conservation of energy and momentum. For positron-electron annihilation, their combined rest mass is converted to energy and shared equally between the two photons (i.e. 511 keV each). If, however, the positron had some residual energy prior to annihilation the photons would neither have identical energy nor collinear trajectories¹². The angular distribution of the annihilation photons has been described by Levin and Hoffman¹⁹ to have Gaussian shape and a full-width at half-maximum (FWHM) on the order of roughly 0.25° . The effects of non-collinearity on the photon energy is more complicated to assess as, according to Iwata and colleagues²⁰, the dispersion of the spectral lines depends not only on the residual positron energy but also on the atomic properties of the absorbing material. They showed the annihilation photon spectral line width (FWHM, at 511 keV) dilated from 1.16 keV to 2.59 keV as a result of non-collinear γ -ray emission. How this additional dispersion translates to other detectors, however, is not obvious. A diagram demonstrating annihilation is provided in Figure 1.2.

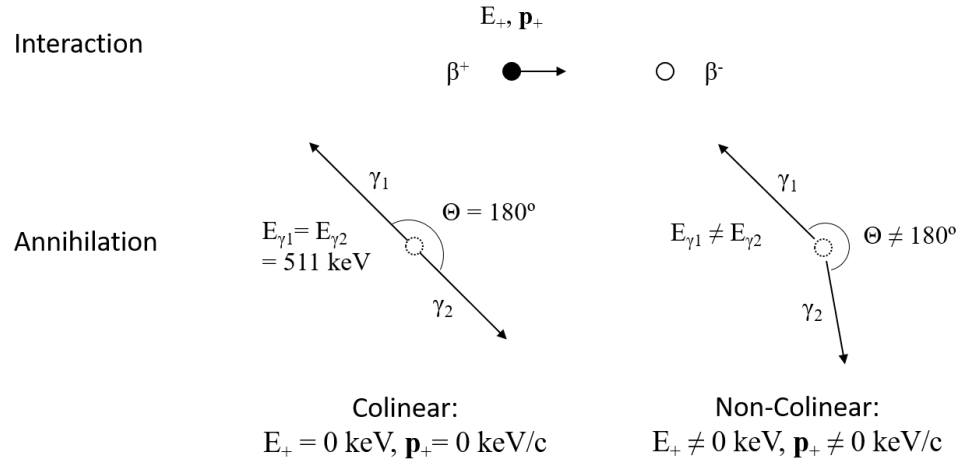


Figure 1.2 Schematic representation of a colinear and non-colinear annihilation of an electron-positron pair. The energy and momentum of the positron, β^+ are indicated as E_+ and \mathbf{p}_+ , respectively in the upper row of the image (“Interaction”). The annihilation photons and their energies are denoted at γ_1 , γ_2 , E_{γ_1} , and E_{γ_2} , respectively in the lower row of the image (“Annihilation”). It is assumed that the electron has zero kinetic energy and momentum.

Electron interactions occur at a distance due to the fact that both collisional and radiative interactions are governed by the Coulomb force that exists between charged objects. The effect is a continual series of interactions as the electron traverses an absorbing medium. In contrast, photons carry no mass and no electric charge and interact due to discrete interactions. The most relevant photon interactions for the work described in this thesis are incoherent (Compton) scatter, and photoelectric absorption. Both of these interaction pathways result in the conversion of the photon energy to kinetic energy of an electron. Photoelectric absorption comes about through interactions of photons with an atom in an absorbing material and results in the complete transfer of the photon energy to an orbital electron. If the photon energy is greater than the binding energy of the electron it will be ejected from the atom with kinetic energy equal to the difference of the photon energy and electron binding energy (ionization). If the photon energy is not

greater than the binding energy, the electron can be excited to a higher valence shell of the atom (excitation). In either event, the incident photon is completely absorbed in the process.

Incoherent, or Compton, scatter corresponds to an inelastic collision between an incident photon and an orbital electron wherein the incident photon energy is partially transferred to the electron. The scattered photon thus has reduced energy compared to the incident photon and usually undergoes a change in direction. The atom can either be excited or ionized depending on the amount of energy transferred to the electron in the process.

The likelihood of either photon interaction depends on the energy of the photon, and the density and atomic number (Z) of the absorbing material. For photoelectric absorption the probability of interaction per atom of absorbing material is proportional to the atomic number raised to the power of $\sim 4 - 5$; the exponent varies with photon energy and atomic number¹³. The probability of Compton scatter per atom varies (approximately) linearly with the atomic number¹⁷. Photoelectric absorption probabilities per atom are inversely proportional to the incident photon energy raised to the power of ~ 3.5 . The probability of Compton scatter, however, has a more complex and much weaker energy dependence. The Compton scatter likelihood and angular distribution is described by the Klein-Nishina formula which models the relativistic and quantum mechanical behaviour of this interaction.¹⁷ For an absorber made of water (or soft tissues), the Compton scatter mechanism dominates over photoelectric absorption for photon energies greater than 30 keV.¹⁷

1.2 Positron Emission Tomography

Positron emission tomography, or PET, is a molecular imaging modality wherein a patient is administered a small amount of a chemical agent of biological interest that has been labeled with an isotope that decays via positron emission which permits the non-invasive assessment of physiologic processes that are occurring within the body. Such an agent is referred to as radiotracer. The biochemical nature of the tracer is chosen to target specific processes and/or organs and to it is attached a radioactive atom that gives rise to photons that penetrate through the body such that they can be detected externally. PET is based upon the coincident detection of annihilation photons that are produced following the β^+ decay of a positron-emitting radionuclide of the tracer. Nuclear medicine imaging procedures, like PET, rely on the so-called *tracer principle* which assumes that the tracer is administered in sufficiently small amounts such that it emulates and does not perturb the natural physiologic processes that are being assessed.²¹ The term *tomography* indicates that the resulting images are arranged as a set of contiguous 2D cross-sectional slices of the object being imaged. PET images represent an estimate of the spatial distribution of the positron-emitting radionuclide. The concatenation of the 2D images thus provides a volumetric representation of this distribution. Within this section the key aspects of a PET imaging system are described, which include details of the photon detection systems, the development of PET imaging devices, tomographic image reconstruction, and data correction techniques that are needed to make PET images quantitatively accurate.

1.2.1 Photon Detection with Scintillators

PET imaging systems detect annihilation photons using an indirect approach based on scintillating materials. Scintillation materials are those that fluoresce, or emit visible light, following an interaction with a gamma ray, like an annihilation photon. To allow for an electronic readout of such a detection, the visible light emitted by the scintillation crystal must be converted to an electrical signal. The conversion has historically been achieved in PET detection systems using a device known as a photomultiplier tube (PMT) but photodiode devices are being increasingly used. A brief description of these devices will be provided shortly but presently we will return to scintillation materials.

The scintillating materials that have been used in PET systems have largely been inorganic materials²² and so the description here will be limited to this type. Inorganic scintillation materials have crystal lattice configurations. An inorganic scintillator's properties are largely determined by its structure and the excited states that are accessible to its valence electrons.¹³ When excited, however, a valence electron may be elevated to the conduction band of the crystal at which point it can migrate about the crystal structure.¹³ A hole remains within the valence shell that will be filled by the de-excitation of an electron in the conduction band. The de-excitation process corresponds to the emission of electromagnetic energy as the electron descends from a higher energy band to a lower. The energy band in between is the forbidden band and is not accessible to electrons of pure crystal materials. The energy gap of the forbidden band corresponds to an electromagnetic emission in the ultra-violet range.²² The crystal material can be intentionally doped with small amounts of impurities, or activators, which leads to the establishment of accessible energy levels within the forbidden band.¹³ The effect of these

intermediate energy levels is to reduce the emission energy of the de-exciting electron such that it falls within the visible range.²³

Several of the most commonly used scintillation materials within PET systems are sodium iodide doped with thallium (NaI(Tl)), bismuth germanate (Bi₄Ge₃O₁₂, or BGO), and lutetium oxyorthosilicate doped with cerium (Lu₂(SiO₄)O, or LSO).²² Several important physical properties of these scintillators are provided in Table 1.1. The density of a scintillating material, along with its effective atomic number, is associated with its capacity to attenuate annihilation photons. This effect is also emphasized in Table 1.1 by comparison of attenuation length of each crystal material. The attenuation length is the mean linear distance that a photon will travel in the crystal before interacting; a short length suggests that an interaction is more probable. The density of NaI(Tl) is slightly greater than half of that for either BGO or LSO and conversely its attenuation length is roughly triple that of the others. When compared to either BGO or LSO, NaI(Tl) thus exhibits a lower detection efficiency for 511 keV photons.

Table 1.1 Selection of physical properties of three inorganic scintillation crystals commonly used in PET systems. Measured values correspond to interactions with 511 keV annihilation photons. These data have been reproduced from Table 2.5 of *Physics and Instrumentation in PET* by D. L. Bailey, J. S. Karp, and S. Surti.²²

	NaI(Tl)	BGO	LSO
Density [g/cm ³]	3.67	7.13	7.4
Attenuation Length [cm]	2.88	1.05	1.16
Decay Time [ns]	230	300	40
Energy Resolution [%]	6.6	10.2	10
Light Output [photons/keV]	38	6	29

A key feature of scintillators is their relationship between light output and the energy deposited by the incident photon. Ideally, a scintillator's light output would exhibit a

linear relationship with deposited energy over a wide range of energies.¹³ The energy resolution of a scintillator is a measure of the precision with which a scintillator (and its accompanied photodetection system) can identify a discrete photon energy. It is often calculated as the full width at half-maximum of the energy response divided by the photon energy being detected and then represented as a percentage. The energy resolution of NaI(Tl) is better than that of BGO and LSO which has implications for a PET system's ability to discriminate between signal and background events. The light output of a scintillator is also associated with enhanced spatial and coincident timing resolution for PET systems when multiple scintillation crystals are coupled to a single photodetector.²²

The rise and decay times of the scintillator determine the duration over which the fluorescence occurs. Short rise and decay times are ideal as they result in quick signal pulses¹³ which enhances the detector's capacity to distinguish events that take place in rapid succession.²³ In general, inorganic scintillators exhibit long decay times but LSO demonstrates a remarkable improvement in decay time over others like NaI(Tl) and BGO.

An auxiliary device is needed to convert the visible light emitted by scintillators into an electrical pulse that indicates the detection of a photon; these are generally referred to as *photodetectors*. Several important properties of these devices are a high efficiency for conversion of visible photons to electrons, rapid charge collection and signal readout, and high amplitude resolution, i.e. high signal gain and low electronic noise.²⁴

Photomultiplier tubes (PMTs) have been widely used for this purpose both in medical imaging applications as well as in basic nuclear physics.¹³ PMTs are composed of three key components: a photocathode, an evacuated electron multiplication chamber, and a

pulse-shaping pre-amplifier.²⁴ The photocathode serves as a window between the scintillator and the PMT and it is triggered by photoelectric interactions of the scintillation photons to emit electrons.²² If the electrons are energetic enough to escape the photocathode, they cascade through the evacuated region of the PMT where a high electric field within the vacuum tube causes the photoelectrons to accelerate. The electrical signal is insufficient to produce a detectable electrical signal, however, without an electron multiplication system.¹³ PMTs achieve signal amplification by accelerating the initial photoelectrons to collide with a series of targets known as dynodes. A single electron will stimulate the emission of approximately 6 secondary electrons after a collision with the dynode.²⁴ It follows that a signal gain on the order of 10^7 is achievable with ~10 dynodes.¹³ The total charge that reaches the anode leads to an electronic pulse which is shaped by the pre-amplifier prior to further processing of the event. Two remarkable features of PMTs are their ability to achieve such high signal gain without introducing significant electronic noise other than the inherent quantum fluctuations of generating secondary electrons, and they do not dilate the initial pulse width of the scintillator.¹³

PMTs have some limiting features which affect the PET system design. Their physical size imposes restrictions on how densely they can be positioned, which means that multiple scintillation crystals must be coupled to a single PMT.²² Additionally, PMTs are highly sensitive to magnetic fields²⁴ which make them incompatible with hybrid PET scanners integrated with magnetic resonance imaging (MRI) scanners. An alternative family of photodetectors based on semiconductor diode technology is well suited to compensate for these disadvantages of PMTs.

Diode-type photodetectors, or photodiodes, consist of lamellar combinations of p-type and n-type semiconductor materials. The type of the semiconductor material is an indication of its doping and the forms of its charge carriers. P-type semiconductors are those that are doped with impurities that have one fewer valence electron than the atoms of the semiconductor material, and as a result these impurities introduce positive charge carriers in the form of electron holes into the crystal structure.¹³ Conversely, n-type materials are doped with impurities that carry an additional valence electron compared to the atoms of the semiconductor and thus supply negatively charge carriers in the form of electrons into the material.¹³ P- and n-type layers are coupled to a pure semiconductor layer to produce *PIN* photodiodes, where *I* in the acronym refers to *intrinsic* and corresponds to the pure, undoped, junction region wherein there are no excess charge carriers. In silicon photodiodes the deposition of roughly 3.6 eV is sufficient to excite valence electrons and produce electron-hole pairs. The presence of positive and negative charges at the p- and n-type layers, respectively, causes the electron and hole to drift away from each other and produce a potential difference within the junction.²⁴ In this manner visible photons may be detected. Without the application of an external electric field, PIN photodiodes have no gain and their signals are very sensitive to electronic noise. Additionally, their pulse width depends on the drift time of the charge carriers within the intrinsic layer.¹³ This photodiode design has been modified in a manner to establish a signal amplification (avalanche) following the production of the initial electron-hole pair. These *avalanche* photodiodes (APDs) come in various configurations but a common one is the *reach-through* design which consists of a highly doped p-type entrance layer, a lightly doped p-type drift region, and p-n⁺ multiplication region.¹³ The

combination of this layered arrangement along with a high external electric field provides a significant amount of kinetic energy to the electron-hole pairs that are produced from photon interaction within the drift region which stimulates a run-away cascade of electron-hole pair production. The typical signal gain achieved with this design is on the order of hundreds.²⁴ The gain of APDs generally exhibit a linear relationship with the applied voltage.²⁵

The gain of an APD, however, has higher variability than that on the PMT which can reduce its energy resolution, but the increased quantum efficiency over PMTs partially compensates for this effect.¹³ The gain of photodiodes is also highly sensitive to the operating temperature and the stability of the high voltage supply and so any system making use of these photodetectors must be able to control both very precisely.²² Lastly, the rise-time of the APD pulse can be twice that of common PMTs and can thus improve the overall timing resolution.²⁴ The APD design has been improved upon by the development of multi-pixel photon counting (MPPC) photodiodes, a common example of which is the silicon photomultiplier (SiPM). MPPCs are a structured array of individual APDs operating at high voltages, typically above 100 V. Under such an external field the gain takes on steeper, i.e. more sensitive, relationship with the applied voltage but maintains reasonable linearity.²⁵ The gain associated with SiPM photodetectors is similar to that of PMTs²⁵ and are typically on the order of 10^6 . In modern PET systems, the energy resolution of the SiPM photodetectors are comparable to that of PMTs; typically around 10%.²⁶ The timing resolution of PET systems using SiPMs, however, have improved over those using PMTs. As an example, the timing resolution of the Philips Vereos PET/CT (uses SiPMs) and GE Discovery 690 PET/CT (uses PMTs) system have

been reported as 332 ps²⁶ and 544 ps²⁷, respectively, and both make use of LYSO scintillators.

While the photon detection system of the PET scanner is an essential component of its performance, the PET system itself is much more complex and represents the combinations of many systems to actually image a patient. In the following section some of the essential components of a PET system are described.

1.2.2 PET System Design and Performance

The purpose of a PET acquisition is to produce an image, or spatial description, of the radiotracer concentration within a patient. Such an image is produced by solving the following inverse problem: How can we determine the radiotracer distribution from the emission data detected by the PET scanner? It turns out that this problem is not unique to PET, nor medical imaging, and various analytic and iterative methods exist that can provide a solution.²⁸ More detail will be provided in the following section on the image reconstruction problem in PET, but for now it is relevant to mention that solving these problems requires that the emission data is sufficiently sampled about the object being imaged.²⁸ In PET sufficient sampling is achieved by arranging a set of detectors along a circular gantry that encompasses the patient. While some systems employ partial ring or flat panel detectors that rotate about the patient, most use full ring configurations.²⁹ Regardless of the configuration the detectors must be arranged such that they oppose each other to permit the detection of collinear annihilation photons. A schematic representation of full ring, multi-slice configuration is shown in Figure 1.3. In this illustration, the coordinate system in the full-ring scanner is indicated along with a single

line-of-response emanating from the annihilation location within the patient which is marked by a lightning bolt.

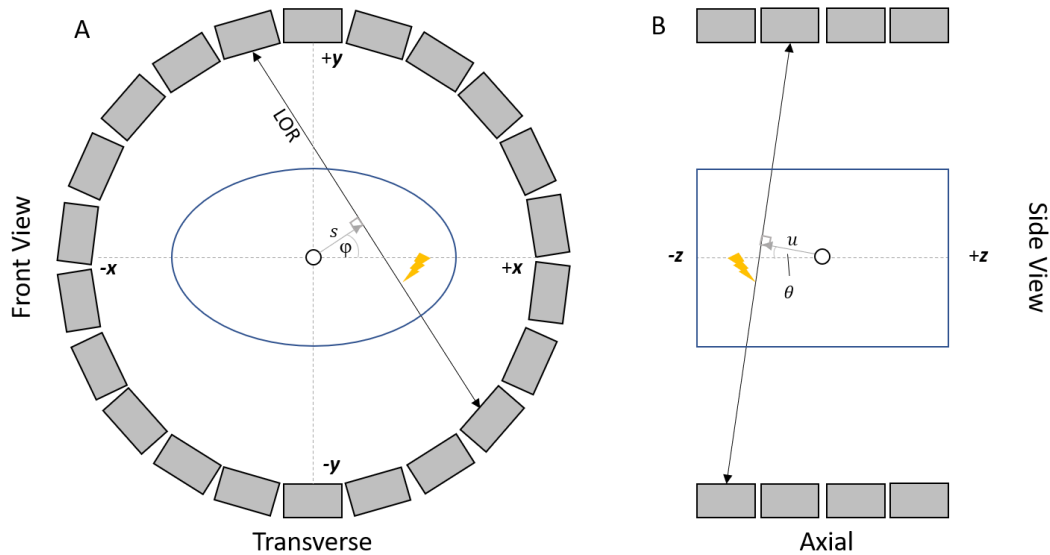


Figure 1.3 Schematic representation of a full-ring multi-slice PET detector configuration. Cross-sectional views from the front face of the gantry and from the side are shown in sub-figures A, and B, respectively. Each gray rectangle represents a detector. In sub-figure A, the transverse coordinate directions, x , and y , are depicted by dashed lines. The transverse origin is shown as a circle at the intersection of the x and y axes. A line of response (LOR), which originates at the position marked by the lightning bolt, subtends an azimuthal angle ϕ with the positive y axis. A model patient is represented by the blue ellipse. In sub-figure B, the span of axial direction, or z axis, is shown. The same LOR subtends a polar angle θ with the positive z axis. The vector $\vec{s}(s, u)$ describes the position of the LOR.

The detector elements have also been designed with various configurations. One of the most successful detector designs is that of the *block detector*.²⁹ In this design, a rectangular grid of individual scintillation crystals is optically coupled to a set of photo-detectors with a relatively high ratio of the number of individual crystals to photo-detectors; 64:4, for example, as depicted in Figure 1.4.

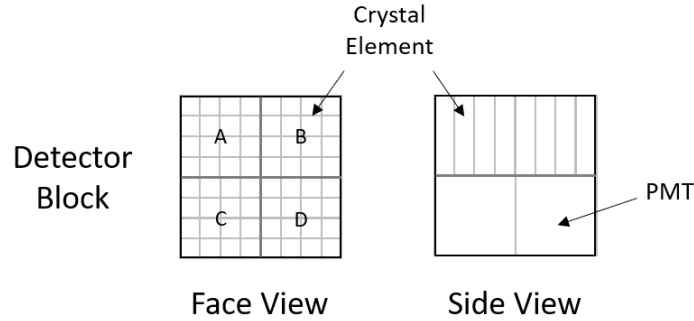


Figure 1.4 Arrangement of 64 scintillation crystal elements and 4 PMTs in detector block design. The block quadrants A, B, C, and D correspond to unique PMTs.

While it is not shown in Figure 1.4, the divisions between individual elements are often incomplete and reflective barriers exist in these regions to help guide scintillation light towards the PMTs and impose limits on the spatial dispersion. By varying the lengths of the reflective barriers across the block, a different amount of light reaches each of the attached PMTs which helps to identify the crystal from which the scintillation occurred.²⁹ The x and y coordinates of the scintillation can be estimated using the relative pulse-heights of the four PMTs (A, B, C, and D) as shown in Eq. 0.4 and Eq. 0.5, commonly referred to as Anger logic, after its originator Hal Anger.²⁹ In the block detector design, all four PMTs are occupied over the span of time that it takes to resolve a single event. This has an impact on the scanner's sensitivity to detection annihilation photons, especially when the count rate is high.

$$x = \frac{(B + D) - (A + C)}{A + B + C + D} \quad \text{Eq. 0.4}$$

$$y = \frac{(A + B) - (C + D)}{A + B + C + D} \quad \text{Eq. 0.5}$$

A single coincident event is described by the crystal indices of each photon detection as well as the time at which the event occurred. Two photons are considered to be in coincidence if they are detected within a relatively short period of time, i.e. within the coincidence window (2τ). The duration of the coincidence window is partially limited by the timing resolution of the detectors which, as described in the previous section, is associated with the rise time of the scintillators and the pulse dispersion of the photodetectors. Additionally, the geometry of the scanner must also be considered when determining an appropriate timing window as the time it takes each annihilation photon to reach a detector may differ due to the difference in distances each photon must traverse (at the speed of light). As an example, while a timing resolution of 0.6 ns has been reported for a barium fluoride (BaF_2) PET system³⁰, a timing difference of up to 3 ns could be expected for annihilation photons in a very large patient, and so setting a coincidence window based on the timing resolution alone would limit the overall sensitivity of the scanner.²² For PET systems that make use of fast scintillators and electronics which have timing resolution < 0.6 ns, the timing delays of the coincidence photons can be resolved sufficiently well to infer where along the LOR the annihilation occurred³¹. Recording the time difference between detection of coincident photons is referred to as the *time-of-flight* (TOF) of the coincidence event. The position of an annihilation event, with respect to the middle point of the LOR, can be calculated as $c\Delta t/2$, where Δt is the time delay between the arrival times of the two annihilation photons and c is the speed of light in air. A timing resolution of 500 ps thus corresponds to a spatial resolution of 7.5 cm of the annihilation event along the LOR. The benefit of

the use of TOF data lies in improved noise characteristics in the reconstructed image.²² Interestingly, if the timing resolution was sufficiently small such that the spatial uncertainty of the annihilation event along the LOR was smaller than the spatial resolution of the system, no image reconstruction would be required.³²

In the following sections spatial resolution, energy resolution, timing resolution, count rate performance, and sensitivity are described.

1.2.2.1 Spatial Resolution

The spatial resolution of an imaging system is a measure of the smallest separation between objects that can be discerned in an image and is often measured as the FWHM of a small object representation in an image.²⁹ Note that for an object to be considered small, it should be no larger than half the size of the spatial resolution of the system.²⁹ There are various factors which affect the spatial resolution of the system: positron range, non-collinearity of the annihilation photons, sizes and separation of detectors, variance in the depth into a crystal (depth-of-interaction) where the ionization occurs³¹, and block-detector decoding in the case of the multi-crystal block configuration. In most full-ring systems the spatial resolution in the transverse plane (x - y) is smaller than that in the axial direction (z) as the transverse field of view is oversampled compared to along the axial direction.²⁹ See Table 1.2 for example measurements; the “Radial” and “Tangential” measurements are made in-plane while the “Axial” measurements are along z . The spatial resolution of a PET system fundamentally limits its ability to determine the spatial distribution of a radiotracer within a patient.

1.2.2.2 Energy Resolution

The energy resolution of the system is associated with the precision with which a detector can determine the energy of detected photons.²⁹ In addition to the emission of a positron during the decay of the radiotracer, other prompt gamma ray emission or scattered annihilation photons may be detected that lead to increased noise and/or artifacts in the reconstructed images. Some of these types of photons are excluded from the emission data through energy discrimination.

1.2.2.3 Timing Resolution

Good timing resolution, as was mentioned, is important for identifying coincidence events and, with sufficiently fast crystals and electronics, for TOF measurement as well. In terms of system performance, a narrower coincidence window helps to exclude random coincidence events that arise from simultaneous detection of two independent annihilation photons. Random coincidences lead to a uniform increase in the background which can reduce the contrast in the resulting image as they carry no useful spatial information and occur stochastically within the field of view.²² The rate of detecting random coincidences is proportional to the width of the coincident window and the square of the activity in the field-of-view of the scanner.²⁹

1.2.2.4 Dead Time and Count Rate Performance

Once a detector is triggered by the detection of a photon, there is a period wherein no additional events can be registered. This time is referred to as *dead time* and is associated with the time needed for the scintillator's response, the electronic response of the photodetector, the integration time of the electronics, and time associated with processing

coincidence events. The count rate performance of a PET system is an indicator of its ability to process detection events over a broad range of system count rates, or activity in the field-of-view. The dead time is a non-linear function of the count rate of the system and is composed of two contributions: paralyzable and non-paralyzable dead times.³³ In the non-paralyzable case, the detector is unresponsive to events that occur within a fixed time τ following a detection; subsequent events are ignored and have no further effect on the detector.¹³ Paralyzable dead time, however, implies that all events lead to a dead time τ , even if they occur while the detector is ‘dead’ from an initial event.¹³ Paralyzable dead time can lead to saturation of the detector wherein the system count rate can decrease in the presence of an increasing event rate.³³ Dead-time corrections must be applied in PET to achieve linear response over the broad range of count-rates so that resulting images can accurately quantify activity concentrations in the subject.

There are three types of coincidence events PET systems detect: true coincidences of annihilation photon pairs, coincidence of photons that have scattered and random coincidences of two photons from two separate decay events. While true coincidence events are the desired signal in PET, the scatter and random events are unavoidable and degrade image quality. A common measure of the count rate performance of a PET system is the *noise equivalent count rate* (NECR). This metric is defined as the count rate of true coincidence events that would give the same signal-to-noise ratio as the real count rate of the system in the absence of random and scattered coincidence events.²⁹

Mathematically it is calculated as shown below (Eq. 0.6), where T , S , and R represent the count rates of the true, scattered, and random coincidence events, respectively.³⁴ The factor K is used to accommodate different methods of correction for random coincidence

events and takes on a value of 1 or 2. In practice the KR term in the denominator of Eq. 0.6 must be scaled by a factor f which represents the ratio of the diameter of the object being imaged to the transaxial field of view.. One approach to correct for random coincidence events is described in the following section.

$$NECR = \frac{T^2}{T + S + KR} \quad \text{Eq. 0.6}$$

1.2.2.5 Sensitivity

The last aspect of PET system performance described here is that of sensitivity. Sensitivity is a measure of the system's ability to detect an annihilation event that occurs within its field-of-view. Sensitivity is largely determined by the geometry of the scanner as well as the intrinsic efficiency of the detectors for annihilation photons.²² As the image noise of a PET acquisition is related to statistical fluctuations in the number of detected coincidence events, improved sensitivity is associated with noise reduction and improved signal-to-noise ratio. Regarding geometric considerations, increasing the solid angle coverage that the scanner exhibits with respect to the target object or tissue being imaged could improve its sensitivity. In particular, when imaging a uniformly distributed cylindrical phantom the rate of true coincidence detection is proportional to the square of the axial field-of view and inversely proportional to the diameter of the transverse field of view^{29,35}. A long and narrow scanner bore would have improved sensitivity over a short and wide bore. The detection efficiency of the scintillation crystal is related to the photon interaction cross-section and the size of the crystal. At photon energies of 511 keV, the dominant photon interactions mechanisms are photoelectric absorption and Compton scattering which have cross-sections (per atom) that are proportional to Z^4 and Z ,

respectively, where Z is the atomic number of an atom in the scintillator.²³ More generally, increased effective atomic number and density within a polyatomic scintillator leads to increased intrinsic detection efficiency and thus scanner sensitivity.

1.2.2.6 Performance Characteristics of GE Discovery 690 PET/CT System

The work described in this thesis largely made use of the Discovery 690 (D690) PET system developed by General Electric (GE) Healthcare (Waukesha, WI), which is a PET system with first generation time-of-flight capability. Performance characteristics of this system were reported by Bettinardi and colleagues²⁷ following the 2007 National Electrical Manufacturers Association (NEMA) standards for positron emission tomographs. The D690 is a hybrid PET system that includes a 64-slice CT scanner mounted at the front of the PET scanner gantry. This PET scanner contains 13,824 lutetium yttrium orthosilicate (LYSO) crystals as scintillators. The crystal dimensions are $4.2 \times 6.3 \times 25 \text{ mm}^3$. The detector units are of the block design style and each contains 54 (9×6) individual crystals. Each block uses only a single position-sensitive photomultiplier tube with four anodes. The blocks are positioned within rectangular module units that hold 8 blocks, two transverse by four axial blocks. In total 32 blocks complete the full ring of the detection system. The axial and transverse field-of-view are 157 mm and 700 mm, respectively. The performance measurements data are provided in Table 1.2.

Table 1.2 Performance measurements of the GE Discovery 690 PET system.²⁷

Measurement		Value
Spatial Resolution (FWHM)	10 cm off-axis	
	Radial	5.34 mm
	Tangential	4.79 mm
	Axial	5.55 mm
Energy Resolution (FWHM)	511 keV	12.40 ± 0.02 %
Timing Resolution (FWHM)		544.3 ± 1.5 ps
Peak NECR	Count rate, and activity concentration	139.1 kcps, 29.0 kBq/mL
Sensitivity	10 cm off-axis	7.6 cps/kBq

1.2.3 Data Correction for Quantitative PET

Ideally, the PET image should have voxel values with units that are associated with activity concentration, e.g. kBq/mL. The detection system, however, records the count of detected coincidence events. It follows that to estimate the activity values in the reconstructed images the raw acquired data, i.e. counts, must be corrected to account for the events that were not seen by the PET system, those that were mispositioned, or unwanted background. Many of the performance characteristics described in the previous section are related to this problem. This section reviews some basic strategies for making PET images quantitatively accurate. The aspects that are covered are corrections for detector normalization, random coincidence events, detector dead time, attenuation, scattered coincidence events, and calibration. For many of these factors, there are multiple common correction methods that have been implemented but the following is limited to the methods used in the GE Discovery 690 PET/CT system. For more detail, please see Chapter 5 of *Positron Emission Tomography: Basic Sciences, Quantitative Techniques in PET* by Meikle and Badawi.³³

1.2.3.1 Normalization correction

Normalization correction corresponds to correcting for non-uniformities in the intrinsic detection efficiencies of individual crystals, geometric effects, structural misalignment of the detectors, and asynchronous timing between detector pairs.³³ Intrinsic detection efficiencies may vary due to crystal non-uniformity or variations in photodetector gain. Additionally, the transverse and axial positions of a crystal within a block may also affect its sensitivity (transverse and axial block profile corrections). Geometric factors consider solid angle coverage and incident angles of detected photons for individual crystal, which vary depending on the acceptance angle of the coincidence system as well as the location of the emission within the FOV. These efficiency components are typically determined using measurements of rod and cylinder sources with uniform activity concentration.³³ Moreover, the acquisitions use low amounts of activity and are long in duration to make measurements that have low noise and to mitigate dead time effects.³³

1.2.3.2 Random Coincidence Correction

For a given detector pair, the rate of random coincidence events can be calculated as the product of the coincidence window, 2τ , with the non-coincident, or singles, detection rates of the two detectors.³¹ The total number of random coincidence events in an acquisition can be estimated by the integral of the random coincidence detection rate over the duration of the acquisition. Prior to reconstruction the total number of random coincidence events, once corrected for radioactive decay, can be subtracted, for each detector pair, to compensate for their effect on the image. This estimation method assumes that the response of every detector pair is uncorrelated and that the spatial distribution of the activity is effectively fixed over time.³³ Generally, the singles rates

will not be uncorrelated due to prompt coincidence events, however, the singles rates may be several orders of magnitude greater than coincidence detection rates and so the error in this assumption is small.³³ Lastly, the singles rates are approximately proportional to the activity concentration in the object being imaged, so it follows that the random coincidence rates are approximately proportional to the square of the activity concentration.³³

1.2.3.3 Dead Time Correction

To correct the count losses associated with dead time, models of the paralyzable and non-paralyzable components can be estimated from decaying source measurements.³³ General formulae for these two components are provided below (Eq. 0.7 and Eq. 0.8) where n and m represent the true and observed count rates, respectively, and τ_d represents the dead time per detection.¹³ In the limit of low activity, or when the fraction of count losses $n\tau_d \ll 1$, both models exhibit the same behaviour. For high activities, however, the non-paralyzable dead time approaches an asymptotic limit proportional to τ_d^{-1} and the paralyzable component leads to declining count rates. The detectors have been associated with paralyzable dead time and the electronics with non-paralyzable dead time and cascaded models have been proposed that account for both effects in series.³⁶

$$\text{Non-paralyzable} \quad n = \frac{m}{1 - m\tau_d} \quad \text{Eq. 0.7}$$

$$\text{Paralyzable} \quad n = me^{n\tau_d} \quad \text{Eq. 0.8}$$

1.2.3.4 Attenuation Correction

To be able to detect the primary annihilation photons emitted from within the body, they must travel through tissue without interaction. The probability of a photon reaching

the detector without being absorbed or scattered depends on the attenuating effect of all the materials that exist along a linear trajectory toward the detector. The attenuating effect of a given material or tissue type can be described by its linear attenuation coefficient μ . This value represents the combined likelihoods of the photon interacting through all of the mechanisms described in Section 1.1.2 and is interpreted as the probability per unit length of an interaction occurring that removes the photon from its original trajectory. If attenuation is not taken into account PET images will appear to have reduced intensity in regions of high attenuation or regions which have a longer pathlength in tissue before the photon emerges from the body (i.e. deep anatomical regions).

It may be surprising to learn that to correct for this effect in PET acquisitions we do not require knowledge of the annihilation point along a LOR. This convenient aspect of a PET acquisition, which simplifies the process of correcting attenuation, falls from the fact that only coincident photon detections are used as signal. Consider a LOR which spans a distance L between two detectors and that the annihilation occurred at a distance x from the first detector. The path lengths of the two photons are thus x and $L - x$ and the probabilities of each photon reaching the corresponding detectors are shown in Eq. 0.9 and Eq. 0.10 below,

$$p_1 = e^{-\int_0^x \mu(x') dx'} \quad \text{Eq. 0.9}$$

$$p_2 = e^{-\int_x^L \mu(x') dx'} \quad \text{Eq. 0.10}$$

where $\mu(x')$ is the attenuation coefficient at any position x' . The likelihood (p) of a coincidence detection of these two independent events is thus given as the product of p_1 and p_2 , shown in Eq. 0.11, which has no dependence on the annihilation position x .

$$p = e^{-\left[\int_0^x \mu(x')dx' + \int_x^L \mu(x')dx'\right]} = e^{-\int_0^L \mu(x')dx'} \quad \text{Eq. 0.11}$$

It follows that attenuation correction factors can be measured using a transmission scan produced from either rotating radioactive sources or from computed tomographic (CT) images. The former approach involves computing the ratio of the intensities along every LOR both with and without an attenuation object in the field of view.³¹ The latter approach involves converting a CT image into a corresponding image of attenuation coefficient values and then computing line integrals of the image values that correspond to all LORs.³⁷ It is important to note, however, that while the units of a CT image are closely related to the attenuation coefficients of the tissue within a given voxel they correspond to the effective energy of the poly-energetic x ray beam of the CT scanner. It follows that a transformation must be applied to determine the corresponding attenuation coefficients for the 511 keV annihilation photon energy. This is typically achieved by application of the bilinear scaling model which provides a piecewise linear transformation for μ within the end points of air and cortical bone³⁸.

1.2.3.5 Scatter Correction

Most modern PET systems acquire data in a fully 3D fashion, i.e. LORs are not restricted to transverse planes that are associated with a single ring of detectors. In this approach the relative number of detected coincidence events that undergo scatter, even after energy discrimination, can range from 35 – 80% of all prompt coincidence events.³¹ While many methods have been proposed to estimate the contribution of scatter to the emission data only one paradigm based on computation simulation is described here as it has been demonstrated to have good performance in 3D PET acquisitions.³³ Analytical

simulation of the scatter process requires knowledge of the attenuation along each LOR, an estimate of the scatter free activity distribution, detector efficiencies and solid angle coverage and a model of the differential cross-section of scatter interactions.³⁹ For some non-linear, iterative, reconstruction algorithms the scatter estimates are produced and subtracted from the emission data following correction for normalization but prior to image reconstruction.⁴⁰ Other algorithms incorporate scatter estimates into the reconstruction process as a separate contribution to the observed counts. Scatter correction based on this simulated approach may be implemented in the following steps: reconstruct an attenuation image, e.g. from a CT image; reconstruct an initial, low resolution, emission image; perform scatter simulation and estimate the scatter contribution to the emission data; scale the scatter estimates to match the emission image outside of the object being imaged, i.e. in the region where only scatter can exist; and finally, subtract the scatter estimate from the emission data.³³ The operation of scaling the scatter estimates to the emission image in the regions outside of the body has implications to the methods proposed in this thesis, as is discussed in Chapter 3 and Chapter 6.

Once all of the previously mentioned corrections are applied all that remains is to verify that activity measured in the PET images is in agreement with the activity measurements made in a calibrated well counter.³³ This procedure could be performed by imaging a phantom which contains a uniform distribution of activity and measuring the activity from a sample drawn from the phantom in a well counter.³³ If discrepancies exist between the PET image and well-counter measurements a well-counter correction factor can be applied to scale the PET images to report quantitatively accurate values, typically in units of Bq/cc.

1.2.4 Tomographic Image Reconstruction

As was mentioned at the beginning of the last section, image tomographic image reconstruction is an inverse problem for which there are various available solutions. In modern PET systems the most employed solutions are iterative processes wherein the solution, i.e. the image, is updated and refined repeatedly until a satisfactory result is reached. While analytical solutions, namely filtered back-projection, may still be used, and indeed can provide valuable insight into image reconstruction processes, they are not described here. This description will be limited to that of the maximum likelihood expectation maximization (MLEM)⁴¹ method as applied to PET.⁴²

Before describing the reconstruction method, it is useful to consider the format of the PET emission data. In its most basic form, the PET data are stored in a format where each coincident detection is simply written to file. In this so-called list-mode data, each event is described (at least) in terms of indicators of the two detectors that observed the event as well as the time at which the event occurred. Additional events may be written to the list-mode data like scheduled time stamp events or trigger events. Triggers are indicators of the state of the patient being imaged and could, for example, mark the beginning of each cardiac cycle that the patient experiences during the acquisition. Triggers are produced by some sort of system which monitors the physiological process of the patient, e.g. an electro-cardiogram (ECG) is used to monitor cardiac contraction. Triggers are described in detail in Section 2.3.2. The list-mode format is often inconvenient for the purposes of image reconstruction as it is not easily adapted for traditional analytic reconstruction algorithms and also imposes significant data storage requirements as the number of detected coincidence events can be on the order of $\sim 10^8$ for a PET acquisition.⁴³

More commonly, the individual detected events are combined into a series of histograms where each corresponds to a parallel set of LORs that form a plane that intersects the FOV at an orientation \vec{n} specified by azimuthal (φ) and polar (θ) angles about the geometric center of the scanner. Each histogram is referred to as a *projection* of the activities along a parallel set of LORs. The number of counts in each bin corresponds to the value of the line integral of the tracer distribution along the LOR within the object being imaged. Each bin center of the histogram is described by a vector $\vec{s} = (s, u)$ for a given projection angle. This notation is consistent with that shown earlier in Figure 1.3, but here a parallel set of LORs is considered instead of just one. The set of all projections at all angles subtended by the support of the PET detection system is referred to as a sinogram. A diagram which describes a single sinogram element $p = (s, \varphi, u, \theta)$ of an eccentric cylinder filled with activity is shown in Figure 1.5. Since the activity distribution is completely described by only three independent variables, e.g. x , y , and z , the projections thus contain redundant information which help to improve the overall sensitivity of the scanner and the signal-to-noise ratio in the reconstructed images.²⁹

The image reconstruction process is effectively a computation of the activity distribution that gave rise the detected projection data given a (forward) model of the imaging system which relates these two data sets. This problem is discrete as we cannot determine continuous distributions of either the projection data or the image data. It follows that projection and image data can be organized as 1D vectors \vec{g} and \vec{f} , respectively. The imaging system can be represented as a matrix H which operates on the image data \vec{f} to generate the projection data \vec{g} . If the image and projection data contain N and M elements, respectively, then H is given as an $M \times N$ matrix and is referred to as the

system matrix. The system matrix can incorporate physical effects that impact the contribution of the n^{th} image element to the signal of the m^{th} projection element. It could be designed to model the effects of attenuation, scatter, non-uniformity in the detector elements, blurring effects associated with limits spatial resolution, or even gaps that may exist between detectors⁴³. The elements of the system matrix $h_{m,n}$ thus correspond to the probability that an emission in the n^{th} image element gets detected in the m^{th} projection element. From this we can say the expectation value of the m^{th} projection element is given as Eq. 0.12.

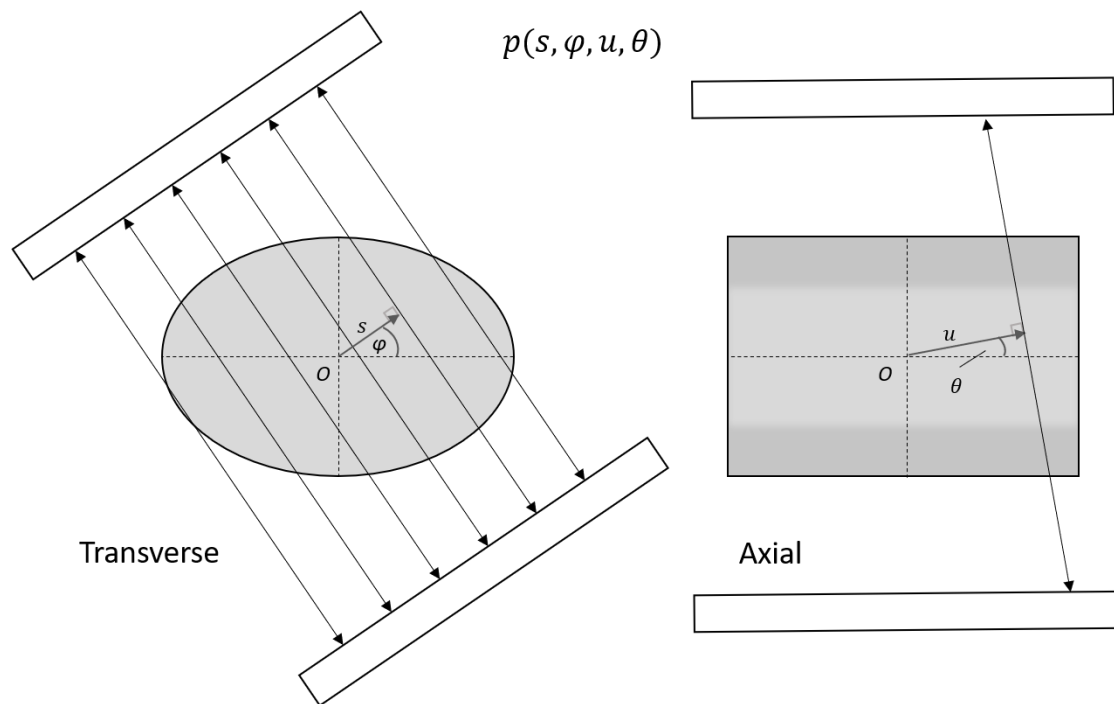


Figure 1.5 An example oblique projection plane intersecting an eccentric cylindrical object. The sinogram elements of this projection are described by $p = (s, \varphi, u, \theta)$. The transverse and axial components of the projection are shown in left and right drawings, respectively. Individual LORs are depicted as double-headed arrows. The origin of the FOV is marked as O .

It is standard practice to treat the number of counts in a projection element as a Poisson-distributed random variable.⁴⁴ It follows that the probability of observing the

projection data \vec{g} given a tracer distribution \vec{f} is the product of the individual probabilities over all M projection elements, as shown in Eq. 0.13.

$$\langle g_m \rangle = \sum_{n=1}^N h_{m,n} f_n \quad \text{Eq. 0.12}$$

$$Pr(\vec{g}|\vec{f}) = \prod_{m=1}^M \frac{e^{-\langle g_m \rangle} \langle g_m \rangle^{g_m}}{g_m!} \quad \text{Eq. 0.13}$$

Here the notation $\langle g_m \rangle$ is used to denote the expectation value of the m^{th} projection element. The MLEM method⁴² seeks to estimate the image \vec{f} that maximizes the log-likelihood function $\mathcal{L}(\vec{f})$, which is given as Eq. 0.14.⁴³ Note that in this expression, terms that do not depend on the image elements f_n are discarded as they will not affect the estimate of \vec{f} as the log-likelihood is maximized through differentiation with respect to f_n .

$$\mathcal{L}(\vec{f}) = \sum_{m=1}^M \left[-\sum_{n=1}^N h_{m,n} f_n + g_m \log \left(\sum_{n=1}^N h_{m,n} f_n \right) \right] \quad \text{Eq. 0.14}$$

The MLEM method is employed for problems which involve incomplete data where a closed form solution of the standard maximum likelihood calculation does not exist and thus needs to be estimated iteratively.⁴¹ Typically, the first estimate of image elements $f_n^{i=0} = 1$ for $n \in [1, N]$. The image updates thereafter are described in Eq. 0.15.⁴³

$$f_n^{i+1} = f_n^i \frac{1}{\sum_{m'=1}^M h_{m',n}} \sum_{m=1}^M h_{m,n} \frac{g_m}{\sum_{n'=1}^N h_{m,n'} f_{n'}^i} \quad \text{Eq. 0.15}$$

This update step determines a ratio of the observed projection data g_m with the projection data that one would expect from current image estimate, $\sum_{n'=1}^N h_{m,n'} f_{n'}^i$ and then maps that ratio to a factor that modifies the n^{th} image element.

The MLEM algorithm guarantees convergence as the number of iterations approaches infinity as the log-likelihood can be shown to increase monotonically upon each iteration.⁴³ While a large number of iterations leads to an unbiased image estimate it also leads to high noise. This is primarily due to the fact the emission data are inherently noisy and so the image estimate that maximizes the consistency with the projection data are also noisy.⁴⁴ In practice this is addressed by applying post-reconstruction smoothing, reducing the number of iterations, or imposing regularization in the likelihood function that enforces smoothness.⁴³ As a final comment, the MLEM method requires the use of the entire projection data set to complete a single iteration which limits its usefulness in a clinical environment due to the duration of the reconstruction. To remedy this, a modification of the original method was proposed by Hudson and Larkin⁴⁵ wherein only a subset of the projection data are used for each update which leads to an acceleration of the reconstruction. If, for example, the projection data were partitioned into five subsets, each of which are assumed to uniformly sample the projection data, then the reconstruction would be accelerated by a factor of five. This acceleration comes at the cost of no longer having guaranteed convergence to the ML image estimate and noise propagates into the image at an accelerated rate compared to MLEM.⁴⁴ An example sinogram and reconstructed transverse image are shown in Figure 1.6 where the sinogram corresponds to a set of projection planes which were perpendicular to the z-axis of the system, i.e. $\theta = 0$. These data were collected as part of the work described in Chapter 4 and correspond to an acquisition of an anthropomorphic torso phantom with a cardiac insert. As you regard the sinogram from its base to its top, you will notice that objects that are not perfectly aligned in the center of rotation exhibit a sinusoidal trajectory, and

hence the name ‘sinogram’. The corresponding image shows the activity distribution within the phantom where there was no tracer injected into regions corresponding to the model lungs, spine and cardiac blood pool. A low activity was injected into the phantom cavity the encompasses the model organs and a higher activity was injected into the walls of the cardiac model. An air-bubble within the cardiac model, which rose to the top, is the cause of the discontinuity that can be seen in the cardiac insert.

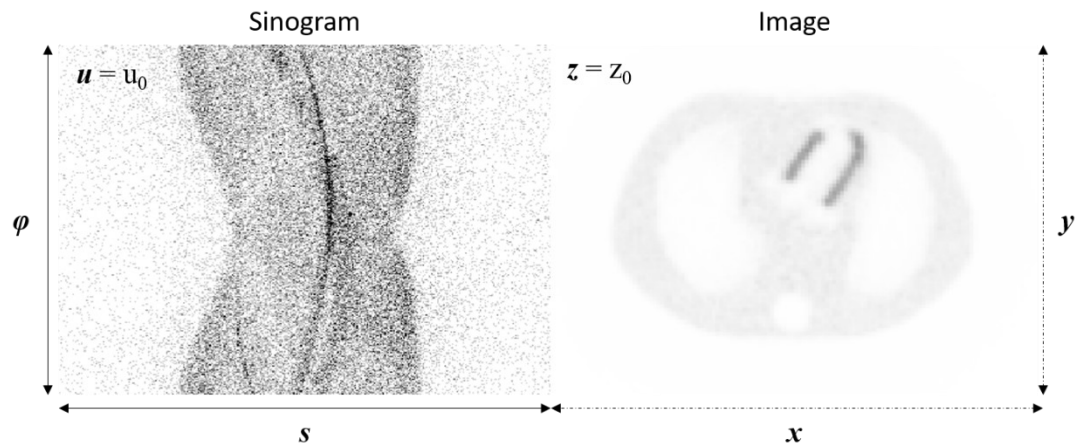


Figure 1.6 An example sinogram and image from a PET acquisition of an anthropomorphic torso phantom. This sinogram corresponds to the set of projections described by (s, φ) with a polar angle $\theta = 0^\circ$ and a fixed u coordinate. A reconstructed transverse image of the phantom is shown on the right and is defined on x and y for a fixed z -coordinate. The most intense feature of the image is the cardiac model which has a horseshoe-like appearance in this perspective. An air-bubble in the cardiac insert caused the void at the highest region of the insert.

1.3 Imaging the Heart with PET

1.3.1 Anatomy of the Heart and Electrocardiographic Signals

The work described in this thesis is aimed at PET imaging of the heart and so a brief description of the anatomy of the heart is provided here to make clear later mention of specific aspects of the heart. The heart is a muscular organ that is composed of four

chambers: the right (RA) and left atria (LA), and the right (RV) and left ventricles (LV). A cross-sectional diagram of the heart is shown in Figure 1.7 wherein all four chambers of the heart are depicted. The atria serve as inlet chambers of blood returning to the heart from elsewhere in the body. In particular, the right atrium is filled by blood from the superior and inferior vena cava which return de-oxygenated blood from, roughly, above and below the shoulders, respectively. The left atrium is filled with oxygenated blood returning from the lungs via the pulmonary veins. Blood passes from each atrium through a one-way valve into the corresponding ventricle. The right atrium and ventricle are separated by the tricuspid valve and the left atrium is separated from the left ventricle by the mitral valve. The right ventricle pushes deoxygenated blood to the lungs via the pulmonary arteries upon passing through the pulmonary valve. The left ventricle pushes blood through the aortic valve to the rest of the body via the aorta.

The walls of the heart are a three-layered structure. From the interior to the exterior, the layers are the endo-, myo-, and pericardium.⁴⁶ The myocardium contains the muscle cells that control cardiac contractions. The thickness of the myocardium, which varies throughout the heart, is associated with the amount of force needed by each chamber to perform its function.⁴⁶ The atria are thin structures as they need only push blood into their adjacent ventricles. The right ventricle (RV) is responsible for driving blood to the lungs, and back, and it has a thicker myocardium than the atria. The left ventricle has the thickest myocardium as it must push blood throughout the entire body.

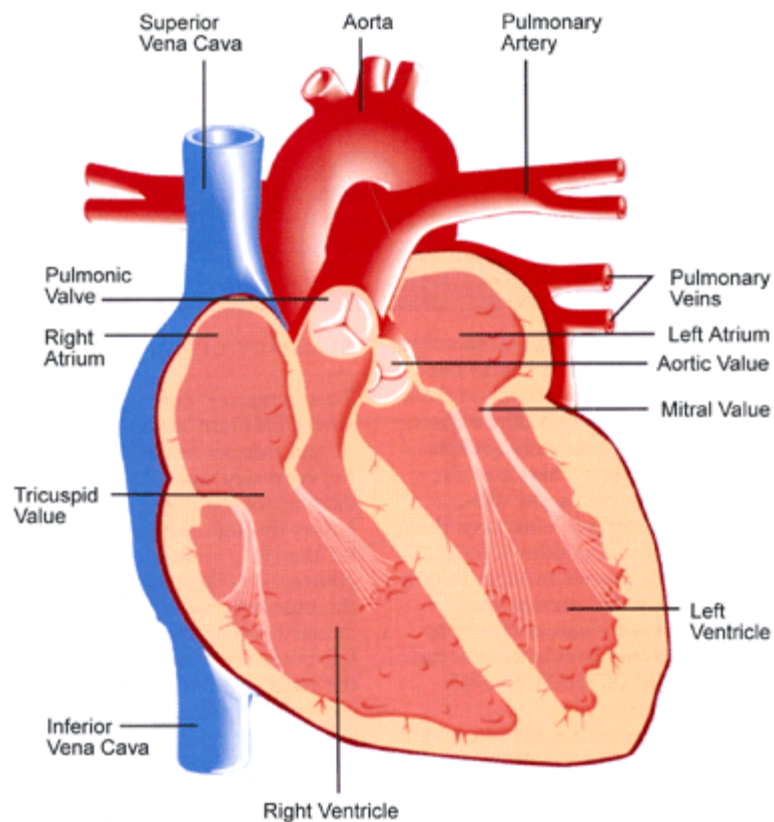


Figure 1.7 Basic anatomical diagram of the heart containing the four chambers, valves and major veins and arteries. This figure has been reproduced from the public domain clipart repository *WPClipart*^{iv}. The file was accessed on February 10, 2020.

Blood is supplied to the heart tissue via the right and left coronary arteries which originate at the base of the aorta. Both the right and left coronary arteries sub-divide fractally to supply blood to all regions of the heart. The major coronary arteries, and which are relevant to this work, are the left-anterior descending (LAD), left-circumflex (LCX), and right coronary (RCA) arteries. These three arteries supply blood to the left ventricle, which, as will be described in the following section, is the primary imaging

^{iv} *WPClipart*: https://www.wpclipart.com/medical/anatomy/heart/heart_diagram.png.html

target of cardiac perfusion imaging studies. A common way of visualizing the LV is to map its 3D structure to a 2D surface, or *polar map*.⁴⁷ An example polar map is shown in Figure 1.8, which is based on the so-called 17-segment model described within the American Heart Association's scientific statement on the *Standardized Myocardial Segmentation and Nomenclature for Tomographic Imaging of the Heart*.⁴⁷ At the center of the polar map is the apex of the heart and as the radial position increases the mapping moves from apex to the base. The apex-to-base extent is divided into four regions: apex, apical-, mid-, and basal-, which are depicted in the polar map as rings with increasing radii. The angular position can be referred to using compass-like directions where the North, East, South, and West positions on the polar map correspond to the Anterior, Lateral, Inferior, and Septal regions of the LV. Anatomical descriptions of each of the 17 segments of this model are specified by a combination of the radial and angular descriptors. Segment 11, for example, is referred to as the *mid-inferolateral* segment. Also depicted in Figure 1.8 are approximate territories of the LV for which blood is typically supplied by the LAD, LCX and RCA (coloured as white, light gray, and dark gray, respectively).

Cardiac contractions, or beats, are controlled by electrically conducted triggers within autorhythmic myocardial cells that are stimulated by the autonomic nervous system⁴⁸. The cardiac cycle is initiated by the polarization of a cluster of cells located within the RA called the sinoatrial (SA) node⁴⁶. Upon electrical depolarization the atria contract (*P-wave*) and blood flows into the ventricles while at the same time the electrical signals propagate to the atrioventricular (AV) node and initiate polarization among these cells⁴⁸.

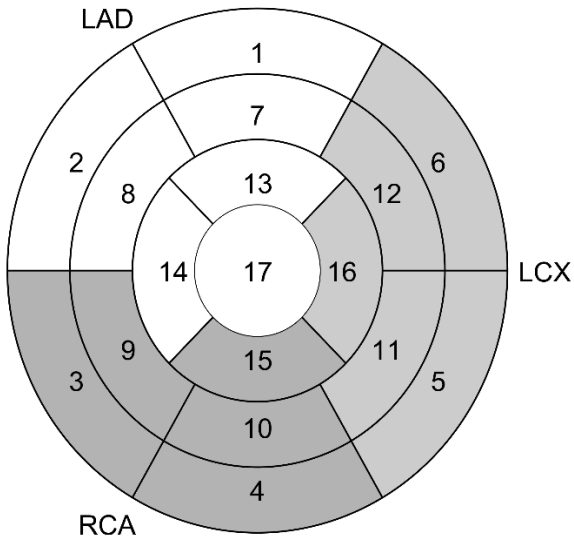


Figure 1.8 The American Heart Association 17-segment model provides a 2D polar map representation of the left ventricle. The coronary artery territories are indicated with gray shading. The region corresponding to the left-anterior descending (LAD), left-circumflex (LCX) and right coronary (RCA) arteries are shown in white, light gray, and gray, respectively. The outer annulus (segments 1 – 6) corresponds to the basal region, the middle annulus (segments 7 – 12) corresponds to mid region, the inner annulus (segments 13 – 16) corresponds to the apical level of the LV, and the apex (segment 17) is shown at the center.

The AV node is located in the interatrial septum and is connected to conductive tissues which travel down the septum and split near the apex before extending upwards toward the bases of the RV and LV.⁴⁶ The polarization and subsequent depolarization of the AV node is referred to as the *QRS-wave* on electro-cardiograms (ECG) and trigger ventricular contraction.⁴⁸ Ventricular relaxation and re-polarization is triggered the *T-wave*.⁴⁸ A schematic representation of the electrocardiographic signals is illustrated in Figure 1.9. The periods of ventricular contraction and relaxation are referred to as *systole* and *diastole*.

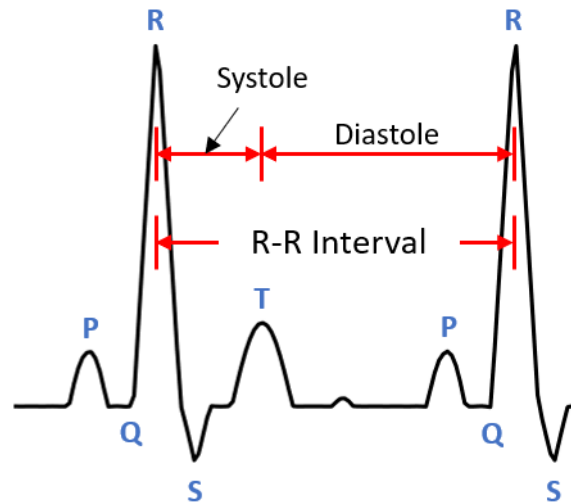


Figure 1.9 Schematic representation of a normal ECG signal. The P, QRS and T waves are indicated along the waveform. So too are the phases of ventricular systole and diastole. The period spanning subsequent R-waves is referred to as the R-R interval. The amplitude of the R-wave makes it easy to detect on ECG signals and serves as an indicator of the start of each cardiac contraction. The waveform shown in this figure was simulated using an open source MATLAB function called *ECG simulation* and was created by R. Karthik^v.

1.3.2 Myocardial Perfusion Imaging with PET

Myocardial perfusion imaging (MPI) is a diagnostic imaging procedure used to assess the effectiveness of transport of blood, and the nutrients it contains, to myocardial cells. Reduced perfusion of blood to the myocardium can be an indication of elevated risk of adverse cardiac events, e.g. heart attack (myocardial infarction).⁴⁹⁻⁵¹ In this section, the essential aspects of MPI in the context of PET are described. The information provided here is largely based on that described in the American Society of Nuclear Cardiology (ASNC) imaging guidelines/ Society of Nuclear Medicine and Molecular Imaging

^v Karthik Raviprakash (2020). ECG simulation using MATLAB (<https://www.mathworks.com/matlabcentral/fileexchange/10858-ecg-simulation-using-matlab>), MATLAB Central File Exchange. Retrieved February 12, 2020

(SNMMI) procedure standard for positron emission tomography (PET) nuclear cardiology procedure⁵². Due to the extent to which this section relies on that report, it will not be explicitly cited throughout. Additional resources have also been used and are cited explicitly.

The goal of MPI is the detection of significant occlusion of coronary arteries that supply blood the myocardium, otherwise known as ischemic Coronary Artery Disease (CAD). Assessment of perfusion can help inform physicians of the best approaches for managing patients with known or suspected CAD. MPI is typically conducted twice for a single study; each corresponds to one of two physiologic conditions: rest or stress. Rest and stress states are distinguished by the flow rate of blood: a resting state corresponds to baseline blood flow rates and stress (or hyperemia) corresponds to elevated blood flow rates. Stress can be induced in patients through exercise or with the use of pharmacologic vasodilators agents that simulate exercise.

Normal perfusion during stress imaging is associated with the absence of significant CAD, whereas reduced perfusion during stress is associated with ischemic CAD and/or prior infarction. In the event that perfusion is abnormally reduced at stress but not at rest, the ischemia is considered to be reversible, stress-induced ischemia. If perfusion defects are matched between stress and rest, the defect is not reversible and is associated with injury to the myocardium from prior infarct. Perfusion defects can exist regionally, or globally within the myocardium depending the number of coronary arteries that exhibit ischemia, e.g. single- versus multi-vessel CAD. The tracers used in MPI accumulate in the myocardium in proportion to the blood flow to the region and integrity of the muscle cells (myocytes). The activity shown on an uptake image also contains that of the tracer

concentration which is still in the blood and has not been taken up by the myocytes.⁵³ As defects are assessed based on the relative reduction in uptake compared to the maximum uptake region (reference), global reduction in perfusion may appear to be normal. This effect may be observed in the case of triple-vessel CAD, in which case standard MPI has been shown to have an increase in false-negative test results. Likewise, global perfusion reduction can result from disease of microvasculature, as is common in uncontrolled diabetes.^{54,55} Determination of the absolute myocardial blood flow (MBF), as opposed to relative perfusion, has been shown to improve the sensitivity of detection of CAD for patients with globally reduced perfusion.^{56,57} MBF is a measure of the specific flow rate of blood transiting through myocardial tissue in units of volume of blood per unit time per gram of tissue (mL/min/g)⁵⁸. Calculation of MBF necessitates dynamic imaging procedures wherein the activity within regions of interest in myocardium can be sampled as a function of time. Kinetic modelling of the radiotracer can then be performed to estimate. This process will be described in greater detail in Section 1.3.3.

Perfusion data can be assessed qualitatively and/or semi-quantitatively to characterize the defect(s). The following represent qualitative descriptors. The location indicates the anatomical region of the myocardium in which a defect was observed. Due to the association of segments of the myocardium with specific coronary arteries, location information can provide insight as to the arteries involved with ischemic perfusion defects. The extent of a perfusion defect corresponds to its relative proportion of the myocardium size. Low, medium and large extents are associated with 5-10%, 10-20%, and >20% of myocardium, respectively. The extent can also be described by the number of left-ventricular segments that exhibit reduced perfusion.

Semi-quantitative assessments can be made as summed stress (SSS), summed rest (SRS), and summed differences (SDS) scores. These measures are based on a 5-point scale that stratify severity of perfusion defects within each of the 17 segments of the myocardium. The point values range from 0 to 4, and correspond no defect, mildly reduced, moderately reduced, severely reduced, and absent of activity, respectively. The SSS and SRS correspond to the sum of the values among all 17 segments from the stress and rest images, respectively. The SDS is the sum of the segmental differences between stress and rest scores across (stress – rest). These scores can simultaneously assess both severity and extent of perfusion defects. SSS scores in the ranges of 0-3, 4-7, and > 8, correspond to normal, mildly abnormal, and moderately to severely abnormal, respectively.

When quantitative MBF is performed, myocardial flow reserve (MFR) can also be reported. MFR is determined as the ratio of MBF at stress to that at rest, indicating the ability of blood supply to increase to meet cardiac demand with exercise. Lower limits on normal stress MBF values, which range greatly among patients based on age, sex, and presence of traditional cardiovascular risk factors, have been reported⁵⁹ as 2 – 5 mL·min⁻¹·g⁻¹. An MFR measurement greater than 2.3 corresponds to low risk of future adverse cardiac events. An MFR less than 1.5 indicates significantly reduced flow and an increase in risk of adverse cardiac events. Some discrepancy in these limits have been reported, e.g. in a review paper by Juneau and colleagues⁶⁰, limits of 2.0 and 1.7 for normal and abnormal MFR were suggested. Stress MBF is often evaluated with MFR, as MFR alone can be erroneously low if rest MBF, its denominator, is unusually high. This can occur in patients with hypertension, for example.

The four most relevant perfusion tracers are ^{82}Rb , ^{13}N -ammonia, ^{15}O -water, and ^{18}F -Flurpiridaz. In North America, PET MPI is largely restricted to the use of ^{82}Rb and ^{13}N -ammonia, whereas ^{15}O -water is also used in Europe and Japan.⁶⁰ ^{18}F -Flurpiridaz⁶¹, however, is currently the topic of a Phase III clinical trial in the United States.⁶²⁻⁶⁴ Several important properties like half-life, production method, kinetic behaviour, extraction fraction, retention fraction, and effective dose per scan are summarized for each of these tracers in Table 1.3.

The half-life of a radiotracer has a significant impact on how it can be used clinically. ^{82}Rb , ^{13}N -ammonia, and ^{15}O -water, are relatively short-lived radiotracers; their half-lives range from approximately 1 to 10 minutes, which necessitates rapid access for clinical use. ^{13}N -ammonia and ^{15}O -water are produced using cyclotron accelerators that must be located at the clinic. ^{15}O production has been reported using the $^{15}\text{N}(p,n)$ reaction⁶⁵ and ^{13}N has commonly been produced via the $^{16}\text{O}(p,\alpha)$ reaction.⁶⁶ Note here that p , n and α in these reaction formulae represent protons, neutrons and alpha particles, respectively. ^{82}Rb , however, is produced using a $^{82}\text{Sr}/^{82}\text{Rb}$ (decay via electron capture) generator⁶⁷ and can be eluted approximately every 10 minutes as the ^{82}Rb activity reaches secular equilibrium with its parent isotope. ^{18}F -based tracers must also be produced using cyclotrons (e.g. via the $^{18}\text{O}(p,n)$ reaction⁶⁸) but its nearly 2 hours half-life allows it to be transported from a production facility to the clinic. The half-lives are also associated with radiation doses committed to the patients. Short-lived tracers generally lead to smaller whole-body effective doses than longer-lived tracers. A typical PET MPI acquisition may lead to effective doses in the range of 1 – 4 mSv. In contrast, SPECT tracers which have

^{99m}Tc as their radionuclide (which has half-life of 6 hours) lead to effective doses in excess of 5 mSv⁵⁹ or nearly as high as 10 mSv.⁶⁹

The energy spectrum of the emitted positron affects its range within human tissue. Of the four tracers listed in Table 1.3, ^{82}Rb has the largest mean positron range. Increased positron range has adverse effects on the spatial resolution of the images as the positron may travel up to several millimeters away from its point of decay before annihilating with an electron in tissue. Positron range thus imposes limits on the precision with which the position of tracer can be estimated within the body.

The biological properties of the tracers also dictate how they can be used clinically. A favourable tracer quality in the context of MPI is a specific biodistribution to the myocardium which leads to enhanced contrast with non-target tissues (e.g. blood, lungs and liver).⁵⁹ Additionally, high retention of the tracer in the myocardium also makes visualizing the myocardium more effective as the tracer distribution is stable for longer periods of time.⁶⁹ If MBF is being quantified, the rate of tracer extraction from the blood into the target tissue is an important factor. When tracer extraction fraction is high, measurements of MBF demonstrate less intra-patient variability as seen in repeated imaging procedures (or test-retest measurements).⁶⁹ Of the tracers listed in Table 1.3, only ^{15}O -water is not suitable for MPI as its retention fraction within the myocardium is effectively zero. This is associated with the passive bi-directional diffusion of water across the myocyte membrane⁵⁹ which does not create stable uptake within the myocardium. For the same reason, though, the extraction fraction for water is unity, which means it is an ideal tracer for MBF quantification. The remaining perfusion tracers have non-zero retention fraction and thus permit high quality visualization of uptake

within the myocardium. They also exhibit extraction fractions that are less than unity, and thus necessitate the use of flow-dependent extraction-corrections functions to determine MBF. ^{13}N -ammonia and ^{18}F -Flurpiridaz have extraction fractions that are relatively high compared to ^{82}Rb and are expected to provide higher precision estimates of MBF.⁵⁹ Nevertheless, accurate MBF estimations has been reported for each of these tracers.⁷⁰⁻⁷³

Table 1.3 Physical and practical characteristics of commonly used PET radiotracers for MPI imaging. The references associated with each characteristic are indicated after their names in the first column.

	^{82}Rb	^{13}N -Ammonia	^{15}O -Water	^{18}F -Flurpiridaz
Half-life [min] ⁶⁰	1.3	10	1.9	110
Mean Positron Range in Tissue ⁶⁰ [mm]	2.6	0.6	1.0	0.2
Production ⁶⁰	Generator	On-site Cyclotron	On-site Cyclotron	Regional Cyclotron
Extraction Fraction ⁶⁹ (Stress - Rest)	0.40-0.70	0.95-0.99	1.00	> 0.9 [†]
Retention Fraction ⁶⁹ (Stress - Rest)	0.30-0.70	0.50-0.90	0.00	0.6-0.9 [†]
Effective Dose ⁵⁹ [mSv]	3 [‡]	1	0.4	4

[†] These extraction and retention fractions for ^{18}F -Flurpiridaz were collected from Juneau and colleagues, unlike the other values provided.

[‡] Note that effective dose in the range of 1-2 mSv have been reported which include rest and stress acquisitions⁷⁴.

1.3.3 Kinetic Tracer Modelling and Estimate of Absolute Myocardial Blood Flow

The use of kinetic modelling in the estimation of absolute MBF was alluded to in the previous section. A description of kinetic modelling is provided here in the context of MBF estimation. A PET image is a discretized representation of the activity concentration within the body but the signal obtained for a given region of interest, or even in a single voxel, represents a superposition of the contributions the tracer concentrations in the constituent tissues contained within the image sampled region of interest (ROI), or voxel. Moreover, these individual contributions are generally integrated over the duration of the acquisition used to produce the image. Such an image is capable

of only spatial information of the tracer distribution within the body and provides limited information regarding the dynamics of the tracer within specific tissues. The purpose of kinetic modelling (KM) is to address such limitations; KM can be used to disentangle the signal contributions of the unique physiologic constituents within a region that is being sampled.⁵³ More specifically, the kinetic model provides a relationship with which the blood flow within myocardial tissue may be inferred from a dynamic series of activity measurements taken from arterial blood and myocardial tissue.

Kinetic models are based upon coupled differential equations that relate the dynamics of tracer molecules into and out of tissues that are relevant to the imaging target. The individual constituents are referred to as *compartments*. Absolute blood flow can be modelled using a two-compartment model (blood and perfused tissue), which is also commonly referred to as a one-tissue-compartment model.⁷⁵ A schematic representation of this is provided in Figure 1.10(A). In this model the only tissue compartment is that of the myocardial tissue to which arterial blood perfuses from the adjacent capillary or capillary bed. The tracer concentration of the arterial blood, which serves as the input to the kinetic model, and myocardial tissue as a function of time are denoted as $C_a(t)$, and $C_t(t)$, respectively. The tracer influx and efflux rates are denoted as K_1 and k_2 , respectively. While the relationship will be shown explicitly in the following, it is worth noting here that K_1 is closely related to MBF and shares the same units. The net tracer flux across the capillary wall, $dC_t(t)/dt$, is the difference between flux into and out of the tissue compartment as shown in Eq. 0.16.⁵³ This first order differential equation has the solution for $C_t(t)$, shown in Eq. 0.17,⁷⁵ where the symbol \otimes denotes a 1D convolution operation.

$$\frac{dC_t(t)}{dt} = K_1 C_a(t) - k_2 C_t(t) \quad \text{Eq. 0.16}$$

$$C_t(t) = K_1 C_a(t) \otimes e^{-k_2 t} \quad \text{Eq. 0.17}$$

This model could be extended to a two-tissue-compartment model where the tissue is further distinguished as the combination of myocytes and extracellular space, as shown in Figure 1.10(B), but the additional parameters are not necessary for accurate MBF estimation.⁶⁷

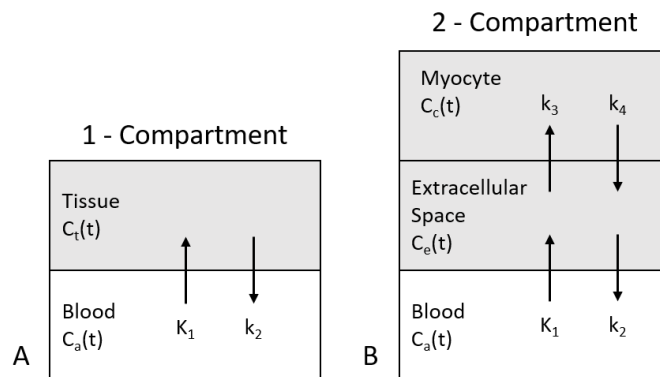


Figure 1.10 One- (A) and Two-Tissue-Compartment (B) model representations of blood flow within the myocardium. In both cases, capillary (Blood) regions and myocardial tissue are coloured as white and gray, respectively. Black arrows indicate the directions of tracer flux across compartmental boundaries, each of which is labelled with its respective rate constant. In the Two-Compartment model the myocardial tissue region is divided into two more specific compartments which are the myocytes and the extracellular space.

MBF estimation is the process of estimating the kinetic model parameters from a series of measurements of the arterial input function and the myocardial tracer concentration. The measurements are derived from a dynamic image reconstruction of the perfusion study which begins with tracer injection and continues for a duration long enough to observe tracer equilibrium. For ⁸²Rb studies, dynamic acquisition with durations of 2 to 6 minutes have been reported.⁶⁷

In practice, the kinetic model must be modified to account for the fact that a single voxel of a PET image contains many capillaries and myocytes and the resultant signal comes from the combination of these. The myocardial tracer concentration, which contains blood and tissue, can be denoted as $C_m(t)$ and is the weighted sum of the arterial blood and tissue tracer concentrations.⁶⁷ The weights correspond to the fraction of the volume being sampled that each component occupies. The fractional blood volume and tissue volume are denoted as f_a and f_t , respectively. If we assume that the volume being sampled is strictly composed of these two components then f_t equates to 1 minus f_a , and we can reduce the complexity of our model by one free parameter. The estimated myocardium tracer concentration $\hat{C}_m(t)$ is defined in Eq. 0.18. If we substitute the tracer concentration of the tissue, defined previously, then our model takes on the form shown in Eq. 0.19.

$$\hat{C}_m(t) = f_a C_a(t) + (1 - f_a) C_t(t) \quad \text{Eq. 0.18}$$

$$\hat{C}_m(t) = f_a C_a(t) + (1 - f_a) K_1 C_a(t) \otimes e^{-k_2 t} \quad \text{Eq. 0.19}$$

Both f_a and f_t are also interpreted as correction factors for the partial volume effect that is associated with the limited spatial resolution of the imaging system which leads to activity spilling into or out of a region of interest.⁵³ The last amendment to this kinetic model formula is the parameterization of K_1 as a function of the myocardial blood flow, MBF. This is necessary for tracers that do not exhibit an ideal first-pass extraction fraction. The Renkin-Crone permeability model is commonly employed to derive the functional form of K_1 .⁵³ In this model K_1 is equal to MBF multiplied by the first-pass

extraction fraction E_0 . The functional form of K_1 is defined in Eq. 0.20, where P represents the permeability of the tracer across the capillary wall and S represents the capillary surface area per unit mass of tissue. When the permeability-surface area product is large compared to blood flow, $PS \gg MBF$, then $K_1 \approx MBF$. However, the converse changes the interpretation of K_1 to be an indicator of the permeability of the capillary wall as when $MBF \gg PS$, $K_1 \approx PS/MBF$.

$$K_1 = MBF \cdot E_0 = MBF \cdot \left(1 - e^{-PS/MBF}\right) \quad \text{Eq. 0.20}$$

The extraction fractions for the four PET perfusion tracers were stated previously in Table 1.3. ^{15}O -water has an ideal extraction fraction which implies that K_1 is equivalent to MBF . The other tracers exhibit non-ideal extraction fractions and thus the Renkin-Crone model is required. The use of the Renkin-Crone model introduces noise in the MBF estimates, the extent of which has been suggested to increase with the magnitude of the correction factor, i.e. more noise may be introduced in MBF measurements for tracers with low extraction fractions.⁵⁹

The problem of estimating MBF is cast as a parameter estimation problem using non-linear regression methods. The data that are used to estimate the kinetic model parameters are derived from measuring the activity at specific regions of interest in a dynamic image reconstruction. Each voxel has a corresponding time-activity curve (TAC) which represents the measured activity at that location as a function of time. The $C_m(t)$ data are acquired from sampling the myocardium throughout the acquisition. The sampling points are determined from a late uptake image where a high contrast of the myocardium can be observed and are replicated for all earlier image frames. Historically, the arterial blood tracer concentrations were acquired from blood samples taken from the patient during

imaging.⁵³ However, sampling methods have also been established for image-based measurements where a blood ROI is defined in the cavity of the left-ventricle or left-atrium.⁵² Additionally, TACs can be derived from large regions-of-interest, segments of LV myocardium, for example, or the individual voxels therein. Figure 1.11 provides an example time-activity curve and LV polar map of blood flow from a clinical acquisition. Figure 1.11(A) shows the measured and modelled TAC data for an example study. The inputs to the one-tissue kinetic model described in Eq. 0.19, i.e. the measured blood pool $C_a(t)$ and myocardium $C_m(t)$ activities, are shown by the red line and blue dots, respectively. The modelled myocardium $\hat{C}_m(t)$ and modelled tissue $C_t(t)$ activities, related as shown in Eq. 0.18, are indicated by the dashed blue and cyan lines, respectively. Figure 1.11(B) shows a polar map of the flow measurements within each of the sampled LV voxels in units of mL/min/g.

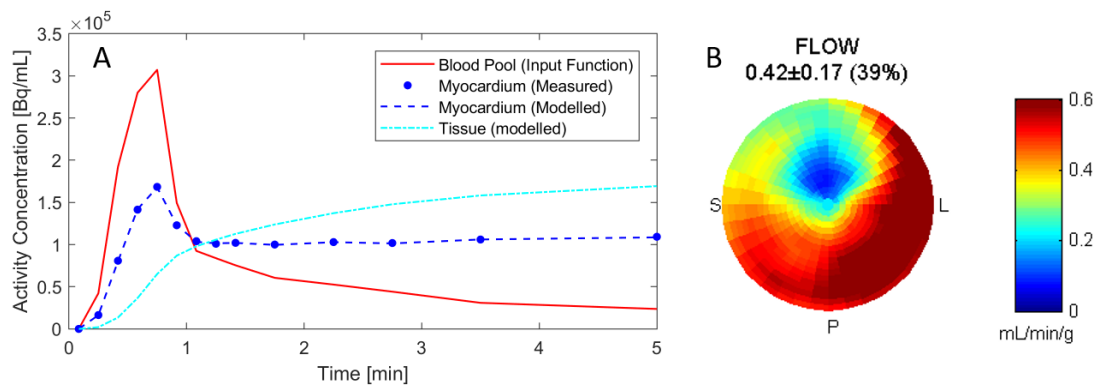


Figure 1.11 Example kinetic modelling data from a clinical dataset. The time-activity curve (A) data are shown for the measured blood pool (red), measured myocardium (blue dots), the modelled activity of the myocardium (blue line), and modelled tissue (cyan) activity. The blood pool data have been averaged over a volume of interest in the LV cavity and the myocardium data shown correspond to an average across the entire LV. The polar map (B) depicts the estimated blood flow values in each of the voxels sampled within the myocardium. The mean \pm SD flow value for this case is also indicated.

Apart from the previously mentioned cardiac spillover effects, which are associated with the partial volume effect, cardiac motion, and blood volume⁷⁵, there are several factors that can affect the precision of MBF estimation. Examples are CT attenuation correction (AC) misalignment, extra-cardiac spillover, patient motion.⁷⁶ CTAC artifacts are most notable at the interface of the antero-lateral wall of the LV with left lung due to the sharp gradient in the attenuation factors at this location, although careful registration of the CT and PET images can largely reduce these artifacts⁶⁷. Extracardiac spillover corresponds to the contamination of activity measurements within the myocardium ROI(s) from tissues that exhibit high uptake outside of the heart. In ¹³N-ammonia perfusion studies late uptake in the left lung can lead to these effects in the lateral wall, and in ⁸²Rb studies stomach wall uptake can potentially interfere with measurements in the infero-lateral segment.⁶⁷

The effects of patient motion are the chief concerns of this thesis. Patient motion can lead to CTAC misalignment artifacts as well as blurring in the PET images. Furthermore, patient motion can lead to incorrect spatial sampling of the arterial blood or tissue ROIs.⁷⁷ A review of patient motion effects and compensation strategies is the topic of Chapter 2.

1.4 Thesis Summary

The work described in this thesis was aimed at applying a data-driven motion tracking technique to clinical cardiac PET/CT perfusion imaging studies to compensate for the degrading effects of patient motion. Motion of the heart due to respiration as well as whole-body motion are two separate problems that were considered. The primary approach to motion compensation was based on tracking the motion of small radioactive

markers placed on patients during imaging. Calculations of the marker motion directly from the raw list-mode data provided information that was used to infer the respiratory patterns of patients or whole-body displacements and subsequently perform various types of motion compensation. To evaluate the performance of the motion compensation methods involving the use radioactive markers other approaches were also employed. A commercial camera system was used to monitor patient respiratory patterns and a previously developed data-driven motion tracking algorithm was implemented to address whole-body motion.

Chapter 2 Patient Motion Tracking and Compensation

2.1 Patient Motions: Respiratory, Cardiac and Body

The problem of patient motion compensation is multi-faceted as there are various forms of patient motion for which various solutions have been proposed. Head motion in the context of brain PET imaging studies is effectively a rigid body problem as the brain remains fixed within the structure of the skull.⁷⁸ As a result, motion compensation strategies that are effective in this application are not necessarily so for others. In the thorax motion exists which can be associated with cardiac contraction, respiratory displacements of the chest wall and the diaphragm, peristaltic motion, voluntary or involuntary body motion⁷⁹ as well as ‘cardiac creep’⁷⁷ – a gradual repositioning of the heart that may be observed during imaging as a patient’s breathing pattern returns to a resting state following the induction of stress by treadmill exercise. For this work, the primary concern is associated with cardio-respiratory, i.e. motion of the heart due to respiration, and body motion, both of which represent non-rigid forms of motion.

Motion of the heart due to respiration was well documented in a study by McLeish and colleagues⁸⁰ where magnetic resonance imaging (MRI) was performed while patients and healthy volunteers held their breath at various respiratory amplitudes ranging from full inspiration to full expiration. They acquired data for approximately 30 seconds for each breath-hold and performed rigid (translation and rotation) and non-rigid image registrations on the resulting images to model the motion of the heart. With respect to rigid motion of the heart during respiration they reported that motion along the superior-inferior axis of the patient was dominant with a mean displacement of 12.4 mm compared to 4.3 mm and 2.0 mm for motion along the anterior-posterior and right-left direction.

More qualitatively, as people inhale their hearts move toward their feet, their chest wall, and slightly to the right. Rotations were more difficult to compare as the center of rotations differed among subjects, however, while considering both translations and rotations some points on the heart were displaced up to 30 mm between full inspiration and expiration. In regard to non-rigid motion of the heart, there was also great inter-subject variability – to such an extent that some exhibited no effective non-rigid cardiac motion due to respiration. Some qualitative findings indicated that deformations were generally greater at the apex compared to the base of the heart. The magnitude of deformation tended to correlate with motion of the diaphragm, and non-rigid motion was weakly correlated with the magnitude of rigid motion.

Body motion is more difficult to define than that of respiratory or cardiac motions. The term *body motion* is vague and is often used to describe generally voluntary or involuntary sources of motion like a deep cough or efforts exerted by a patient to re-position themselves when in discomfort.⁷⁷ Body motion is frequently modelled using only translational descriptors which is certainly an oversimplification but also one that has been demonstrated to be beneficial in regards to improving image quality and quantification.⁸¹ In regard to cardiac perfusion PET studies several groups have published reports on the prevalence, magnitude, and time of occurrence of rigid patient motion. Hunter and colleagues⁸² reported that body motion with magnitudes ranging from 5 mm to more than 10 mm was identified in 62% of cases among a cohort of 236 patients who underwent ⁸²Rb dynamic imaging aimed at measuring absolute myocardial blood flow. They also reported that motion did not appear to be more frequent for any particular time point during the 8-minute acquisitions. From most to least prevalent, they found that

motion prevalence was ordered as follows: the superior-inferior, anterior-posterior and right-left axes. Among these, patients tended to move superiorly, posteriorly and equally left and right. A similar study by Lee and colleagues⁸³ examined body motion among 225 patients that underwent ⁸²Rb myocardial perfusion imaging studies. They reported a time-dependent motion prevalence noting that motion was found more frequently in the early time frames when the tracer had not yet perfused into cardiac tissue particularly during stress acquisitions. During stress acquisitions motion occurred more frequently toward the inferior and septal (approximately to the right) directions. During rest, however, motion in the inferior direction was predominant.

The long acquisition times associated with PET imaging make them more susceptible to artifacts⁸⁴ from all forms of motion that have just been described. The effect of patient motion is largely that of inaccurate tracer distribution estimation due to a loss in spatial resolution as well as mis-alignment with PET emission data and corresponding attenuation correction map.⁸⁵ When the motion extent is relatively large compared to the spatial resolution of the scanner the effects become more severe which can potentially lead to degradation in image quality which affects the interpretation of the images and, possibly, misdiagnosis of the patient.⁸⁴ Moreover, as PET systems continue to advance with respect to hardware and reconstruction techniques the spatial resolution will continue to improve thus leading to greater influence of patient motion on image quality.⁸⁴

Kortelainen and colleagues⁸⁶ performed SPECT/CT acquisitions of a moveable cardiac phantom wherein respiratory motion was simulated with varying magnitudes. They demonstrated the perfusion defects became less pronounced in the presence of respiratory

motion compared to a motion-free acquisition. Additionally, the effects of motion were predominant in the anterior and inferior walls of the cardiac phantom. In another study by the same group, dual cardiac-respiratory gating was performed to assess the effect of these forms of motion on function MPI measurements like LV volume, wall motion and thickening.⁸⁷ They demonstrated that dual gating for cardiac and respiratory motion compensation led to small, but significant, increases in LV volume, and reductions in wall thickening throughout the cardiac contraction. They did not, however, demonstrate significant changes in relative perfusion measurements. It is important to note that both of these studies were performed using SPECT/CT acquisitions which generally have spatial resolution that is poorer than that of PET/CT. While trying to apply these measurements to PET MPI, it is not unreasonable to expect that these effects could become more pronounced.

For dynamic cardiac acquisition where absolute blood flow quantification is being performed patient motion can affect not only image quality, as described for MPI, but also the dynamic activity sampling within the blood pool and the myocardium.⁸⁵ Incorrect sampling due to patient motion often presents itself in the time-activity curves and manifests as discontinuities or spikes along the measured curves.⁷⁷ In a small clinical sample of seven patients, Yu and colleagues demonstrated that respiratory motion correction led to substantial increases in MBF and CFR, e.g. mean increase of 15% and 19%, respectively. The increases tended to be larger when motion was more severe. In a study by Hunter and colleagues⁸² that used an extensive computer simulated dataset based on clinically observed translational motion, it was shown that errors in MBF as high as 250% could be expected and as high as 500% in extreme cases.

2.2 Motion Tracking

To address the problem associated with patient motion many researchers have proposed methods to compensate or correct for patient motion. Motion compensation may be achieved through patient coaching and/or immobilization. This framework involves communicating the importance of remaining motion-less to the patient, providing them with training or explanations of the methods/devices that will be used to immobilize them or minimize motion, as well as coaching during imaging. Immobilization methods are largely applied within the domain of oncologic PET/CT studies used for radiation therapy treatment planning⁸⁸, but patient coaching or breath-hold techniques are more generally applicable to PET studies covering the thorax, e.g. cardiac PET/CT. A discussion of these methods is provided in Section 2.3.1.

Alternatively, there are also motion compensation or correction approaches that are predicated on the use of a model of the patient's motion, that do not require immobilization and are less dependent on patient compliance with training or coaching. To attain such motion information some sort of motion tracking system is needed. Two general categories exist with which different tracking methods can be distinguished: hardware and data-driven methods. The hallmark of the former category is the use of some ancillary device that is used in addition to the medical imaging system that can track a patient's movement. The specific device used often depends on the type of motion that is being tracked, but some common hardware systems consist of optical cameras which track fiducial markers placed on the patient or non-visual systems that monitor physiologic functions of the patient like respiration or electrocardiographic signals. A brief review of some common hardware-based motion tracking systems is provided in

Section 2.2.1. Data-driven methods, however, seek to perform the same tracking tasks without the use of ancillary devices. In particular, data produced by the imaging device itself are used to generate information about a patient's movement. The signal of a PET scanner comes from the coincident detection of annihilation photons which are initially collected in a simple list, sorted into emission sinograms, and then reconstructed into tomographic images; various data-driven tracking methods have attempted to measure patient motion using each of the data forms. The elegance of the data-driven methods stems from their use of data that already exist without the need for additional, and often expensive, equipment to track patient motion. The corollary of which is that patient setup and preparation becomes more efficient which can be beneficial for patient comfort as well as for the operation of the PET clinic. While these characteristics have significant potential benefit, data-driven tracking methods are not well established in clinical use compared to their hardware-based alternatives which are more established. While data-driven methods remain largely in the domain of research⁸⁹, several major PET scanner vendors have now also begun offering commercial data-driven solutions for motion tracking^{vi} and indeed it will be interesting to see if their use becomes more commonly adopted. A brief overview of various data-driven motion tracking methods is also provided in Section 2.2.2.

The bulk of the work presented in this thesis, however, is aimed at one particular motion tracking algorithm which is, in a way, a hybrid technique of the two categories just described. The positron emission tracking algorithm, or PeTrack, is a computational

^{vi} Examples of commercially available data-driven motion correction solutions: MotionFree, GE Healthcare; and OncoFreeze, Seimens Healthcare.

method designed to track the motion of point-source positron-emitting markers using the list-mode coincidence data. This method was originally designed for applications in radiation therapy⁹⁰ but was extended for use during positron emission tomography.^{91,92} PeTrack will be described in the following section.

2.2.1 Hardware-Based Tracking

Earlier in this section, the concept of a hardware-based tracking system was introduced. In this section, more details about their use and several common commercial examples are provided. This list is not exhaustive, but they are included here primarily to provide the reader with some scope of the available options.

In the context of PET imaging, hardware-based tracking systems monitor, either directly or indirectly, physiologic processes like respiration or cardiac contraction for the purpose of modifying the image acquisition or the reconstruction to compensate for associated motion artifacts. They are largely external monitors that are placed on the patient and do not require invasive methods such as interstitial insertion which is used in some radiation therapy applications.⁹³ A principal assumption of their use is that the external signal correlates well with internal motion of the imaging target. When designing such devices several aspects must be taken into consideration: the invasiveness of the device, patient comfort and tolerability, adaptability for different patients, and the ease of set-up and/or use by the operator.⁹⁴ Additionally, a good tracking system should respond quickly to variations of the signal, not introduce shifts in the baseline signal, should have high signal-to-noise ratio, and must not produce artifacts in the acquired image.⁹⁴ These systems monitor physiologic signals of the patient either directly or indirectly; the latter is much more common. With respect to respiratory monitoring

systems, a direct monitor would consist of measures of the flow of air into and out of the lungs, whereas indirect monitors usually correspond to monitoring movement of the external surface of the patient's chest or abdomen. These systems generally track respiratory motion at a frequency of 25 to 40 Hz and can respond quickly to human breathing rhythms which have principal frequencies in the approximate range of 0.1 to 0.5 Hz. For applications in PET, these systems generate respiratory triggers that mark specific phases or amplitudes of the respiratory cycles. The respiratory triggers of devices that can be integrated with the PET system can be included in the coincidence event stream (list-mode data) and retrospectively used to gate the raw data according to phase or amplitude. If the tracking system cannot be integrated with the PET system in this way, the recorded signals can be processed retrospectively to allow a user to reconstruct a respiratory-gated image series. Table 2.1 provides details of several respiratory monitoring systems that have been used in respiratory-gated PET/CT studies. The two most used respiratory monitoring devices are the Real-time Position Management (RPM) system (Varian Medical Systems, Palo Alto, United States of America) and the Respiratory Gating System AZ-733V (Anzai Medical, Tokyo, Japan).⁹⁴ Details on these are included in the table below, but briefly, the RPM is an optical tracking system which records the motion of a plastic block with reflective markers placed on the patient's chest or abdomen and the Anzai system is a belt-device worn by patients that produces an electric signal that is correlated with pressure induced by its expansion during respiration.

Table 2.1 Five commercial respiratory gating systems are described. Comments about their use, strengths, and weaknesses are also provided. Information about these systems has largely been attained from the following review papers on the topic of motion management in PET imaging: *Motion-tracking hardware and advanced applications in PET and PET/CT* by V. Bettinardi et al.⁹⁴; and *Respiratory Motion in Positron Emission Tomography/Computed Tomography: A Review* by S. A. Nehmeh and Y. E. Erdi.¹⁰⁰

Tracking System	Description	Comments
Real-time Position Management System (Varian Medical Systems, Palo Alto, United States of America)	A CCD system that both emits and detects light in infrared and visible spectrum monitors the motion of a block placed on the patient with passive reflective markers. The camera is typically mounted at the end of the patient table and the block is placed by technologists on the chest/abdomen ⁹⁴ .	The most widely used commercial respiratory monitoring system. The line of sight between the reflective marker and the camera can become obstructed by a patient's body or by the use of warming blankets ¹⁰¹ . Correlation between the RPM signal has been compared to that of tumour motion (lung and liver) as seen from 4D CT; good correlations were observed with inferior-superior tumour motion during respiration ¹⁰² .
Respiratory Gating System AZ-733V (Anzai Medical, Yokyo, Japan)	A belt system which is worn by the patient that monitors chest/abdomen expansion and compression. The belt contains load cells which generate an electronic signal according to variations in the tension on the belt ⁹⁴ .	A popular commercial respiratory gating system. The tension sensor requires calibration prior to each use ⁹⁴ . Has been shown to correlate well with the signals generated by the Varian RPM system ¹⁰³ , except in some cases of irregular breathing where phase shifts occurred between the two systems when they were set to trigger at particular respiratory phases ¹⁰⁴ .
PMM (Siemens, Medical Systems, Erlangen, Germany)	A spirometer device that directly measures the volume and rate of air flow during respiration. Consists of a mouth-piece through which a patient must breathe ⁹⁴ .	Provides direct measurement of the respiration. Shown to be accurate ¹⁰⁵ and reproducible ¹⁰⁶ . Trigger generation is hindered by susceptibility to baseline signal drifts ¹⁰⁷ . A nasal clip is used on patients to force mouth breathing, which is not always tolerated well and complicates patient setup ⁹⁴ .
BioVET CT1 (Spin Systems, Brisbane, Australia)	A temperature sensitive probe placed at the nostril of a patient which measures the changing air temperature during respiration with respect to the ambient room temperature ¹⁰⁰ .	The use of a similar device was reported to provide practical benefit in oncology PET studies in spite of the need for occasional intervention by technologist to adjust the temperature trigger thresholds ¹⁰⁸ .
Respiratory Bellows Systems (Medspira, Minneapolis, United States of America)	A bellows fixed to a belt that is worn around a patient's chest or abdomen which changes in size during compression and expansion of the chest. A pressure sensor within the bellows tube generates a respiratory wave form as the bellows compresses and decompresses the air in the tube ⁹⁴ .	The bellows has been coupled with the Mayo Clinic respiratory feedback system (Mayo Clinic, Rochester, United States of America) which produces a visual indicator of respiratory phase. Together these devices can be used to coach patient breathing and/or for breath-hold acquisitions ⁹⁴ .

Other optical tracking systems have been designed to monitor (in)voluntary rigid patient motion. Two commonly used systems during neurological PET studies are the Polaris⁹⁵ and Vicon⁹⁶ tracking devices (Northern Digital, Waterloo, Ontario, Canada). These devices track the rigid (rotations and translation) motion of passive reflective markers that are fixed to a support structure that is mounted on a patient's head during an imaging procedure.⁹⁵

2.2.2 Data-Driven Tracking

One of the earliest, and perhaps most intuitive, methods of tracking patient motion using data derived from the PET scanner was based on multiple acquisition frame (MAF) image reconstructions. Within this framework, many images would be reconstructed from short time intervals of the acquisition from which the motion of the patient could be inferred. The MAF approach was initially proposed by Picard and Thompson⁹⁷, although in their implementation the motion information was derived from an external optical tracking system. Nevertheless, the MAF approach was later adapted for use in PET motion tracking without an external tracking system. Feng et al.⁹⁸, proposed a method of extracting patient motion information from a time-series of tomographic SPECT or PET images by identifying a generalized set of center-of-mass point within image volumes and tracking their motion dynamically. Mukherjee et al.⁹⁹ estimated patient motion during brain PET studies via mono-modality image registration of short duration (5 s).

Using modern hybrid PET/MR scanners, simultaneous dynamic MR acquisitions have been used to estimate high-resolution patient motion also with the use of image

registration techniques. This approach has been applied to estimate cardiac and respiratory motions.^{109,110}

A significant limitation of the MAF motion estimation approach is the computational burden of reconstructing many images. To address this issue, others have implemented data-driven motion estimation/tracking methods that rely, instead, on the raw emission data acquired by the scanner. In the case of PET scanners, these data are typically stored in three-dimensional sinograms. If the scanner has TOF capability, then the raw emission data may instead be stored as a four-dimensional sinogram. This format of the data includes all prompt coincidence detections which have not been corrected for losses due to deadtime, detection efficiency, attenuation or decay of the radiotracer, yet many have shown that raw emission data contains useful information from which patient motion can be inferred.

Klein and Huesman¹¹¹ demonstrated that the temporal fluctuations of the axial center-of-mass of the emission data could be used to derive meaningful respiratory signals of patients undergoing PET acquisitions with stable radiotracer distributions, e.g. ¹⁸F-FDG. Others have identified sets of voxels in the 3D raw data space that exhibit large magnitudes in the power spectra in the range of frequencies that correspond to respiratory motion and then derived respiratory signals from the intensity fluctuations within this set of voxel throughout the PET acquisition.^{112,113} Thielemans et al¹¹⁴ proposed the application of principal-component analysis (PCA) on short frames of the raw emission data to extract motion signals that correspond to cyclical motions.

The most basic form of the data acquired by PET scanner is the list-mode data, which is simply a record of each prompt coincidence event detected by the scanner interspersed

with regular time-stamp events. The coincidence events contain indices of the crystal-pair that detected the event from which the geometric information about the event, or LOR, can be determined. Others have proposed tracking methods using list-mode data in which no radioactive markers were used. The capability of storing list-mode data is relatively new compared to the lifespan of PET systems, and so data-driven methods using this data format are also relatively new. One of the earliest approaches was proposed by He et al¹¹⁵, in which the coincidence count-histogram of the list-mode events over short time frames was used to estimate a respiratory signal. This method, based on knowledge of the geometric sensitivity profile of common PET scanners with a limited axial FOV, assumed that respiratory motion would cause temporal fluctuations in the scanner count rate as tissues with high radiotracer uptake move within regions of spatially variant detection sensitivity. Others calculated the axial component of the trajectories of the center-of-mass of LORs corresponding to regions-of-interest about the imaging targets, e.g. the heart in cardiac PET acquisitions, over short time frames to derive respiratory signals.^{116,117} Lastly, investigators at the Yale PET Center have developed centroid-of-distribution tracking methods to estimate respiratory and whole-body (or bulk) patient motion signals.^{118,119} In this approach, the geometric centroid of a set of LORs, either associated with full scanner FOV or a region-of-interest, is tracked over short time intervals to derive a 3D motion signal of the patient.

In addition to the data-driven approaches just mentioned, several other groups have studied the use of tracking the motion of external radioactive fiducial markers with the PET system. These methods constitute a hybrid approach between hardware and data-driven methods in that the PET scanner is being used to produce the tracking signal, but

the signal is derived from an external radioactive source placed within the PET scanner's FOV. Interestingly, radioactive markers have been used in each of the data-driven frameworks just described, i.e. image-based MAF motion tracking, motion tracking with emission data, and also using list-mode data. Examples of MAF motion tracking are found in the work of Naum et al.¹²⁰ who used external markers to retrospectively track patient motion in dynamic $H_2^{15}O$ cardiac blood flow studies and also Nazarpour et al.¹²¹ who reconstructed 0.5 s duration frames during brain PET simulation studies to estimate head motion during the acquisitions. Büther et al.¹²² reported their use of radioactive marker motion tracking in short duration sinograms for respiratory gating during liver and lung oncological PET studies. The PeTrack algorithm, proposed in this thesis, is an example of a radioactive marker-tracking approach that operates on list-mode data which has been applied to respiratory gating (see Chapter 3) and whole-body motion tracking (see Chapter 4 and Chapter 5) in cardiac perfusion PET studies. The PeTrack algorithm will be described in Section 2.4 along with a motivation for its use compared to these alternative methods.

2.3 Compensation and Correction

2.3.1 Breath-hold Techniques and Patient Immobilization

Prior to the inclusion of motion tracking systems in the clinical environment, and currently in busy clinics or those without resources to invest in additional motion-tracking equipment, motion compensation is attempted by a combination of patient training prior to imaging, patient coaching during imaging, and immobilization devices.

Even in the presence of motion compensation systems, educating patients on the importance of remaining as motionless as possible during imaging is essential.

Breath-hold techniques are characterized by acquiring data during periods when the patient is not breathing. As there are limits to the amount of time that a person can comfortably hold their breath, multiple acquisitions are typically required during breath-hold and are then summed to generate a final image from a sufficient number of counts. Typically, the patient is instructed or coached to hold their breath at a specific respiratory phase. Deep-inspiration breath-holds during PET acquisitions have been investigated extensively¹⁰⁰, particularly in the context of oncologic studies of the thorax where respiratory motion can significantly reduce the apparent uptake of small lesions in the lungs or liver.¹²³ Breath-hold techniques have also been investigated in the context of myocardial perfusion imaging¹²⁴ but the clinical use has been marred by the potential for extended imaging time, reduced throughput, patient discomfort, and, possibly, increased radiation dose¹²⁵. The specific breath-hold protocols vary in terms of the number of acquisitions and duration of individual breath-holds, and breath-holds ranging from 20 seconds to as long as comfortably tolerated by patients have been reported.^{123,126,127} Mitsumoto and colleagues¹²⁸ sought to investigate various protocols to determine the best with respect to enhancing thoracic lesions uptake and recommended that at least three, 20 second, breath-hold acquisitions be used. Kini and colleagues¹²⁹ have also found that the methods used to coach patient-breathing also have an impact on the overall performance. Coaching methods included a combination of audible prompts and visual feedback of the patient's real-time respiratory displacement.

Immobilization devices have also been proposed to control or suppress respiratory and/or body motion during PET acquisitions.⁸⁸ In the context of cardiac perfusion studies, Ichikawa and colleagues¹³⁰ investigated the use of an abdominal belt worn by patients to suppress the extent of respiratory motion. They found that the belt system, which the study participants reported as being well tolerated, significantly reduced the motion of the heart due to respiration compared to free-breathing: 8 mm of motion compared to 12 mm, respectively. They also showed that the belt aided in reducing the frequency of artifactual reductions in tracer uptake associated with respiratory motion during free-breathing. A pulsatile flow ventilation (PFV) system, not unlike a sleep apnea machine, was investigated by Prior and colleagues¹³¹ in a cohort of four patients to immobilize patient respiration while still providing constant oxygen supply and carbon dioxide extraction. While breath-holds may be maintained for periods up to 30 seconds by most patients, the PFV system was able to produce an apnea-like state among these patients for periods greater than 8.5 minutes. The authors indicated that nearly 45 minutes was required for patient preparation and device setup.

2.3.2 Respiratory and Cardiac Gating

For PET studies where the imaging targets are located in the thorax, cyclical respiratory and cardiac motion are present that can lead to motion-induced artifacts. Aside from the breath-hold and respiratory suppression techniques just described, motion tracking systems can be employed to monitor patient respiration to provide a form of motion compensation known as gating. Gating is a process by which acquisitions are limited to particular phases (or amplitudes) of a cyclical physiological process. In regard

to respiration, a gating system can be used to collect or group raw data from numerous respiratory cycles at a specific phase, e.g. end-expiration or end-inspiration, such that the image reconstructed from the gated data is effectively motion-free. This process comes at the cost of increased image noise, or prolonged acquisition times, as all the data that do not correspond to the selected phase are discarded. Multiple gates can be generated simultaneously resulting in a series of images corresponding to each gate. When displayed in a loop, or cine image, the cyclical motion can be visualized. For cardiac perfusion studies, gating based on the cardiac cycle is routinely performed to assess for left-ventricular function and volumes.⁵² Cardiac gating is facilitated through synchronized acquisition of PET data along electrocardiographic (ECG) signals from the patient. Cardiac triggers are generated and stored in the list-mode data and subsequently used to gate the raw data into a number of frames for each recorded R-R interval. Figure 2.1 provides a graphical representation of these two gating methods.

Respiratory gating was reported by Livieratos and colleagues⁷⁹ for cardiac PET studies using an inductive respiration monitor which allowed them to retrospectively gate the raw data and reconstruct a respiratory-gated image series. Analysis of the gated images revealed cardiac motion due to respiration with magnitudes that were similar to the wall thickness of the left ventricle, e.g. mean motion of 8.5 mm along the inferior-superior direction. They demonstrated that respiratory gating could be employed successfully to mitigate motion-induced artifacts. In a study by Wells and colleagues¹⁰¹, respiratory gating was used to assess the frequency and extent of segmental errors in relative myocardial perfusion imaging in PET/CT due to the mis-alignment of the attenuation correction maps associated with respiratory motion.

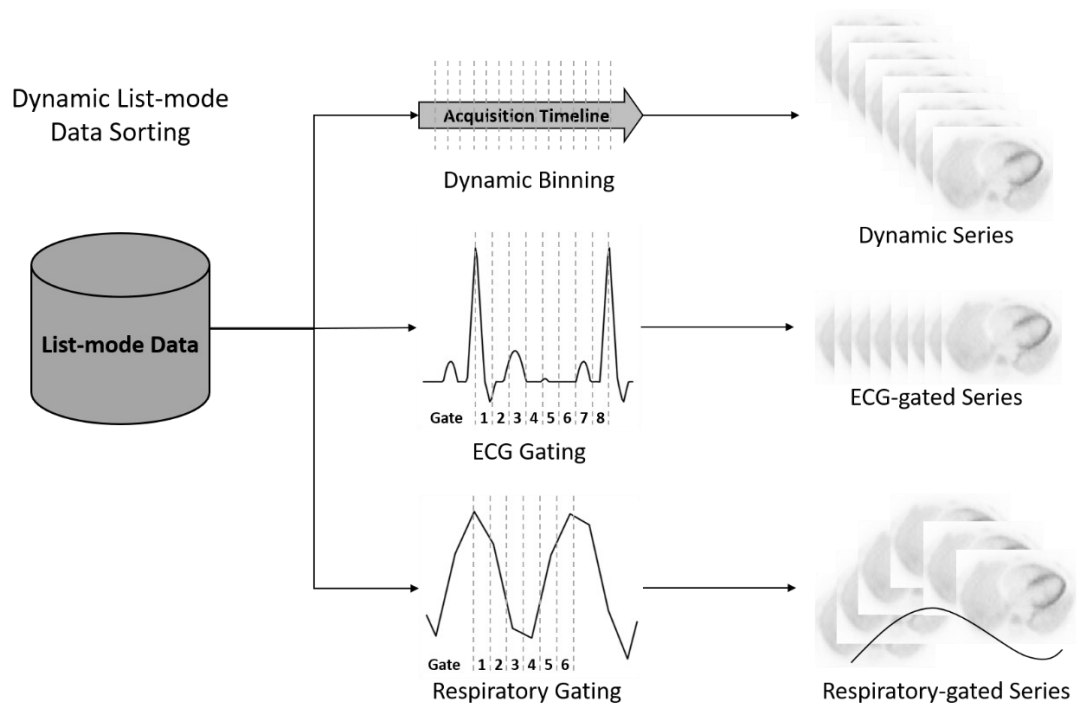


Figure 2.1 Schematic representation of the gating process. Triggers can be derived from physiologic monitoring devices, e.g. ECG or respiratory monitoring systems, as well as based on pre-defined dynamic time frames. In the dynamic acquisition the list-mode data from each reconstructed frame come from contiguous blocks. In the ECG or respiratory gated acquisitions, the data corresponding to each frame are sampled throughout the original data set in a repeating fashion corresponding to the physiologic state of each frame. The ECG signal shown here was produced using an open-source function by Kathrik Raviprakash (2020)^{vii}.

The Varian RPM system was used to monitor respiratory motion. Within a cohort 190 patients, 310 scans acquired at rest or stress were initially evaluated. From these, nine were exhibited significant motion and significant segmental perfusion differences between the end-inspiration and end-expiration gates. The reconstructions for these 9

^{vii} Kathrik Raviprakash (2020) ECG simulation using MATLAB, <http://www.mathworks.com/matlabcentral/fileexchange/10858-ecg-simulation-using-matlab>, accessed January 14, 2020.

scans were repeated with respiratory-phase matched attenuation correction. The segmental perfusion errors were corrected in 8 of the 9 cases.

While cardiac gating is not generally performed for the purpose of motion compensation, research on that topic is not uncommon, an example of which was reported by Martinez-Möller and colleagues¹³² in a study where both cardiac and respiratory gating were applied to generate images corresponding to end-diastole at various respiratory phases. In their study they reported information about non-rigid cardiac deformations that occurred due to respiratory motion alone, i.e. they showed that greater motion was observed for the inferior LV wall compared to the anterior wall. In another study by Germino and Carson⁷⁵, cardiac gating was used to perform kinetic modelling of myocardial blood flow in simulated and human (N = 1) ⁸²Rb studies such that both blood flow and cardiac function could be assessed simultaneously. Additionally, respiratory motion compensation was also applied based on respiratory motion tracking using the Anzai pressure belt system described previously (see Table 2.1).

2.3.3 Motion Correction

In a similar fashion to the data-driven motion tracking methods described previously, motion correction has been employed before, during, and after the image reconstruction process on different formats of available data. In this section an overview of the most common classes of motion correction strategies are introduced.

One of the most common approaches to motion correction corresponds to the extension of the multiple-acquisition frame (MAF) motion estimation approach described in Section 2.2.2 where a final motion-corrected image is produced after averaging the set of

registered frames. An early example of this method was reported by Klein and colleagues¹³³ where a non-rigid image registration technique was employed to transform a set of gated images to the reference gate and then sum the images. In their study they tested their approach on a cardiac-gated PET study performed on a dog but only attempted registration (and summation) of images corresponding to end-diastole and end-systole. They reported qualitative improvements observed in the motion-corrected images compared to summation without motion correction. A more recent study by Slomka and colleagues¹³⁴ reported the use of the MAF motion correction approach applied to dual-gated cardiac perfusion PET studies. In their approach both respiratory and cardiac motion triggers are inserted into the list-mode data and using these they separately reconstructed cardiac or respiratory-gated images. From each gated series, cardiac and respiratory motion are estimated independently using image registration techniques. The two motion models were then combined to produce a single motion-corrected image. They showed significant improvements in myocardial contrast and significant reductions in image blur as measured by LV wall thicknesses.

Prior to image reconstruction the available data correspond to the list-mode or raw projection (sinogram) data. Several groups have developed event-by-event motion correction methods wherein individual LORs in the list-mode data are transformed to account for the motion exhibited by a patient. One of the earlier examples of this approach was studied by Bloomfield and colleagues⁹⁵ in the context of neurological PET studies. In their work, an optical motion tracking system was used to monitor 3D real-time head motion, which was retrospectively used to transform individual LORs to correspond to a reference position. Using data from a physical phantom and a single

patient acquisition promising results were shown. Most notably, while performing the kinetic modelling on the patient data set, motion correction was shown to improve the obvious motion-induced irregularities of the time-activity curves. Livieratos and colleagues¹³⁵ also applied rigid transformation to individual LORs using motion data gleaned from image-registration of respiratory-gated images in cardiac PET studies. They demonstrated improvements in the contrast recovery coefficient in phantom studies where respiratory-like motion was simulated. In both of these approaches, care must be taken after transforming LORs to account for the spatially variant changes in the scanner detection efficiency as well as attenuation correction as transforming a given LOR results in different trajectories through the patient's body as well as crystal-pair end points.

Another approach is to incorporate motion data into the image reconstruction process by extending the scanner system matrix to be four dimensional where the fourth dimension is a temporal component that includes patient motion information. The forward and back-projectors could be modified, for example, to have different photon trajectories for specific frames or instances throughout the acquisition. Qiao and colleagues¹³⁶ demonstrated such an approach using numerical and physical phantom simulation studies of respiratory-gated cardiac PET/CT studies. In their work they assumed that 4D respiratory-gated CT images were available, from which a respiratory motion-model could be established and applied to the gated PET data for respiratory motion correction. They demonstrated image quality improvements like increased signal-to-noise ratios and reduced bias when performing motion correction by modifying the PET system matrix with measured motion data. Deriving motion information from 4D CT data, however, is generally not desirable due to the increased radiation exposure¹³⁷ to

patients compared a single, static, CT acquisition. Additionally, 4D CT acquisitions may also lead to increased complexity of imaging protocols.¹⁰¹ It follows that these data are often unavailable to generate patient-motion models.

Others have developed methods that extended the statistical likelihood model to include transformation parameters, rigid or otherwise, such that joint estimation of the motion parameters and the image occur during the reconstruction process. Jacobson and Fessler¹³⁸ proposed such an approach which was tested on numerical phantom studies. They found that the joint estimation approach led to more accurate motion estimation but did not improve lesion uptake when compared to post-reconstruction image registration methods. More recently, Kalantari and colleagues¹³⁹ developed a similar approach but they reportedly used non-rigid image registrations to initialize motion models prior to the joint image and motion estimation. They reported significant reduction in blurring of lesions of various size and uptake using numerical phantom studies which included respiratory motion.

One common drawback among these motion correction approaches is that they make use of raw data that have already been gated and it follows that intra-gate motion may exist for which they are not able to account. In some of the methods where motion estimation was achieved from a system that is independent of the images, e.g. the optical tracking system used by Bloomfield⁹⁵ in the brain PET studies, this problem may be obviated. Moreover, Klein et al¹³³ reported that caution should be exercised when estimating motion information from PET images as they are generally noisy and of low spatial resolution and it follows that errors may propagate into the motion estimates.

2.4 Positron Emission Tracking (PeTrack)

2.4.1 The Tracking Algorithm

Before describing PeTrack it is helpful to review quickly the β^+ decay process which effectively terminates following the detection of the resulting annihilation photons. Recall from Section 1.1.2 that following a β^+ decay, the positron will travel some distance in its surrounding medium before annihilating with an electron. The resulting annihilation photons will then be emitted in an approximately collinear fashion (180°) and be observed by a detection system which has some finite spatial resolution. Each of these cascading processes influences one's ability to determine the position from which the decay originated. It follows that a model of the probability density function (PDF) that describes this spatial distribution can be produced to help make inferences about the position of the radioactive source based on detection of the annihilation photons. This is the approach that was developed for PeTrack to track the motion of physically small positron-emitting markers. The following description of the PeTrack algorithm is largely based on work reported elsewhere. The basic tracking algorithm was originally described by Xu and colleagues⁹⁰ and then extended for use during PET by Chamberland and Xu.⁹¹ The PeTrack formalism is described in the following and is based upon the description of these two sources.

An essential assumption of the PeTrack method was that the PDF can be modelled by a Gaussian function with a mean value that corresponds the true marker position and a standard deviation which results from the combined effects that limit the spatial resolution of the detection system. Consider that in some span of time a set of N lines-of-

response $\{\mathbf{L}_n\}$ were detected, each of which at a perpendicular displacement $\vec{d}(\mathbf{L}_n, \vec{m})$ from the estimated position of the marker \vec{m} , defined as a vector pointing from point m onto \mathbf{L}_n and perpendicular to \mathbf{L}_n . It follows that the Gaussian PDF (Eq. 0.1) can be described as

$$p_n(\vec{d}(\mathbf{L}_n, \vec{m}), \sigma) = \left(\frac{1}{\sqrt{2\pi}\sigma}\right)^3 \exp\left(-\frac{|\vec{d}(\mathbf{L}_n, \vec{m})|^2}{2\sigma^2}\right), \quad \text{Eq. 0.1}$$

For p_n , the mean is chosen as zero and its standard deviation is denoted by σ .

The task of the maximum-likelihood expectation maximization (MLEM) approach is to estimate the parameters \vec{m} and σ that maximize the joint likelihood associated with all the LORs in the set $\{\mathbf{L}_n\}$. The joint likelihood \mathcal{L} is given in Eq. 0.2,

$$\mathcal{L}(\vec{m}, \sigma) = \prod_{n=1}^N p_n. \quad \text{Eq. 0.2}$$

which is maximized by determining the parameter values that satisfy the following conditions shown in Eq. 0.3.

$$\frac{\partial \mathcal{L}}{\partial \vec{m}} = 0; \text{ and } \frac{\partial \mathcal{L}}{\partial \sigma} = 0. \quad \text{Eq. 0.3}$$

As was shown in Section 1.2.4 on image reconstruction techniques, the MLEM equations are solved more easily by maximizing the log-likelihood instead of the likelihood itself. The two-step MLEM approach commences with the *expectation step* in which we estimate the PDF based on the current parameter estimates $p_n^{(i)}$ and is followed by the *maximization step* in which the current parameter estimates are updated. The updates for the current marker location $\vec{m}^{(i)}$ and the standard deviation of the PDF $\sigma^{(i)}$ are given by Eq. 0.4 and Eq. 0.5, respectively.

$$\vec{m}^{(i+1)} = \vec{m}^{(i)} + \vec{V}^{(i)} \quad \text{Eq. 0.4}$$

$$\sigma^{(i+1)} = \sqrt{\frac{\sum_{n=1}^N p_n^{(i)} |\vec{d}(\mathbf{L}_n, \vec{m})|^2}{\sum_{n=1}^N p_n^{(i)}}} \quad \text{Eq. 0.5}$$

The position update contains the step vector $\vec{V}^{(i)}$ which is computed as shown in Eq. 0.6.

$$\vec{V}^{(i)} = \frac{\sum_{n=1}^N p_n^{(i)} \vec{d}(\mathbf{L}_n, \vec{m})}{\sum_{n=1}^N p_n^{(i)}} \quad \text{Eq. 0.6}$$

The initial estimate of the standard deviation is set to 5 mm. The initial estimate of the marker position is more involved in the application of PeTrack to PET imaging and will be described more carefully in Chapter 3. Convergence of the MLEM method was defined as position updates that are smaller in magnitude than 0.05 mm.

The original PeTrack algorithm was extended for use during PET imaging by Chamberland, deKemp, and Xu and is referred to as Adaptive Region of Interest (ADROI) PeTrack.⁹² Note that the ADROI PeTrack algorithm will be referred to hereafter as PeTrack. This modification included additional processing steps to overcome challenges not incurred during radiation therapy: the separation of the positron-emission signal of the fiducial markers from that of the radiotracer administered to the patient. To address this issue, knowledge of the physical characteristics of the fiducial markers and spatial distribution of the radiotracer have been exploited. The first step in the background rejection is to generate a spherical region-of-interest with a radius of 30 mm about the initial marker position. LORs with a perpendicular distance, $|\vec{d}(\mathbf{L}_n, \vec{m})|$, greater than 30 mm are excluded from the active set of LORs and thus are not included during the iterative PeTrack method. The second step makes use of the time-of-flight delay of

each coincident event, assuming it is available, to impose further restrictions. As was mentioned in Section 1.2.2.3, the TOF resolution of a PET camera is a measure of the degree of precision with which the most likely annihilation (MLA) position can be estimated along a given LOR. This knowledge was used such that LORs with MLA position greater than 80 mm from the current marker position are excluded from further processing. A third step is employed that excludes LORs with a perpendicular distance that is less than a specific cut-off from the central axis of the PET scanner. This step is useful as the marker is placed on the skin of a patient and physically cannot be closer to the central scanner axis than the patient's body size permits. In regard to the work described in this thesis, the cut-off distance was estimated on a per-patient basis as a fraction of the initial marker's vertical (anterior-posterior) distance from the central axis, i.e. $0.8 \cdot |\vec{m}_y^{(0)}|$. Lastly, the adaptive region-of-interest (ADROI) method was developed which models the spatial distribution of the radiotracer near the marker to further constrain the set of LORs that are used for tracking with PeTrack. It was previously demonstrated that if the 3D probability density function (PDF) of $\vec{d}(\mathbf{L}_n, \vec{m})$ could be modelled as an isotropic Gaussian function with standard deviation σ , then the distance follows a 1D PDF shown in Eq. 0.7.⁹²

$$PDF(|\vec{d}(\mathbf{L}_n, \vec{m})|) = 4\pi |\vec{d}(\mathbf{L}_n, \vec{m})|^2 \left(\frac{1}{\sqrt{2\pi}\sigma}\right)^3 \exp\left(-\frac{|\vec{d}(\mathbf{L}_n, \vec{m})|^2}{2\sigma^2}\right) \quad \text{Eq. 0.7}$$

Additionally, the local tracer background can be modelled as a linear function of $|\vec{d}(\mathbf{L}_n, \vec{m})|$ which increases with increasing distance from the ROI centroid.⁹² The background can be fit using simple linear regression and then subtracted from the

histogram. The ROI size is adapted by truncating the histogram up to the first histogram bin in which the number of LORs is less than or equal to zero after background subtraction. A schematic diagram of this fitting procedure is provided in Figure 2.2. In the event the radius of the ROI become so small that fewer than 10 LORs are included, it is expanded by a factor of 3 and the adaptive ROI fitting method is repeated. This entire process is repeated for subsequent tracking instances, i.e. those of the following time frames. Each subsequent tracking instances uses the final position of the previous run as the new initial marker position estimate.

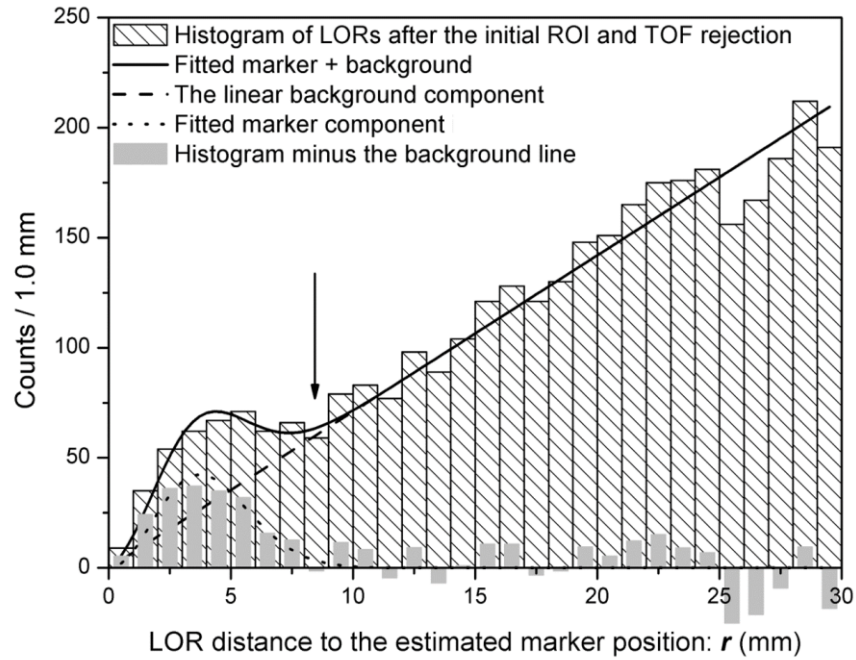


Figure 2.2 The adaptive region-of-interest procedure is exemplified in this figure which shows the histogram of LORs with a perpendicular distance ‘ r ’ (denoted in this work as $|\vec{d}(\mathbf{L}_n, \vec{m})|$) from the estimated marker position from a phantom acquisition. The columns with hashed lines indicate the events following the initial ROI and TOF based rejection techniques. The solid black line represents a fit of the combined marker PDF and linear background model. The marker PDF and linear background fits are shown as the dotted and dashed lines, respectively. The solid gray bars indicate the events that remain following subtraction of the linear background fit. In this example the ADROI size was set as 8 mm. This figure was used with permission from the work of Chamberland, deKemp and Xu.⁹²

Currently, no parallelization acceleration techniques are employed during tracking with PeTrack. It takes approximately 15 minutes to generate a 3D marker motion trace for a typical ^{82}Rb cardiac perfusion study ($\sim 10^8$ LORs), on a PC workstation with an Intel Core i7-6700 processor (3.40 GHz). Execution times tend to increase when convergence is slow, e.g. if the marker signal is too weak compared to the background radiotracer activity. In the event that a particular tracking instance fails to converge, the marker position is not updated, but rather remains equal to that of the previous instance.

2.4.2 Motivation for the Use of PeTrack in PET

Data-driven methods of motion tracking are appealing as they have the capacity to simplify imaging protocols when compared to hardware-driven approaches. An important consideration for their use, however, is that motion information may be confounded by changes in the tracer distribution in the body which leads to uncertainty in their accuracy. In regards to respiratory motion tracking, only a few data-driven tracking approaches have been implemented in cardiac PET applications.^{111,116,140} These studies showed promising results for motion tracking in ^{13}N -ammonia and ^{18}F -fluorodeoxyglucose (FDG) PET when compared to external hardware-based methods. There are two aspects of cardiac PET acquisition, like cardiac viability studies, which use ^{18}F -FDG that make them well suited for data-driven motion tracking. First, the acquisitions are performed after a post-injection delay of sufficient time such that the tracer distribution has reached equilibrium in the body. Second, the physical half-life ^{18}F is nearly 2 hours which mitigates the loss of signal used to derive the motion information over the durations of the acquisition. The use of ^{13}N -ammonia for PET perfusion imaging is similar to ^{18}F -

FDG in that it too exhibits a relatively long physical half-life (20 minutes) and will not significantly decay during the acquisition.

The authors of these studies^{111,116,140} have consistently reported that the quality of the derived respiratory signal is likely to be reduced in imaging studies that exhibit low contrast/count statistics as well as when tracer uptake is changing rapidly. Schleyer and colleagues¹⁴⁰ developed a successful method to address the issue of rapid tracer kinetics in the early time frames on ^{13}N -ammonia perfusions studies, but little else has been published that addresses these challenging applications.

Cardiac PET MPI studies predominantly use ^{82}Rb as the perfusion tracer⁶⁰ and with a half-life of 76 s these studies exhibit even more rapid changes in the tracer distributions as well as relatively low count statistics in the late frames.⁵⁹ In their study on data-driven respiratory tracking, Büther et al.¹²² reported that a data-driven method that tracks external radioactive markers with a fixed activity may be a viable application for tracking patient motion.

This thesis is primarily focused on motion compensation strategies in the domain of ^{82}Rb cardiac PET studies. The PeTrack algorithm has features that lends itself to this problem. PeTrack does not require external devices to be used in addition to the PET camera and thus can simplify patient setup prior to imaging as it only relies on the use of low activity fiducial markers. Additionally, as was suggested by Büther et al.,¹²² data-driven methods that infer patient motion based on long-lived sources that also do not redistribute during the acquisition may be advantageous in challenging applications like ^{82}Rb MPI. Another useful aspect of PeTrack is that as the list-mode data are used to generate motion data, there is no requirement to produce multiple short frames sinograms

or reconstructed images which reduces the computational burden of this approach compared to some others described previously in this chapter. The application of PeTrack to respiratory-gated cardiac PET studies is the topic of Chapter 3.

Several studies have been performed to assess the impact of patient motion^{82,83,141–145} and many others have been performed with the aim of establishing methods to compensate or correct for it.^{81,146–149} A recent review on the impact of patient motion in cardiac PET/CT studies emphasizes the importance of correcting body motion, particularly if kinetic modelling is to be employed for the estimation of absolute myocardial blood flow.⁷⁷ The studies mentioned above that proposed body motion correction (MC) methods commonly employed the MAF approach using a set of pre-defined dynamic frames. While these methods have typically demonstrated improvement in image quality, they are limited to the correction of inter-frame motion only. An editorial by Lu and Liu⁸⁵ published in 2018 make the claim that this family of approaches should be extended to higher temporal resolution methods that do not rely on pre-defined image sequences. Some recently developed data-driven approaches provide motion information directly from the raw PET data^{119,150} to help address intra-frame motion blurring. These approaches have only been applied to PET studies that make use of long-lived, ¹⁸F-based tracers. Their utility in myocardial perfusion imaging (which uses ⁸²Rb or ¹³N-ammonia) has not yet been demonstrated.

These arguments support the potential utility of PeTrack beyond tracking respiratory motion. The information provided by tracking external radioactive markers can also be applied to the problem of whole-body patient motion either for single frame acquisition, as in MPI, or dynamic acquisition used for kinetic modelling. Indeed, motion information

can be assessed with PeTrack at a temporal resolution that is finer than the smallest frame durations used during dynamic acquisitions. The applications of PeTrack to whole-body motion detection and correction are described in Chapter 4 and Chapter 5, for single frame MPI and for absolute myocardial blood flow quantification, respectively.

Chapter 3 Respiratory Gating in Cardiac Perfusion PET

The ability of PeTrack to track respiratory motion and provide motion compensation through respiratory gating was evaluated in the context of cardiac perfusion imaging. The content of this chapter is a modified version of previously published work¹⁵¹ © Wiley 2020, Spencer Manwell, Ran Klein, Tong Xu, Robert deKemp, “*Clinical comparison of the Positron Emission Tracking (PeTrack) algorithm with the Real-Time Position Management System for respiratory gating in cardiac positron emission tomography*”, *Medical Physics* 2020; 47(4): 1713-1726, reproduced with permission from the authors, all rights reserved. The Version of Record can be found online at <https://doi.org/10.1002/mp.14052>.

3.1 Motivation

While respiratory gating is not widely performed in regular clinical practice in cardiac PET¹⁵², case studies like that from Arasaratnam and colleagues¹⁵³ help to indicate its utility when severe heart motion during respiration is suspected. Moreover, a recent editorial published in the *Journal of Nuclear Cardiology* makes the case that cardiac PET/CT studies must navigate toward the inclusion of some form of respiratory motion compensation in the future and that the most elegant mechanism for this step is likely associated with data-driven approaches provided that their ability to add incremental clinical diagnostic value is proven.¹⁵⁴

In this study, the use of PeTrack was investigated as a hybrid data-driven alternative to a commercial hardware-based tracking device for respiratory motion tracking and gating.

PeTrack was used to generate one-dimensional respiratory signals from its three-dimensional motion signal; an approach which has been suggested to be more robust in the presence of breathing irregularities compared to one-dimensional signals which most respiratory monitoring systems provide.⁹⁴ The aims of this study were to use PeTrack for respiratory tracking in ^{82}Rb cardiac PET MPI and benchmark its performance of this against that of the Real-Time Position Management (RPM) system (Varian Medical Systems). The RPM system has been chosen as the standard for comparison in respiratory gating performance as it is currently one of the two most widely used gating systems in diagnostic PET/CT⁸⁸. In this retrospective study the correlation of the respiratory motion signals of the two systems was compared along with various quantitative metrics of image quality extracted from respiratory-gated reconstructed images in a patient cohort that underwent MPI studies using ^{82}Rb . These quality metrics include the medians and widths of distributions of patient respiratory-rate histograms, left-ventricular (LV) wall thicknesses, and cardiac motion due to respiration.

3.2 Methods

3.2.1 Respiratory-Gated Acquisition

All acquisitions were performed as part of standard clinical care by technologists at the University of Ottawa Heart Institute (UOHI) in Ottawa, Canada on a GE Discovery 690 PET/CT scanner (Waukesha, WI) with list-mode and time-of-flight capabilities. The scanner is shown in a photograph include here with annotations indicating its coordinate system in Figure 3.1. The performance specifications for this scanner were shown previously in Table 1.2. Each patient underwent a ^{82}Rb myocardial perfusion imaging

study at rest and during pharmacologic stress.⁶⁷ Acquisitions were 8 minutes in length, starting at the time of tracer injection. Tracer administrations of approximately 10 MBq/kg were delivered intravenously to each patient for both rest and stress scans.¹⁵⁵

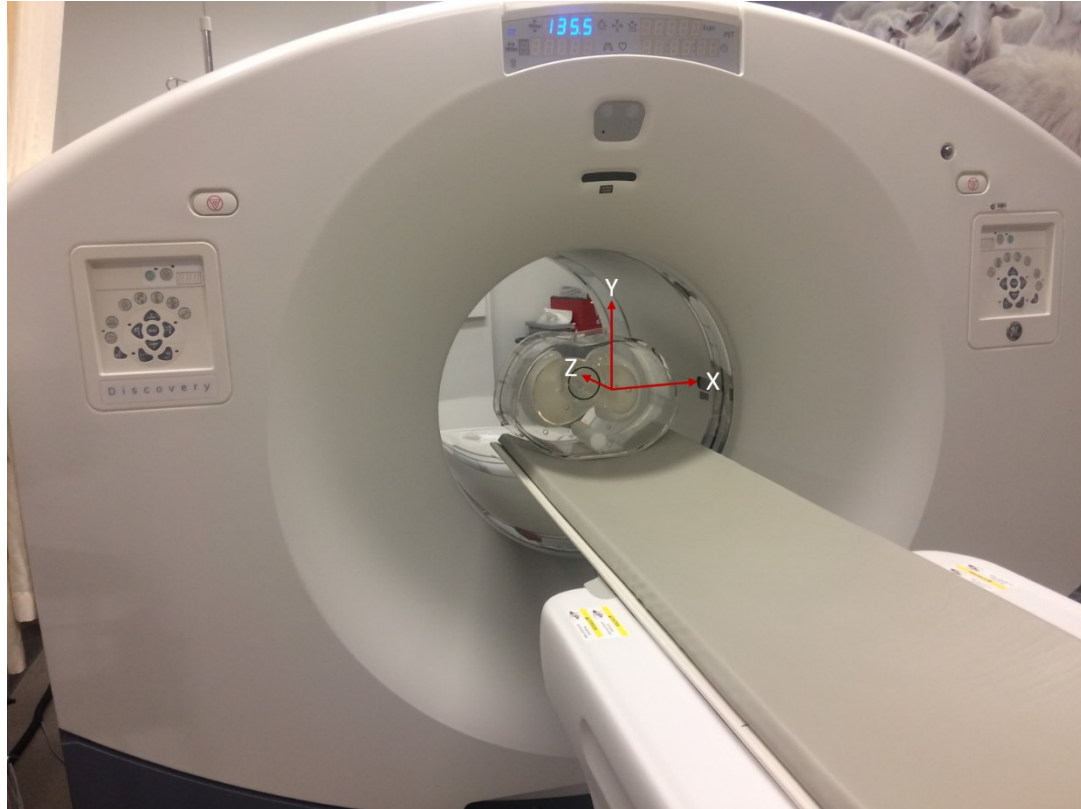


Figure 3.1 Photograph of the GE Discovery 690 PET/CT scanner used in this work. An anthropomorphic torso phantom is set on the bed and its situated at the level of the CT system the lies near the front face of the scanner. The geometric axes have been annotated using red arrows. The x -axis corresponds to the lateral direction in the photo. The y -axis corresponds to the vertical direction. The z -axis, shown here going to the page, corresponds to the axial direction of the scanner coordinate system.

The clinical protocol at UOHI included respiratory monitoring with the RPM system as well as with a single sodium-22 fiducial marker (30 kBq) placed near the patient's diaphragm on the right-anterior chest wall. The marker was encased in water-based modelling clay to prevent interference with the scatter correction algorithm which

assumes that unattenuated activity outside the contour of the patient's body must be scatter. A scout CT was used to position the patient and check that the marker was within the field-of-view prior to the PET acquisition. An additional CT acquisition was performed prior to the rest PET scan for the purpose of attenuation correction. Patients were permitted to breathe freely during the CT acquisitions and technologists attempted to acquire the CT image while the patients were in the normal end-expiration phase of their breathing via monitoring the RPM motion signal. Respiratory triggers generated by the RPM system, which occur when the respiratory signal begins to rise following end-expiration, were inserted into the list-mode data during image acquisition which were used for subsequent analyses and respiratory-gated reconstructions. The first 90 seconds of each acquisition were excluded from reconstructions to allow for clearance of the tracer from the left-ventricular blood pool.⁶⁷

3.2.2 Patient Population

This retrospective study was approved by the Ottawa Health Science Network Research Ethics Board (Protocol 20170375-01H). This study initially included the rest and stress acquisitions collected from 35 patients referred to UOHI for myocardial perfusion imaging. Acquisitions were randomly selected from the clinical database between April and October of 2017.

Acquisitions were not considered for the initial cohort if they met the following criteria: the list-mode data were unavailable; and the RPM respiratory trace was not available for post-processing. Acquisitions were excluded from the initial cohort for the following reasons: the fiducial marker was not placed within the field of view (n = 11);

RPM generated no or too few respiratory triggers to permit synchronization of RPM motion trace with the list-mode data ($n = 2$); and motion tracking with PeTrack was unsuccessful ($n = 6$). Lastly, one case was excluded after processing as the intensity of the LV wall did not have sufficient contrast compared to the blood pool to permit the measurement of the thickness. Of the 70 acquisitions initially screened for this study, 50 acquisitions (24 rest and 26 stress) remained. The mean \pm SD body-mass index of the cohort was 35 ± 10 kg/m².

3.2.3 Respiratory-Signal Generation

Motion traces of the fiducial marker were generated by applying the ADROI PeTrack algorithm to each of the list-mode data sets. As is the case with other data-driven gating schemes, the respiratory signal for the marker is inherently synchronized with the emission data. Aside from the fiducial marker, this system requires no additional hardware. PeTrack currently requires an initial marker position estimate so that the background rejection techniques mentioned above can be applied accurately. The initial position was acquired via automatic segmentation of the marker in the last time-frame of the clinical dynamic PET images and calculated as the centroid. Using a single core 3.40 GHz processor the tracking algorithm required 15 minutes, on average, to compute the motion trace from a ~ 2 GB list-mode file with a position sampling frequency of 2 Hz, throughout the 8-minute acquisitions.

Following the production of the three-dimensional motion trace, a respiratory signal was derived from the weighted combination of motions in the anterior-posterior and inferior-superior directions. This combination preserves information from both 1D

signals but emphasizes that with the larger amplitude. The resulting motion traces were smoothed by applying a low pass filter (rectangular function from 0 to 0.5 Hz) to the frequency spectra of the combined trace, to reject observed respiratory periods of less than 2 seconds. The peak detection algorithm developed by Lu and colleagues¹⁵⁶ was then implemented to identify the time points, or triggers, corresponding to the end of expiration. These were then used as alternative respiratory triggers for the gated reconstructions. The peak detection approach rejected peaks with a height less than 20% of the mean signal amplitude. Additionally, triggers that were found to be temporally too close to the previous trigger were also rejected; the threshold was 10% of the patient's mean breathing period. These threshold parameters were determined heuristically using a small set of scans from a preliminary study.¹⁵⁷

3.2.4 Respiratory-Gating and Image Reconstruction

For this study, images were reconstructed using phase-based respiratory gating as per standard clinical practice using RPM generated respiratory triggers. Displacement-based gating was not employed in the study although technically possible using PeTrack. The benefits of respiratory gating can be marred by the increased image noise that stems from creating multiple low-count images. Previous work suggests that six respiratory gates is the optimal number for phase-based gating schemes in PET¹⁵⁸ to minimize blurring due to diaphragm motion while at the same time preserving the signal-to-noise ratios as much as possible. Hence, six gates were used for all respiratory-gated image reconstructions. Note that cardiac gating was not implemented in these reconstructions, hence only respiratory motion was addressed.

All respiratory gated images were reconstructed using the vendor's standard three-dimensional ordered subset expectation maximization algorithm (3 iterations with 24 subsets) with corrections for attenuation as well as random and scattered coincidence events. Reconstructed image volumes were $128 \times 128 \times 47$ voxels in size and the reconstructed field-of-view was $50 \text{ cm} \times 50 \text{ cm}$ in the transaxial plane and 15.7 cm in the axial direction. As a result, the transaxial and axial sizes of each voxel were 3.96 mm and 3.27 mm , respectively. No post-reconstruction smoothing was applied. Reconstructed images were reoriented to standard left-ventricle short axis slices using tools from the FlowQuant¹⁵⁹ software package developed at UOHI. A small amount of smoothing is anticipated from the tri-linear interpolation that is needed to perform the reorientation, but this should be negligible compared to the spatial resolution of the system.

3.2.5 Measurements for Comparison

An ideal gating system is one that is reliable, accurate, reproducible, has sufficient temporal resolution to respond to signal variations and does not introduce additional image artifacts.⁹⁴ The implications of these properties are that the respiratory pattern is accurately captured and that the respiratory gated images display very little blur from respiratory motion. It follows that in the case of cardiac PET, the LV walls will appear thinner and with higher peak intensity compared to those seen in the presence of motion blurring. When measuring the displacement of the LV between the end-expiration and end-inspiration respiratory phases, one would also expect that accurate gating would lead

to larger displacement measurements compared to that observed if gating performance was poor.¹⁵⁸

3.2.6 Comparing Respiratory Signals and Triggers

To compare the performance of these two gating systems the respiratory signals and the corresponding set of respiratory triggers were evaluated. Assuming both systems were measuring the respiratory motion of the patient accurately one would expect that the respiratory signals of the two systems would be correlated. It follows that the correlation coefficient of the respiratory signals from the two systems was measured for each scan. The respiratory signals of the patients were sampled at 2 Hz and 30 Hz using PeTrack and RPM, respectively. To measure the correlation between these two signals, the RPM signal was down-sampled to match the reduced temporal resolution of PeTrack. The original RPM signals, sampled at 30 Hz, were used for trigger generation.

It is important to note that the RPM and PeTrack systems were not designed to produce respiratory triggers at the same respiratory phases. PeTrack has been designed to trigger at end-inspiration while the RPM device triggers following end-expiration when the respiratory signal begins to rise due to inspiration. These two phases correspond to maxima and minima, respectively in the respiratory waveforms. Additionally, the method with which triggers were identified and recorded also differs between these two systems. RPM triggers are recorded in real-time and inserted into the list-mode data. PeTrack, however, is a completely retrospective process. In this study there was an interest in comparing these two systems in the context of their intended clinical implementations, but it follows that some of these differences may confound our measurements, e.g.

differences in the trigger generation method. This study also includes, therefore, a third respiratory gating approach which corresponds to retrospective processing of the original RPM respiratory signals with the same trigger detection method implemented for PeTrack. The first comparison between PeTrack and the original RPM data therefore constitutes a practical comparison of the two gating systems. The second comparison between PeTrack and the retrospectively processed RPM data corresponds to a more equal, or ‘apples to apples’, comparison. The two RPM approaches are distinguished throughout this report as “RPM” and “RPMretro”, for the original prospective and retrospective implementations, respectively.

Based on the characteristics of an ideal gating system it was assumed that the distribution of respiratory rates, defined as the inverse of the time intervals between adjacent respiratory triggers, should fall within a physiologically relevant range and that the distribution of an optimal system would be narrower and exhibit fewer outliers than a non-optimal system. The distributions of respiratory rates were quantified using non-parametric descriptive statistics, median and interquartile range (IQR), to characterize the behavior of the two systems and the frequency of non-physiological respiratory cycles was examined.

A quality control approach was employed to deduce limits on the observed respiratory rates such that individual respiratory cycles could be classified as acceptable or non-physiologic, i.e. an outlier. In this study outlier cycles were not rejected during image reconstructions, but the relative rates of cycle outliers were recorded as a quality metric for each gating system. For each acquisition, respiratory rates were normalized to their corresponding median rate and log-transformed to reduce the extent of skewness. Box

plots were generated for outlier estimation such that the cycles with a respiratory rate that fall outside of the box plot whiskers were classified as outliers. In this approach the standard box plot whiskers, which extend 1.5 times the IQR below and above the first and third quartiles, respectively, were used. Outlier limits were computed in two steps. A preliminary set of limits was estimated using data from all scans as well as both gating systems. Based on these limits, cases where respiratory cycle outlier rates were less than 10% were considered to have adequate gating quality. The subset that was considered adequate was then used in the second iteration to determine the limits for respiratory cycle outlier detection based on respiratory signals/triggers of adequate quality.

3.2.7 Comparing Image-Based Measurements

Four image sets were reconstructed for each acquisition in the study, each of which consisted of a non-gated image and three gated images. The list-mode data were gated using the prospectively acquired RPM triggers, the PeTrack-derived triggers, and retrospectively derived RPM triggers. Note that in the case of the non-gated reconstruction, the list-mode data were randomly sampled to include 16.7% (or one-sixth) of the counts such that they were noise-matched with the gated images. Image characteristics like LV wall thickness and cardiac motion were measured using an automated tool developed for this study. The non-gated images were included only to provide baseline LV width measurements.

Respiratory motion of the LV was measured using utilities of the FlowQuant software package. Beginning with a phase-averaged image, an ellipsoidal structure was fit to the contours of the left-ventricle and its size and orientation were determined. This

ellipsoidal model was then fit to the six gated images to determine the three-dimensional location of the LV. The centroid position of the ellipse was recorded for each gate. The gates at which the LV was in the most superior or inferior position were assumed to correspond to the end-expiration or end-inspiration phases, respectively. Cardiac motion was estimated as the magnitude of the displacement of the LV centroid along the superior-inferior (SI) direction of motion measured between the end-expiration and end-inspiration images. Following the reorientation process the image was arranged as stack of short-axis slices of LV, where the central plane of the volume corresponds to the mid vertical-long axis slice. LV wall thicknesses were estimated as the activity-weighted full-width at half-maximum measured from line-intensity profiles along the anterior-inferior direction at the mid-level of the LV for both Anterior and Inferior walls. As cardio-respiratory motion is predominantly in the SI direction^{101,160}, the anterior and inferior regions were expected to be most sensitive to respiratory motion blurring. After identifying the end-expiration gate, an automatic multi-resolution method was employed to segment the anterior and inferior wall regions in a set of five contiguous 1D profiles. A single set of limits was deduced in an automated fashion for the set of five profiles. A detailed description of this automated approach is included in Appendix A.

An example of these profiles and paths along which they are extracted is provided in Figure 3.2. Only images that were found to correspond to the end-expiration phase were used for thickness measurements as these were assumed to be phase-matched with the CT images used for attenuation correction as per the instructions provided to technologists for starting the CT acquisition based on patient free-breathing. Thicknesses were thus measured at the mid anterior and inferior LV regions. The one-dimensional profiles were

segmented to place limits on the extent of each wall region prior to calculation of their thicknesses.

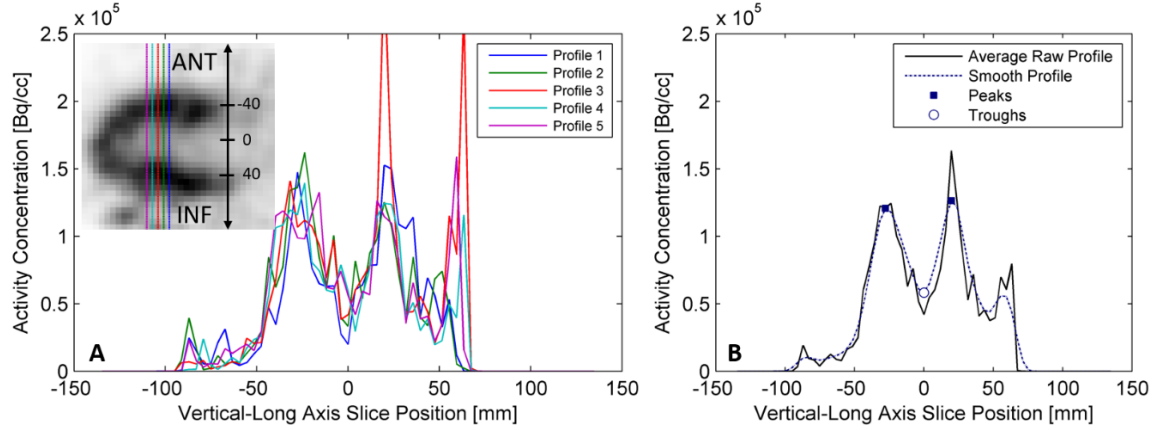


Figure 3.2 Anterior-inferior activity profiles acquired from the reoriented images of one patient. Image A depicts five 1D profiles that are indicated in the inset vertical long-axis slice image. Image B depicts the average of the five raw profiles as well as the smooth profile which was extracted from the same image volume after convolution with a 3D 7.5 mm FWHM Gaussian smoothing kernel. Image B also depicts the peak and trough locations, which were automatically generated to identify the anterior wall, LV blood pool and inferior wall regions. Note that the inset image corresponds to the smoothed volume.

In Figure 3.2 an example set of profiles and the corresponding mean raw and smooth profiles are shown. For a segmented region of the profile with K elements with positions $\mathbf{d} = [d_1, \dots, d_K]$ and weights $\mathbf{a} = [a_1, \dots, a_K]$, the activity weighted full-width at half-maximum, \hat{w}_a , was calculated as follows

$$\hat{w}_a = 2\sqrt{2\ln(2)} \sqrt{\frac{K}{K-1} \frac{\sum_{i=1}^K a_i (d_i - \mu')^2}{\sum_{j=1}^K a_j}} \quad \text{Eq. 0.1}$$

where the activity-weighted mean of the segment, μ' , was calculated as

$$\mu' = \frac{\sum_{i=1}^K a_i d_i}{\sum_{j=1}^K a_j} \quad \text{Eq. 0.2}$$

Thicknesses were measured in this way to avoid assumptions about the shapes of the profiles. Note that the weights α were the activities of the 1D segments after min/max normalization to subtract the background.

3.2.8 Statistical Methods

The paired Students' t -test was used to test the hypotheses that there was no statistically significant difference between any two gating methods for each of the quality metrics mentioned previously. Statistical significance was assumed for all tests at the level of $p < 0.05$. A paired hypothesis test was used as all subjects (PET acquisitions) were evaluated multiple times with the using each of the different gating methods. Moreover, paired hypothesis tests demonstrate greater statistical power than their unpaired analogues.

3.3 Results

The correlation coefficient (ρ) of the amplitudes of the respiratory signals between PeTrack and RPM systems was found to be statistically significant in 45 of the 50 scans. The mean \pm SD correlation coefficient was 0.43 ± 0.28 . Similarly, between PeTrack and RPMretro the mean \pm SD correlation coefficient was 0.47 ± 0.26 and 47 of the 50 scans were significantly correlated. Retrospectively processing the RPM signal included spectral filtering and subtraction of the running average which explains the subtle differences in the correlation coefficients just mentioned. Additionally, the mean \pm SD correlation coefficient between the RPM and RPMretro respiratory motion signals was 0.84 ± 0.10 , all 50 of which were statistically significant.

For the entire cohort (i.e. 50 acquisitions using both RPM and PeTrack) the time intervals between all respiratory triggers ($n = 3802$ and 4186 for prospective RPM and PeTrack, respectively) were compiled and the corresponding normalized, log-transformed, respiratory rates were summarized in the histogram shown in Figure 3.3. Using the box plot approach described previously, normalized respiratory cycle outlier limits of 38.3% and 161.7% were determined from the acquisitions which were deemed to have adequate quality based on the preliminary acceptance limits (35/50 and 33/50 acquisitions using RPM and PeTrack, respectively). Respiratory cycles that fell within and outside the acceptance window are indicated by the shaded and white areas, respectively. Respiratory cycle outlier rates were recorded for each acquisition, for each gating method.

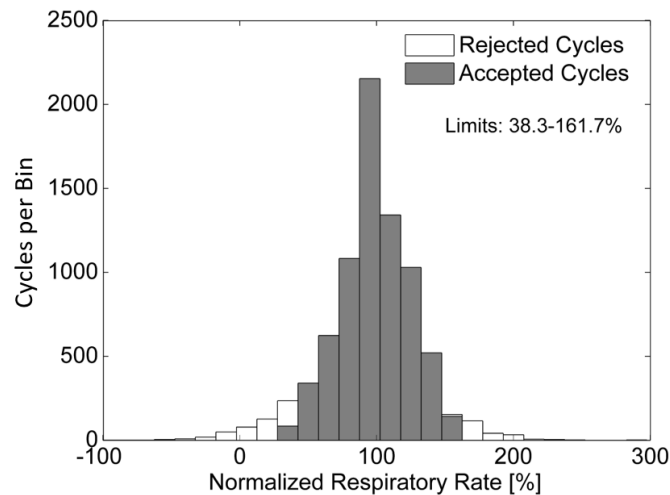


Figure 3.3 Histogram of log-transformed, normalized respiratory rates pooled from RPM and PeTrack gating systems for all 50 acquisitions. The shaded area corresponds to the respiratory cycles that fall within the acceptance criteria determined using the boxplot approach. The limits determined using this method were found to be [38.3, 161.7%] of the patient-specific median respiratory rate after the log-transformation was applied.

To enhance the reader's sense of the analysis that took place, Figure 3.4 depicts an example of the respiratory signal data from each gating system. In Figure 3.4(A), the respiratory signals of the three systems are overlaid on each other for visual comparison. In this case PeTrack and RPM signals were highly correlated ($\rho = 0.81$, $p < 0.001$). The respiratory triggers identified with each approach are also included as markers and superimposed on their respective waveforms. In this example there was a discrepancy in the number and frequency of the triggers between PeTrack and RPM. After retrospective processing of the RPM signal, RPMretro contained respiratory triggers that very closely matched those of PeTrack. The corresponding respiratory rate histograms are presented in Figure 3.4(B). The distributions of PeTrack and RPMretro closely resemble each other and are highly peaked about the normalized median respiratory rate (100%). The RPM distribution, however, has a more uniform shape across the range. The respiratory cycles that were classified as outlier are indicated by the faded bars. The relative frequencies of outlier respiratory cycles are also indicated; the prospective RPM method depicted the highest rate of outliers at 7.5% while PeTrack and RPMretro exhibited lower outlier rates of 4.2% and 2.1%, respectively. The differences described for this particular case resulted in substantial changes in the gated images, which will be discussed in more detail later.

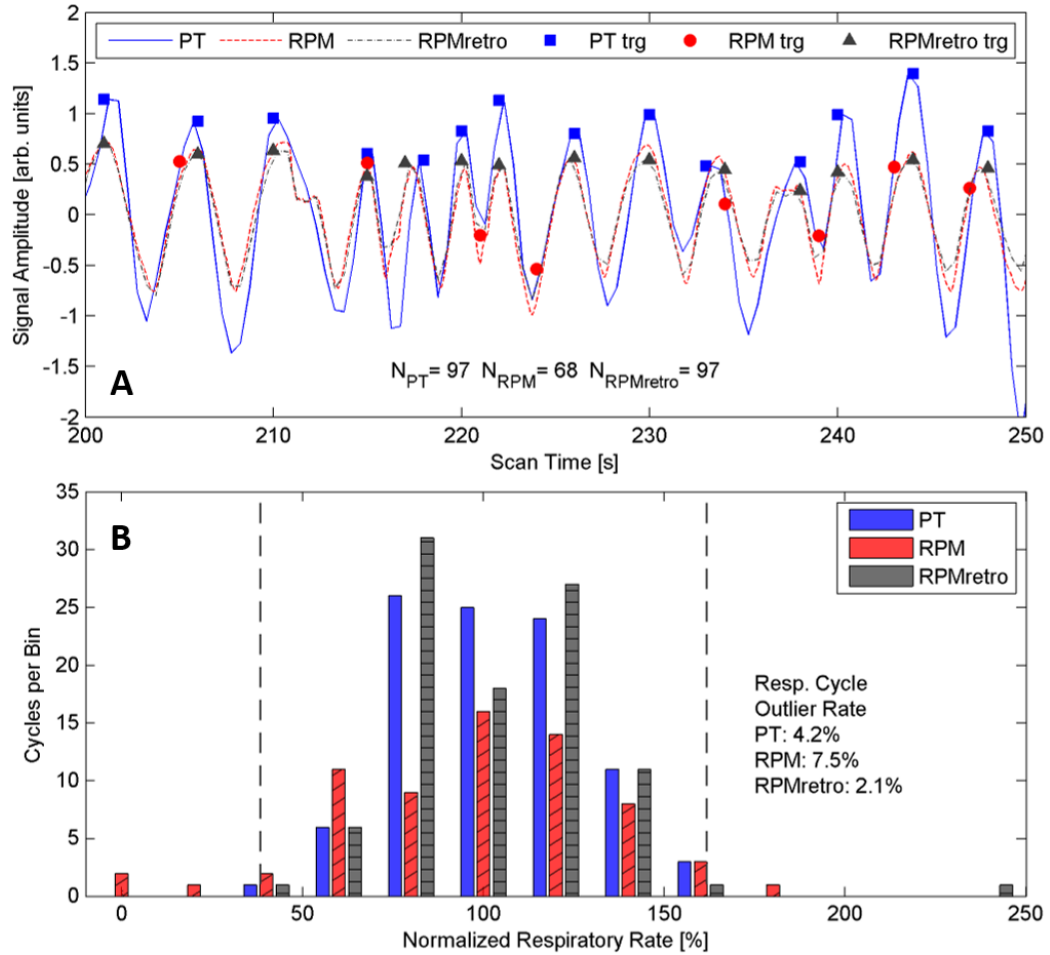


Figure 3.4 Example respiratory signals and triggers (A) and respiratory rate histogram (B) from a single acquisition. Data are shown for each gating system. Image A shows high concordance between RPM and PeTrack signals ($\rho = 0.81$, $p < 0.001$) within a randomly selected temporal window of 200 s to 250 s. Additionally, the respiratory triggers generated by each approach are overlaid on their corresponding signals. The number of triggers for each are indicated. Image B shows the respiratory rate histogram for the same case. Respiratory rate acceptance limits are denoted by the vertical dashed lines. The percentage of respiratory cycles identified as outliers is indicated for each gating approach.

Comparison of median and IQR respiratory rates are shown in Figure 3.5(A) and (B), respectively. These data indicate that across the cohort the patient-specific median respiratory rates observed did not exhibit a statistically significant difference between the PeTrack and RPM ($p = 0.3$) or between PeTrack and RPMretro ($p = 0.1$). There was,

however, a statistically significant difference between the median respiratory rates measured with RPM and RPMretro ($p = 0.003$), as is shown in Figure 3.5(A).

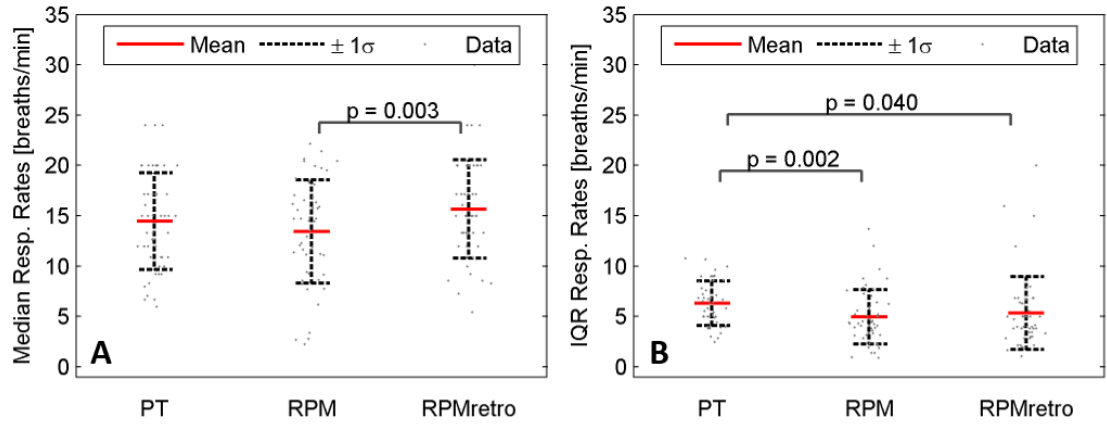


Figure 3.5 Median respiratory rates (A) and IQR (B) for each gating system for the entire cohort. Mean, ± 1 SD, and individual measurements are represented as solid-red lines, dashed-gray lines, and gray points, respectively. P-values produced from paired t -tests are shown in instances where statistically significant differences were observed.

The IQRs of the respiratory rate distributions, shown in Figure 3.5(B), showed a significant difference of the respiratory rate IQRs observed with PeTrack compared to those observed with the RPM and RPMretro. This indicated greater variability in the observed respiratory rates on a per-patient basis across the cohort. The mean paired differences were 1.4 breaths/min ($p = 0.002$) and 1.0 breaths/min ($p = 0.04$) between PeTrack and RPM and PeTrack and RPMretro, respectively. No significant differences were observed for IQR between RPM and RPMretro, suggesting similar patient-specific variability across the cohort.

The percentage of respiratory cycle outliers for each gating system are shown in Figure 3.6. These data indicate that there was a statistically significant difference between the RPMretro system with both of the other approaches. These differences gave rise to a

reduction in the patient-specific respiratory cycle outlier rates of 6.0% ($p < 0.001$) and 5.5% ($p = 0.001$) compared to PeTrack and RPM, respectively. The reduction in outlier frequency is not mirrored by the changes in IQR shown previously. This is not surprising as the IQR values, by definition, are relatively insensitive to outlier data points of each distribution.

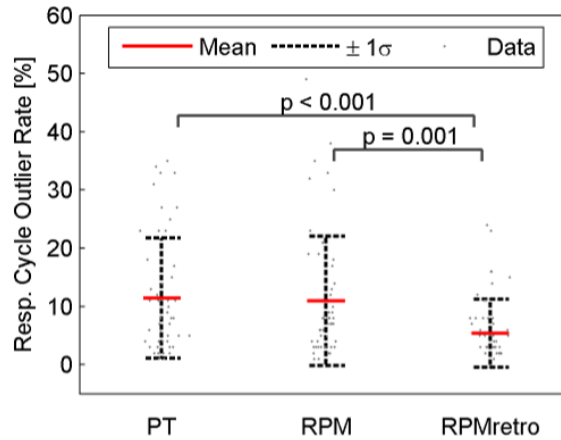


Figure 3.6 Respiratory cycle outlier rates for each of the gating systems. Mean, ± 1 SD, and individual measurements are represented as solid-red lines, dashed-gray lines, and gray points, respectively. P-values produced from paired t -tests are shown in instances where statistically significant differences were observed. RPMretro had significantly fewer outliers compared to RPM and PT

All LV width measurements are summarized in Table 3.1 and Figure 3.7. All gated image reconstructions led to statistically significant reductions in the LV width compared to the non-gated images. When compared to each other, however, no single gating system indicated a statistically significant difference compared to the others. A trend was observed, however, of larger LV widths observed while gating with PeTrack compared to RPMretro ($p = 0.08$). While LV widths were significantly smaller for gated images compared to non-gated, the effect sizes (mean differences in Table 3.1) correspond to practically small changes in the mean non-gated LV width, approximately -1%.

Table 3.1 Mean anterior and inferior LV wall widths for each reconstruction method for the entire cohort as well as for the subset of cases with SI motion ≥ 7 mm. Additionally, the mean differences are shown for each paired comparison. Comparisons with statistically significant differences ($p < 0.05$) are written in bold font.

Mean LV Widths (\pm SD) [mm]				
Images	Cohort	SI Motion ≥ 7 mm		
Non-Gated	12.3 (2.8)	12.5 (2.3)		
PeTrack	12.0 (2.5)	12.0 (2.4)		
RPM	11.8 (2.7)	12 (3)		
RPMretro	11.8 (2.6)	11.3 (2.3)		
Mean Differences in LV Width (\pm SD) [mm]				
Image Pairs	Cohort	P	SI Motion ≥ 7 mm	P
'PeTrack – Non-Gated'	-0.13 (1.3)	0.02	-0.19 (0.12)	> 0.05
'RPM – Non-Gated'	-0.2 (1.1)	< 0.001	-0.22 (0.14)	> 0.05
'RPMretro – Non-Gated'	-0.2 (1.1)	< 0.001	-0.48 (0.11)	< 0.001
'PeTrack – RPM'	0.1 (1.1)	> 0.05	0.03 (0.13)	> 0.05
'PeTrack – RPMretro'	0.1 (1.1)	> 0.05	0.29 (0.10)	0.009
'RPMretro – RPM'	0.0 (1.1)	> 0.05	-0.26 (0.15)	0.08

The comparisons were repeated for the subset of acquisitions where the mean SI LV motion was ≥ 7 mm (averaged across all gating systems) where the effect sizes were expected to be larger. These data are provided in the right column of Table 3.1 and shown graphically in Figure 3.7(B). Within this subset the reduction in LV widths due to gating was larger compared to that seen in the entire cohort. Compared to the non-gated measurements, thickness reductions compared to non-gated images ranged from -1.6% with PeTrack to -3.9% for RPMretro. Within this subset, the differences between PeTrack and RPM were not statistically significant when compared to the non-gated images in spite of the increased effect size. This is likely due to the reduced statistical power of this small subset size. While no differences were observed between PeTrack and RPM, there was a statistically significant difference between PeTrack and RPMretro ($p = 0.009$) as well as a trend toward smaller LV widths with RPMretro compared to RPM ($p = 0.08$).

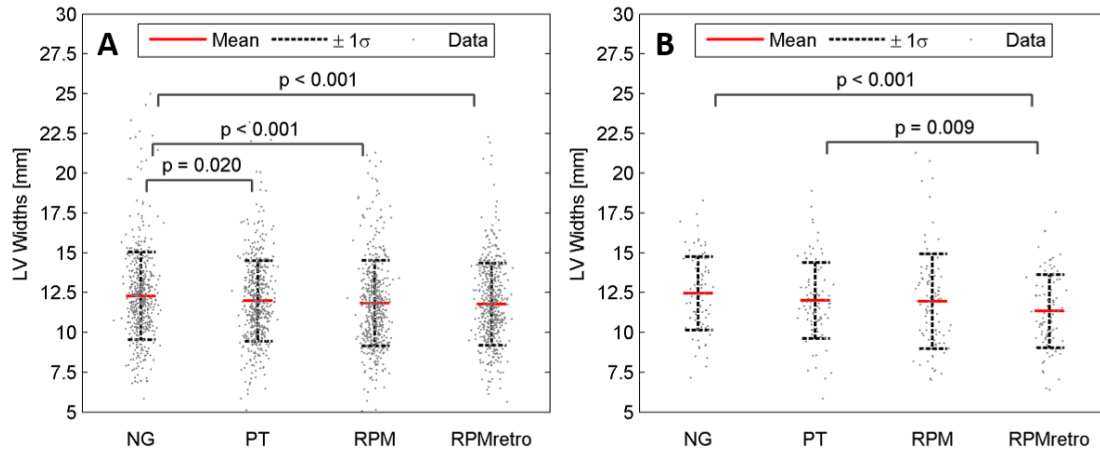


Figure 3.7 LV width measurements for both anterior and inferior regions for entire cohort (A) as well as the subset of cases with mean SI LV motion ≥ 7 mm (B). The means, ± 1 SD ranges, and individual measurements for each are indicated by the solid-red lines, dashed-gray lines, and gray points, respectively. Statistically significant p-values, computed from paired t -tests, are indicated.

Table 3.2 SI motion measurements for each gated reconstruction method for the cohort as well as for the subset of cases with motion ≥ 7 mm. Additionally, the mean differences in SI motion among all paired comparisons are shown. Statistically significant differences ($p < 0.05$) are emphasized with bold font.

Images	Mean SI Motion (\pm SD) [mm]			
	Cohort	SI Motion ≥ 7 mm		
PeTrack	4.4 (2.4)	7.6 (2.6)		
RPM	4.7 (2.5)	8.3 (2.5)		
RPMretro	5.7 (2.6)	9.5 (2.7)		
Image Pairs	Mean Differences in SI Motion (\pm SD) [mm]			
	Cohort	P	SI Motion ≥ 7 mm	P
'PeTrack – RPM'	-0.4 (0.3)	> 0.05	-0.7 (1.4)	> 0.05
'PeTrack – RPMretro'	-1.4 (1.8)	< 0.0001	-1.9 (0.5)	0.008
'RPMretro – RPM'	1.0 (2.1)	0.002	1.2 (1.2)	> 0.05

The results of the SI motion measurements are provided in Table 3.2 and shown in Figure 3.8. Across the cohort (left column of Table 3.2 and Figure 3.8(A)) statistically significant differences were observed between PeTrack and RPMretro ($p < 0.0001$) as well as RPMretro and RPM ($p = 0.002$). The results for the subset of the study with mean SI LV motion ≥ 7 mm are shown in Figure 3.8(B) and the right column of Table 3.2. For

all gating approaches the mean motion values increased by roughly 70% of the cohort measurements. The same conclusions are noted in this subset as were found for the entire cohort with the exception that no statistically significant difference between RPM and RPMretro was detected.

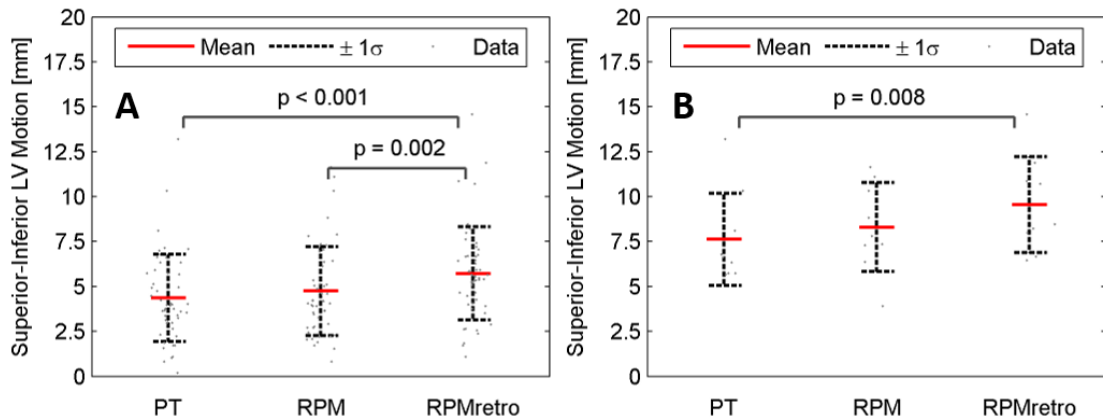


Figure 3.8 SI motion of the LV observed from each gated image series for the entire cohort (A) and the subset of cases with mean motion ≥ 7 mm (B). The mean differences, ± 1 SD ranges, and individual measurements for each are indicated by the solid-red lines, dashed-gray lines, and gray dots, respectively. Statistically significant p-values, computed from paired t -tests, are indicated.

No statistically significant differences were observed for SI LV motion between rest and stress states across the cohort ($p > 0.4$ for each gating approach, using a two-sample t -test). This finding did not change when a paired t -test was performed exclusively on the patients for whom both rest and stress scans were included in the test (23 patients, 46 acquisitions).

3.4 Discussion

In this work we sought to evaluate a new data-driven fiducial marker tracking algorithm, PeTrack, as an alternative method for respiratory gating by comparing it to a

well-accepted hardware-based alternative, RPM. No attempt was made to compare the respiratory tracking performance to other data-driven approaches, especially those that use no external markers, as no studies currently exist that reported their performance for ^{82}Rb cardiac MPI studies. Additionally, these approaches are currently not as well established or widely used as the commercial hardware-based systems. The evaluation of other data-driven approaches for this application may be explored in future work.

3.4.1 Respiratory Signal and Trigger Measurements

PeTrack respiratory motion signals were significantly correlated with those of the RPM in nearly all cases (45/50, mean $\rho = 0.49$). Noticeable discrepancies were noted in some acquisitions. Discrepancies in the respiratory signals may be attributed to several factors. Firstly, the temporal resolution is reduced for PeTrack compared to the RPM (2 Hz compared to 30 Hz) which may have a modest blurring effect on the PeTrack signal. Secondly, the PeTrack respiratory signal accounts for motion in the inferior-superior and anterior-posterior directions, which may not always correlate well with the anterior-posterior motion tracked by RPM. Lastly, the tracking precision with PeTrack is affected, to some extent, by the radiotracer activity in the patient which leads to substantial background to the marker's signal. It follows that there may be some time (tracer activity) dependence for the tracking precision. A more detailed discussion of the PeTrack system is included later in this section. The 95% central range of respiratory rates observed with RPM and PeTrack across the cohort corresponded to 0.07 to 0.5 Hz. It follows that a 2 Hz sampling rate, which is greater than the Nyquist frequency (1 Hz), was not expected to lead to aliasing.

Some context for the signal correlations reported here can be gleaned from previous studies involving data-driven respiratory tracking systems that were compared to hardware-based approaches. Schleyer et al.,¹⁴⁰ examined the data-driven spectral analysis method (SAM) and a modified version referred to as the kinetic respiratory gating (KRG) method for deriving respiratory signals in ^{13}N -ammonia MPI studies. The latter was designed specifically to attempt to overcome the typical loss of signal quality in the early time frames of PET procedures when the tracer distributions are changing rapidly. They reported mean correlation coefficients of 0.5 ± 0.2 and 0.75 ± 0.08 between the SAM and KRG versus the RPM system. The SAM results are similar to the mean correlation coefficient reported in this study. While the KRG method has not yet been applied to ^{82}Rb MPI studies, its reported success in the early-frames of ^{13}N -ammonia studies is encouraging. Additionally, the good overall correlation reported in this work between a data-driven and hardware-based methods has been previously reported in a study comparing several data-driven respiratory gating methods with a pressure-belt apparatus in a clinical FDG-PET study for lung lesion detection.¹¹² Mean correlation coefficients were also reported by Büther et al.,¹¹⁶ in cardiac ^{18}F -FDG studies for the sensitivity¹¹⁵ and center-of-mass¹¹¹ data-driven methods with respect to video-camera monitoring. The authors reported Spearman rank correlation coefficients of 0.65 and 0.68 for the sensitivity and center-of-mass methods, respectively. While these values appear larger than that reported in this work the author asserted that cardiac PET studies involving shorter-lived tracers, e.g. ^{13}N -ammonia or H_2^{15}O , would be expected to reduce the overall signal quality.

Three metrics were used to compare the quality of the respiratory triggers derived using different gating systems: the median respiratory rates, their corresponding IQRs and the respiratory cycle outlier rate using our quality control method. Median respiratory rates are not an indication of performance, but their comparison between the gating methods can give a sense of the similarity of the output of each. From our results it was found that generating respiratory triggers retrospectively from the RPM signals led to a small but statistically significant change in the median respiratory rates. This finding indicates that the information produced by the RPM was sensitive to the way in which the triggers were identified/recorded. That said, the mean respiratory rates and the corresponding relative standard deviations observed with RPM and PeTrack in this study are in good agreement with those reported for retrospective gating by Didierlaurent et al., while using the RPM system.¹⁶¹ Based both on trigger-based and image-based metrics we observed overall improvement in RPM performance following retrospective processing as was reported by Didierlaurent et al.¹⁶¹ A statistically significant difference was observed for the IQRs of the respiratory rates distributions suggesting greater variability in the triggers reported with PeTrack compared to the RPM and RPMretro. The effect size amounted to an increase in respiratory variability of approximately 1-1.4 breaths/min compared to a typical respiratory rate of 15 breaths/min. Note that this effect was not found to be correlated with the reduced motion resolution of PeTrack compared to RPMretro in the subset of cases with motion ≥ 7 mm.

3.4.2 Quality Control

The method used to identify outlier respiratory cycles was inspired by those described by Boning and Hacker¹⁶² for quality control of ECG-gated PET studies. In their investigation, limits on cycle outliers were estimated based on the cycle rate relative to individuals' median respiratory rates. Additional modifications were implemented to account for the non-Gaussian and irregular nature of the human respiratory patterns, namely the application of a log-transformation to the data. Interestingly, no literature on the topic of quality control or cycle rejection of respiratory triggers was found at the time of the present study. Boning and Hacker have also recommended visual quality control methods with which physiological explanations of poor ECG-trigger quality can be inferred, one of which involves inspection of raw signals superimposed with the trigger events, an example of which was shown in Figure 3.4(A). This process was implemented for PeTrack and RPM signals for a subset of the acquisitions in this study to identify trends and/or explanations for cases where respiratory cycle outlier rates were relatively high between the two gating methods.

A qualitative investigation of the 17 acquisitions where the respiratory cycle outlier rates observed using RPM or PeTrack differed by more than 10% was performed. Within this group, 8 cases (47%) indicated that the RPM outlier rate was greater than PeTrack. Visual inspection of the respiratory signals along with markers of the trigger events, indicated that some RPM triggers were absent from the list-mode data files. In all but one of these cases the respiratory signals were smooth and well resolved so while the explanation of the inability of RPM to trigger at the correct phase is not completely understood it appears to not be associated with the precision of the optical tracking

system. The most extreme example of this issue was identified by an interval of 200 seconds between respiratory triggers. A less extreme example of this was observed for the example case described in Figure 3.4. By visual comparison, it is evident that respiratory triggers are missing from the RPM trace and those that are present occur at inconsistent phases of the respiratory cycle. In stark contrast to the RPMretro data that are shown, respiratory cycles occurring at 210 s, 217 s, 225-232 s and 235 s are not marked by respiratory triggers. In this example, LV motion was severely underestimated while gating with RPM compared to PeTrack and then recovered after retrospective processing to generate the respiratory triggers. This can be seen in Figure 3.9 which shows a common coronal slice for each of the non-gated, PeTrack, RPM, and RPMretro images as well as a plot of IS LV displacement at each respiratory gate. Increased blurring at the anterior LV region as well as increased uptake non-uniformity at the inferior LV region are clearly visible in the non-gated and RPM images compared to that observed with PeTrack or RPMretro. The number of cases for which the respiratory cycle outlier rate was >10% for RPM compared to PeTrack was reduced from 8 to 1 after deriving respiratory trigger retrospectively.

Two acquisitions from the initial cohort were excluded from this study as they had either no, or too few, RPM triggers to synchronize the respiratory signal data to the list-mode data. Technical limitations associated with this device have been previously reported^{101,163} where signal quality was reduced or signals were not recorded due to baseline drifts in the patient position, operator errors, restrictions associated with patient size, involuntary patient motion, and the use of warming blankets. In the 9 cases (53%) where the cycle outlier rate was greater for PeTrack than for the RPM, the cause was

typically attributed to reduced signal-to-noise ratio in the motion trace of the fiducial marker throughout the acquisition.

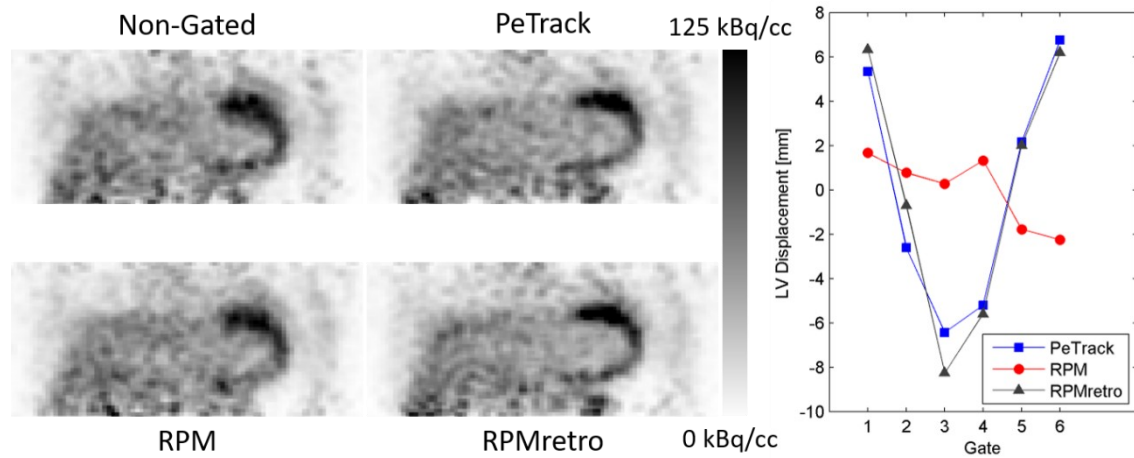


Figure 3.9 Inter-gate motion comparison for the exemplary case selected for Figure 3.4. On the left, coronal views at end-expiration are shown for comparison from non-gated, PeTrack, RPM, and RPMretro images. Note that the non-gated images were statistically sampled such that they were noise-matched with the gated images. On the right, the superior-inferior displacement of the LV as observed across the six gates using each gating system is plotted: PeTrack in blue squares, RPM in red circles, and RPMretro in gray triangles. Displacements were recorded with respect to the corresponding phase-averaged position. In this example the motion extent observed while gating with PeTrack and RPMretro was substantially larger than that observed with RPM. Note that the images shown here were smoothed with a 10 mm FWHM 3D Gaussian kernel for display purposes.

The respiratory cycle outlier rates of both systems exceeded 10% in 7/50 cases (14%) and these cases exhibited recurring instances of irregularities in the respiratory signals. These irregularities manifested as extended breath-holds, usually at inspiration, or steep gradients in the signals that may be associated with abrupt whole-body patient motion or coughing.

Statistically significant negative correlations were found between the paired respiratory cycle outlier rates and the paired LV motion measurements across the entire cohort

between PeTrack and RPM ($\rho = -0.45$, $p = 0.001$) as well as PeTrack and RPMretro ($\rho = -0.49$, $p < 0.001$), indicating that increases in the outlier rates led to reductions in the detected LV motion between the systems, and vice versa. This intuitive finding supports the validity of the respiratory cycle outlier rate as a metric of respiratory tracking quality. Outlier respiratory cycles were not excluded from the reconstructions in this study but the effect of such an action remains as an interesting research question and warrants further investigation.

3.4.3 Image based motion estimates

From the reconstructed images there appeared to be no statistically significant difference in LV thickness measurements, indicating no systematic difference in blurring between PeTrack and RPM gated images. This was not the case, however, when considering only those acquisitions with more severe respiratory motion, i.e. ≥ 7 mm. For this subset, no differences in LV widths were detected between either PeTrack or RPM and non-gated images but differences, i.e. smaller widths, were detected for RPMretro. This finding was supported by the reduced motion resolution of PeTrack in this subset. The mean SI LV displacements observed in this study were in excellent agreement with value of 4.6 mm reported by Wells et al., for a comparatively larger cohort of ^{82}Rb and ^{13}N -ammonia MPI studies.¹⁰¹ Additionally, no statistically significant difference was detected in the extent of motion between rest and stress states for ^{82}Rb scans, as was the case in this study. Larger mean LV displacements were reported by Büther et al., in a cohort of 17 patients while using the sensitivity and center-of-mass based gating methods, but the radiotracer used was ^{18}F -FDG which has improved spatial resolution

over ^{82}Rb making comparisons difficult. This apparent increase in SI LV displacement is likely associated, however, with increased number of respiratory gates (10 gates rather than 6) which would enhance the motion resolution for the gated images.¹⁵⁸

3.4.4 Considerations for PeTrack

Most data-driven gating algorithms derive motion signals directly from the activity of the tracer within the patient and while this approach may explicitly estimate motion of the organs of interest, the accuracy/precision of the signal is highly dependent on the tracer distribution which varies in time.¹⁴⁰ The use of an external marker with a long-lived positron emitting isotope has been proposed for use as a motion tracking tool in a previous study.¹²² While differences in phase and/or amplitude in the motion of an external marker compared to that of the thoracic organs or lesions have been reported^{102,105,164}, the external motion measured at the abdomen has been shown to have good correlation with inferior-superior motion of internal regions of interest.^{102,122,164}

There are several factors that can limit the effectiveness of the PeTrack system for patient-motion tracking. As was mentioned previously, since PeTrack relies on the positron-emission signal of a fiducial marker there exists substantial interference in the form of LORs from the radiopharmaceutical tracer. Selecting for coincidence events associated with the marker alone is not a trivial task. Cardiac perfusion studies at our institution that make use of ^{82}Rb can produce scanner count rates in excess of 10^7 counts per second, at which time the activity of the fiducial marker used in this study corresponds to less than 0.01% of the scanner count rate. Although the current implementation of PeTrack includes a background rejection step that excludes most of

the LORs originating in the patient, the tracer background in some studies may reduce the signal-to-noise ratio of the marker too much to allow PeTrack to track the marker with sufficient precision. This effect can be accounted for by the exclusion of the initial portion of the acquisition that includes the peak count rate from the image reconstructions (as was essentially the case in this study). In the case of ^{82}Rb , which has a half-life of 76 s, the exclusion of the first 90 - 120 s of the acquisition required for clearance of the LV blood pool is generally sufficient for this purpose.¹⁶⁵ Additionally, when using radiotracers with short half-lives the position of the marker can be tracked in reverse, i.e. from end of the acquisition to the beginning, to begin when the SNR of the marker's signal is much more favorable. This challenge is expected to be less significant for longer-lived tracers that exhibit a much narrower dynamic range of count rates throughout the acquisition. The conditions in this work, therefore likely evaluated PeTrack performance under one of the most challenging settings. Regardless, this and other work^{157,166} have demonstrated feasibility in clinical practice, especially for the post-bolus stages of a cardiac acquisition. Büther and colleagues¹²² did not report similar difficulties while tracking radioactive fiducial markers in projection space although they reported using markers with activity that was roughly three times greater than those in this study. Additionally, they placed the markers on structural supports to separate the markers from the skin of the patients which resulted in a greater patient setup complexity, and potential interference with scatter correction.

Another important consideration is the placement of the PeTrack marker on a patient. As the geometric sensitivity of the scanner decreases at the edge of the axial field of view, it follows that placement of the marker too near to the edge (i.e. too inferior or

superior) will lead to a significant signal reduction. Placement of the marker too near to the heart in perfusion studies may also lead to complication as the activity of the tracer accumulates in the myocardium leading to a higher interference level for the PeTrack system throughout the scan. To help compensate for these issues one could simply increase the activity of the fiducial marker to increase the ratio of its signal over that of the administered PET tracer. At the Cardiac PET Centre at UOHI, the use of low activity external markers is part of the clinical imaging protocol as a quality control measure. As these data were collected as part of a clinical quality improvement study, the use of higher activity markers was not considered. Apart from increasing the marker activity to enhance tracking precision, the marker should ideally be placed in the middle of the axial field of view but distally from regions where high uptake is expected, e.g. the heart in perfusion studies. Training of technologists is essential to ensure optimal marker placement on the patient. Cardiac PET studies with tracers that are administered with lower initial activities may be ideal candidates for motion tracking with PeTrack. Additionally, the use of long bore PET systems will enable better separation between heart and marker placement while ensuring both remain well within the field of view. A previously reported technical limitation of the RPM is the reduced visibility of the reflective marker in long-bore scanners which may preclude its use on these systems.⁷⁹

3.4.5 Clinical Use of PeTrack for Respiratory Gating

While this work focused on evaluating PeTrack as an alternative to hardware-based respiratory gating devices, another practical application, as demonstrated in our practice, is to use both systems in concert. This approach affords the option to select the more

reliable of the two gating sources on a post-hoc basis and/or use the respiratory signal from PeTrack to supplement the respiratory triggers produced by the RPM system. It was noted previously that the RPM and PeTrack systems were configured to trigger at different respiratory phase which may complicate the combination of the respiratory tracking data of the two. As was shown, this challenge could be overcome by retrospectively processing the RPM signals to generate respiratory triggers at end-expiration using the same utilities that have been used for PeTrack. The use of an external marker for PeTrack increases the complexity of patient setup compared to alternative data-driven approaches but the added difficulty is minimal as no support structure or adhesives are needed. Unlike many data-driven methods that have been proposed, the PeTrack signal can additionally be used to track whole-body motion of the patient as the absolute 3D position of the marker is determined as opposed to temporal fluctuations of signal intensity in list-mode or projection spaces. Some early work on this application has been performed already¹⁶⁷ and will be further explored in future investigations. In our clinic fiducial markers are already used in all cardiac PET scans as an indication of patient motion, particularly for dynamic acquisitions. It follows that PeTrack can be applied without modification to current patient setup procedures. Beyond placing the marker on the patient, technologists must verify that the marker is within the axial field-of-view. This task is satisfied by visual inspection of the initial scout CT scan which is used in the clinical workflow for patient positioning prior to each PET acquisition. When compared to the RPM system, significantly less setup is required as PeTrack requires no setup of dedicated hardware or staff monitoring during imaging.

3.5 Conclusion

A data-driven respiratory gating system was developed that utilizes a low activity, positron emitting, fiducial marker and we compared its performance to an established hardware-based system in a practical clinical setting. Despite the challenging conditions posed by ^{82}Rb cardiac PET/CT for data-driven approaches, PeTrack appears feasible for retrospective respiratory gating with no practical loss in the ability to capture patient respiratory motion or in respiratory-gated image quality compared to the established real-time gating available with the RPM system. The performance of both PeTrack and prospective RPM was generally reduced in comparison to the retrospective RPM approach. This data-driven approach has the potential to reduce the need for expensive ancillary hardware systems to monitor respiratory motion but could benefit from additional implementation development.

Chapter 4 Whole-Body Motion Correction in Myocardial Perfusion

Imaging with PET/CT

In this and the following chapter, the ability of PeTrack to detect and estimate whole-body motion was considered. The content of this chapter is largely based on work that was presented at the IEEE Nuclear Science Symposium and Medical Imaging Conference in 2018¹⁶⁷ and 2019¹⁶⁸. Conference record publications were submitted following each of these events. Some figures from these conference record publications are reproduced here with permission from the authors.

4.1 Motivation

Various studies have been reported that sought to measure the prevalence and effects of patient motion in cardiac PET/CT, the results of which indicated that motion was present in as high as 52% of patients studied.⁸² Others indicated that motion prevalence and severity was affected by the state of rest or stress in the patient, and in the stress cases by choice of exercise or pharmacologic stressing agents used.^{148,149,169} Average whole-body motion magnitudes have also been reported in the range of 6 to 10 mm^{82,148} but with maximum magnitudes at or greater than 18 mm.^{82,169}

At a minimum, it has been recommended in cardiac PET/CT that motion be assessed visually while others recommend that motion correction strategies be implemented, particularly while patients are in a stress state after pharmacological vasodilation or treadmill exercise testing. Although several motion correction strategies have been proposed^{147–149} translation into clinical practice is uncommon.¹⁴⁸ Typically, motion correction is attempted by spatial registration of dynamic images of pre-defined

durations.^{81,147-149} As a result, they are neither able to correct for intra-frame motion nor do they address the issue of PET-CT misalignment. Indeed, there is a need for a whole-body motion correction algorithm in PET/CT that can correct for patient motion and PET-CT mis-alignment prior to image reconstruction.¹⁶⁹

We sought to evaluate a WBM correction method with information from tracking fiducial markers using the data-driven Positron Emission Tracking (PeTrack) algorithm. Within this current framework 3D translational motion correction is achievable without the need for a priori choice of multiple acquisition frames. Additionally, image registration techniques are not required to estimate patient motion. This latter feature is useful as the spatial registration of PET images with limited count statistics is challenging due to increased image noise as well as changes in image intensity associated with tracer dynamics.¹⁷⁰ A combination of phantom and patient data was used to demonstrate this approach. As PeTrack has only been applied previously on studies using ^{82}Rb as the PET tracer, a secondary objective of this study was to validate the tracking performance of PeTrack in clinical data sets which used ^{13}N -ammonia as a perfusion tracer.

4.2 Methods

4.2.1 Whole-Body Motion Correction Framework

Unlike what was described in the previous chapter where gated images were reconstructed to compensate for motion, here the MAF motion correction paradigm was implemented such that individual reconstructed frames are spatially aligned using motion information provided by PeTrack.

A 3D reference position was established for each acquisition in this study which was subtracted from every position element of the PeTrack motion trace. This operation transformed the motion information from a set of positions to a set of motion vectors with respect to the reference position. The magnitudes of the motion vectors were compared to a pre-defined threshold such that instances of relatively significant deviations away from the reference position could be determined. In particular, the motion vectors were averaged within a 5-second sliding window and then compared to the threshold vector. If the mean vector within the window exceeded the threshold a motion-trigger was generated at the central time of the 5-second window. Each of the 3D components was tested against their corresponding threshold to identify instances of motion. The thresholds were directly related to the physical size of the voxel in the corresponding reconstructed image. Minor variation in the thresholds were considered between the two datasets included in this chapter, and so the specific values will be stated later in this section.

A 5-second sliding window duration was chosen for the application of this approach for motion correction during dynamic cardiac PET/CT studies that are performed for absolute blood flow quantification. In these studies, the shortest frames used in the perfusion protocols at the University of Ottawa Heart Institute are 10-seconds in duration. It follows that motion detection at a time scale of 5-seconds would permit intra-frame motion correction for these dynamic studies. Additionally, smoothing the original trace within the 5-second sliding window can reduce the impact of an external respiratory signal while trying to detect whole-body motion. Using this approach, the motion correction was limited to the re-alignment of pre-defined dynamic frames.

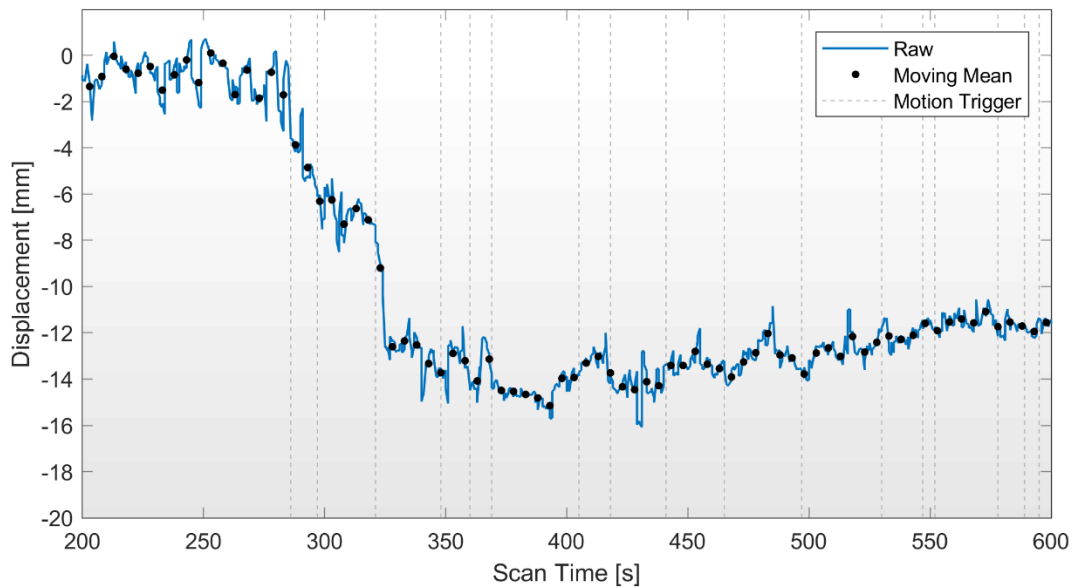


Figure 4.1 An example 1D motion trace is shown from the patient cohort to demonstrate the production of motion triggers after applying the moving mean filter. To simplify the example, only the motion the left-right direction is shown here. The original and filtered traces are depicted by blue and black curves, respectively. The motion triggers are shown as vertical, dashed lines. The motion thresholds are also indicated as the vertical limits of the gray bands which span the domain of the plot.

As was stated previously, this motion correction framework was designed to compensate for motion-induced CTAC misalignment as well as the loss in signal-to-noise ratio in the target tissues. To achieve this, a separate image was reconstructed for each ‘motion frame’, i.e. a reconstructed frame that includes the data bound by two motion triggers, that was identified and were registered and averaged post-reconstruction using the motion vectors produced by PeTrack averaged over the duration of each motion frame. In the event that non-adjacent motion frames were found to correspond to the same position, a form of whole-body motion amplitude gating was applied. In this approach, the raw list-mode data were combined to reduce to the total number of reconstructed frames. If this occurred, corrections for radioactive decay, dead time, and

random coincidence events were adjusted to account for the differences between the multiple frames. This spatial registration addresses the motion-induced blurring that would exist in the presence of motion if no compensation was applied. To address the motion-induced CTAC misalignment, the CT image used for attenuation correction was transformed prior to the reconstruction of each motion frame using the same frame-average PeTrack motion vectors. In doing so, the CTAC image was, in principle, spatially registered with the emission data belonging to each individual frame.

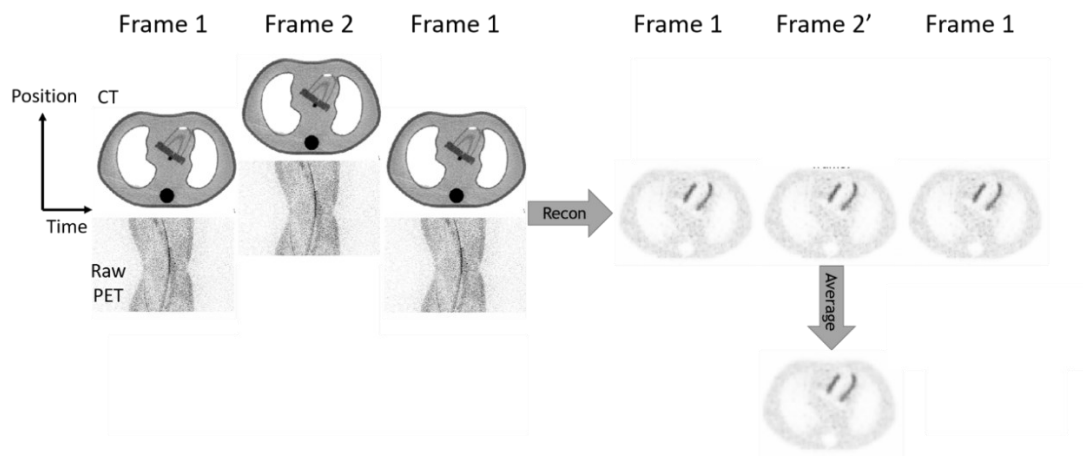


Figure 4.2 A schematic representation of the whole-body motion correction algorithm. Prior to the reconstruction of each motion frame, the AC map was transformed rigidly (3D) based on the mean displacement of the marker during the frame. After reconstruction, motion frames were spatially aligned using the reversed transformations. After alignment, a single weighted-average image was produced where the weights were determined by the number of coincidence events in each frame. This figure has been reused¹⁶⁸ with some modification with permission; original copyright 978-1-7281-4164-0/19 ©2019 IEEE

It follows that reconstructed motion frames were free of CTAC misalignment artifacts prior to combining them into a single reconstructed image. A weighted-mean was used to combine the individual motion frames where the weights were chosen as the total number of prompt coincidence events that were detected within each frame. The weight value of

each bin of data to the final image was the number of coincidence counts. A schematic diagram of this workflow is presented in Figure 4.2. In this diagram only three frames were considered, the second of which is shown as being shifted away from the others.

4.2.2 Validation Using an Anthropomorphic Torso Phantom

Myocardial perfusion studies were simulated with the use of an anthropomorphic torso phantom that included a cardiac insert that models the left-ventricle of the heart.

Acquisitions were carried out on a GE Discovery 690 PET/CT scanner (Waukesha, WI) with time-of-flight PET and list-mode capability after the injection of 3 MBq and 27 MBq of ^{18}F -FDG into the cardiac insert and thorax cavities, respectively. Whole-body motion was simulated by physically translating the phantom during the acquisition.

Motion was applied in the three cases along superior-inferior and lateral directions as well as diagonally along both. One motion-free acquisition was used as a reference for comparison for the acquisitions with motion both before and after motion correction.

Translations were approximately 5 mm in magnitude and occurred at 60 second intervals.

Images were reconstructed using the vendor's standard 3D OSEM offline reconstruction toolbox with a transaxial and axial field-of-view of 500 mm and 150 mm, respectively, and a 128 x 128 x 47 matrix size. Post-reconstruction filtering was applied using a 5 mm FWHM Gaussian smoothing kernel and nearest neighbour weighted averaging in the axial direction (the relative nearest neighbour weights were 1, 2, 1).

Motion tracking was performed at a frequency of 2 Hz using the PeTrack algorithm to calculate the position of a radioactive fiducial marker (^{22}Na , ~30 kBq) placed on the anterior surface of the phantom. A reference position was recorded at the beginning of

the acquisition where emission data were aligned with CT data used for attenuation correction. The motion thresholds that were used were 3.91 mm and 3.27 mm in the lateral direction and axial directions, respectively. These thresholds correspond to the physical sizes of the voxels in each of the directions of motion that was considered. Motion detection and estimation were performed using the approach described above.

4.2.3 Application to ^{13}N -Ammonia Perfusion Studies

The rest and dipyridamole-stress scans of three patients ($N = 3$) were used in this study (weight 135-158 kg, height 173-178 cm). Two patients were imaged on a GE Discovery 690 PET/CT system and one on a GE Discovery 600 PET/CT system. Patients were injected with 3 MBq/kg of ^{13}N -ammonia for each of the rest and stress imaging protocols. The acquisition duration for both protocols was 20 min commencing with tracer administration. A CT image acquired prior to the rest PET acquisitions was used for attenuation correction for both rest and stress images. Note that the patients are labelled as A, B, and C throughout this chapter.

Image reconstructions were performed offline using the vendor's reconstruction toolbox. A 3D OSEM algorithm with 16 sub-iterations and 4 iterations was used. The dimensions of the images were $128 \times 128 \times 47$ voxels with sizes of $3.91 \times 3.91 \times 3.27$ mm³, respectively. Corrections for attenuation, random and scatter prompt coincidences were applied. Post-reconstruction smoothing was not applied to the images; an exception to this is mentioned below. Reconstructions ignored the early time phase where the tracer has not yet been taken up in the tissue. These start times were 120 s and 300 s for the Discovery 690 and Discovery 600 scanners, respectively.

In this study, the same fiducial marker (^{22}Na , ~ 30 kBq) was placed on the chest, to the right of midline, on each patient. The motion thresholds were reduced for the clinical data sets as compared to those of the phantom experiment. The motion simulated in the phantom studies represented a relatively extreme case and the transitions were rapid. As motion is often not so well defined for humans, the thresholds for detecting motion were relaxed. The thresholds were set to half the voxel sizes, 1.96 mm and 1.64 mm for transaxial and axial directions, respectively, for the clinical data sets.

A reference position was determined as the mean position of the marker during the entire reconstructed frame (120 s – 1200 s and 300 s to 1200 s for acquisitions on the GE Discovery 690 and 600 scanners, respectively). This was done so that the PET reference position has the best alignment with the CT image used for attenuation correction. This assumption is based on the use of a 3D displacement vector stored in the metadata of the raw files used in the offline reconstruction. This 3D vector was produced by technologists in the clinic to rigidly register the CT image to the PET image to enhance the quality of the attenuation correction.

4.2.4 Quantitative Measurements

Several image-based quantitative measurements were performed to evaluate the quality of the image reconstructions both prior to and following motion correction. The following measurements were performed for both the phantom and patient data sets. Several additional measurements, which will be described below, were exclusively performed on the patient images. All measurements were performed after reorienting the image volume into the short-axis representation. All motion-corrected images were

reoriented using the transformation matrix that was used for the corresponding non-corrected image to enhance spatial agreement between the pair; this was done especially for comparison of LV thicknesses within specific segments. The reorientation method was described previously in Section 3.2.4. LV wall-thicknesses and contrast-to-noise ratios (CNR) were measured as quality metrics of the images.

The LV wall thicknesses were measured using a modified version of the approach described in Section 3.2.7. Unlike the method used in Chapter 3, radial profiles emanated from the center of the LV blood pool and extended beyond the epicardium. Profiles were produced at 16 equally spaced angular positions on 14 short axis slices. Note that 20 angular samples were acquired for some clinical images where patients had left ventricles that were considerably larger than the of the anthropomorphic phantom. The rationale for not applying post-reconstruction smoothing was to not affect these thickness measurements in the reconstructed images. An example of the profiles is provided in Figure 4.3. While a multi-resolution approach was once again used, there was no averaging among adjacent profiles as was described in Section 3.2.7. Individual measurements were averaged based on the left-ventricular segment to which they belonged, i.e. there are multiple radial profiles belonging to each segment. The American Heart Association 17-segment model⁴⁷ was used. The apex was excluded from phantom measurements due to the presence of an air bubble within the model LV wall of the phantom that was completely vacant of activity. Additionally, as the curvature of the apex did not lend itself to the radial sampling method, it was also not performed among the clinical data set.

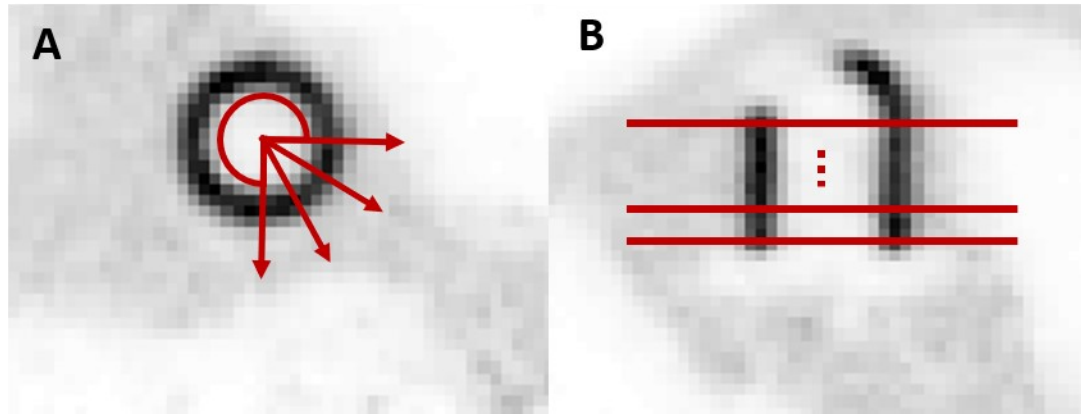


Figure 4.3 Diagram of the radial profile locations cast on the reoriented image volumes for the purpose of making LV thickness measurements. Image A shows a single short-axis slice on which four radial profiles can be seen originating at the LV center and spanning outward across the LV wall. Image B shows a horizontal long-axis image slice depicting the series of short axis slices that were used. The figure is derived from the reference trial reconstruction of the anthropomorphic phantom. A region within the model LV wall can be seen within the apex to be void of activity; this region corresponds to an air-bubble. Note that these profile indicators are only qualitative representations of the profile locations that were actually used for the measurements.

Contrast-to-noise ratios were calculated as the difference in the mean activity concentrations between the LV and a background volume of interest ($\overline{A_{BKGD}}$) divided by the standard deviation measured in the background ($\sigma_{A,BKGD}$).

$$CNR = \frac{\overline{A_{LV}} - \overline{A_{BKGD}}}{\sigma_{A,BKGD}} \quad \text{Eq. 0.1}$$

The LV was segmented using the radial profile fitting procedure that was used to measure the LV thicknesses. From each radial profile, the coordinates corresponding to the extent of one FWHM about the centroid were recorded. The inner and outer limits from each profile were used to construct two polygonal masks on each short-axis slice that was sampled. The two masks roughly correspond to the endocardial and epicardial

limits of the LV; the difference between the two masks provides a single mask which represents the LV myocardium. A 3D VOI containing the LV (excluding the apex) was then produced by concatenation of the set of 2D masks.

In the case of the phantom studies the background VOI was a rectangular prism which contained $6 \times 6 \times 14$ voxels and was parallel to the model LV and just outside of the septal region. The exact position was unique to each trial, but it was chosen to contain a volume of uniform background activity. In the patient data sets a cubic background VOI with an edge length of 4 voxels was placed approximately within the left atrium.

The tracking precision of PeTrack was assessed by measuring the centroid position of the marker in a dynamic series of images, each with a duration of 60 seconds. To measure the agreement between these two sets of measurements, the PeTrack motion trace was averaged over the same time frames. Correlation and Bland-Altman analysis was carried out to quantify the agreement. The image-based centroids were computed as activity-weighted mean (see Eq. 0.2) position of marker within a cubic VOI centered about the marker with an edge size of 11 voxels.

For the clinical data sets the regional and global relative myocardial perfusion were measured. Regional measurements correspond to the left-anterior descending (LAD), right-coronary (RCA) and left-circumflex (LCX) arteries territories. The global measurement included the entire left ventricle (LV). Lastly, the LV blood pool volume was also measured. Perfusion measurements were performed using the automated Corridor 4DM (INVIA Medical Solutions, Ann Arbor, Michigan) software. Unlike the image quality measurements described previously, a 5 mm FWHM Gaussian smoothing kernel was applied using tools within the Corridor 4DM application to prior to making

these measurements. No manual interventions regarding LV segmentation or reorientation were performed while using Corridor 4DM. The LV blood pool volumes were calculated as the volume of the inner, or endocardial, mask that was described previously.

4.3 Results

4.3.1 Motion Tracking Validation

The axial and lateral components of the PeTrack motion traces for the four phantom acquisitions are shown in Figure 4.4. Changes in the anterior-posterior position were not included in the experiment so this component of the trace is not shown. The axial components shown in Figure 4.4(A) provide clear demonstration of the instances of motion (and non-motion in the Reference and Lateral cases). The lateral motion component did not demonstrate the same level of tracking precision in the diagonal motion case. The correlation and Bland-Altman analyses, shown in

Figure 4.5, indicated excellent agreement between the marker displacements reported by PeTrack and those measured from dynamic image reconstructions. The correlation coefficient (ρ) of 0.96 and a RMSE of 1.1 mm was observed between the two sets of measurements. The Bland-Altman plot shows that there is no statistically significant difference between the two sets of motion measurement as determined by a two-tailed, paired, Student's t-test. Across all three trials the mean bias was -0.26 mm, well below the size of a single voxel. Only the dominant motion dimension is used for each case, e.g.

only axial motion was considered for the Diagonal case.

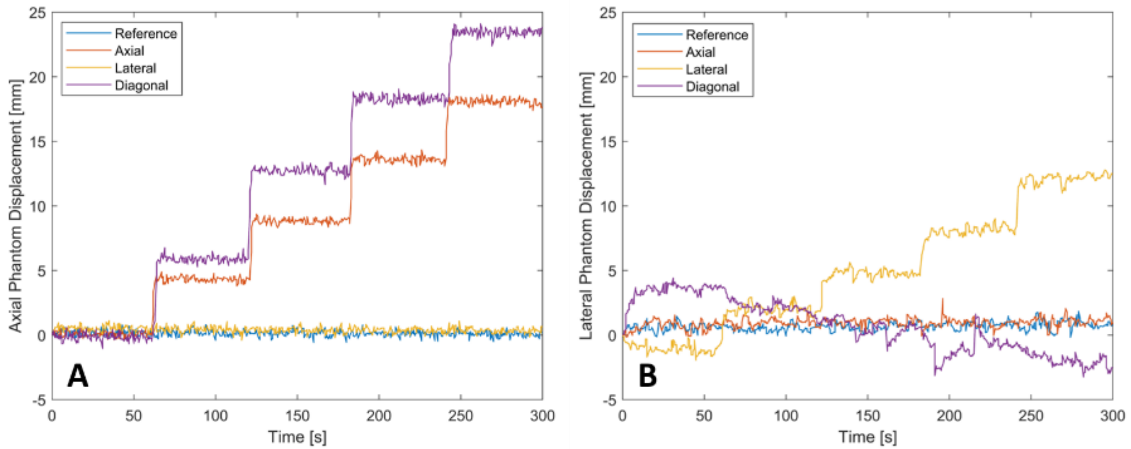


Figure 4.4 Phantom motion trace derived from PeTrack algorithm. Images A and B depict the axial and lateral displacements as a function of time during the acquisitions. Traces are shown for each acquisition: reference (blue); axial motion (red); lateral motion (yellow); and diagonal motion (purple).

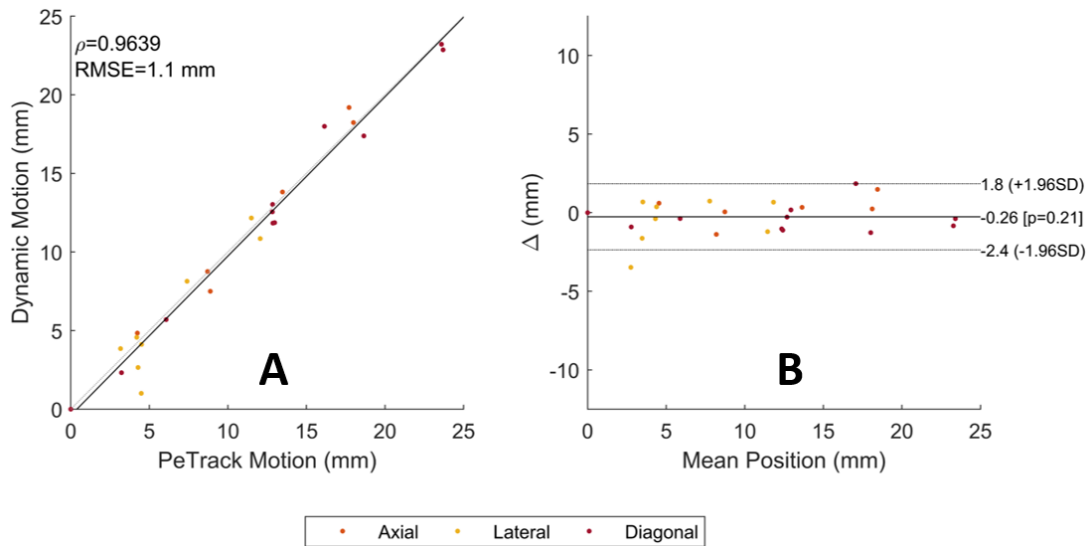


Figure 4.5 Correlation (A) and Bland-Altman (B) plots for the phantom study indicating the agreement of motion measured using PeTrack to that measured in each of the non-corrected (Dynamic) ‘motion-frames’. Measurements for the axial, lateral, and diagonal motion trials are indicated by red, yellow and purple points, respectively. Plot A contains a grey line of identity and a black line of best fit. Only the dominant motion component was used for each case, e.g. axial motion is considered for the Diagonal case. In plot B, the paired differences between the dynamic image and PeTrack measurements are denoted by ‘ Δ ’.

The quality of the PeTrack motion tracking for ^{13}N -ammonia studies was evaluated in a similar fashion except that the marker displacements were determined from reconstructed dynamic series with 1-minute frames. From each, the activity-weighted centroid of the marker and its standard deviation (as per Eq. 0.1) were determined from within a cubic volume of interest (VOI) set around the marker. The activity-weighted mean and standard deviations were defined earlier in Section 3.2.7. The VOI had an edge size of 11 voxels. An example of these measurements is shown in Figure 4.6 where a high concordance between the PeTrack and image-based measurements can be observed. These data were produced for all 6 acquisitions in this study. Bland-Altman (see Figure 4.7) and correlation analyses indicated a Pearson correlation coefficient of 0.91 ($p < 0.0001$), RMSE of 0.77 mm, mean paired difference of 0.02 mm with limits of agreement ($\pm 1.96\text{SD}$) of [-1.49,1.59] mm; all of which indicate excellent agreement.

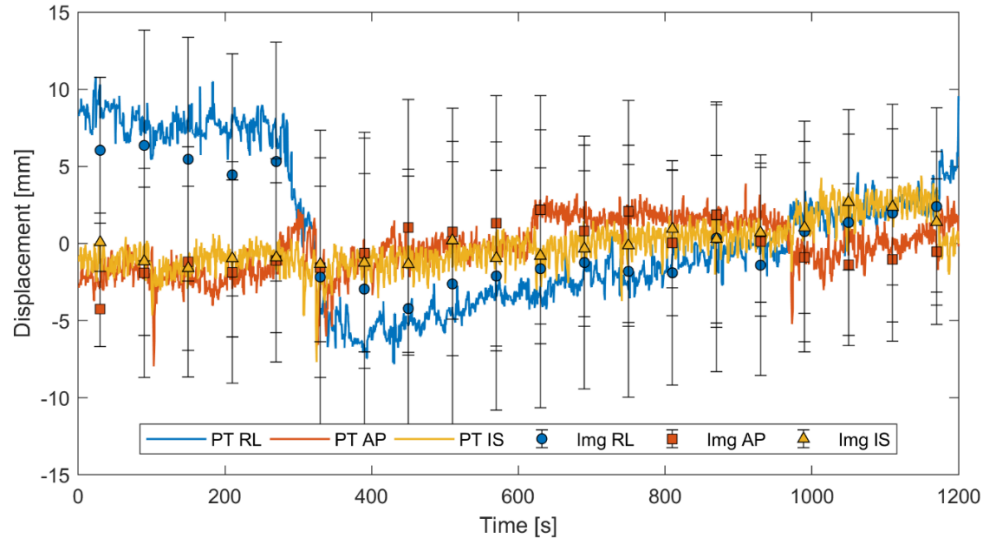


Figure 4.6 Comparison of marker 3D displacements from PeTrack (PT) and image-based (Img) measurements for the stress acquisition of patient B. Image measurements were made from dynamic reconstructions of the entire acquisition with 1-minute frames. Symbols with error bars indicate the centroid and ± 1 SD limits of the marker in each dimension (RL = right-left, AP = anterior-posterior, IS = inferior-superior) for each of the frames. Note that the standard deviations of the centroids were calculated by using Eq. 0.1. This figure has been reused¹⁶⁸ with permission and was modified from its original version; original copyright 978-1-7281-4164-0/19 ©2019 IEEE

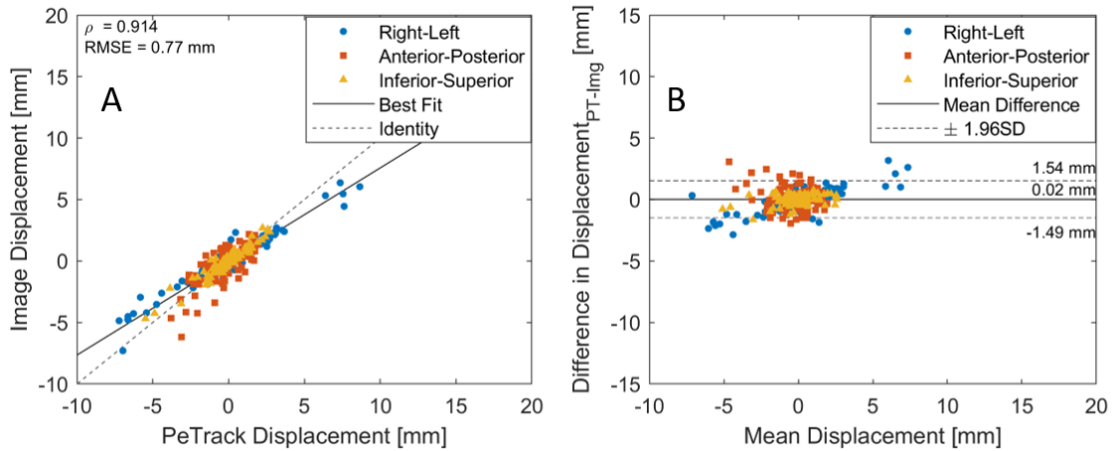


Figure 4.7 Correlation (A) and Bland-Altman (B) plots comparing PeTrack and image-based marker displacements for all human acquisitions. The PeTrack displacements shown here were averaged over the 1 min duration of each dynamic frame. The paired differences in B were computed as ‘PeTrack - Image’. The Bland-Altman plot shows excellent agreement giving strong evidence for tracking quality with PeTrack in this cohort.

4.3.2 LV Wall Thickness and Blood Pool Volume Comparison

To emphasize the effects of motion among the phantom acquisitions 17-segment polar maps of the LV were produced wherein the value of each segment corresponds to the change in thickness compared to that of the reference image. These are shown in Figure 4.8. For each non-corrected case (sub images A, C, and D) the changes in thickness are clearly shown to predominantly follow the direction of motion, e.g. along the anterior-inferior (A-I) direction for the axial motion case. The motion-corrected polar maps indicated a much closer agreement with the reference image measurements, as indicated graphically by segment colours that are less intense and closer to white.

A summary of the LV thicknesses for the four phantom acquisitions is provided in Table 4.1. The values represent the means across each of 16 LV segments that were sampled. The mean values for the reference and motion-corrected images demonstrate good agreement whereas those of the non-corrected images exhibit substantial increases. Paired Student's t-tests were performed between the thickness measurements of each trial case compared to the reference where LV thickness measurements were paired by segment. All non-corrected images indicated significant thickness increases compared to the reference. A significant difference was also detected for the diagonal motion-corrected image which suggested some residual blur that was not adequately compensated. That said, the mean paired differences for this case was 0.8 ± 1.2 mm, which is a small effect compared to the mean LV thickness of the reference case (14.3 mm). The mean paired differences for the non-corrected diagonal motion case was 4 ± 4 mm and represents a much larger effect.

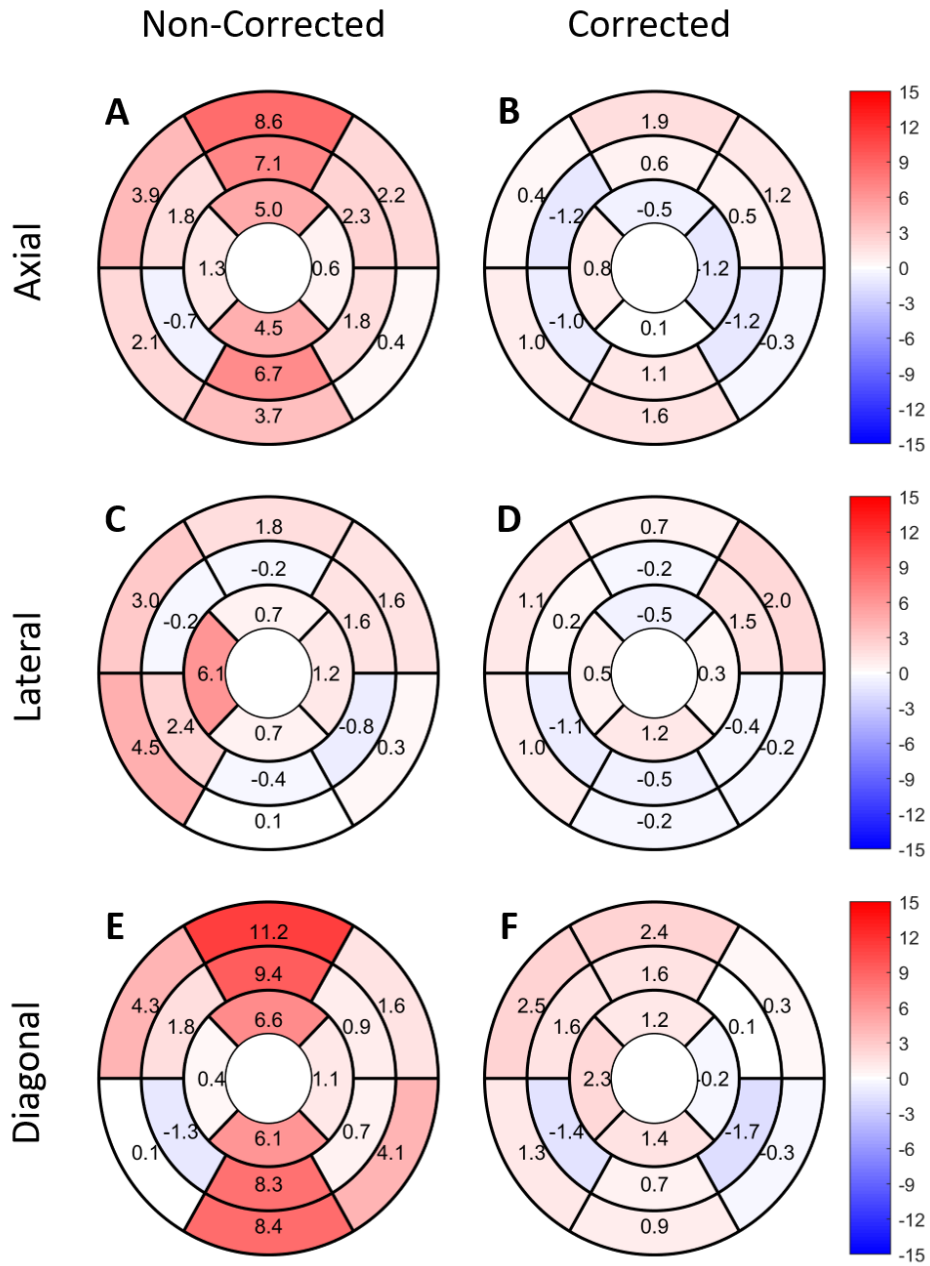


Figure 4.8 17-segment polar maps of the model LV of the phantom indicating absolute changes in the thickness compared to the reference image for each motion case before ('Non-Corrected': A, C, and E) and after motion correction ('Corrected': B, D, and F). All values are in units of millimeters. Graphically, the colour intensity reflects the severity of mismatch between a segment thickness of a trial image with that of the reference. Note that the colour map is identical for all sub-figures.

Table 4.1 LV thicknesses measured for each phantom trial averaged among all 16 segments. Standard deviations (SD) are also provided. Reported p-values correspond to a two-tailed paired Student's *t*-test for each trial compared to the reference measurements – data were paired by segment for these tests. The image label 'MC' indicates motion correction.

Image	LV Thickness Mean ± SD [mm]	p
Reference	14.3 ± 1.8	-
Axial	17.5 ± 1.4	0.0002
Axial – MC	14.6 ± 1.7	0.4
Lateral	15.8 ± 1.9	0.009
Lateral – MC	14.7 ± 1.7	0.13
Diagonal	18.3 ± 1.6	0.0009
Diagonal – MC	15.1 ± 2.0	0.02

The analogous LV thickness measurements within the clinical dataset are shown in Table 4.2. The changes were relatively small with a mean, minimum and maximum paired difference of -0.2 mm, 0.0 mm, and -1.0 mm, respectively. Negative values imply smaller thicknesses after motion correction. The most substantial changes in thickness were observed for the stress scans of patients B and C: -0.6 ± 0.5 mm, and -0.7 ± 1.3 mm, respectively. Statistically, only the stress scan of Patient B corresponded to a significant difference ($p = 0.0002$). The measurements of the stress scan of Patient C, however, indicate a trend toward narrower LV thicknesses after motion correction ($p = 0.05$). Several metrics of patient motion were also tabulated for the cohort to provide context for the thickness measurements. The number of recorded motion-triggers, the number of motion-frames, and the Euclidean magnitude of the maximal displacements are shown in Table 4.2.

Table 4.2 LV thicknesses measured for the clinical dataset averaged among all 16 segments. Standard deviations (SD) are also provided. Reported p-values correspond to a two-tailed paired Student's *t*-test for acquisition between non-corrected and corrected images – data were paired by segment for these tests. Patients were labelled with the characters A, B, and C, and the physiologic state of each acquisition is indicated. Patient motion indicators such as the number of triggers and motion frames as well as the maximum displacement magnitudes are also provided

Scan	Mean LV Thickness \pm SD [mm]			Patient Motion		
	Non-Corrected	Corrected	p	No. Triggers	No. Motion Frames	Max Displacement Magnitude [mm]
Patient A: Rest	19.1 \pm 1.8	19.1 \pm 1.8	0.6	14	6	5.8
Patient A: Stress	19.6 \pm 1.5	19.5 \pm 1.5	0.8	42	11	12.8
Patient B: Rest	18.1 \pm 1.3	18.1 \pm 1.4	0.9	35	6	8.1
Patient B: Stress	18.5 \pm 1.3	17.9 \pm 1.2	0.0002	67	17	11.2
Patient C: Rest	22.0 \pm 2.8	21.8 \pm 2.6	0.5	43	8	9.8
Patient C: Stress	22.4 \pm 2.3	21.7 \pm 2.2	0.05	42	8	11.2

The LV blood volume measurements for the clinical data set are shown in Figure 4.9. Volumes range from 23 cm³ to 61 cm³ among this cohort. In all cases other than of the rest scan of Patient B, the volumes were observed to increase after applying motion correction. The mean paired difference and standard deviation between the Non-Corrected and Corrected image measurements was 1.0 \pm 1.6 cm³. The average increase in volume was not statistically significant. Moreover, the changes were relatively small compared to absolute values of the volumes. The changes, after applying motion correction, ranged from -3% to 7%.

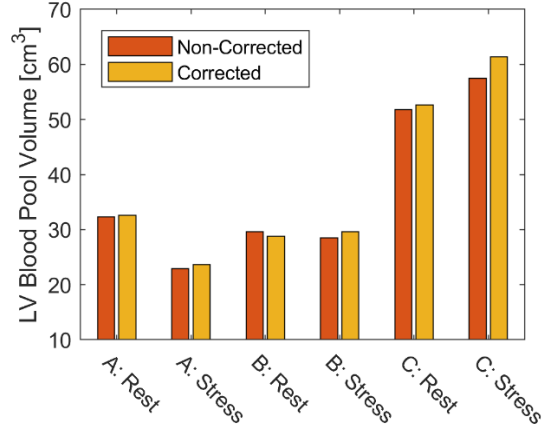


Figure 4.9 LV blood pool volume measurements for each of the clinical acquisitions. Values from the Non-Corrected and Corrected images are shown in red and yellow, respectively.

4.3.3 Effects of Motion Correction on CNR

Example short axis slices of the phantom images are shown in Figure 4.10. The image corresponding to the Reference image is repeated on each row of the matrix to make visual comparison easier. The non-corrected images demonstrate obvious motion artifacts, namely blurring and reduced contrast in the LV compared to the surrounding regions. These effects are largely compensated for following motion correction. Quantitatively, marked losses in CNR were observed for the non-corrected phantom images which was largely recovered by applying motion correction. Figure 4.11(A) shows the measurements for each trial both before and after motion correction. Non-corrected images exhibited reductions of 43%, 34%, and 45%, whereas reductions of only 7%, 14%, and 9%, were observed for motion corrected images of the axial, lateral, and diagonal motion cases, respectively.

The effects of motion correction within the clinical data set were much more subtle than in the phantom measurements. The example images from the stress scan of the three

patients are shown in Figure 4.12. Motion correction led to an average (percent) increase in CNR of 11.3%, with a minimum and maximum of -13.9% and 61.2%, respectively.

The CNR measurements for each individual image are shown in Figure 4.11(B).

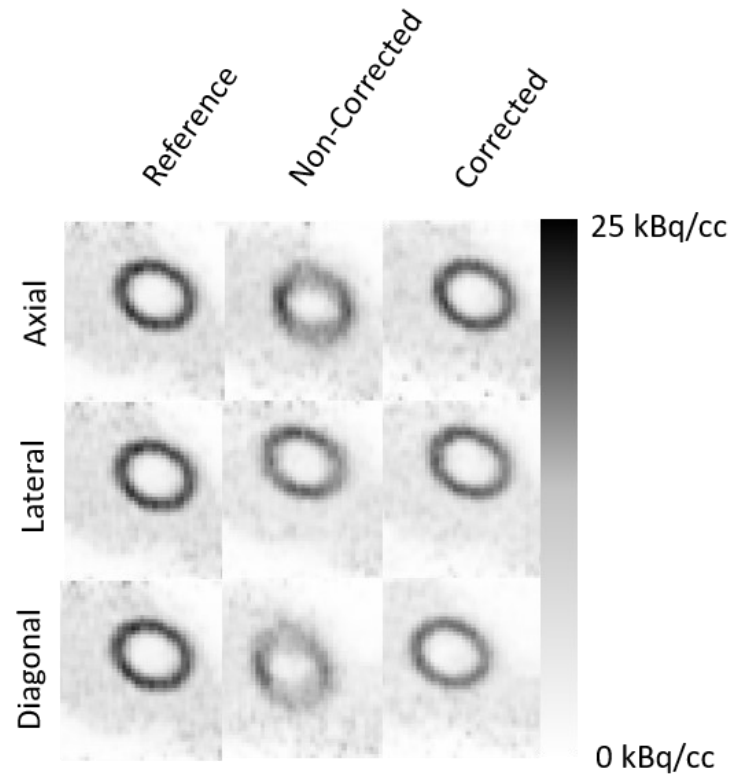


Figure 4.10 Example short axis images from the four phantom acquisitions. The Reference, Non-Corrected, and Corrected images for each motion case are shown to emphasize the effects of motion correction on this data set. All images are displayed on the same intensity range. This figure has been reused¹⁶⁷ with permission; original copyright 978-1-5386-8495-5/18 ©2018 IEEE.

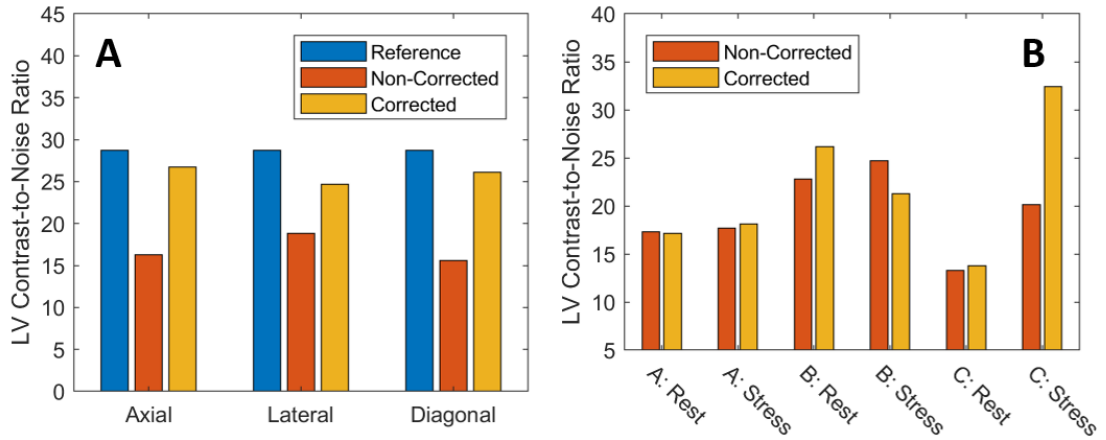


Figure 4.11 CNR bar plots for the phantom (A) and ^{13}N -ammonia (B) acquisitions. Reference, non-corrected and motion-corrected data are shown in blue, orange, and yellow, respectively. Note that in sub-figure A, the Reference column is repeated for each of the three motion cases. In sub-figure B, individual patients are indicated by the character labels A, B, and C and the physiological state or rest or stress is also indicated.

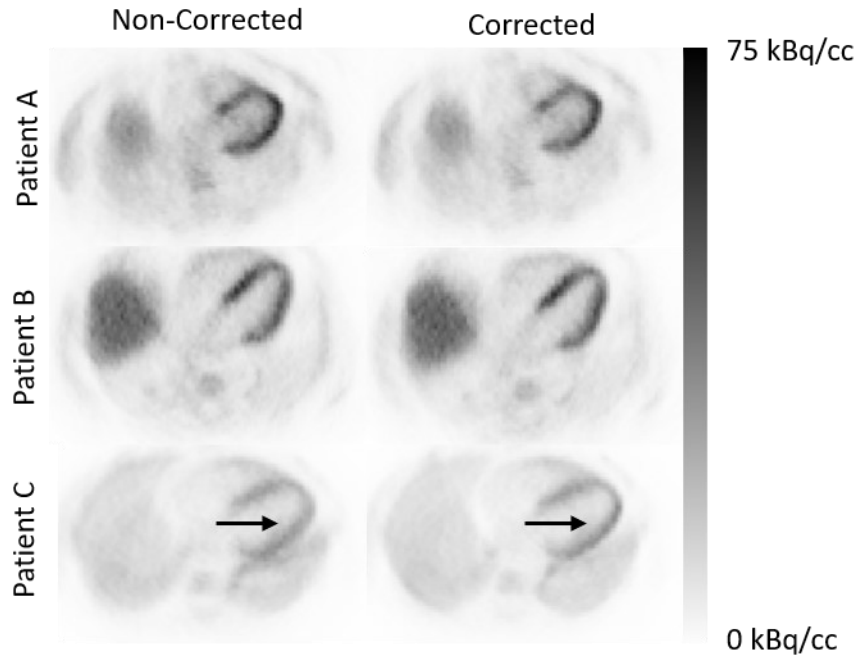


Figure 4.12 Example images of the stress scans of the clinical data set. Non-corrected and corrected images are shown in the first and second columns, respectively. All images are displayed on a common intensity range. The arrows on the images of Patient C demark the most pronounced intensity change associated with motion correction. This case demonstrated the largest maximum displacements among the clinical data set.

4.3.4 Relative Perfusion and Left-Ventricular Volumes

The relative regional and global perfusion measurements are shown in Table 4.3. Across all domains, the measurements made from the Non-corrected and Corrected images are in good agreement which suggests that motion corrections had no effective impact on relative perfusion values in this clinical data set. The mean paired differences between the non-corrected and motion-corrected images, averaged across all six acquisitions, are all less than 1% for each of measurement domains.

Table 4.3 Mean relative myocardial perfusion in the LV among the clinical dataset of this study. Measurements are reported within the LAD, LCX, and RCA territories as well as for the entire LV. The measurements were made from the non-corrected and motion-corrected images.

Scan	Reconstruction	Mean Relative Perfusion \pm SD [%]			
		LAD	LCX	RCA	LV
A: Rest	Non-corrected	71 \pm 11	81 \pm 7	72 \pm 6	74 \pm 12
	Corrected	71 \pm 11	81 \pm 7	71 \pm 7	73 \pm 11
A: Stress	Non-corrected	75 \pm 11	80 \pm 7	77 \pm 7	76 \pm 10
	Corrected	73 \pm 11	78 \pm 7	75 \pm 7	74 \pm 11
B: Rest	Non-corrected	86 \pm 11	91 \pm 5	84 \pm 5	87 \pm 9
	Corrected	89 \pm 9	89 \pm 4	83 \pm 5	86 \pm 8
B: Stress	Non-corrected	82 \pm 12	79 \pm 6	82 \pm 8	81 \pm 10
	Corrected	81 \pm 13	81 \pm 6	82 \pm 8	80 \pm 11
C: Rest	Non-corrected	86 \pm 8	93 \pm 4	83 \pm 7	86 \pm 9
	Corrected	87 \pm 7	94 \pm 4	83 \pm 7	87 \pm 9
C: Stress	Non-corrected	81 \pm 7	92 \pm 6	83 \pm 7	84 \pm 9
	Corrected	82 \pm 7	96 \pm 4	83 \pm 7	86 \pm 9

4.4 Discussion

In the original paper in which PeTrack was first described⁹⁰, Xu and colleagues demonstrated a tracking precision of 0.27 mm when 62 LORs (on average) were used for localization in simulation studies. In their study, the active radionuclides that were considered were ¹²⁴I, ⁸⁴As, and ⁸⁴Rb and the measurements were made within a radiation

therapy context using a custom detector system consisting of two pairs of position-sensitive scintillating crystal arrays. While a meaningful comparison between the tracking precision observed in this study to that of Xu et al. cannot be made, the stated tracking precision of 0.27 mm serves as a useful benchmark. The tracking precision was estimated in this work using the motion traces of the phantom experiments. From the Reference acquisition where no motion existed the precision was estimated as the standard deviation from the first 60 s (120 samples) of the acquisition. In the left-right, anterior-posterior and inferior-superior directions, tracking precisions were 0.31 mm, 0.26 mm, and 0.25 mm, respectively. The mean number of LORs per tracking instance, averaged across the first 60 s, was 124 ± 11 . In the first reported use of PeTrack within the context of PET, Chamberland and colleagues¹⁶⁶ reported a 3D precision of 0.8 mm. The addition in quadrature of the individual components stated above yields a 3D precision estimate of 0.47 mm. From this it seems that the tracking precision achieved within the present phantom experiments is in good agreement with previous studies of the PeTrack tracking method. Qualitatively, the tracking precision of the left-right (or lateral) component of the Diagonal motion case appears to exhibit reduced precision, particularly in the first 60 seconds of the acquisition. Indeed, the tracking precision for this segment of the motion was 0.76 mm, more than twice that observed for the reference acquisition. The mean number of LORs per tracking instance within this time frame was 81 ± 10 , which based on previous PeTrack studies should generally provide sufficient tracking quality. Nevertheless, the exact reason for the reduction in tracking precision for this acquisition remains unclear.

In the Bland-Altman plot shown in Figure 4.7(B) a trend is apparent that suggests that when the magnitude of the mean displacements increase, the image-based measurements are low compared to those of PeTrack. This effect manifests as a negative slope among the data points shown on this plot. The reason for this is most likely associated with attenuation correction artifacts for the frames that deviate furthest from the reference position, at which adequate attenuation correction was expected. This result is not surprising as no motion correction was implemented for this dynamic reconstruction to minimize CTAC artifacts.

In the original conference record publication¹⁶⁷, the CNR measurements of the phantom scans used a background VOI within the model LV blood pool, but this led to confounding measurements as there was no tracer injected into this region. As a result, as the initial injected activity within the LV decayed there was no similar decay within the background region which reduced the relative improvement in CNR due to motion correction. Therefore, the CNR measurements were repeated using a background VOI that contained water in the body of the phantom in which a uniform activity distribution existed. Nevertheless, only a single injection into the phantom was performed for the four acquisitions that were performed. While the ^{18}F -based tracer has a relatively long half-life of 1.83 hours, non-negligible tracer decay occurred over the course of the experiment that was not compensated for prior to comparing CNR values between the reference and subsequent motion cases. In a simple model of a radioactive signal amid a lower activity background, of the same radioisotope, the CNR can be shown to decay at half the rate of this signal itself. An example of the model is shown in Figure 4.13 where the signal and background are associated with the β^+ decay of ^{18}F . The solid curve of the figure

represents the activity of the signal region as a function of time, the dashed line corresponds to the CNR (normalized to the initial value), and the markers indicate the expected CNR at the start time of each of the phantom acquisitions with respect to the start of the Reference scan. Simply due to decay, the CNR of the Axial, Lateral and Diagonal acquisitions are reduced compared to the Reference by approximately 4%, 8%, and 12%, respectively. These relative losses correspond to dominant proportions of the reductions in CNR stated previously for the motion-corrected images. While these effects apply equally to the non-corrected images, they represent a smaller fraction of the measured losses.

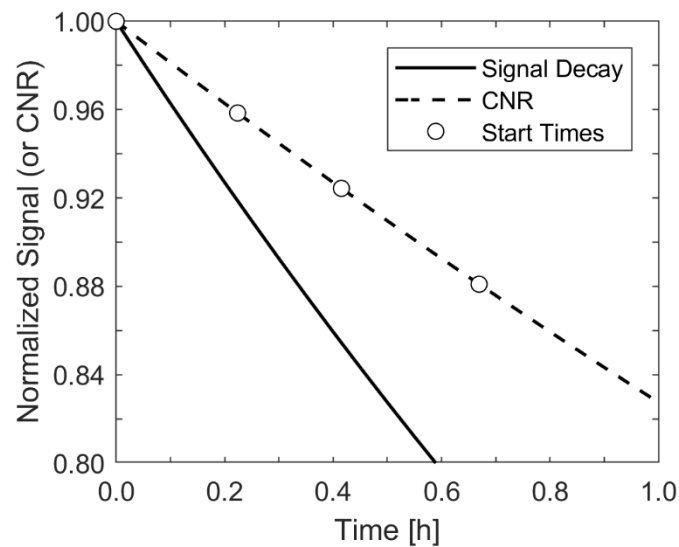


Figure 4.13 Effect of radioactive decay between phantom acquisitions on CNR. The signal decay, CNR and acquisition start times are indicated by the solid line, dashed line, and markers, respectively. All data have been normalized to their respective initial value to focus on their relative changes over time.

In contrast to the relatively large increases in CNR observed for the phantom experiment following motion correction, the effects of motion correction within the clinical dataset are much less substantial. The primary reason for this is that the patients

in the clinical dataset were selected randomly and were not screened for patient motion. The phantom experiments exhibited motion displacements up to approximately 20 mm in magnitude. As a reference of scale, the typical LV wall thickness is roughly 10 mm. Moreover, the phantom motion was persistent in moving away from the reference location. In clinical studies, however, patient motion has been found to exhibit motion that either non-returning or returning motion.¹⁴² The latter type of motion implies that a displacement from the reference position is transient which mitigates the effects of motion. Indeed, within this cohort the mean displacements (averaged across the acquisition duration) were typically less than 1 mm. The root-mean-squared displacements ranged from 1.3 – 4.7 mm but are not indicative of the changes in the direction of motion throughout the acquisition. Thus, it appeared as though patient motion was transient and, on average, the patients deviated only marginally from the reference position. Due to the limited extent of motion within this group, the detection of changes among the metrics indicated previously between Non-Corrected and Corrected images was limited.

The maximal displacements, among all Cartesian directions, observed for each acquisition indicated that the stress acquisitions had larger maximal displacements than those of rest: 10.1 – 12.3 mm compared to 5.1 – 8.1 mm, respectively. These maximal displacements agree with those reported previously by Hunter et al.⁸² The stress scans of Patients B and C exhibited the highest maximal displacements, largely along the right-left direction. Not surprisingly, it was for these two acquisitions that the largest changes in LV thickness were observed between the non-corrected and motion-corrected images.

This effect was also mirrored by a substantial increase in CNR for Patient C, but not, however, for the stress acquisition of Patient B.

The relative perfusion and LV volume measurements seemed quite insensitive to the choice of non-corrected or motion-corrected image reconstructions. Across the LV, or individual LV territories, the standard deviations ranged from 4% to 11%. It may be that the intra-subject perfusion variation is sufficiently high to mask the effects of mild motion. An effect of patient motion within cardiac PET imaging is to blur regions of reduced uptake, which could correspond to disease, in such a way as to mask the severity of the reduced perfusion. Within this cohort, as shown in Table 4.3, there did not appear to be any cases of markedly reduced perfusion in a particular territory. While LV blood pool volumes were shown to increase after applying motion correction, the changes were relatively small compared to the Non-corrected volumes. In future work, the inclusion of patients with suspected or confirmed coronary artery disease would be useful for evaluating the potential of the motion correction approach for enhancing the perfusion defects.

This method was designed to address whole-body patient motion, but it is not yet clear how other types of motion could potentially limit the performance of the PeTrack motion correction algorithm. In principle, severe respiratory motion (as measured with the external marker) could give rise to motion triggers and thus confound the proposed body-motion detection approach. The use of a sliding window smoothing kernel is expected to limit the sensitivity of this approach to respiratory motion. As was shown in Chapter 3, the IQR of the respiratory rates observed (roughly across all gating methods) ranged from 10 – 20 breaths/min. These rates correspond to breath periods in the range of 3 – 6 s. As

the sliding window span was 5 s, we expect that the respiratory signal of the marker will be suppressed for most patients and most respiratory cycles. That said, future work remains to demonstrate this assertion. Moreover, both whole-body and respiratory motion could be characterized for each acquisition and dual body-respiratory motion correction could be implemented.

4.5 Conclusions

In this study the feasibility of whole-body motion correction using 3D motion information derived from tracking radioactive markers using the PeTrack algorithm was demonstrated. The phantom experiments provided strong evidence that rigid whole-body motion correction based on motion tracking with PeTrack can significantly reduce the blurring artifacts associated with patient motion.

PeTrack was shown to exhibit 3D motion information of the marker during ^{13}N -ammonia cardiac perfusion PET studies that was in excellent agreement with image-based measurements. Within this small sample of patients with limited motion, image quality was not obviously degraded by motion artifacts and thus motion correction was not found to improve image quality or have impact on relative perfusion measurements in the LV. Future investigations are warranted to assess the impact that this motion correction algorithm may have in the clinic, not only in static imaging but also dynamic protocols where inter- and intra-frame patient motion need to be considered to improve the precision of absolute blood flow quantification.

Chapter 5 Whole-Body Motion Correction for Absolute Blood Flow Quantification

The content of this chapter represents an extension of the methods developed in Chapter 4 in the context of dynamic myocardial perfusion imaging studies wherein kinetic modelling is employed to calculate left-ventricular absolute blood flow. The work described here has not been published or presented previously.

5.1 Motivation

Given the growing body of evidence that suggests that body motion should be accounted for in cardiac PET/CT studies and given the observed limitations of frame-wise correction methods, we sought to investigate two data-driven methods for motion correction prior to kinetic modelling in cardiac perfusion PET/CT studies to estimate absolute myocardial blood flow (MBF). Refer to Section 1.3.3 for details and definitions regarding MBF estimation. In the proposed framework we exploit the high temporal resolution of data-driven tracking methods to detect intra- and inter-frame motion. Additionally, we also designed our MC approach to address the problem of mis-registration between PET emission data and attenuation correction data which is derived from a static CT acquisition. Two data-driven motion tracking/detection systems were employed and compared. These consist of the positron emission tracking (PeTrack) algorithm¹⁶⁷ and the centroid of distribution (COD) method.¹¹⁹ Both methods use only list-mode data from the PET scanner to generate a motion tracking signal. They differ, however, in that the former tracks the motion of low-activity point sources placed on the patient while the latter uses only emission data from the radiotracer. While other data-

driven motion tracking approaches have been proposed or demonstrated to detect body motion^{117,171}, they are technically similar to the COD approach and were not implemented for this study.

5.2 Methods

5.2.1 Centroid of Distribution (COD) Motion Tracking

The COD algorithm described in the work of Lu and colleagues¹¹⁹ was implemented for this study with only minor modification. This data-driven approach to tracking patient motion is based on calculating the mean position of the most likely annihilation (MLA) points (calculated from TOF) from a set of LORs belonging to a specific time interval. This calculation is repeated for each adjacent time window throughout the acquisitions to derive a 3D motion trace of the centroid. This technique is advantageous in that it relies only on the tracer activity administered to a patient and is relatively fast to compute as it does not employ iterative methods. Generating a motion trace from list mode data typically required 1 minute of processing time using a standard desktop workstation.

In its original implementation for tracking body motion, all LORs acquired by the PET system were used for tracking. Lu and colleagues¹¹⁹ developed this method using animal and human PET studies which considered several different ¹⁸F-based tracers with various targets within the torso. Since the imaging target of this work is the heart, LORs that were unlikely to have originated within a cubic volume of interest (VOI) centered about the heart were excluded from the centroid calculation. Additionally, the time interval used for each centroid calculation was fixed at 1 second in its original implementation. In this study, a tracking interval of 0.5 s was used to match that which is used for PeTrack.

The VOIs were created manually for each acquisition included in this study using a custom graphic user interface developed using MATLAB (MathWorks®, Natick, Massachusetts, USA). The VOIs were drawn on static uptake images where the myocardium has a relatively high contrast compared to the extracardiac space. The VOIs were intentionally drawn larger than the heart to allow for motion of the heart within that space. LORs in any time interval were initially excluded if their MLA points did not fall within the VOI. A one-dimensional probability density function (PDF) was used to describe the distribution of the possible annihilation location along a LOR. The PDF was integrated within the limits set by its intersection points of the VOI to determine the probability that the LOR originated from within the VOI. The PDF was assumed to be a Gaussian function centered at the MLA point with a FWHM of 80 mm, to match the TOF resolution of the Discovery 690 PET/CT system that was used to acquire the data (see Table 1.2). The probability cut-off was chosen to be 10% after evaluating the COD motion traces using various values ranging from 0 – 50%. The cut-off of 10% was shown to provide a reasonable balance between signal noise and accuracy. This LOR rejection method is illustrated in Figure 5.1. The phantom studies described in Chapter 4 were used for this assessment. Examples of these traces are provided in the results, Section 5.3.

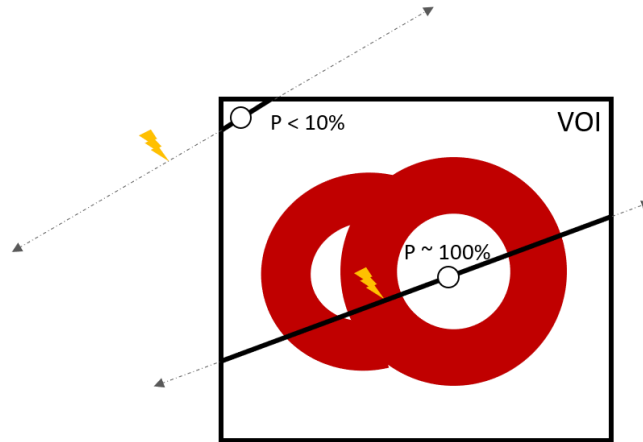


Figure 5.1 Schematic representation of the acceptance/rejection method used to determine the set of LORs used for COD tracking. The volume of interest (VOI) was drawn about the heart (shown in red) as a black rectangle. Two LORs are drawn as dashed arrows originating from the annihilation locations indicated by the lightning bolts. While the true annihilation locations cannot be known, they are indicated here for demonstration purposes. The most-likely annihilation (MLA) points are indicated as empty circles. While both LORs have MLA points within the VOI, the probability of the LOR shown in the upper left is small and is thus rejected. The other, however, likely originated within the LV myocardium and has high probability of being included.

The use of the COD algorithm has only been evaluated when the tracer has equilibrated within the imaging target, i.e. when tracer concentration has reached a steady state. This is achieved either with delayed start of the acquisition following administration of the tracer or by excluding emission data acquired before some predefined time-period. The reason for this is to not misinterpret normal tracer dynamics in the body with patient motion. In this study however, the COD traces were not limited to the steady-state (or uptake) portion of the acquisition as patient motion in the early frames can affect the image derived blood input function used for kinetic modelling.¹⁷²

5.2.2 Whole-Body Motion Detection

A novel motion detection algorithm was developed for this study which was applied to both PeTrack and COD motion traces. It was designed to detect and record instances along the motion trace which corresponded to patient motion. These instances of motion are referred to hereafter as body motion triggers, or triggers. Several different approaches were developed for this purpose, which employed either physical threshold, signal processing techniques or statistical arguments to indicate that a relatively significant change in the position of the motion trace has occurred. They were developed with the use of the phantom studies described in Chapter 4 where the motion triggers were known a priori. The final method was chosen as that which indicated the best agreement between the PeTrack and COD tracking approaches.

The selected approach is a graphical method which is closely related to measurements of the velocity components of each 1D component on the motion trace. In this approach the position and time were treated as generalized coordinates. A linear fit of these the position and time coordinates was performed on each component within a 20 s sliding window. The elevation angle of the fitted line, which represents the degree of change in the position, was measured between the vector normal to the line and the positive vertical direction, i.e. the generalized vector which has components in the time and position domains of 0 and 1, respectively. The spatial and temporal units of the motion traces were millimeters and seconds, respectively. This approach is similar to imposing thresholds on the average velocity of each component computed over the duration of the sliding window. Figure 5.2 provides an example 1D motion trace on which the normal vectors are overlaid for each sliding window position.

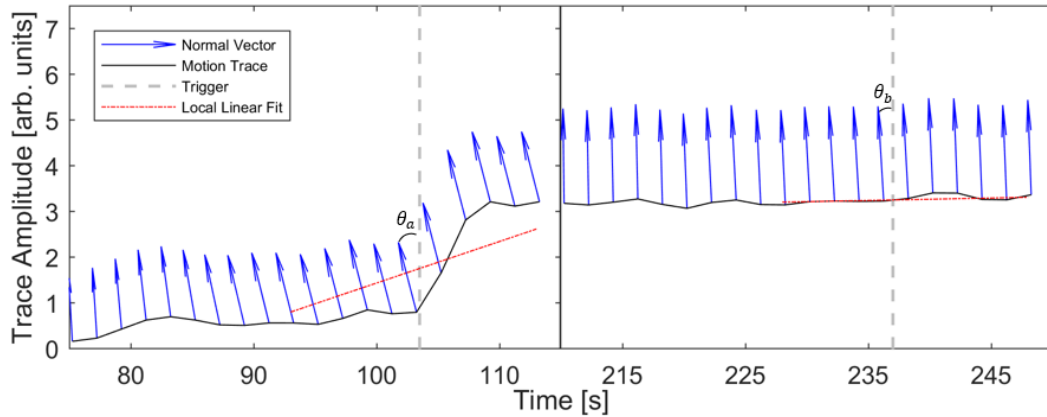


Figure 5.2 Example motion detection where the processed trace is depicted along the calculated normal vector. Only the anterior-posterior component of the motion trace is shown. The time domain is split to isolate two body motion triggers (dashed vertical lines) that were identified at 103 s and 238 s. The trigger at 103 s (trigger ‘a’) corresponds to change in position with a relatively steep gradient, whereas the trigger at 238 s (trigger ‘b’) corresponds to a low gradient, steady change in position. The local linear fits at each of the triggers are shown by red dashed lines. The angles between the generalized vectors and the vertical direction are indicated as for each trigger. Note that the length of the arrows is arbitrary as they are scaled automatically to ensure the arrow tips do not cross adjacent arrows.

The window was incremented with a step size of 0.5 seconds until it reached the end of the acquisition. When motion was detected, a body motion trigger was inserted at the mean temporal position of the window. Motion was considered to be present if either of the following criteria were met: the instantaneous deflection angle exceeded a threshold (θ_1), or when the accumulated deflection angle exceeded a threshold (θ_2). Note that the accumulated deflection angle was initialized at 0° and was modified by each time window; it was reset to 0° if it reached θ_2 and accumulation began again. These two events correspond to rapid changes and gradual drifts of the position in each direction of motion. The two thresholds were initially selected by assessment of the performance of both tracking methods to correctly identify triggers in the phantom studies. The phantom-derived deflection thresholds (θ_1 , θ_2) were set as 15° and 90° , respectively. Note that $\theta_1 =$

15° is equivalent to an average velocity of 0.27 mm/s over the sliding window duration, whereas the $\theta_2 = 90^\circ$ could be reached, for example, if an average velocity of 0.016 mm/s were maintained over a 70 s period.

The phantom-derived thresholds were ultimately found to be unsuitable for human studies due to the abruptness and magnitude of the motion in the phantom studies. A small set of studies which exhibited either abrupt and/or gradual motion, as observed in the motion traces, were used to determine the deflection thresholds for human studies. The instantaneous deflection threshold (θ_1) was adjusted to be 24° (or 0.45 mm/s), although in practice only gradual motion (accumulated deflection $\geq 90^\circ$) appeared to be relevant.

The motion traces were filtered at the outset to make motion detection less susceptible to noise. The signals were convolved with an averaging kernel with a span of 5 seconds. An additional low pass filter was employed for the human studies, to reduce the impact of respiratory motion on body-motion detection; the cut off frequency was chosen as 0.17 Hz, which removes signal components with periods less than 6 seconds.

Motion triggers were produced independently within each dimension of the 3D motion traces. Triggers associated with each direction of motion were concatenated into a single set. Triggers from different directions of motion that agreed with each other were merged. In the event that a pair of triggers were separated by 5 seconds or less, only the first of the two was kept. Triggers that were identified in the first 10 seconds of an acquisition were ignored as in some cases signal artifacts were present as a result of the low pass filter due to the finite dataset. The first 10 seconds of an acquisition, which

immediately followed tracer administration, was observed to be very count deficient and so ignoring triggers in this window was expected to be of little to no effect.

5.2.3 Motion Estimation and Correction

Motion correction was performed in a two-step process. Patient motion was first estimated and subsequently incorporated into the reconstruction workflow to correct it. In the following we describe the motion correction framework and then the motion estimation approaches.

The original list-mode data were divided into a set of ‘motion frames’ that was determined by a combination of the body-motion triggers (t_{bm}) identified in the motion detection step and the start times of the dynamic frames used for clinical reconstructions. Body-motion triggers were inserted into the list of the frame start times of the dynamic series. When a body-motion trigger was within 2.5 seconds of a dynamic frame start point, the start point was adjusted to match the trigger. If the trigger was further than 2.5 seconds from the nearest start point a new frame was created which began at the trigger and ended at the earlier of either the next body-motion trigger or dynamic frame start time. The original dynamic frame definitions are retained in the workflow and are considered as parents to all motion frame children that exist within their duration. The way in which the motion frames are combined to return to the original parent dynamic frames is described later in the section.

Two motion estimation methods were considered for use in this study to derive the transformation parameters. In the first approach, motion estimates were based on the direct use of the 3D displacements determined from the motion tracking results. The

frame-wise displacement for each motion frame was calculated from the motion trace displacement with respect to the reference position averaged across the frame duration.

In the second approach, the transformation matrices were produced from a 6D rigid image registration of non-attenuation corrected images. Non-attenuation corrected images were used to avoid the propagation of potential PET/CT mis-alignment artifacts into registration errors.¹¹⁹ Given that the activity distribution is not fixed for dynamic PET acquisitions that commence with tracer administration, a sequential image registration approach was employed. This approach is based on the assumption that the adjacent frames in a dynamic acquisition are more similar than a pair of temporally distant images and thus registration should be more accurate. To make this explanation more explicit, consider a dynamic reconstruction that contains n frames and the reference was chosen as the n^{th} frame. Then in a sequential registration, the first frame is registered to the second, the second to the third, and so on, until the $(n-1)^{\text{th}}$ was registered to n^{th} , reference frame. To align the first frame to the reference, one would need to apply all $(n-1)$ transformations or compose each and apply a single transformation. Sequential registration for dynamic images where the tracer distribution has not equilibrated has been reported elsewhere.^{119,173}

In this work, the reference images were selected as the frame that occurred later than 2 minutes after the acquisition, with greatest number of counts. This time window corresponds to images with myocardial uptake and clearance of the activity in the blood pool. This reference image was chosen to help ensure good alignment with the CT images used for attenuation correction which were manually aligned to the static uptake images by technologists at the time of the original PET acquisitions. The frame in the

uptake window with the greatest number of counts was expected to be most like the static images.

Image registrations were performed using the Elastix software package.¹⁷⁴ Mutual information was chosen as similarity metric between the moving and references images. A multi-resolution registration using a gradient descent optimization algorithm was used to estimate the transformation parameters. More complex motion models such as affine and non-rigid were also initially considered for use but did not provide robust motion estimates. This was observed during registration of the motion frames of the phantom scans described in Chapter 4, where the manually applied motion was well known. In these tests, non-rigid motion models were not able to reproduce the expected translations. Regarding the choice of similarity metric, mutual information^{175,176} evaluates the entropy in the joint distribution of grey-level values observed in two images. With respect to registration, it is hypothesized that the mutual information is maximized when the like structures are aligned as the joint histogram exhibits the highest level of organization, or lowest entropy. Mutual information serves as a useful similarity metric between images that do not have similar intensity and has thus been used for image registration between different modalities^{177,178} or for dynamic data sets.^{119,179} There were numerous user-specified input parameters that can impact the outcome of the registrations results which related to the choice of transformation model, similarity metric, interpolation, and optimization. Following the recommendations of the user documentation, many default parameters were specified. The input parameter file that was used to specify all nondefault parameters is included as Appendix B.

Prior to reconstruction, the static CT image used for attenuation correction was transformed using the inverse of the transformation matrices used to align the PET motion frames to achieve accurate attenuation correction of each reconstructed frame. Following the reconstruction of the set of motion frames, each were aligned with the reference frame by applying the forward transformation matrices. They were subsequently combined into the original dynamic frame sequence by computing the weighted average of any new motion frames which fell within the duration of an original dynamic frame to form the final, motion-corrected dynamic series. The weights used in the weighted average corresponded to the relative number of coincidence counts observed in each frame compared to the total in the entire list mode data set. As an example, consider an acquisition which took place over 360 s with dynamic frames of 120 s duration beginning at 0, 120, and 240 s. If body-motion triggers were detected at 30 and 90 s, it follows that the parent frame beginning at 0 s would be divided into three motion frames (with start times of 0, 30, and 90 s). In total, 5 motion frames would be reconstructed but the motion frames starting at 0, 30, and 90 s would be combined via weighted averaging to produce the motion corrected parent frame beginning at 0 s and ending at 120 s. The remaining parent frames would also be motion corrected but would not require recombination.

Note that weights based on counts help to suppress noise in the average frame, but this could come at the expense introducing bias in the pixel values when tracer decay between motion frames was relatively significant. Alternatively, weights based on frame duration would be more accurate, but the added noise could make image registration more challenging. The need for reconstruction of individual motion frames was a limitation of

the vendor reconstruction software as it was not possible to incorporate motion estimations directly into the reconstruction algorithm as has been described in other work related to body motion correction.^{119,180}

5.2.4 Clinical Dataset

To evaluate our proposed MC framework and compare these two data-driven motion tracking approaches a combination of phantom and clinical scans were used. All data were acquired at the University of Ottawa Heart Institute, Ottawa, on a GE Discovery 690 scanner²⁷ (Waukesha, WI). The anthropomorphic torso phantom acquisitions that were described in Section 4.2.2 were used in this study to develop the motion detection method and also for validation of the implementation of the Elastix image-registration software.

The clinical data consisted of 9 patients that underwent ^{13}N -ammonia (NH_3) or ^{82}Rb myocardial perfusion studies at rest and/or stress. In total 17 acquisitions were included, five ($N = 5$) $^{13}\text{NH}_3$ acquisitions from three patients, and twelve ($N = 12$) ^{82}Rb acquisitions from six patients. The 6 patients that underwent ^{82}Rb perfusion studies are referred to as patients ‘A’ – ‘F’, whereas the 3 patients that underwent $^{13}\text{NH}_3$ perfusion studies are referred to as patients ‘G’ – ‘I’. Note that some of the data sets included here were used previously in Chapter 4. Patients H and I in this chapter corresponds to patients B and C, respectively, in Chapter 4. Acquisitions were 20 minutes and 8 minutes in duration for $^{13}\text{NH}_3$ and ^{82}Rb studies, respectively. Physiologic stress was induced using intravenous injection of dipyridamole. The dose protocols at our institution for these studies are 3 MBq/kg and 9 MBq/kg for $^{13}\text{NH}_3$ and ^{82}Rb , respectively. Low dose CT scans were

acquired prior to each PET acquisition for attenuation correction. In our clinic technologists perform a manual 3D co-registration between an initial static reconstruction and the CT image used for attenuation correction. These translations were used in this work to define the reference position of the patient that provides good emission/transmission overlap.

In all cases image reconstructions were performed offline using research reconstruction software supplied by the vendor. An OSEM algorithm was used (4 iterations and 24 subsets) which included corrections for random and scatter coincidence events, and attenuation correction. For each acquisition included in this study five types of dynamic image reconstruction were considered: dynamic without motion correction (NMC); motion correction using PeTrack (PT); and motion correction using COD (CD). Note that two approaches of motion estimation were employed for both PeTrack and COD. The resulting images correspond to PT3D, PT6D, CD3D, and CD6D where the label '3D' corresponds 3D motion estimation using the motion trace directly and '6D' corresponds to the use of 6D rigid image registration for motion estimation. The dynamic frames were pre-defined based on the standard imaging protocols used at UOHI. For ^{82}Rb perfusion studies they consisted of 14 frames (including the first 6 minutes of each acquisition) configured as 10×10 s frames, 1×30 s frame, 1×60 s frame, and 1×120 s frame. The $^{13}\text{NH}_3$ perfusion studies consisted of 17 frames configured as 9×10 s frames, 3×30 s frames, 1×60 s frame, 1×120 s frame, 1×240 s frame, and 2×300 s frames.

The visual motion assessment of the NMC images was performed using a 3D DICOM image viewer which displays transverse, coronal, and sagittal views simultaneously. Motion of the myocardium and the radioactive fiducial marker were both considered.

Additionally, it was noted whether patient motion exhibited returning behaviour, i.e. was a given change on patient position followed by a another with similar magnitude but reversed direction.

5.2.5 Verification of COD Tracking and Image Registration Methods

Initial testing was performed to verify that the COD tracking method was implemented correctly and determine the probability threshold associated with the exclusion of LORs from the cardiac VOI. The COD traces were initially produced for the phantom acquisitions described in Chapter 4. This test was largely qualitative to confirm that COD tracking could accurately estimate the translations that were manually applied to the phantom during the reference (no motion) and axial motion acquisitions. To determine a suitable probability threshold associated with excluding LORs from the cardiac VOI, COD tracking was performed multiple times for a range of probability cut-off values and the effect on mean and standard deviations of the observed translations was measured. The best probability cut-off was chosen as that which exhibited the best trade-off between noise and accuracy.

The image registration software was also configured and tested using the phantom acquisitions. The phantom acquisition that contained only axial translations was used to assess the quality of the image registration's estimates. Given the high precision that was demonstrated by PeTrack to measure the motion in this acquisition (see Section 4.3.1), its recorded translations were used for comparison against those from image registration. Each of the frames corresponding to one of the five phantom positions was registered directly to a reference frame and the translation between each with the reference frame

were recorded. This process was repeated five times with each motion frame serving as the reference frame in turn. The registration accuracy was measured as the root mean square error ($RMSE_{reg}$) between the translation indicated by PeTrack with those from the registration among all five trials. The variability of the registration process due to changes in the reference frame was considered as the precision of the registration. The translation values for each trial were shifted as though the first frame was the reference. The precision of the registration was measured as the mean absolute difference (MAD) of the shifted translation of each motion frame with the first. The definitions of the $RMSE_{reg}$ (accuracy) and MAD (precision) are defined as

$$RMSE_{reg} = \sqrt{\frac{1}{N_F N_T} \sum_{i=1}^{N_F} \sum_{j=1}^{N_T} (\Delta z_{ij}^{IR} - \Delta z_{ij}^{PT})^2} \quad \text{Eq. 0.1}$$

$$MAD = \frac{\sum_{i=2}^{N_F} \sum_{j=2}^{N_T} |\Delta z_{ij}^{IR'} - \Delta z_{i1}^{IR'}|}{(N_F - 1)(N_T - 1)} \quad \text{Eq. 0.2}$$

where $N_F = 5$ and $N_T = 5$ represent the number of frames and trials, respectively. The translation between the i^{th} frame with the reference frame of the j^{th} trial is denoted as Δz_{ij}^{IR} and Δz_{ij}^{PT} , for the image registration and PeTrack estimates, respectively. Lastly, $\Delta z_{ij}^{IR'}$ represents $\Delta z_{ij}^{IR} - \Delta z_{1j}^{IR}$, the estimated translation between frame i and the first frame, calculated as the difference between the translations of the two frames to the reference frame with trial j as reference. Note that in the MAD calculation, the indices start at 2 as $\Delta z_{ij}^{IR'} \equiv 0$ for the first frame ($i = 1$) for all trials (j).

As the phantom acquisitions did not contain rotational motion, image rotations were artificially introduced to the first frame of the axial motion case to ensure that the

registration could estimate rotations. Image rotations of $\pm 5^\circ$, $\pm 10^\circ$, and $\pm 20^\circ$ about z-axis (longitudinal axis of the PET field of view) were performed. The root mean square error between the known and estimated rotations was determined as a measure of the accuracy. The phantom acquisitions were not suitable for testing the effect of tracer kinetics and tracer decay, as they were injected with ^{18}F -FDG and the tracer distribution within the phantom was static.

5.2.6 Absolute Blood Flow Quantification and Figures of Merit

Blood flow quantification was performed using the FlowQuant© (version 2.7) software package which was developed at the University of Ottawa Heart Institute.¹⁵⁹ This research tool is a graphical-user-interface application which permits automated analysis of cardiac PET images and includes kinetic modelling workflows. For the acquisitions which used ^{82}Rb a one-tissue compartment model¹⁵⁹ was employed on the first 6 minutes of data.¹⁸¹ For the $^{13}\text{NH}_3$ studies, the two-tissue compartment model was used¹⁸² which used the entire 20-minute dynamic acquisition. In both cases, the kinetic models were constrained such that the tissue-to-blood ratio of activity concentration was fixed. At equilibrium, this ratio is equivalent to the ratio of K_1 to k_2 kinetic model parameters, as defined in Section 1.3.3. The specific value was determined based on the unconstrained model parameters determined in a region of normal uptake, i.e. with a relative uptake greater than 80%. This constraint was shown previously to improve inter-operator repeatability of blood flow measurements using FlowQuant.¹⁵⁹

The tissue and blood regions are defined using an average uptake image which used all frames in the ranges of 1.5 – 6 minutes and 2.5 – 20 minutes for ^{82}Rb and $^{13}\text{NH}_3$,

respectively. Prior to defining these sampling regions the uptake images were reoriented into the short-axis representation using the same method that was described in Section 3.2.7. The myocardial uptake sampling points were determined by fitting spline-based contours based on a set of control points automatically initialized within the myocardium. Control points were defined at the level of the apex, cavity, and base of the LV and as well at the level of the left-atrium (LA). Once the fitted model of the LV was achieved, the image was sampled on 24 slices which span from the apex to the level of the LA. On each slice 36 angular positions were sampled using 10° increments. Slices 10 – 24 correspond to planar short axis slices whereas slices 1 – 9 are projections of the intersection of a conical surface with the myocardium. This approach provides a set of sampling profiles which are roughly normal to the myocardium regardless of the region being sampled. Figure 5.3 provides an example of the spline model fit to an LV along with its control points and sampling profiles. At each sampling point the average image intensity within a region of ± 2 mm from the spline curve is used as the activity concentration at that point. This range limits the sampling to be within the endo- and epicardial tissue. Only the first 17 slices were used to sample the myocardium for kinetic modelling. Blood activity concentrations were sampled as the median values among three volumes of interest within LA and the cavity and base of the LV.

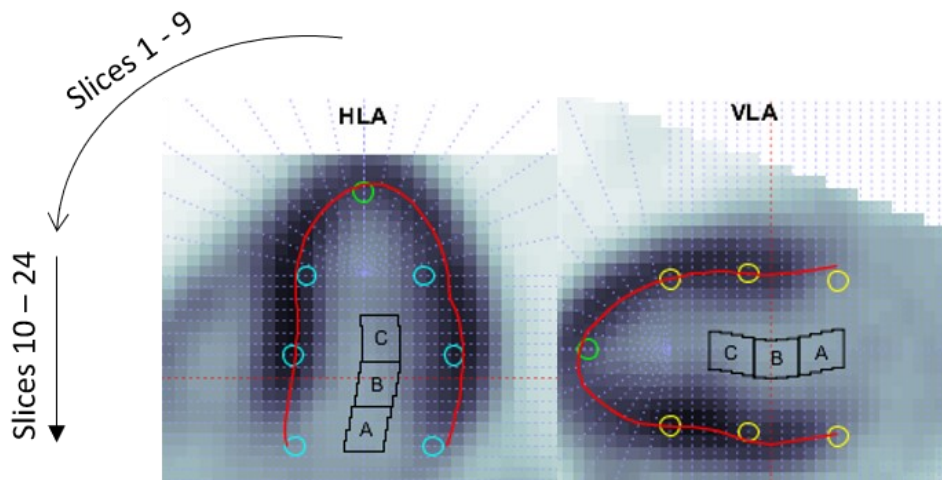


Figure 5.3 Demonstration of the FlowQuant LV sampling method. The spline fit, shown as a solid red curve, and its control points, empty circles, are shown on horizontal long-axis (HLA) and vertical-long axis (VLA) images. The blood sampling volumes of interest are indicated as regions bounded by a solid black border with the labels A (atrium), B (base), and C (cavity). Dashed lines represent the profiles along which the myocardium is sampled. Note that the apical slices which appear to fan outward are defined by conical surfaces which intersect the myocardium; all other slices are planar short-axis slices. The red dashed line additionally indicates the basal extent of the LV used for myocardial sampling.

The FlowQuant GUI permits opportunities for manual intervention if the automatic sampling tool failed but this was generally not needed. Manual intervention was required for one $^{13}\text{NH}_3$ acquisition where the spline fit was hindered by reduced uptake in the apical anterior region as well as by extra-cardiac uptake in the left lung.

As described previously in Section 2.1, patient motion can lead to reduced accuracy of myocardial blood flow quantification. In human studies, however, the motion-free flow values are not known, and so blood flow alone is insufficient to identify and characterize the effect of patient motion on dynamic cardiac PET studies. Other metrics related to the goodness-of-fit of the myocardial TACs⁷⁷, e.g. root-mean-square errors (RMSE_{TAC}) and coefficient of determination (R^2), and voxel-wise uncertainty of kinetic model parameters

like MBF¹⁸³ (or K1) and total blood volume¹⁸⁴ (TBV) have been proposed elsewhere and were adopted for this work. Hereafter, the uncertainty of MBF and TBV will be referred to as FlowSD and TBVSD, respectively. These are estimated from a non-linear fitting procedure and are based on the sensitivity of the cost function to the fit parameters. In the presence of motion, one would expect to observe higher variance (worse precision) in kinetic model parameters as well as poorer goodness-of-fit of the TACs. The myocardium goodness-of-fit measures reflect the agreement between the image-based (measured) and model-derived (estimated) myocardial activity concentrations among all time points. Recall that the measured and modelled myocardium TACs were defined previously in Section 1.3.3 and are represented as $C_m(t)$ and $\hat{C}_m(t)$, respectively. Definitions of the $RMSE_{TAC}$ and R^2 goodness-of-fit measures are provided below, where y_i and f_i represent the i^{th} measured and regressed TAC values, and N is the number of data points on the TAC (or number of dynamic frames included in the kinetic model). Additionally, SS_{res} and SS_{tot} represent the residual sum-of-squares between the measures and regressed values and the total sum-of-squares of the measures data, respectively. FlowQuant calculates these metrics on a voxel-by-voxel basis during kinetic modelling.

$$RMSE = \sqrt{\frac{1}{N} \sum_i (y_i - f_i)^2} \quad \text{Eq. 0.3}$$

$$R^2 \equiv 1 - \frac{SS_{res}}{SS_{tot}} = 1 - \frac{\sum_i (y_i - f_i)^2}{\sum_i (y_i - \bar{y})^2} \quad \text{Eq. 0.4}$$

5.3 Results

5.3.1 Verification of COD Tracking

The no-motion phantom acquisition was considered first. As the phantom did not move during this acquisition any change fluctuation in the COD motion trace would indicate either a mistake in the implementation or the susceptibility of the method to noise in its signal. The COD tracking results for the reference phantom acquisitions are shown in Figure 5.4. Figure 5.4(A) shows the example motion trace where the LOR probability cut-off, or “pCut”, was 0.0. Figure 5.4(B) and (C) show the mean and standard deviations of each dimension of the centroid position as a function of pCut. COD tracking for this acquisition provided a consistent representation of the mean position regardless of the choice of pCut. The standard deviation of each component of the position demonstrated an exponential relationship with the choice of pCut indicating that the signal noise level was strongly affected by the severity of the exclusion criteria of LORs used for COD tracking.

The COD traces for the various values pCut were also examined for the phantom acquisition where axial motion was included; the inferior-superior components for the subset of the pCut values are plotted along with that from the PeTrack trace in Figure 5.5. The most notable aspect of this comparison is the limited extent of motion observed using COD tracking compared to PeTrack. The magnitude of displacements reported by COD tracking were roughly 20% of that measured using PeTrack. The reason for this effect is suspected to be associated with spatial dependence of the sensitivity of the PET system as well as the presence of scattered coincidence events. When the phantom acquisition

began the cardiac insert was roughly centered within the PET field-of-view. As it was moved, however, the inferior aspect of the cardiac model moves to a location with reduced sensitivity and thus the movement of the centroid of the LORs is damped. Since scattered coincidence events are more uniformly distributed this leads to a stable background of LORs which are not likely to change with the motion of the heart and thus would have a similar damping effect on the LOR.

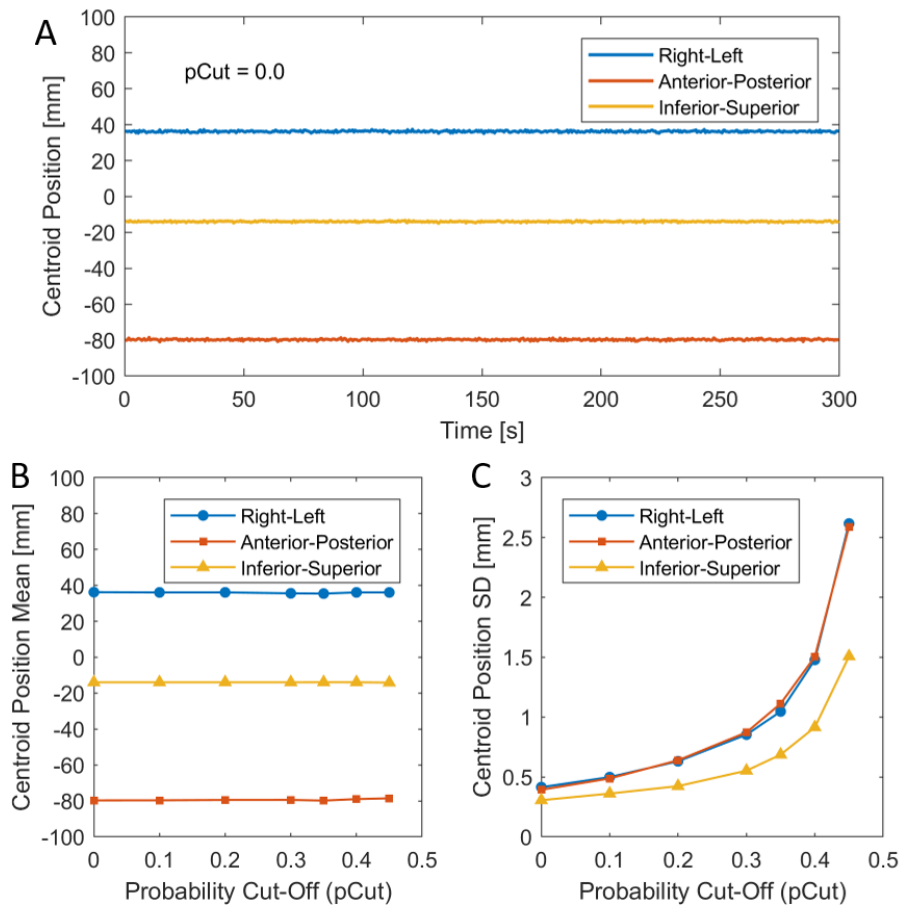


Figure 5.4 Centroid of Distribution (COD) motion trace (A) derived from the reference phantom acquisition where no motion occurred and the LOR probability cut-off (pCut) was set as 0.0. The components belonging to the right-left, anterior-posterior, and inferior-superior directions of motion are shown as blue, orange, and yellow, respectively. The mean position of each component and the corresponding standard deviation (SD) are plotted as functions of pCut in sub-figures (B) and (C), respectively.

Similar results were observed for the phantom acquisition in which lateral motion was applied although the damping was not as severe; the ratio of the displacement observed with COD compared to PeTrack was roughly 50%.

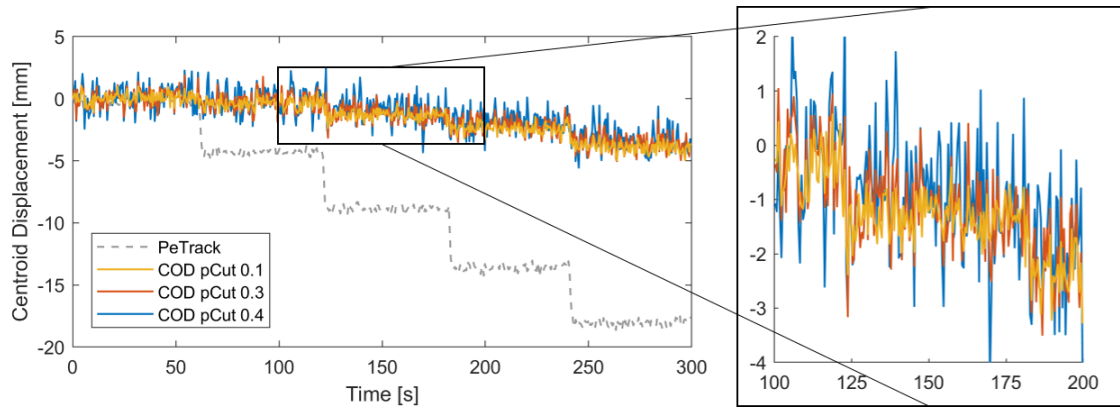


Figure 5.5 Inferior-superior motion trace components observed while tracking the phantom motion using COD and PeTrack. The COD traces are shown for $pCut \in [0.1, 0.3, 0.4]$ to simplify the figure. The domain of 100 – 200 s is shown on the right to enhance the differences among the various COD traces.

From these tests several insights were gleaned. First, the absolute magnitude of motion indicated by COD tracking is not as accurate as that observed with PeTrack. It follows that employing 3D motion correction based on the COD displacement alone is unlikely to be successful unless some sort of calibration is employed. As such, the CD3D approach to whole-body motion correction was not pursued further. Secondly, the principal effect of changing the value of the probability cut-off for exclusion of LORs for each tracking instance was to modify the signal noise. As shown in Figure 5.4 and Figure 5.5, there appeared to be no benefit associated with increasing $pCut$ among the phantom acquisitions. Tracer distributions in humans are more complex than that of the phantom acquisitions and interference from extra-cardiac uptake is more likely. When ^{82}Rb is used

uptake in the stomach wall and/or spleen is common^{185,186} whereas when $^{13}\text{NH}_3$ is used, uptake in the lung⁷³ and pancreas¹⁸⁷ is expected. It follows that $p\text{Cut} = 0.1$ was used when COD tracking was applied to the human acquisitions.

5.3.2 Verification of the Image Registration Method

The phantom acquisition in which axial motion was applied was used once more to validate the image registration method. The RMSE_{reg} of the inferior-superior inter-frame translation between registration and PeTrack was found to be 1.2 mm. The MAD associated with varying the reference frame of the registration was 1.5 mm. Together, these metrics demonstrated that the motion estimation using image registration of these phantom acquisitions was in good agreement with an independent approach: PeTrack, and that the method was self-consistent and showed a small overall variability associated with changes in the reference frame. The RMSE_{reg} associated with rotations which ranged from $5^\circ - 20^\circ$ about the longitudinal axis was 0.008° . Since the target and moving images of this test were identical, save for the rotations imposed on them, this test simply indicates that the registration algorithm could account for rotations and does not truly represent its accuracy when applied to unique dynamic frames. This suggests that the registration method was correctly initialized with reasonable parameter choices. It is worth re-iterating that these tests could not assess the usefulness of the registration method when a time-varying tracer distribution is present, as is the case in dynamic perfusion studies performed on the patient cohort.

5.3.3 Evaluation of the Body-Motion Detection and Estimation Methods

As a final assessment of the motion correction workflow, motion-correction reconstructions were performed for the phantom acquisition in which axial motion was applied. Motion triggers were produced from both PeTrack and COD motion traces and image registration was used for motion estimation, i.e. PT6D and CD6D motion correction methods were employed. The two motion traces and their corresponding triggers are shown in Figure 5.6.

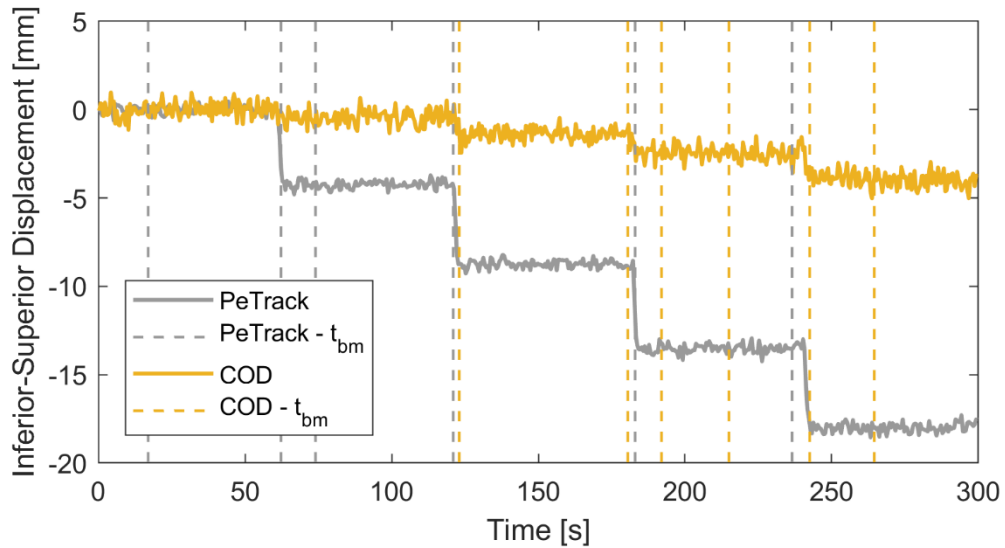


Figure 5.6 Inferior-superior component of the motion traces of PeTrack (gray) and COD (yellow) for the axial motion phantom acquisition. The triggers (t_{bm}) identified for each trace are also shown as dashed lines; they are colour-matched with the trace to which they belong. Due to the limited ability of COD to estimate motion, the trigger corresponding to the first change in position near 60 s was not detected.

The motion detection algorithm was designed such that PeTrack and COD showed produced comparable results during the task of identifying the instance of motion within the phantom acquisitions. Perfect agreement could not be achieved given the difference in scale of the two traces. The most notable difference is that the first transition around 60

seconds after the beginning of the acquisition was not detected from the COD trace. To ensure that obvious transitions were generally detected by both tracking methods they became marginally too sensitive. This can be seen from the triggers that were detected at time points between major transitions, e.g. COD triggers at 192 s, 215 s, and 264.5 s and PeTrack triggers at 17 s and 74 s.

The two motion corrected images are shown in Figure 5.7 for a qualitative comparison of the improvement in LV contrast compared to the non-corrected image. All three images are resampled along a common coronal plane to allow a clear view of the blurring effect of motion on the model heart structure. Both PT6D and CD6D images show marked improvement with respect to recovered spatial resolution and LV contrast over the background compared to the non-corrected image. Some residual blurring can be seen, however, in the CD6D image compared to PT6D at the lung-liver interface (indicated by the arrows in the figure). The residual blurring is associated with the missed trigger that occurred at approximately 60 second into the acquisition when using COD for tracking.



Figure 5.7 Comparison of PeTrack (PT6D) and COD (CD6D) motion correction when image registration was used to estimate motion. The non-corrected image is shown for comparison. Both motion corrected images demonstrated reduced blurring compared to the non-corrected image. The PT6D image shows marginally higher contrast in the model LV walls compared to CD6D. Some residual blurring at the lung-liver interface (indicated by arrows) is apparent in the CD6D image.

5.3.4 Sensitivity of Kinetic Modelling Quality Metrics to Motion

The reconstructed dynamic image series (NMC) were visually inspected to assess the extent of motion in each of the 17 acquisitions. Of those, 4 were identified as severe motion cases; they exhibited translational motion ≥ 6 mm. The remaining acquisitions exhibited no motion or very minor motion, i.e. translations < 3 mm, and are referred to here as mild motion cases. These categorical labels are similar to those described in other work.^{82,188} To verify that the quality metrics that were proposed above were indeed correlated with increased patient motion, the mean values for the motion-positive and motion-negative groups were calculated from the kinetic modelling outputs. The measurements for the two groups are provided in Table 5.1 below and they generally support the suppositions that TAC goodness-of-fit measures and precision of the estimated kinetic model parameters are worsened in the presence of patient motion. An exception, however, was observed for the myocardium TAC $RMSE_{TAC}$ metric which was reduced by 20% between the mild and severe motion groups. This finding was not expected and some suggestions as to why $RMSE_{TAC}$ appeared worse for the mild motion group will be discussed later.

Table 5.1 Summary statistics of proposed motion correction figures of merit for motion-negative ($N_{MN} = 13$) and motion-positive ($N_{MP} = 4$) groups. The relative change in the value from the motion-negative to motion-positive groups are also provided.

Metric	Motion-Negative (mean \pm SD) $N_{MN} = 13$	Motion-Positive (mean \pm SD) $N_{MP} = 4$	Relative Change [%]
FlowSD [mL/min/g]	0.04 \pm 0.01	0.12 \pm 0.08	+230 %
TBVSD	0.026 \pm 0.003	0.05 \pm 0.02	+90 %
R ²	0.93 \pm 0.04	0.8 \pm 0.1	-10 %
$RMSE_{TAC}$ [Bq/mL]	4000 \pm 1000	3200 \pm 900	-20 %

5.3.5 Patient Motion Assessment Among Severe Motion Cases

The acquisitions included in the severe motion groups were D(stress), H(rest), H(stress), and I(stress), which include one ^{82}Rb perfusion study (D(stress)), and three $^{13}\text{NH}_3$ perfusion studies. In the following, descriptions of the motion observed from visual assessment, PeTrack traces, COD traces, and from image registrations are provided.

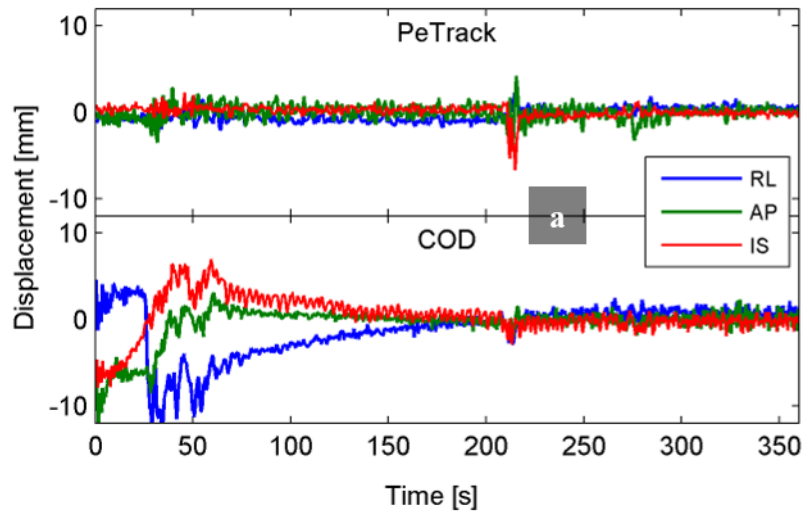


Figure 5.8 PeTrack (upper plot) and COD (lower plot) motion traces for the D(Stress) acquisition. Right-left, anterior-posterior, and inferior-superior motion trace components are shown as blue, green, and red lines, respectively. Visual assessment indicated a 6 mm translation in the superior direction at 240 s, indicated by point **a**.

Based on visual assessment, the stress acquisition of patient D exhibited a 6 mm translation in the superior direction between frames 13 (180 – 240 s) and 14 (240 – 360 s). Motion was considered non-returning in this case as only a single translation was noted and it was not followed by a similar, but reverse, movement. Motion of the marker was not apparent in the NMC image series of this case. The PeTrack and COD motion traces are shown in Figure 5.8 along with annotations of the visual assessment. The

PeTrack motion trace indicated a rapid change in the marker position beginning around 210 s and lasting roughly 10 s, where the marker moved in the inferior direction and then superiorly, coming to rest around 220 s at a position slightly inferior to its initial position. The COD trace indicated a protracted shift from right to left, and anterior to posterior starting with the acquisitions and ending around 175 s. Additionally, motion toward the superior and then inferior directions was observed over the same span of time. Both PT6D and CD6D approaches (image registration based) indicated frequent translation of 2 mm magnitude in all directions of motion between 50 s and 125 s as well as rotational motion around 30 s.

Visual assessment of the rest acquisition of patient H exhibited protracted translations beginning at frame 14 (240 – 360 s) and continued thereafter until the end of the acquisition (1200 s). The accumulated motion consisted of translations in the superior direction of roughly 7 mm, and smaller translation (~ 3 mm) in the left and posterior directions. Superior and posterior translations of 10 mm and 3 mm, respectively, were observed for the fiducial markers over the same span of time. Patient motion was non-returning in this case. The PeTrack and COD motion traces are shown in Figure 5.9 along with annotations of the visual assessment. The PeTrack motion trace indicated a consistent superior and posterior drift from the beginning of the acquisition until the end which spanned approximately 8 mm, and 5 mm, respectively. The COD traces indicated a rapid rise near the beginning of the acquisition suggesting the COD position moved from right to left, inferior to superior and anterior to posterior and then an asymptotic decay toward the right, inferior, and anterior direction. Both PT6D and CD6D indicated similar translation as for the D(Stress) acquisition and effectively no rotational motion.

The stress acquisition of patient H exhibited the largest extent and most complex motion of any acquisitions included in this study. In the span of frames 13 (180 – 240 s) to 15 (360 – 600 s) a lateral (to the right) translation of roughly 10 mm was evident. Within this span, a counter-clockwise rotation in the transverse plane was also observed

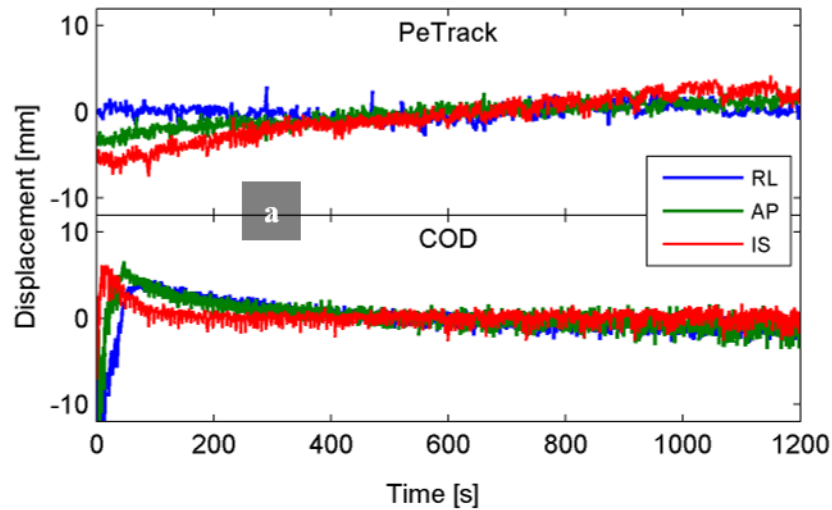


Figure 5.9 PeTrack (upper plot) and COD (lower plot) motion traces for the H(Rest) acquisition. Right-left, anterior-posterior, and inferior-superior motion trace components are shown as blue, green, and red lines, respectively. Visual assessment indicated a protracted 7 mm translation in the superior direction beginning between 240 and 360 s (indicated by point **a**) and continuing until the end of the acquisition.

between frames 13 and 14 (240 – 360 s). Frame 14 exhibited obvious motion blur.

Subsequently, clockwise rotations were observed in the transverse view between frames 15 and 17 (900 – 1200 s) which had an effect like lateral (to the left) and posterior translations of roughly 3 mm and 5 mm, respectively. Motion was considered to be returning for this case. Similar translations to those just described were observed for the fiducial marker, although the translation to the right between frames 13 and 15 had a greater extent; roughly 12 mm. The PeTrack and COD motion traces are shown in Figure 5.10 along with annotations of the visual assessment. The PeTrack motion trace appeared

to capture the lateral motion well as an initial shift 12 mm to the right beginning around 300 s is apparent, followed by a slow return to the left until the end of the acquisition. The COD trace indicated a subtle discrete shift to the right around 320 s but did not suggest returning motion thereafter. PT6D and CD6D translations again, showed

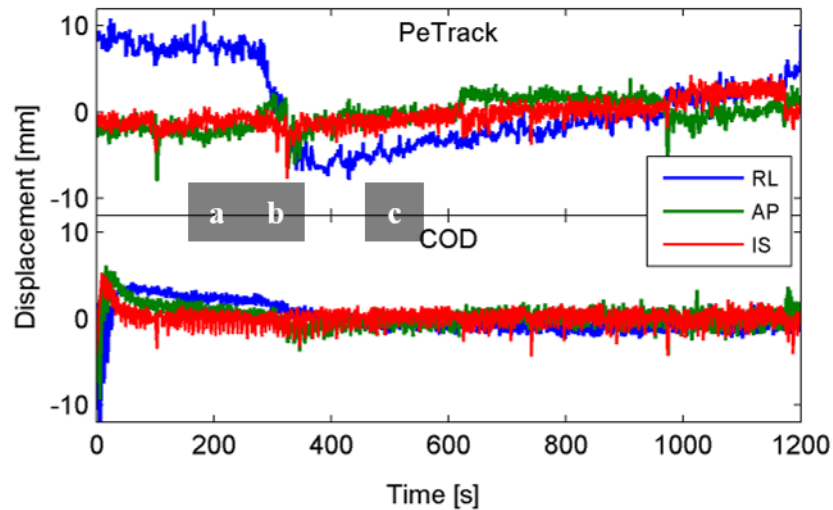


Figure 5.10 PeTrack (upper plot) and COD (lower plot) motion traces for the H(Stress) acquisition. Right-left, anterior-posterior, and inferior-superior motion trace components are shown as blue, green, and red lines, respectively. Visual assessment indicated a protracted 10 mm translation toward the right which occurred between 180 and 600 s, indicated by point **a**. A counter-clockwise rotation about the inferior-superior axis of the patient around 240 s, indicated by point **b**. A series of clockwise rotations about the inferior-superior axis of the patient began around 480 s (indicated by point **c**) and continued until the end of the acquisition.

frequent, yet irregular, translational motion and very little rotational motion except a 3D rotation about the superior-inferior axis (i.e. within the transverse plane) around 300 s into the acquisition. Transverse uptake images from each reconstruction are shown in Figure 5.11 for this case; they were produced by averaging the dynamic frames between 90 and 1200 s. The PT3D motion correction approach produced the best quality image

within the group as indicated by the improved contrast, uniformity, and resolution within the myocardium.

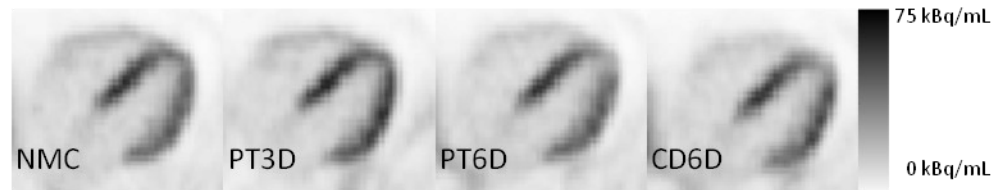


Figure 5.11 Transverse uptake images of the LV for acquisition H(Stress) for each of the reconstruction methods. These images were averaged from frames 10 – 17 of each series, which corresponds to 90 – 1200 s of the acquisition. The PT3D image shows the most well resolved representation of the LV with the greatest contrast and uptake uniformity.

The final example is the stress acquisition of patient I, which exhibited a large lateral translation of roughly 10 mm to the left between frames 13 (240 – 360 s) and 14 (360 – 600 s) in addition to a protracted superior translation of roughly 5 mm between frames 14 and 17 (900 – 1200 s). Motion was non-returning in this case. The lateral shift between frames 13 and 14 was also apparent for the marker with a similar magnitude. The PeTrack and COD motion traces are shown in Figure 5.12 along with annotations of the visual assessment. The PeTrack trace motion indicated a significant translation from right to left between 400 s and 450 s into the acquisition with an extent of roughly 12 mm. A rapid shift in the inferior direction was also observed around 360 s with a magnitude of roughly 3 mm; opposite to the direction observed from visual assessment. The COD trace exhibited a similar pattern to those described above but a translation from right to left was visible near 400 s. PT6D and CD6D translation were typically less than 2 mm in magnitude but appeared irregular. CD6D indicated a translation of 12 mm in the superior

direction around 50 s. Effectively no rotational motion was indicated for either PT6D or CD6D.

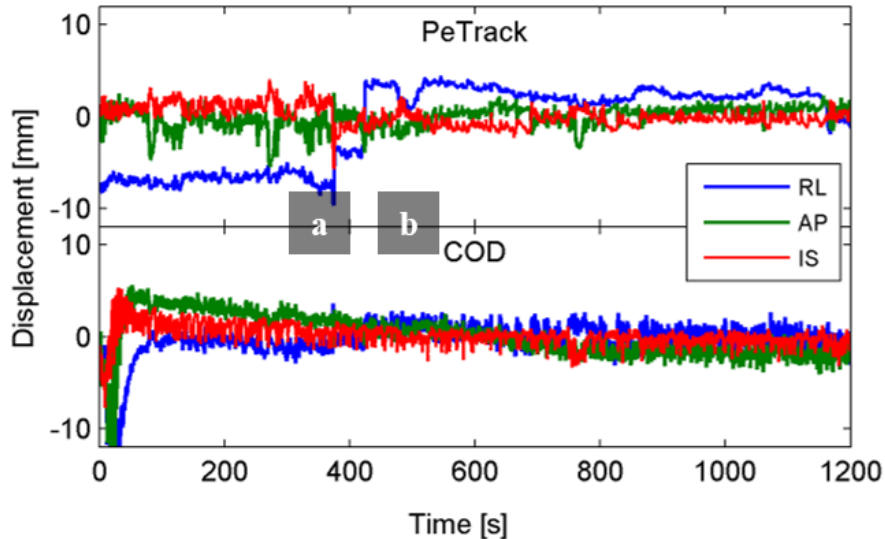


Figure 5.12 PeTrack (upper plot) and COD (lower plot) motion traces for the I(Stress) acquisition. Right-left, anterior-posterior, and inferior-superior motion trace components are shown as blue, green, and red lines, respectively. Visual assessment indicated a 10 mm translation toward the left which occurred around 360 s, indicated by point **a**. A protracted superior translation of 5 mm was also observed starting after 360 s and continuing until the end of the acquisition, indicated by point **b**.

5.3.6 Kinetic Modelling Results Among Severe Motion Cases

Absolute myocardial blood flow was compared for the severe motion cases before and after each motion correction approach. A summary of the MBF measurements is shown in Figure 5.13. In this plot the data are categorized by acquisition with data points for each reconstruction method. The PT6D and CD6D motion correction methods generally exhibited increased MBF variability across the myocardium compared to the measurements from the NMC reconstructions. Otherwise, no obvious trends in these measurements were apparent. The mean values of MBF, for instance, did not have

tendencies to increase or decrease after motion correction was applied. This is in line with our previous assumptions that the effect of patient motion on MBF may be ambiguous without also considering the corresponding quality metrics.

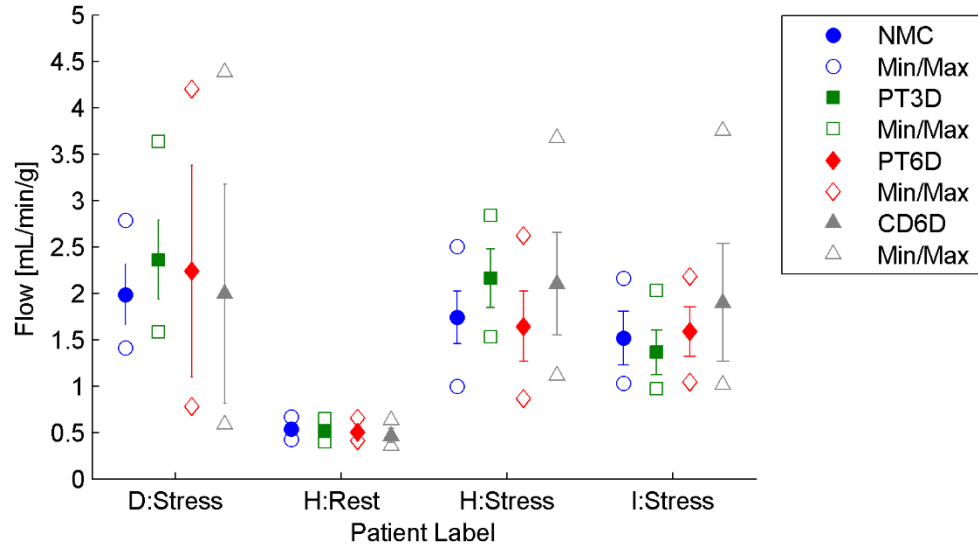


Figure 5.13 MBF measurements for the severe motion acquisitions. Mean measurements are shown as solid markers with error bars that span ± 1 SD. Minimum and maximum measurements for each reconstruction are indicated as empty markers. Data points corresponding to NMC, PT3D, PT6D, and CD6D reconstructions are shown as blue circles, green squares, red diamonds, and gray triangles, respectively.

Summary measurements for goodness-of-fit metrics, myocardium: TAC coefficient of determination (R^2) and $RMSE_{TAC}$, are provided in Figure 5.14 and Figure 5.15, respectively. When considering the R^2 metric, TAC fit quality improved for PT3D motion-corrected images compared to NMC images with an average increase of 3.9%. PT6D and CD6D images, however, suggest that fit quality worsened after motion correction compared to no motion correction.

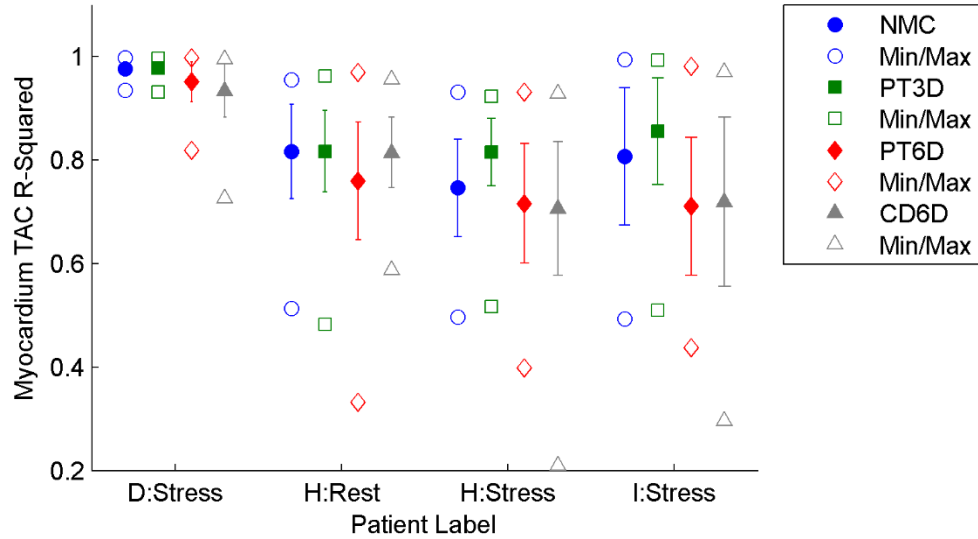


Figure 5.14 Coefficient of determination (R^2) goodness-of-fit measurements for the myocardial TACs for the severe motion acquisitions. Mean measurements are shown as solid markers with error bars that span ± 1 SD. Minimum and maximum measurements for each reconstruction are indicated as empty markers. Data points corresponding to NMC, PT3D, PT6D, and CD6D reconstructions are shown as blue circles, green squares, red diamonds, and gray triangles, respectively.

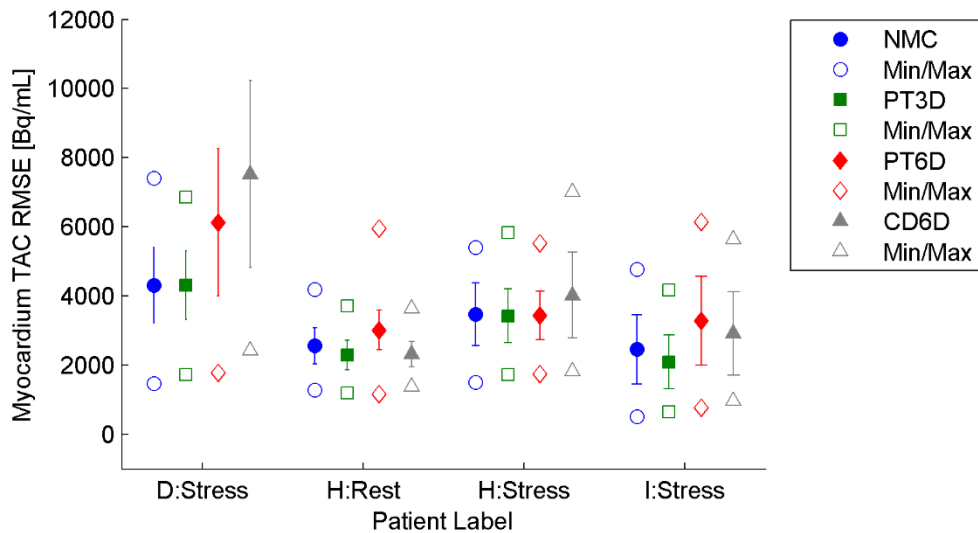


Figure 5.15 Root-mean-square error ($RMSE_{TAC}$) goodness-of-fit measurements for the myocardial TACs for the severe motion acquisitions. Mean measurements are shown as solid markers with error bars that span ± 1 SD. Minimum and maximum measurements for each reconstruction are indicated as empty markers. Data points corresponding to NMC, PT3D, PT6D, and CD6D reconstructions are shown as blue circles, green squares, red diamonds, and gray triangles, respectively.

Average decreases in R^2 for PT6D and CD6D were 6.4% and 5.2%, respectively, with respect to NMC values. R^2 values also appeared much more variable across the LV for PT6D and CD6D reconstructions compared with both NMC and PT3D.

Similar findings were observed for $RMSE_{TAC}$ values for the PT6D and CD6D reconstructions as for the R^2 measurements, i.e. $RMSE_{TAC}$ indicated the TAC fit quality worsened compared to NMC image measurements. On average, $RMSE_{TAC}$ increased by 23% and 25% for PT6D and CD6D images compared to measurements from the NMC images. Motion correction using the PT3D reduced the $RMSE_{TAC}$ observed for NMC images by 6.7% among these acquisitions. As is shown in Figure 5.15, $RMSE$ values were less variable across the LV in each of the four acquisitions.

Summary measurements of the kinetic modelling precision metrics: FlowSD and TBVSD, are shown in Figure 5.16, and Figure 5.17, respectively.

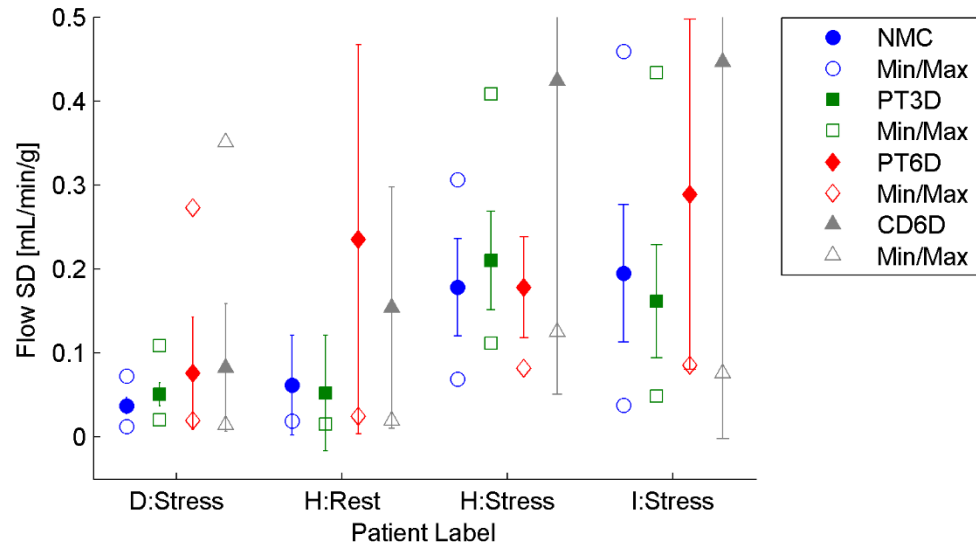


Figure 5.16 Voxel-wise MBF precision (FlowSD) measurements for the severe motion acquisitions. Mean measurements are shown as solid markers with error bars that span ± 1 SD. Minimum and maximum measurements for each reconstruction are indicated as empty markers. Data points corresponding to NMC, PT3D, PT6D, and CD6D reconstructions are shown as blue circles, green squares, red diamonds, and gray triangles, respectively.

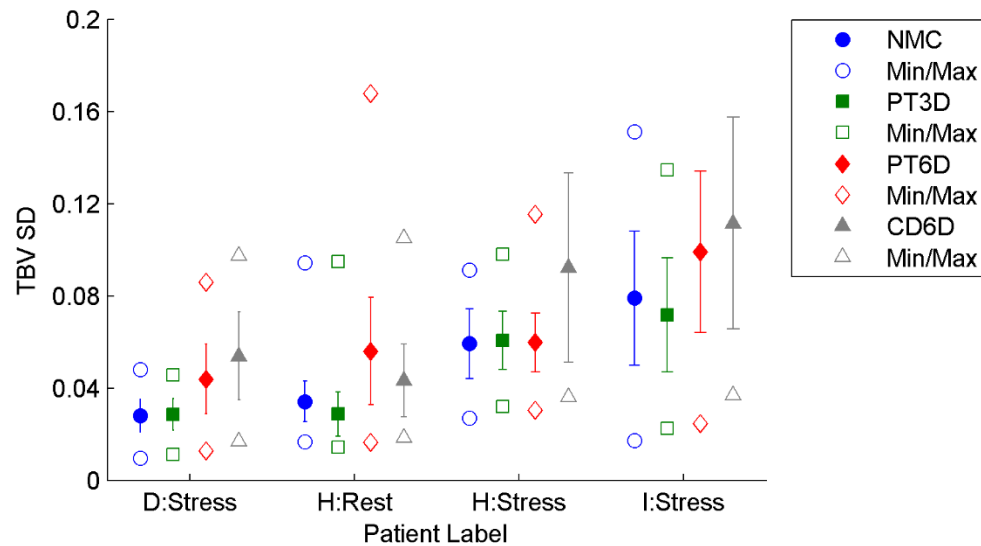


Figure 5.17 Voxel-wise total blood volume precision (TBVSD) measurements for the severe motion acquisitions. Mean measurements are shown as solid markers with error bars that span ± 1 SD. Minimum and maximum measurements for each reconstruction are indicated as empty markers. Data points corresponding to NMC, PT3D, PT6D, and CD6D reconstructions are shown as blue circles, green squares, red diamonds, and gray triangles, respectively.

Among the four severe motion acquisitions, average FlowSD values increased by 5.2%, 110%, and 130% compared to values measured from NMC images, for PT3D, PT6D, and CD6D motion correction reconstructions, respectively. As FlowSD values were expected to increase with motion, this metric did not indicate a benefit from employing motion correction. The precision of the total blood volume estimates showed a modest improvement for the PT3D motion corrected images; TBVSD was reduced by -5.2% with respect to values of the NMC images. TBVSD was increased for the PT6D and CD6D reconstructions compared to the NMC images by 37% and 54%, respectively. Once more this suggests that the PT6D and CD6D approaches to motion correction did not improve MBF precision.

5.4 Discussion

Overall, the results suggested that motion tracking with either PeTrack or COD methods is feasible but only the PT3D motion correction method seemed to be robust enough for use during MBF estimation from dynamic cardiac PET perfusion studies. Image registration did not demonstrate successful ability to compensate for the motion that was observed among the severe motion cases. These results are largely preliminary, however, as the size of the cohort was relatively small and, more importantly, the number of the acquisitions which exhibited severe motion was very limited. It follows that a rigorous statistical analysis of the measured data is not appropriate and conclusive evidence regarding the use of any of these motion correction approaches was not demonstrated within a general population of patients. Nevertheless, when treated as a

series of case studies, various valuable insights were gleaned that are discussed in the following.

5.4.1 Motion Estimation with PeTrack

Generally, PeTrack produced patient-motion estimates that agreed with visual assessment of the original NMC images. Among the severe motion cases detailed above, the PT3D approach to motion corrections generally led to improvements in the various quality metrics that were considered. The H(Stress) acquisition was the most compelling example of the benefit of the PT3D motion correction approach. Polar maps of myocardium TAC R^2 values are shown for the NMC and PT3D reconstructions for the H(Stress) acquisition in Figure 5.18. The NMC images exhibited returning motion predominantly along the lateral direction. The R^2 polar map from the NMC images shows that TAC goodness-of-fit was reduced within the septal and lateral walls as would be expected for severe lateral motion. Following PT3D motion correction, fit quality in these regions was markedly improved which resulted in an increased MBF estimation for this acquisition.

In one of the mild motion cases, acquisition C(Rest), marker motion indicated a non-returning translation of roughly 5 mm in the inferior direction around 100 s into the acquisition; this motion was confirmed at the marker by visual assessment. The marker motion was discordant however with the motion of the LV and the PT3D motion correction images led to a 10% increase in MBF, which was predominantly associated with changes in the inferior wall at the apical level.

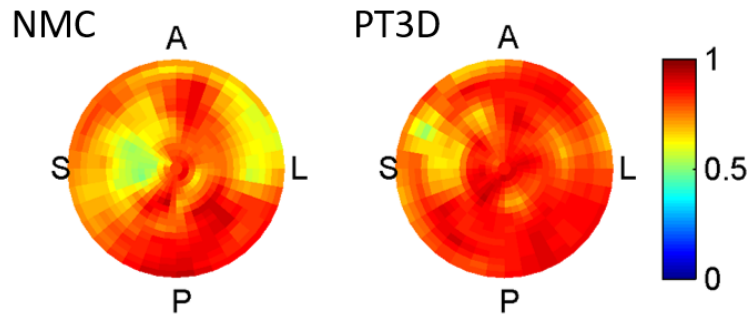


Figure 5.18 LV polar maps depicting coefficient of determination (R^2) values for the myocardium TACs for the NMC and PT3D images for the H(Stress) acquisition. Anatomic labels ‘A’, ‘S’, ‘L’, and ‘P’ correspond to the anterior, septal, lateral, and posterior regions of the LV, respectively. Motion correction with PT3D approach improved R^2 values in the septal and lateral regions of the LV in the presence of severe lateral patient motion.

These two examples contrasted one another in the sense the marker motion may or may not be an accurate surrogate for the body motion that occurred during the acquisition and thus have varying degrees of success, or failure, to align dynamic frames prior to MBF estimation via kinetic modelling. The use of PeTrack with a single marker is limited to 3D translation motion estimation. Future work should extend to the use of multiple markers such that the assessment of various rotations can also be included. Based on the visual assessment performed of the NMC images, rotations about the superior-inferior axis of the patient would be of principal interest.

5.4.2 COD Motion Estimation

As was expected from the initial phantom studies, the COD motion traces were dominated by the redistribution of the perfusion tracers within the body. A characteristic pattern was apparent among all the COD motion traces for the patient cohort. The COD trace of the B(Stress) acquisition is shown in Figure 5.19 to help describe the behaviour.

Along inferior-superior direction (shown in red), the COD would move initially in the superior (positive) direction, peak 30 s into the acquisition, and then slowly drift in the inferior (negative) direction as it approached a steady position. Along right-left direction, the COD would begin toward the patient's right (negative) and drift toward the left (positive) as it approached a steady position. Along the anterior-posterior direction, the COD would commence toward the anterior (negative) direction and move posteriorly (positive) as it approached a steady position. This pattern very closely matches the change in tracer distribution in the heart beginning with venous administration which enters the right side of the heart and then transits toward the left where it reaches the LV blood pool and subsequently gets taken up into the myocardium. The anterior-posterior motion is also explained by this process as the right chambers of the heart are situated anterior to the left chambers.

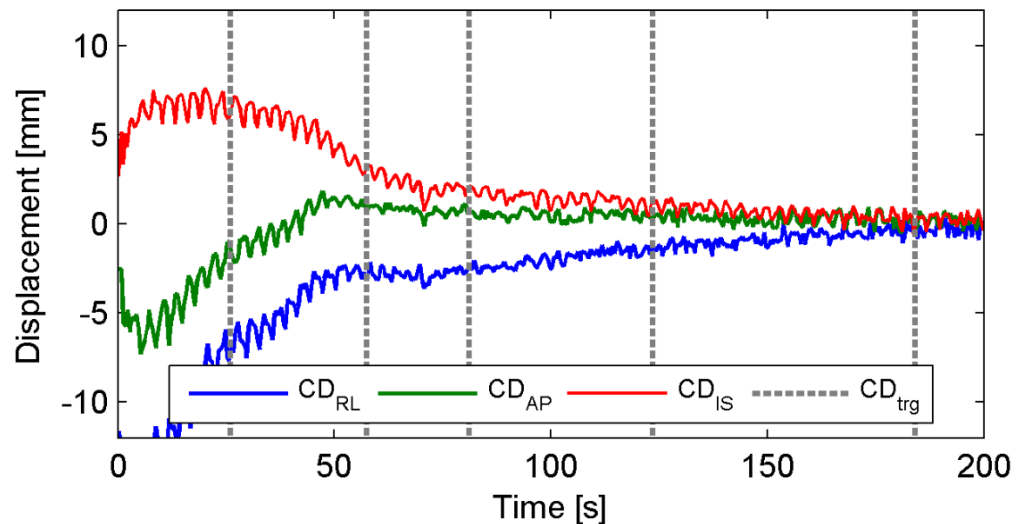


Figure 5.19 Centroid-of-Distribution motion trace for acquisition B(Stress) along each anatomical direction. Right-left, anterior-posterior, and inferior-superior components of the COD displacement are shown in blue, green, and red, respectively. The body-motion triggers are shown as vertical dashed lines. This case exhibited no apparent motion following visual assessment of the NMC image.

While the COD trace was dominated by tracer dynamics, especially, prior to steady-state uptake in the LV, detecting body motion was challenging. This is demonstrated in Figure 5.19 by the large number of body motion triggers that were detected. In comparison, the PeTrack motion trace for this acquisition demonstrates a very stable position with displacements from the reference position < 1 mm for all directions of motion. Moreover, no triggers were detected for this acquisition from the PeTrack motion trace. PT6D and CD6D motion correction approaches both introduced inter-frame motion that was not present in the NMC series, which had adverse effects on the kinetic modelling outcomes for this acquisition like an artifactual increase in MBF, increased MBF heterogeneity across the LV, and reduced TAC goodness-of-fit as indicated by lower R^2 values.

A periodic signal component is also visible within the COD trace shown (Figure 5.19) for the B(Stress) acquisition which has a larger amplitude earlier in the acquisition before the tracer has experienced much decay. The period appears to be on the order of 3 seconds which suggests that it is associated with respiratory motion. While respiratory, and possibly, cardiac motion tracking was not a focus of this study, it appears that COD motion tracking may be useful for these applications within cardiac perfusion PET studies. While COD motion tracking has been applied to respiratory motion compensation in previous studies^{118,189}, it has not been demonstrated for cardiac perfusion PET. This would be an interesting future research question.

5.4.3 Optimization of Motion Detection

The placement of the body-motion triggers appeared appropriate for most acquisitions based on correlation of triggers with visual assessment of the NMC images for instance of motion. There are several examples, however, where relatively conspicuous features of the PeTrack motion traces were not detected. Partial PeTrack motion traces are shown for acquisitions C(Stress) and D(Stress) in Figure 5.20(A) and (B), respectively, where only the dominant 1D component of the trace is shown. Arrows are shown to indicate features of the motion trace which were not detected as motion.

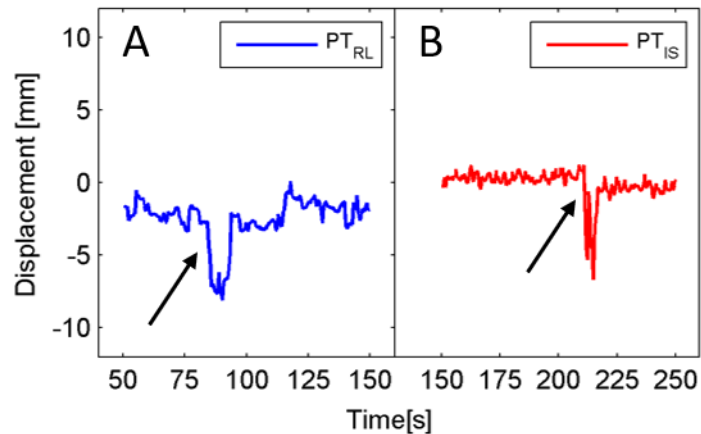


Figure 5.20 Partial PeTrack motion traces for C(Stress) (A) and D(Stress) (B) acquisitions where conspicuous translations were not detected as body motion triggers. Only the component of the trace which exhibited the dominant motion signal is shown here.

Acquisition C(Stress) was a mild motion case and indeed visual assessment did not suggest apparent motion in the lateral direction near 80 s after the beginning of the acquisition which corresponds with the feature. Nevertheless, the feature of the motion trace itself was pronounced and should have been detected. The D(Stress) acquisition was one of the severe motion cases, although it exhibited the smallest motion extent among

that group. The missed feature appeared as a very short pulse in the motion trace but corresponded to the beginning of a non-returning shift of the patient in the superior direction as seen on the NMC image series. Marker motion was not apparent in NMC image and, interestingly, the PeTrack motion trace suggested that the marker was translated toward the inferior direction following a sharp pulse near 215 s.

The method by which body motion triggers were detected was developed with the use of a relatively small subset of the acquisitions included in this study and the method is unlikely to be optimized with respect to sensitivity and specificity for a general patient population. The optimization process would involve adjusting the parameters of the method related to smoothing of the traces as well as the size of the sliding window used to compute the local normal vector orientation. As was indicated previously, other methods were considered for the motion detection. The first approach was described in Chapter 4, which involved the use of local displacement thresholds which, when exceeded, resulted in a motion trigger. While this method worked very effectively for PeTrack, it did not translate well for use with COD tracking. Another approach was based on the two-sample Student's t-test, where significant changes in the mean displacement among adjacent windows led to a motion trigger. This method required careful tuning of the significance level that corresponded to instances of suspected motion. This method worked effectively for either PeTrack or COD (using different criteria), but not both. A final method made use of a common signal-processing methods for peak detection; the Laplacian of a Gaussian filter¹⁹⁰ was applied to the traces in order detect peak in the signals. Once again, however, the nature of the PeTrack and COD traces were too

different to permit similar sets of body-motion triggers among the test cases used for development.

Sun et al.¹⁸⁰ examined the use of data-driven motion tracking method which was technically very similar to the COD method. They developed a novel approach to detect instance of body motion which was based on a single scalar metric which was computed as the sum of the eigenvalues of the covariance matrix and the 3D motion trace within a sliding window. Their results suggested that body motions of 12 mm or rotations of 20° could be detected with good accuracy. The PET studies in their work used ¹⁸F-based tracers with delayed acquisitions and so they did not evaluate their work under the conditions presented here. The authors caution that their method may not translate well to perfusion studies such as discussed herein.

Others have circumvented issues associated with limited motion detection sensitivity/specificity by incorporating high temporal resolution motion estimation directly into the reconstruction process. Such an approach was recently investigated by Armstrong et al.¹⁹¹ where they performed 3D image registrations on low resolution back-projected images of 1-second durations to estimate motion during static ⁸²Rb cardiac PET MPI studies. In their preliminary work they incorporated the axial component of motion only directly into the reconstruction process ignoring lateral or anterior-posterior motion. Such an approach is likely to be more appropriate to compensate specifically for respiratory motion. In dynamic cardiac PET studies lateral motion of the LV, specifically towards the left lung, has been shown to lead to significant changes in MBF estimation.⁸² A similar approach which used PeTrack was recently reported by Chamberland, Xu, deKemp⁹² with promising results, but in their case individual LORs were re-positioned

prior to reconstruction. To apply such an approach directly to the motion tracking data may not always be effective, however, if the PeTrack marker motion does not accurately represent motion of the heart. Similar arguments may apply to COD tracking.

As a final comment regarding motion detection while using COD tracking, the fact that a relatively consistent COD motion trace pattern was observed among the cohort suggests that a model motion trace could be estimated from a large cohort where no patient motion occurred. The model could potentially be fit to future COD motion traces to assess whether any significant deviation from the model occurred. These deviations, if not associated with the pattern of normal tracer dynamics in the body, could be interpreted as instances of motion.

5.4.4 Motion Estimation Using Image Registration

Despite the initial efforts to set up the image registration framework in a robust and accurate fashion using the phantom acquisitions, the PT6D and CD6D images generally produced varying degrees of motion artifacts in the dynamic series. Visually, this often appeared as jittering of adjacent dynamic frames. In other cases, it was clear that changes in the tracer distribution in the earlier frames, as seen from the NMC images, were interpreted as spatial misalignment during image registration and they were over-corrected. These limitations of the image-registration scheme for estimation of patient motion significantly limit the assessment of the COD tracking approach as no other motion estimation approach was considered for it.

The most extreme example of failure of the image registration to estimate motion was observed for acquisition B(Rest) for both PT6D and CD6D images. The largest inter-

frame translations and rotations were ~ 40 mm, and $\sim 20^\circ$, respectively, for both PT6D and CD6D images. In contrast, this acquisition was considered as a mild motion case using visual assessment and the largest inter-frame translation (based on changes in mean PeTrack positions between adjacent frames) was 2 mm. The registration failure in this case may be associated with low count motion frame images within the registration sequence as well as disparate tracer distributions among early frames. The sequential registration method is inherently sensitive to the problem of poor registrations within the sequence. The novel approach to automated alignment of dynamic cardiac perfusion frames described by Lee and colleagues⁸¹ which uses distinct reference frames in the early blood pool and late uptake portions of the dynamic series could be implemented here to overcome this issue.

It could be argued that extending the motion model to include rotations disadvantaged the PT6D and CD6D compared to PT3D. Complex models with a larger number of free parameters are generally less robust to noise and small data sizes. This pitfall was not obvious at the outset of this work, as the motion model with six degrees of freedom is still a rigid model and each image volume contains more than 7.7×10^5 voxels which contribute to the registration process. Moreover, others have reported successful registration results using more complex motion models¹¹⁹, although not in the application of dynamic cardiac PET perfusion studies.

The performance of the image registration technique described in this work could be enhanced in future work by considering the following amendments. First, the motion model could be reduced to include only 3D translations. Second, the initial non-attenuation corrected dynamic reconstruction used for image registration could

completely ignore the clinical dynamic sequence and reconstruct only frames that are identified in the motion detection step. In doing so, many fewer frames would be reconstructed (enhancing the counts in each) and the estimated motion model would be applied to all dynamic frames that fall within the corresponding motion frame. Third, the image registration could be regularized by applying additional smoothing to the non-attenuation corrected images used to estimate motion. Later, when applying the registration transformations for motion correction, the original (un-smoothed) images could still be used. Fourth, the duration of the smallest permissible motion frames could be adjusted throughout the acquisition based on the decay of the tracer. In this way, at later time points in the acquisition the shortest frame duration would be increased to have similar lower limits on the counts compared to earlier time points before the tracer has appreciably decayed. Lastly, the sensitivity of the motion detection method could be reduced such that fewer frames are reconstructed, and each would have a higher count density; although this would impair the overall effectiveness of the motion correction method.

5.4.5 Classification of Cases Which Could Benefit from Motion Correction

As was observed in this cohort, the majority of acquisitions corresponded to no or mild motion and did not benefit from the application of motion correction. More importantly, the quality of MBF estimation for some cases was negatively affected following motion correction (particularly for the PT6D and CD6D approaches). This finding leads to the question: how does one choose which scans would benefit from motion correction? In some case motion may be so severe that this decision would be obvious. The cohort in

this study, however, largely does not meet that criterion. Nevertheless, patient motion correction has regularly been identified as a contributing factor to the overall repeatability of MBF estimation^{77,81,85,184} and so a robust and automated method with which cases could be classified as those which would benefit from motion correction could be very clinically useful, especially for fringe cases where the motion effects are not obvious.

Carrying on with this notion, a metric (or set of metrics) must be determined which can flag acquisitions where motion either possibly or probably affected the accuracy of the MBF estimation. The quality metrics examined in this work have been suggested by others as being relevant indicators of the presence patient of motion, but they may not all agree with each other on an individual basis. In Table 5.1 it was shown that the coefficient of determination (R^2) and root-mean-square error ($RMSE_{TAC}$) of the myocardial TAC fits did not show the same trend between the mild and severe motion cases. Moreover, the changes observed in all of the quality metrics between the mild and severe motion groups may be confounded by the choice of perfusion tracer, the duration of the acquisition, and/or the number of dynamic frames used as part of the kinetic model. For example, 3 out of the 4 severe motion cases corresponded to $^{13}\text{NH}_3$ perfusion studies which are 20 minutes in duration and use 17 dynamic frames. Conversely, 11 out of the 13 mild motion cases were ^{82}Rb perfusion studies only 6 minutes of which (14 dynamic frames) were used for kinetic modelling.

Relying on visual assessment of motion within the dynamic images may not always be reliable. In this work, visual motion assessment in the early frames prior to myocardial uptake was very challenging largely due to the rapid changes in tracer distribution as well as its diffuse appearance throughout the body. It follows that visual detection of motion

was limited to the later uptake frames and thus corresponds to a relatively small number of frames used in kinetic modelling. This issue was also reported in the work of Lee et al.,⁸¹ in regard to automated alignment of dynamic frames of ^{82}Rb cardiac PET perfusion studies.

It may be that within a general population of patients that a multivariate analysis of MBF quality metrics and automated motion estimation approaches would provide more satisfactory and robust classification. Such a problem seems to lend itself to machine learning solutions which can combine different sources of data to make classification predictions. No other published research on this specific topic was found at the time this work was written.

5.5 Conclusions

Motion correction in cardiac PET perfusion studies based on the 3D translational motion information produced by PeTrack appeared feasible and more robust than image-registration approaches. Additional research on this application is warranted with a larger patient population and with more cases of severe motion to further develop the proposed motion correction algorithm. While the COD method demonstrated potential benefits over PeTrack like its independence of any additional equipment and its fast computation time, its use in cardiac PET perfusion studies is limited as the absolute displacement indicated by COD does not accurately represent the observed motion of the heart and necessitates the use of image-registration techniques to estimate motion. Additionally, the COD trace is inherently linked to the tracer dynamics in the body and detecting instances of patient motion prior to myocardial uptake remains challenging. Future work regarding

the classification of clinical cases that would benefit from motion correction remains as an interesting research question.

Chapter 6 Conclusions and Future Work

6.1 Summary of Findings

The motion information derived from the PeTrack ADROI algorithm was used to implement a data-driven alternative to respiratory motion tracking and gating, as well as a body-motion detection and compensation tool for cardiac PET perfusion imaging studies. This thesis described the most comprehensive application of the PeTrack algorithm in a clinical setting.

When used for respiratory gating in a general population of patients for which cardiac perfusion PET was indicated, it was shown that respiratory gating with PeTrack is feasible and its performance was comparable to one of the most commonly used hardware-based respiratory motion tracking systems. Respiratory signal quality was generally better for the optical tracking system but its efficacy for respiratory gating was hindered by its technical limitations. The gating quality of the optical system was improved using the retrospective respiratory trigger detection technique that was implemented for PeTrack in this thesis. This work also exposed shortcomings of the PeTrack algorithm that will need to be addressed before this tool could be shown to be unequivocally beneficial in the presence of significant respiratory motion.

Whole body motion correction was explored in the context of static and dynamic cardiac PET perfusion studies. For this purpose, a novel framework for including the PeTrack motion information was developed and incorporated into the research reconstruction software. A series of phantom acquisitions with relatively extreme motion showed significant benefit from motion correction using the PeTrack approach with

respect to recovery of image quality metrics like myocardial contrast-to-noise, and signal-to-noise ratios as well as the LV wall thickness (an indicator of the effective spatial resolution in the presence of motion). The same motion correction strategy was also employed for a small cohort of ^{13}N -ammonia perfusion studies for which the benefits of PeTrack-based motion correction were not as obvious. While image quality metrics generally showed improvement after motion correction, especially reduced LV wall thickness, no apparent effect could be demonstrated on the relative perfusion measurements among this group. This work suggested that patient motion using this approach was feasible and generally led to improve image quality. The clinical significance of the approach, however, may not be realized without the presence of non-returning patient motion in excess of 10 mm.

Finally, the body motion correction framework was extended to dynamic studies and absolute blood flow quantification. The data-driven centroid-of-distribution motion tracking method which was reported to be successful for dynamic PET studies was also implemented for comparison with the PeTrack approach. This work showed that tracking the motion of a fiducial marker as opposed to the centroid-of-distribution may be more robust when applied to cardiac PET perfusion imaging when motion tracking is required in the early frames before the tracer distribution has reached equilibrium in the body. Inferring patient motion from the purely data-driven motion signal was challenging as the signal was dominated by tracer dynamics. Additionally, image registration techniques did not appear to be sufficiently robust to adequately estimate patient motion from the dynamic series of motion frames. Motion correction based on 3D motion estimation directly from the PeTrack motion trace was more reliable in this context than the

approaches which used image registration. Various quality metrics related to blood flow quantification that are generally regarded to be correlated with motion severity were considered. These data suggest that motion correction was not beneficial unless patient motion magnitude exceeded 10 mm. In some cases, kinetic modelling quality metrics suggested that motion correction had adverse effects, especially when image registration was employed for motion estimation. Motion correction was thus not indicated for the majority of acquisitions in the cohort. It follows that a decision algorithm based on a combination of motion estimates and kinetic modelling quality metrics may be necessary to select cases that are most likely to benefit from motion correction.

6.2 Final Thoughts and Suggestions for Future Work

This thesis indicated that additional work is required to enhance the motion tracking signal as well as the robustness of the algorithm in the presence of high count rates associated with high tracer activity concentrations in the patient. Under these conditions, the noise in the PeTrack signal appeared to limit the accuracy of detecting respiratory triggers when the external motion amplitudes were very small. In spite of the measures implemented in ADROI to adapt the PeTrack algorithm for use in PET, marker tracking failed in several cases when marker activity was very low in comparison to the scanner count rates, i.e. less than 0.01%. To improve performance the most obvious solution is to increase the marker activity. This solution was attempted with markers that had an activity roughly three times that used for the work presented here, but their use was suspended after observing deleterious effects on the scatter estimation of the GE Discovery 690 scanner at UOHI. The activity of the marker was identified by the scanner

as existing outside the body and led to over-estimation of scatter and under-estimation of the tracer activity within the body. It follows that a careful examination of the limits of the marker activity and/or preparation of the attenuating material that surrounds the marker to mimic extension of the body contour is needed to permit increasing the marker activity.

Another important consideration is that the GE Discovery 690 PET/CT scanner is no longer a state-of -the-art system. Digital PET/CT systems are now available, some with an extended axial FOV, which exhibit much higher sensitivity, count-rate performance, and improved TOF resolution. To date, motion tracking with PeTrack has not been evaluated on one of these devices. It stands to reason that the hardware improvements would be beneficial for PeTrack signal quality as well, as the systems are likely to have improved sensitivity and specificity for detecting LORs coming from the marker which are then used for tracking. Additionally, PeTrack may be of particular interest for extended axial FOV scanners, like those engineered by the EXPLORER consortium^{192,193}, as optical motion tracking systems may be of limited use as the cameras may not be able to monitor the patient effectively from outside the long bore.

To date, tracking multiple fiducial markers has only been attempted for phantom acquisitions and has yet to be employed for clinical acquisitions. Tracking multiple markers would permit the estimation of rotations as well as translations. To perform such a task in the clinical environment would necessitate either a dedicated prospective study or a modification to current clinical protocol at our clinic which already makes use of single fiducial marker. Neither of these were seriously considered in the work presented here. There are also several limitations associated with the use of multiple markers that

should be considered. PeTrack processing time would be expected to increase with the number of markers used as only a single marker can be tracked in one instance of the algorithm. Perhaps parallel computing technique could be explored to overcome this obstacle. Additionally, a carefully designed system would likely be needed to fix the markers in place on the patient. Use of a support like this is not favourable, however, as it requires additional patient preparation and may not be tolerated well by all patients.

For future work for either evaluation or further development of PeTrack, special care should be taken in accruing larger clinical data sets where patient motion (respiratory or whole-body) is suspected to be significant. The work presented here included clinical cohorts that were randomly selected from a general population. They did not encompass enough cases with severe patient motion for which the benefits of respiratory gating and/or motion compensation could be demonstrated with confidence. For the present work, the possibility of including more studies with significant patient motion was limited for several reasons. First, there was a limitation of the software of the PET system to access list-mode data. In particular, the large data files are compressed using a proprietary technique shortly after acquisition. The decompression software failed to fully decompress large list-mode files that were acquired as part of a trial for a novel ^{18}F -based innervation tracer taking place at UOHI. These acquisitions are roughly 40 minutes in duration and good candidates for significant patient motion. It was learned, however, that the list-mode files which are required for PeTrack could not be decompressed for use. Unfortunately, time did not permit working with the vendor to overcome this issue and it was decided to make use of the 20-minute ^{13}N -ammonia perfusion studies instead. At UOHI, ^{13}N -ammonia studies are almost exclusively acquired on the older GE

Discovery 600 PET/CT system which does not have TOF capability – an important aspect of the ADROI extension of PeTrack. One acquisition was included from this scanner for the work in Chapter 4, and ^{13}N -ammonia acquisitions were few for the GE Discovery 690 PET/CT system.

The work presented in this thesis supports the clinical usefulness of the PeTrack ADROI algorithm for motion detection, estimation, and compensation in the context of cardiac perfusion PET studies. This method simplifies patient preparation compared to alternative hardware tracking systems and does not require technical integration with the PET system. Furthermore, PeTrack was used in several cases to provide patient motion information when hardware tracking systems failed during clinical use. PeTrack is easily implemented in a high throughput clinical setting and can provide patient motion information which characterizes both respiratory and body movements. To date, PeTrack ADROI has only been implemented for GE Discovery series PET/CT scanners but it could be adapted to other systems assuming that access to scanner geometry and specifications can be attained. Lastly, the high temporal resolution motion vectors provided by PeTrack could be readily incorporated into modern motion-compensated image reconstruction algorithms. Further development of PeTrack holds promise for a robust and easy-to-use motion compensation tool that can track multiple forms of patient motion.

Appendices

Appendix A Left-Ventricular Wall Segmentation from 1-D Profiles

The following is a description of the method by which left-ventricular (LV) wall regions were segmented from 1D intensity profiles. In particular, the anterior (Ant) and inferior (Inf) regions of the LV were delineated from a single image slice sampled at the mid vertical long-axis of the LV. This method was first mentioned in Section 3.2.7. As the reorientation process was already described in the main text it will not be repeated here. In this supplemental section it is assumed that the image volume of the cardiac PET study was already reoriented into the standard, short-axis representation.

An example image of the selected slice is shown in Figure A.1. In this figure, five contiguous profiles are indicated which represent the 1D intensity profiles that are used to segment the LV wall regions of interest such that their thicknesses could be estimated. The segmentation task in this instance was to determine a set of pixel indices from the 1D profiles that reflect the physiologic limits of the LV myocardium. This was done using a 1D, multi-resolution approach which is described in the following.

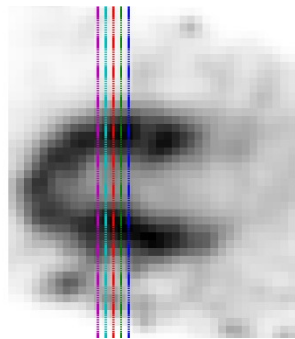


Figure A.1 Example vertical long-axis slice depicting the locations of five sampled 1D profiles. Note that the image slice shown corresponds to the smoothed volume.

The original image volume did not undergo any post-reconstruction smoothing. It thus contained the highest spatial resolution representation of the image. It is referred to here as the ‘raw’ volume. It was from this raw volume that the Ant and Inf wall region thicknesses were determined. The noise level in the raw volume makes the task of segmentation very challenging so it follows that a duplicate of the raw volume was produced and then smoothed to initialize estimates of the relevant regions of interest within the profiles. The smoothing kernel was a 3D Gaussian volume with a FWHM of 7.5 mm with a size of $5 \times 5 \times 5$ voxels. Figure A.2 shows the 1D intensity profiles extracted from the raw volume of the case shown in Figure A.1 and it is apparent that identification of the Ant and Inf wall limits is not obvious. An assumption was made in the development of this approach that over the short-axis span of the five profiles a single set of limits could be generated that would accurately represent the limits of all of the five profiles. Following this assumption, the five 1D profiles from each of the raw and smooth volumes were averaged along the short-axis dimension to include the information from all five profiles to aid the estimation of a single set of limits for each wall region. The resulting mean profiles are referred to as the ‘avgRaw’ and ‘smooth’ profiles.

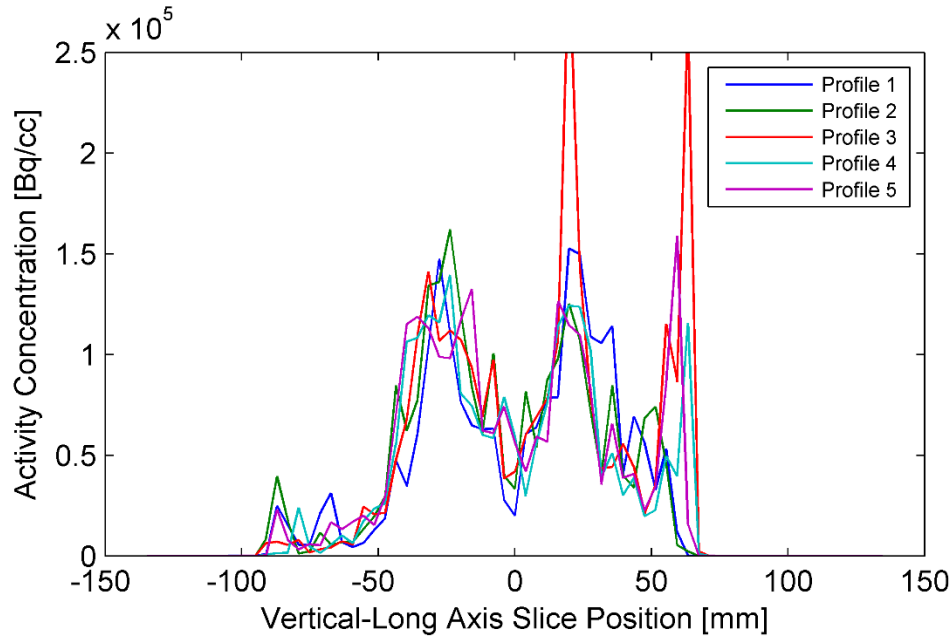


Figure A.2 Example of five contiguous 1-D profiles extracted from a raw volume. The vertical-long axis slice position is shown on the horizontal axis. A position equal to, less than, and greater than 0 mm corresponds approximately to the center of LV blood pool, the anterior region, and the inferior region, respectively. The activity concentration, i.e. intensity, is indicated on the vertical axis. In this example the Ant wall region is located approximately between -40 mm and -10 mm. The Inf wall region is located approximately between 10 mm and 40 mm. Note also the extracardiac uptake region found near 50-60 mm.

Additionally, a 1-D Gaussian smoothing kernel (span of 3 pixels and FWHM of 2.25 pixels) was also applied to the smooth profile. A simple gradient-based algorithm was then applied to the smooth profile to determine a set of maxima and minima (peaks and troughs) that marked changes in the sign of the gradient from negative to positive, or visa versa. A series of tests was applied to the initial set of peaks to discriminate against those that are unlikely to correspond to the maxima that are expected to be observed at the Ant and Inf wall. These logical gates imposed lower limits on the ratio of their heights to that of the highest peak ($> 40\%$) as well as their prominence over their nearest trough ($> 5\%$).

The specific limits were determined empirically. The final Ant and Inf peak positions were taken as the two that encompassed the central position of the 1-D profiles. The position of the LV blood pool was denoted by the lowest trough found between the two peaks. With these reference regions in hand, the limits on the Ant and Inf walls could be determined. Figure A.3 shows the avgRaw and smooth profiles corresponding to the five 1-D profiles shown in Figure A.2.

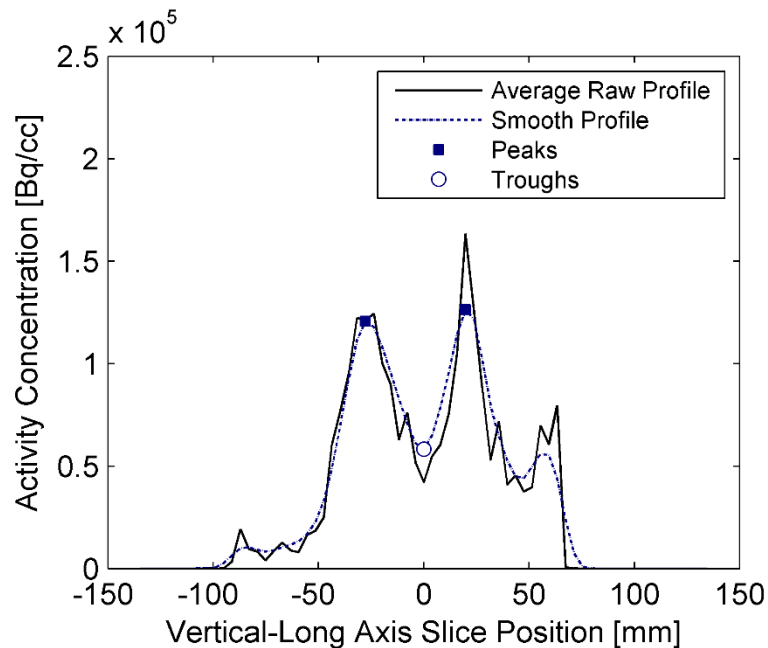


Figure A.3 AvgRaw (solid, black) and smooth (dashed, blue) profiles of the five 1-D profiles shown previously in Figure A.1. The Ant and Inf wall peaks are indicated by blue squares and the LV blood pool position, trough, is shown as an empty circle.

Once the peaks representing center of the Ant and Inf walls are found, the wall segment limits were then determined on the smooth profile and later updated using the avgRaw profile. Let the peak-trough activity value difference to be Δ . Beginning with the smooth profile, the limits were set at, or just below, the point at which the activity is no more than 0.1Δ above the trough value, i.e. blood pool activity. The pixel position that satisfied

this criterion, on both sides of the peak, was marked. Then using the avgRaw profile, a search was performed for a point lower than the LV blood pool activity of the smooth profile where an inflection occurred. The search space was limited to the region between the smooth profile peak and the initial limit, i.e. the updated limit could not be further separated from the peak than the initial limit. This process was applied in the following order: outer Ant wall, inner Ant wall, inner Inf wall, and outer Inf wall. Its aim was to constrain the domain of each wall region to myocardium and exclude the blood pool and extracardiac regions. The final segmented wall regions are indicated in Figure A.4, which is a duplicate of Figure A.3 except that the limits of the Ant and Inf walls are denoted and the segmented Ant and Inf regions are shown in red and green, respectively.

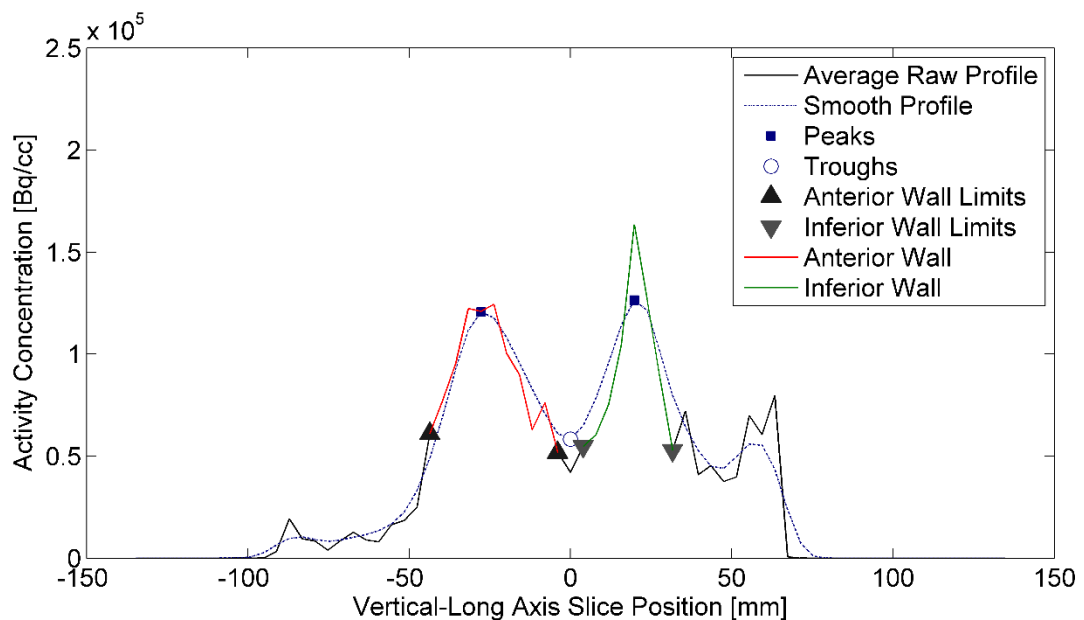


Figure A.4 Replication of the avgRaw and smooth profiles shown in Figure A.3 but with the addition of demarcations of the Ant and Inf wall limits (upward and downward triangles, respectively) and segmented regions (red and green lines, respectively).

It is important to note that this process was executed in a completely automated fashion such that user bias did not affect the thickness measurements. Lastly, the segmentation results were visually inspected for all images included in this study to evaluate their success. In doing so, no cases were found that violated the assumption made previously that a single set of limits would accurately represent the five unique short-axis positions.

Appendix B Elastix Image Registration Input Parameters

The following text is a duplication in the input parameters passed to the Elastix image registration software package. This information was first cited in Section 5.2.3.

(FixedInternalImagePixelType "float")

(FixedImageDimension 3)

(MovingInternalImagePixelType "float")

(MovingImageDimension 3)

(Registration "MultiResolutionRegistration")

(FixedImagePyramid "FixedSmoothingImagePyramid")

(MovingImagePyramid "MovingSmoothingImagePyramid")

(Interpolator "BSplineInterpolator")

(Metric "AdvancedMattesMutualInformation")

(Optimizer "AdaptiveStochasticGradientDescent")

(ResampleInterpolator "FinalBSplineInterpolator")

(Resampler "DefaultResampler")

(Transform "EulerTransform")

(NumberOfResolutions 3)

(ImagePyramidSchedule 8 8 8 4 4 1 1 1)

(AutomaticTransformInitialization "true")

(AutomaticScalesEstimation "true")

(HowToCombineTransforms "Compose")

(ComputeZYX "true")

(MaximumNumberOfIterations 500)

(NumberOfHistogramBins 16)

(FixedLimitRangeRatio 0.001 0.01 0.01)

(MovingLimitRangeRatio 0.001 0.01 0.01)

(FixedKernelBSplineOrder 1)

(MovingKernelBSplineOrder 3)

(WriteTransformParametersEachIteration "false")

(WriteTransformParametersEachResolution "false")

(WriteResultImage "true")

(CompressResultImage "false")

(ResultImageFormat "mhd")

(ResultImagePixelType "float")

(ShowExactMetricValue "false")

(ErodeMask "true")

(UseDifferentiableOverlap "false")

(ImageSampler "Random")

(NumberOfSpatialSamples 2000)

(NewSamplesEveryIteration "true")

(BSplineInterpolationOrder 1)

(FinalBSplineInterpolationOrder 3)

(DefaultPixelValue 0)

References

1. Röntgen W. Sitzungsberichte Würzburger Physik-med. *Gesellschaft*. 1895;137:132-141. <https://web.lemoyne.edu/~giunta/ROENTGEN.HTML>.
2. Taylor JR, Zafiratos CD, Dubson MA. *Modern Physics For Scientists and Engineers, 2nd Edition*. Upper Saddle River, NJ: Pearson Prentice Hall; 2003.
3. Dalton J. On the Absorption of Gases by Water and other Liquids. In: *Memoirs of the Literary and Philosophical Society of Manchester*. 2nd ed. London: R. Bickerstaff, Strand; 1805:271-287.
4. Thomson JJ. XL. Cathode Rays . *London, Edinburgh, Dublin Philos Mag J Sci*. 1897;44(269):293-316. doi:10.1080/14786449708621070
5. Rutherford E. LXXIX. The scattering of α and β particles by matter and the structure of the atom. *London, Edinburgh, Dublin Philos Mag J Sci*. 1911;21(125):669-688. doi:10.1080/14786440508637080
6. Rutherford E. LIV. Collision of α particles with light atoms . IV. An anomalous effect in nitrogen . *London, Edinburgh, Dublin Philos Mag J Sci*. 1919;37(222):581-587. doi:10.1080/14786440608635919
7. Chadwick J. Possible Existence of a Neutron. *Nature*. 1932;129(3252):312-312. doi:10.1038/129312a0
8. Becquerel H. Sur les radiations invisibles émises par les corps phosphorescents. *Comptes-rendus l'Académie des Sci séance du 1er mars 1896*. 1896:501-502.
9. Sklodowska Curie M. Rays Emitted by Compounds of Uranium and of Thorium. *Comptes Rendus Hebd des Séance l'Académie des Sci Séance 12 April 1898*.

1898;126:1101-1103.

10. Levin C. Basic Physics of Radionuclide Imaging. In: Wernick MN, Aarsvold JNBT-ET, eds. *Emission Tomography*. San Diego: Academic Press; 2004:53-88.
doi:<https://doi.org/10.1016/B978-012744482-6.50007-7>
11. Krane KS. *Introductory Nuclear Physics, 3rd Edition*. Hoboken, NJ: John Wiley & Sons, Ltd; 1987.
12. IAEA. *Nuclear Medicine Physics*. Vienna: International Atomic Energy Agency; 2015. <https://www.iaea.org/publications/10368/nuclear-medicine-physics>.
13. Knoll GF. *Radiation Detection and Measurement*. 3rd ed. New York: John Wiley & Sons, Ltd; 2000.
14. Bé M-M, Chisté V, Dulieu C, et al. *Table of Radionuclides*. Vol 8. Pavillon de Breteuil, F-92310 Sèvres, France: Bureau International des Poids et Mesures; 2016.
http://www.bipm.org/utis/common/pdf/monographieRI/Monographie_BIPM-5_Tables_Vol8.pdf.
15. Rutherford Ernest. *Radio-Activity*. (Neville FH, Whetham FA, eds.). Cambridge, UK: Cambridge: At the University Press; 1904.
<https://www.biodiversitylibrary.org/item/127262>.
16. Bateman, H. The solution of a system of differential equations occurring in the theory of radio-active transformations. *Proc Cambridge Phil Soc*, 1908. 1908;15:423-427. <http://ci.nii.ac.jp/naid/10020715519/en/>. Accessed March 6, 2020.
17. IAEA. *Diagnostic Radiology Physics*. Vienna: International Atomic Energy

- Agency; 2014. <https://www.iaea.org/publications/8841/diagnostic-radiology-physics>.
18. Bethe H. Zur Theorie des Durchgangs schneller Korpuskularstrahlen durch Materie. *Ann Phys*. 1930;397(3):325-400. doi:10.1002/andp.19303970303
 19. Levin CS, Hoffman EJ. Calculation of positron range and its effect on the fundamental limit of positron emission tomography system spatial resolution. *Phys Med Biol*. 1999;44(3):781-799. doi:10.1088/0031-9155/44/3/019
 20. Iwata K, Greaves RG, Surko CM. γ -ray spectra from positron annihilation on atoms and molecules. *Phys Rev A - At Mol Opt Phys*. 1997;55(5):3586-3604. doi:10.1103/PhysRevA.55.3586
 21. Wernick MN, Aarsvold JN. Introduction to Emission Tomography. In: Wernick MN, Aarsvold JNBT-ET, eds. *Emission Tomography*. 1st ed. San Diego: Academic Press; 2004:11-23. doi:<https://doi.org/10.1016/B978-012744482-6.50005-3>
 22. Bailey DL, Karp JS, Surti S. Physics and Instrumentation in PET. In: *Positron Emission Tomography*. London: Springer-Verlag; 2005:13-39. doi:10.1007/1-84628-007-9_2
 23. Wilkinson F. Scintillators. In: Wernick MN, Aarsvold JNBT-ET, eds. *Emission Tomography*. San Diego: Academic Press; 2004:229-254. doi:<https://doi.org/10.1016/B978-012744482-6.50016-8>
 24. Pichler BJ, Ziegler SI. Photodetectors. In: Wernick MN, Aarsvold JNBT-ET, eds. *Emission Tomography*. San Diego: Academic Press; 2004:255-267. doi:<https://doi.org/10.1016/B978-012744482-6.50017-X>

25. Ghassemi A, Kobayashi K, Sato K. *A Technical Guide to Silicon Photomultipliers (MPPC)*. Hamamatsu City, Japan; 2018.
<https://hub.hamamatsu.com/us/en/technical-note/sipm-mppc-technical-note/index.html>.
26. Zhang J, Maniawski P, Knopp M V. Performance evaluation of the next generation solid-state digital photon counting PET/CT system. *EJNMMI Res.* 2018;8(1):97.
doi:10.1186/s13550-018-0448-7
27. Bettinardi V, Presotto L, Rapisarda E, Picchio M, Gianolli L, Gilardi MC. Physical Performance of the new hybrid PET/CT Discovery-690. *Med Phys.* 2011;38(10):5394-5411. doi:10.1118/1.3635220
28. Kinahan PE, Defrise M, Clackdoyle R. Analytic Image Reconstruction Methods. In: Wernick MN, Aarsvold JNBT-ET, eds. *Emission Tomography*. San Diego: Academic Press; 2004:421-442. doi:<https://doi.org/10.1016/B978-012744482-6.50023-5>
29. Bailey DL. Data Acquisition and Performance Characterization in PET. In: *Positron Emission Tomography*. London: Springer-Verlag; 2006:41-62.
doi:10.1007/1-84628-007-9_3
30. Ishii K, Orihara H, Matsuzawa T, Binkley DM, Nutt R. High resolution time-of-flight positron emission tomograph. *Rev Sci Instrum.* 1990;61(12):3755-3762.
doi:10.1063/1.1141549
31. Lewellyn T, Karp J. PET Systems. In: Wernick MN, Aarsvold JNBT-ET, eds. *Emission Tomography*. San Diego: Academic Press; 2004:179-194.
doi:<https://doi.org/10.1016/B978-012744482-6.50013-2>

32. Surti S. Update on time-of-flight PET imaging. *J Nucl Med.* 2015;56(1):98-105.
doi:10.2967/jnumed.114.145029
33. Meikle SR, Badawi RD. Quantitative Techniques in PET. In: *Positron Emission Tomography*. London: Springer-Verlag; 2006:93-126. doi:10.1007/1-84628-007-9_5
34. Strother SC, Casey ME, Hoffman EJ. Measuring PET Scanner Sensitivity: Relating Countrates to Image Signal-to-Noise Ratios using Noise Equivalent Counts. *IEEE Trans Nucl Sci.* 1990;37(2):783-788. doi:10.1109/23.106715
35. Derenzo SE, Zaklad H, Budinger TF. Analytical Study of a High-Resolution Positron Ring Detector System for Transaxial Reconstruction Tomography. *J Nucl Med.* 1975;16(12):1166-1173.
<http://jnm.snmjournals.org/content/16/12/1166.short>.
36. Cranley K, Millar R, Bell TK. Correction for deadtime losses in a gamma camera/data analysis system. *Eur J Nucl Med.* 1980;5(4):377-382.
doi:10.1007/BF00445626
37. Watson CC, Townsend DW, Bendriem B. PET/CT Systems. In: Wernick MN, Aarsvold JNBT-ET, eds. *Emission Tomography*. San Diego: Academic Press; 2004:195-212. doi:https://doi.org/10.1016/B978-012744482-6.50014-4
38. Townsend DW. Positron Emission Tomography/Computed Tomography. *Semin Nucl Med.* 2008;38(3):152-166.
doi:http://dx.doi.org/10.1053/j.semnuclmed.2008.01.003
39. Watson CC. New, faster, image-based scatter correction for 3D PET. *IEEE Trans Nucl Sci.* 2000;47(4 Part 2):1587-1594. doi:10.1109/23.873020

40. Watson CC, Newport D, Casey ME, DeKemp RA, Beanlands RS, Schmand M. Evaluation of simulation-based scatter correction for 3D PET cardiac imaging. In: *IEEE Nuclear Science Symposium & Medical Imaging Conference*. Vol 3. IEEE; 1995:1373-1377. doi:10.1109/nssmic.1995.500258
41. Dempster AP, Laird NM, Rubin DB. Maximum likelihood from incomplete data via the EM algorithm. *J R Stat Soc Ser B*. 1977;39(1):1-38. <https://www.jstor.org/stable/2984875>.
42. Shepp LA, Vardi Y. Maximum Likelihood Reconstruction for Emission Tomography. *IEEE Trans Med Imaging*. 1982;1(2):113-122. doi:10.1109/TMI.1982.4307558
43. Defrise M, Kinahan PE, Michel CJ. Image Reconstruction Algorithms in PET. In: *Positron Emission Tomography*. London: Springer-Verlag; 2006:63-91. doi:10.1007/1-84628-007-9_4
44. Lalush DS, Wernick MN. Iterative Image Reconstruction. In: Wernick MN, Aarsvold JNBT-ET, eds. *Emission Tomography*. San Diego: Academic Press; 2004:443-472. doi:<https://doi.org/10.1016/B978-012744482-6.50024-7>
45. Hudson HM, Larkin RS. Accelerated Image Reconstruction Using Ordered Subsets of Projection Data. *IEEE Trans Med Imaging*. 1994;13(4):601-609. doi:10.1109/42.363108
46. Jarvis S SS. Cardiac system 1: anatomy and physiology. *Nurs Times [online]*. 2018;114(2):34-37. <https://www.nursingtimes.net/clinical-archive/cardiovascular-clinical-archive/cardiac-system-1-anatomy-and-physiology-29-01-2018/>. Accessed February 10, 2020.

47. Cerqueira MD, Weissman NJ, Dilsizian V, et al. Standardized myocardial segmentation and nomenclature for tomographic imaging of the heart: A Statement for Healthcare Professionals from the Cardiac Imaging Committee of the Council on Clinical Cardiology of the American Heart Association. *Circulation*. 2002;105(4):539-542. doi:10.1161/hc0402.102975
48. Gordan R, Gwathmey JK, Xie L-H. Autonomic and endocrine control of cardiovascular function. *World J Cardiol*. 2015;7(4):204. doi:10.4330/wjc.v7.i4.204
49. Murthy VL, Naya M, Foster CR, et al. Improved cardiac risk assessment with noninvasive measures of coronary flow reserve. *Circulation*. 2011;124(20):2215-2224. doi:10.1161/CIRCULATIONAHA.111.050427
50. Dorbala S, Hachamovitch R, Curillova Z, et al. Incremental Prognostic Value of Gated Rb-82 Positron Emission Tomography Myocardial Perfusion Imaging Over Clinical Variables and Rest LVEF. *JACC Cardiovasc Imaging*. 2009;2(7):846-854. doi:10.1016/j.jcmg.2009.04.009
51. Herzog BA, Husmann L, Valenta I, et al. Long-Term Prognostic Value of 13N-Ammonia Myocardial Perfusion Positron Emission Tomography. *J Am Coll Cardiol*. 2009;54(2):150-156. doi:10.1016/j.jacc.2009.02.069
52. Dilsizian V, Bacharach SL, Beanlands RS, et al. ASNC imaging guidelines/SNMMI procedure standard for positron emission tomography (PET) nuclear cardiology procedures. *J Nucl Cardiol*. 2016;23(5):1187-1226. doi:10.1007/s12350-016-0522-3
53. Morris ED, Endres CJ, Schmidt KC, Christian BT, Muzic RF, Fisher RE. Kinetic

- Modeling in Positron Emission Tomography. In: Wernick MN, Aarsvold JN, eds. *Emission Tomography*. San Diego: Elsevier; 2004:499-540. doi:10.1016/B978-012744482-6.50026-0
54. Levelt E, Rodgers CT, Clarke WT, et al. Cardiac energetics, oxygenation, and perfusion during increased workload in patients with type 2 diabetes mellitus. *Eur Heart J*. 2015;37(46):3461-3469. doi:10.1093/eurheartj/ehv442
55. Beckman JA, Creager MA. Vascular complications of diabetes. *Circ Res*. 2016;118(11):1771-1785. doi:10.1161/CIRCRESAHA.115.306884
56. Parkash R, deKemp RA, Ruddy TD, et al. Potential utility of rubidium 82 PET quantification in patients with 3-vessel coronary artery disease. *J Nucl Cardiol*. 2004;11(4):440-449. doi:10.1016/j.nuclcard.2004.04.005
57. Ziadi MC, DeKemp RA, Williams K, et al. Does quantification of myocardial flow reserve using rubidium-82 positron emission tomography facilitate detection of multivessel coronary artery disease? *J Nucl Cardiol*. 2012;19(4):670-680. doi:10.1007/s12350-011-9506-5
58. Camici PG, Rimoldi OE, Crea F. Coronary Microvascular Dysfunction. In: *Chronic Coronary Artery Disease*. Philadelphia: Elsevier; 2018:55-68. doi:10.1016/B978-0-323-42880-4.00005-4
59. Driessen RS, Raijmakers PG, Stuijzand WJ, Knaapen P. Myocardial perfusion imaging with PET. *Int J Cardiovasc Imaging*. 2017;33(7):1021-1031. doi:10.1007/s10554-017-1084-4
60. Juneau D, Erthal F, Ohira H, et al. Clinical PET Myocardial Perfusion Imaging and Flow Quantification. *Cardiol Clin*. 2016;34(1):69-85.

doi:10.1016/j.ccl.2015.07.013

61. Yu M, Nekolla SG, Schwaiger M, Robinson SP. The next generation of cardiac positron emission tomography imaging agents: Discovery of flurpiridaz F-18 for detection of coronary disease. *Semin Nucl Med.* 2011;41(4):305-313.
doi:10.1053/j.semnuclmed.2011.02.004
62. Calnon DA. Will 18F flurpiridaz replace 82rubidium as the most commonly used perfusion tracer for PET myocardial perfusion imaging? *J Nucl Cardiol.* 2019;26(6):2031-2033. doi:10.1007/s12350-017-1153-z
63. Maddahi J, Bengel F, Czernin J, et al. Dosimetry, biodistribution, and safety of flurpiridaz F 18 in healthy subjects undergoing rest and exercise or pharmacological stress PET myocardial perfusion imaging. *J Nucl Cardiol.* 2019;26(6):2018-2030. doi:10.1007/s12350-018-01484-z
64. Moody JB, Poitrasson-Rivière A, Hagio T, et al. Added value of myocardial blood flow using 18F-flurpiridaz PET to diagnose coronary artery disease: The flurpiridaz 301 trial. *J Nucl Cardiol.* January 2020:1-17. doi:10.1007/s12350-020-02034-2
65. Powell J, O'Neil JP. Production of [15O]water at low-energy proton cyclotrons. *Appl Radiat Isot.* 2006;64(7):755-759. doi:10.1016/j.apradiso.2006.02.096
66. Nkepan G, Houson H, Gali H, Awasthi V. Feasibility of 13N-ammonia production by 13C(p,n)13N reaction on a 7.5 MeV cyclotron. *J Nucl Med.* 2018;59(supplement 1):663.
http://jnm.snmjournals.org/content/59/supplement_1/663.abstract.
67. Klein R, Beanlands RSB, deKemp RA. Quantification of myocardial blood flow

and flow reserve: Technical aspects. *J Nucl Cardiol*. 2010;17(4):555-570.
doi:10.1007/s12350-010-9256-9

68. Ruth TJ, Wolf AP. Absolute Cross Sections for the Production of ^{18}F via the $^{18}\text{O}(\text{p}, \text{n})^{18}\text{F}$ Reaction. *Radiochim Acta*. 1979;26(1):21-24.
doi:10.1524/ract.1979.26.1.21
69. deKemp RA, Renaud JM, Klein R, Beanlands RSB. Radionuclide Tracers for Myocardial Perfusion Imaging and Blood Flow Quantification. *Cardiol Clin*. 2016;34(1):37-46. doi:10.1016/j.ccl.2015.08.001
70. Lortie M, Beanlands RSB, Yoshinaga K, Klein R, DaSilva JN, DeKemp RA. Quantification of myocardial blood flow with ^{82}Rb dynamic PET imaging. *Eur J Nucl Med Mol Imaging*. 2007;34(11):1765-1774. doi:10.1007/s00259-007-0478-2
71. Schelbert HR, Phelps ME, Huang SC, et al. N-13 ammonia as an indicator of myocardial blood flow. *Circulation*. 1981;63(6 I):1259-1272.
doi:10.1161/01.CIR.63.6.1259
72. Harms HJ, Knaapen P, De Haan S, Halbmeijer R, Lammertsma AA, Lubberink M. Automatic generation of absolute myocardial blood flow images using ^{15}O H_2O and a clinical PET/CT scanner. *Eur J Nucl Med Mol Imaging*. 2011;38(5):930-939.
doi:10.1007/s00259-011-1730-3
73. Nekolla SG, Reder S, Saraste A, et al. Evaluation of the novel myocardial perfusion positron-emission tomography tracer ^{18}F -BMS-747158-02: comparison to ^{13}N -ammonia and validation with microspheres in a pig model. *Circulation*. 2009;119(17):2333-2342. doi:10.1161/CIRCULATIONAHA.108.797761
74. Klein R, Celiker-Guler E, Rotstein BH, DeKemp RA. PET and SPECT Tracers for

- Myocardial Perfusion Imaging. *Semin Nucl Med.* 2020;50(3):208-218.
doi:10.1053/j.semnuclmed.2020.02.016
75. Germino M, Carson RE. Cardiac-gated parametric images from 82 Rb PET from dynamic frames and direct 4D reconstruction. *Med Phys.* 2018;45(2):639-654.
doi:10.1002/mp.12710
76. Bateman TM, Case JA. Variability in normal myocardial blood flow measurements: Physiologic, methodologic, or protocol related? *J Nucl Cardiol.* 2015;22(1):85-88. doi:10.1007/s12350-014-0007-1
77. Piccinelli M, Votaw JR, Garcia E V. Motion Correction and Its Impact on Absolute Myocardial Blood Flow Measures with PET. *Curr Cardiol Rep.* 2018;20(5):34. doi:10.1007/s11886-018-0977-8
78. Rahmim A, Dinelle K, Cheng J-C, et al. Accurate Event-Driven Motion Compensation in High-Resolution PET Incorporating Scattered and Random Events. *IEEE Trans Med Imaging.* 2008;27(8):1018-1033.
doi:10.1109/TMI.2008.917248
79. Livieratos L, Rajappan K, Stegger L, Schafers K, Bailey DL, Camici PG. Respiratory gating of cardiac PET data in list-mode acquisition. *Eur J Nucl Med Mol Imaging.* 2006;33(5):584-588. doi:10.1007/s00259-005-0031-0
80. McLeish K, Hill DLG, Atkinson D, Blackall JM, Razavi R. A study of the motion and deformation of the heart due to respiration. *IEEE Trans Med Imaging.* 2002;21(9):1142-1150. doi:10.1109/TMI.2002.804427
81. Lee BC, Moody JB, Poitrasson-Rivière A, et al. Automated dynamic motion correction using normalized gradient fields for 82rubidium PET myocardial blood

- flow quantification. *J Nucl Cardiol*. November 2018. doi:10.1007/s12350-018-01471-4
82. Hunter CRRN, Klein R, Beanlands RS, DeKemp RA. Patient motion effects on the quantification of regional myocardial blood flow with dynamic PET imaging. *Med Phys*. 2016;43(4):1829-1840. doi:10.1118/1.4943565
83. Lee BC, Moody JB, Poitrasson-Rivière A, et al. Blood pool and tissue phase patient motion effects on 82rubidium PET myocardial blood flow quantification. *J Nucl Cardiol*. 2019;26(6):1918-1929. doi:10.1007/s12350-018-1256-1
84. Rubeaux M, Doris MK, Alessio A, Slomka PJ. Enhancing Cardiac PET by Motion Correction Techniques. *Curr Cardiol Rep*. 2017;19(2):14. doi:10.1007/s11886-017-0825-2
85. Lu Y, Liu C. Patient motion correction for dynamic cardiac PET: Current status and challenges. *J Nucl Cardiol*. November 2018:1-4. doi:10.1007/s12350-018-01513-x
86. Kortelainen MJ, Koivumäki TM, Vauhkonen MJ, Hakulinen MA. Effect of respiratory motion on cardiac defect contrast in myocardial perfusion SPECT: a physical phantom study. *Ann Nucl Med*. 2019;33(5):305-316. doi:10.1007/s12149-019-01335-y
87. Kortelainen MJ, Koivumäki TM, Vauhkonen MJ, et al. Respiratory motion reduction with a dual gating approach in myocardial perfusion SPECT: Effect on left ventricular functional parameters. *J Nucl Cardiol*. 2018;25(5):1633-1641. doi:10.1007/s12350-017-0844-9
88. Bettinardi V, Picchio M, Muzio N Di, Gilardi MC. Motion Management in

Positron Emission Tomography/Computed Tomography for Radiation Treatment Planning. *Semin Nucl Med.* 2012;42(5):289-307.

doi:<http://dx.doi.org/10.1053/j.semnuclmed.2012.04.001>

89. Kesner AL. The relevance of data driven motion correction in diagnostic PET. *Eur J Nucl Med Mol Imaging.* 2017;44(13):2326-2327. doi:10.1007/s00259-017-3794-1
90. Xu T, Wong JT, Shikhaliev PM, Ducote JL, Al-Ghazi MS, Molloy S. Real-time tumor tracking using implanted positron emission markers: Concept and simulation study. *Med Phys.* 2006;33(7):2598-2609. doi:10.1118/1.2207213
91. Chamberland M. Application of Three-Dimensional Motion Tracking of Low-Activity Fiducial Positron-Emitting Markers in Radiation Therapy and Positron Emission Tomography [PhD Thesis]. Carleton University. 2015.
doi:10.22215/etd/2015-10992
92. Chamberland MJP, DeKemp RA, Xu T. Motion tracking of low-activity fiducial markers using adaptive region of interest with list-mode positron emission tomography. *Med Phys.* 2020;47(8):3402-3414. doi:10.1002/mp.14206
93. Djukelic M, Waterhouse D, Toh R, et al. Evaluation of a mobile C-arm cone-beam CT in interstitial high-dose-rate prostate brachytherapy treatment planning. *J Med Radiat Sci.* 2019;66(2):112-121. doi:10.1002/jmrs.331
94. Bettinardi V, De Bernardi E, Presotto L, Gilardi MC. Motion-tracking hardware and advanced applications in PET and PET/CT. *PET Clin.* 2013;8(1):11-28.
doi:10.1016/j.cpet.2012.09.008
95. Bloomfield PM, Spinks TJ, Reed J, et al. The design and implementation of a

- motion correction scheme for neurological PET. *Phys Med Biol.* 2003;48(8):959-978. doi:10.1088/0031-9155/48/8/301
96. Jianhua Yan, Planeta-Wilson B, Carson RE. Direct 4-D PET List Mode Parametric Reconstruction With a Novel EM Algorithm. *IEEE Trans Med Imaging.* 2012;31(12):2213-2223. doi:10.1109/TMI.2012.2212451
97. Picard Y, Thompson CJ. Motion correction of PET images using multiple acquisition frames. *IEEE Trans Med Imaging.* 1997;16(2):137-144. doi:10.1109/42.563659
98. Feng B, Bruyant PP, Pretorius PH, et al. Estimation of the Rigid-Body Motion From Three-Dimensional Images Using a Generalized Center-of-Mass Points Approach. *IEEE Trans Nucl Sci.* 2006;53(5):2712-2718. doi:10.1109/TNS.2006.882747
99. Mukherjee JM, Lindsay C, Mukherjee A, et al. Improved frame-based estimation of head motion in PET brain imaging. *Med Phys.* 2016;43(5):2443-2454. doi:10.1118/1.4946814
100. Nehmeh SA, Erdi YE. Respiratory Motion in Positron Emission Tomography/Computed Tomography: A Review. *Semin Nucl Med.* 2008;38(3):167-176. doi:http://dx.doi.org/10.1053/j.semnuclmed.2008.01.002
101. Wells RG, Ruddy TD, DeKemp RA, DaSilva JN, Beanlands RS. Single-phase CT aligned to gated PET for respiratory motion correction in cardiac PET/CT. *J Nucl Med.* 2010;51(8):1182-1190. doi:10.2967/jnumed.109.070011
102. Chi P-CM, Balter P, Luo D, Mohan R, Pan T. Relation of external surface to internal tumor motion studied with cine CT. *Med Phys.* 2006;33(9):3116-3123.

doi:10.1118/1.2241993

103. Li XA, Stepaniak C, Gore E. Technical and dosimetric aspects of respiratory gating using a pressure-sensor motion monitoring system. *Med Phys*. 2005;33(1):145-154. doi:10.1118/1.2147743
104. Otani Y, Fukuda I, Tsukamoto N, et al. A comparison of the respiratory signals acquired by different respiratory monitoring systems used in respiratory gated radiotherapy. *Med Phys*. 2010;37(12):6178-6186. doi:10.1118/1.3512798
105. Ozhasoglu C, Murphy MJ. Issues in respiratory motion compensation during external-beam radiotherapy. *Int J Radiat Oncol Biol Phys*. 2002;52(5):1389-1399. doi:10.1016/S0360-3016(01)02789-4
106. Kimura T, Hirokawa Y, Murakami Y, et al. Reproducibility of organ position using voluntary breath-hold method with spirometer for extracranial stereotactic radiotherapy. *Int J Radiat Oncol Biol Phys*. 2004;60(4):1307-1313. doi:10.1016/j.ijrobp.2004.07.718
107. Ha JK, Perlow DB, Yi BY, Yu CX. On the sources of drift in a turbine-based spirometer. *Phys Med Biol*. 2008;53(16):4269-4283. doi:10.1088/0031-9155/53/16/004
108. Boucher L, Rodrigue S, Lecomte R, Bénard F. Respiratory gating for 3-dimensional PET of the thorax: feasibility and initial results. *J Nucl Med*. 2004;45(2):214-219. <http://www.ncbi.nlm.nih.gov/pubmed/14960638>. Accessed May 28, 2019.
109. Polycarpou I, Tsoumpas C, Marsden PK. Analysis and comparison of two methods for motion correction in PET imaging. *Med Phys*. 2012;39(10):6474-6483.

doi:10.1118/1.4754586

110. Robson PM, Trivieri M, Karakatsanis NA, et al. Correction of respiratory and cardiac motion in cardiac PET/MR using MR-based motion modeling. *Phys Med Biol.* 2018;63(22):225011. doi:10.1088/1361-6560/aaea97
111. Klein GJ, Reutter BW, Botvinick EH, Budinger TF, Huesman RH. Fine-scale motion detection using intrinsic list mode PET information. In: *Proceedings IEEE Workshop on Mathematical Methods in Biomedical Image Analysis (MMBIA 2001)*. Kauai, HI, USA: IEEE Comput. Soc.; 2001:71-78.
doi:10.1109/MMBIA.2001.991701
112. Kesner AL, Kuntner C. A new fast and fully automated software based algorithm for extracting respiratory signal from raw PET data and its comparison to other methods. *Med Phys.* 2010;37(10):5550-5559. doi:10.1118/1.3483784
113. Schleyer PJ, O'Doherty MJ, Barrington SF, Marsden PK. Retrospective data-driven respiratory gating for PET/CT. *Phys Med Biol.* 2009;54(7):1935-1950.
doi:10.1088/0031-9155/54/7/005
114. Thielemans K, Rathore S, Engbrant F, Razifar P. Device-less gating for PET/CT using PCA. In: *2011 IEEE Nuclear Science Symposium Conference Record*. IEEE; 2011:3904-3910. doi:10.1109/NSSMIC.2011.6153742
115. He J, O'Keefe GJ, Gong SJ, et al. A Novel Method for Respiratory Motion Gated With Geometric Sensitivity of the Scanner in 3D PET. *IEEE Trans Nucl Sci.* 2008;55(5):2557-2565. doi:10.1109/TNS.2008.2001187
116. Büther F, Dawood M, Stegger L, et al. List Mode-Driven Cardiac and Respiratory Gating in PET. *J Nucl Med.* 2009;50(5):674-681. doi:10.2967/jnumed.108.059204

117. Feng T, Wang J, Sun Y, Zhu W, Dong Y, Li H. Self-Gating: An Adaptive Center-of-Mass Approach for Respiratory Gating in PET. *IEEE Trans Med Imaging*. 2018;37(5):1140-1148. doi:10.1109/TMI.2017.2783739
118. Ren S, Jin X, Chan C, et al. Data-driven event-by-event respiratory motion correction using TOF PET list-mode centroid of distribution. *Phys Med Biol*. 2017;62(12):4741-4755. doi:10.1088/1361-6560/aa700c
119. Lu Y, Gallezot J-D, Naganawa M, et al. Data-driven voluntary body motion detection and non-rigid event-by-event correction for static and dynamic PET. *Phys Med Biol*. 2019;64(6):065002. doi:10.1088/1361-6560/ab02c2
120. Naum AA, Laaksonen MS, Tuunanen H, et al. Motion detection and correction for dynamic cardiac PET water studies. *J Nucl Cardiol*. 2005;12(2):S44-. doi:<http://dx.doi.org/10.1016/j.nuclcard.2004.12.146>
121. Nazarpour B, Shamsaei M, Rajabi H. Correction of head movements in positron emission tomography using point source tracking system: A simulation study. *Ann Nucl Med*. 2012;26(1):7-15. doi:10.1007/s12149-011-0532-9
122. Büther F, Ernst I, Hamill J, et al. External radioactive markers for PET data-driven respiratory gating in positron emission tomography. *Eur J Nucl Med Mol Imaging*. 2013;40(4):602-614. doi:10.1007/s00259-012-2313-7
123. Nehmeh SA, Erdi YE, Meirelles GSP, et al. Deep-inspiration breath-hold PET/CT of the thorax. *J Nucl Med*. 2007;48(1):22-26. <http://www.ncbi.nlm.nih.gov/pubmed/17204695>. Accessed January 8, 2020.
124. Benz DC, Fuchs TA. Breathless or breathtaking: Respiratory motion correction. *J Nucl Cardiol*. 2018;25(2):429-432. doi:10.1007/s12350-016-0590-4

125. Benz DC, Buechel RR. How to stop breathing: On the matter of getting respiratory motion under control. *J Nucl Cardiol*. 2017;24(5):1608-1609. doi:10.1007/s12350-016-0542-z
126. Yamashita S, Yokoyama K, Onoguchi M, et al. Feasibility of deep-inspiration breath-hold PET/CT with short-time acquisition: Detectability for pulmonary lesions compared with respiratory-gated PET/CT. *Ann Nucl Med*. 2014;28(1):1-10. doi:10.1007/s12149-013-0774-9
127. Kawano T, Ohtake E, Inoue T. Deep-Inspiration Breath-Hold PET/CT of Lung Cancer: Maximum Standardized Uptake Value Analysis of 108 Patients. *J Nucl Med*. 2008;49(8):1223-1231. doi:10.2967/jnumed.107.049296
128. Mitsumoto K, Abe K, Sakaguchi Y, et al. Determination of the optimal acquisition protocol of breath-hold PET/CT for the diagnosis of thoracic lesions. *Nucl Med Commun*. 2011;32(12):1148-1154. doi:10.1097/MNM.0b013e32834bbda7
129. Kini VR, Vedam SS, Keall PJ, Patil S, Chen C, Mohan R. Patient training in respiratory-gated radiotherapy. *Med Dosim*. 2003;28(1):7-11. doi:10.1016/S0958-3947(02)00136-X
130. Ichikawa Y, Tomita Y, Ishida M, Kobayashi S, Takeda K, Sakuma H. Usefulness of abdominal belt for restricting respiratory cardiac motion and improving image quality in myocardial perfusion PET. *J Nucl Cardiol*. 2018;25(2):407-415. doi:10.1007/s12350-016-0623-z
131. Prior JO, Peguret N, Pomoni A, et al. Reduction of Respiratory Motion During PET/CT by Pulsatile-Flow Ventilation: A First Clinical Evaluation. *J Nucl Med*. 2016;57(3):416-419. doi:10.2967/jnumed.115.163386

132. Martinez-Möller A, Zikic D, Botnar RM, et al. Dual cardiac-respiratory gated PET: Implementation and results from a feasibility study. *Eur J Nucl Med Mol Imaging*. 2007;34(9):1447-1454. doi:10.1007/s00259-007-0374-9
133. Klein GJ, Reutter BW, Huesman RH. Non-rigid summing of gated PET via optical flow. *IEEE Trans Nucl Sci*. 1997;44(4 Part 1):1509-1511. doi:10.1109/23.632704
134. Slomka PJ, Rubeaux M, Le Meunier L, et al. Dual-Gated Motion-Frozen Cardiac PET with Flurpiridaz F 18. *J Nucl Med*. 2015;56(12):1876-1881. doi:10.2967/jnumed.115.164285
135. Livieratos L, Stegger L, Bloomfield PM, Schafers K, Bailey DL, Camici PG. Rigid-body transformation of list-mode projection data for respiratory motion correction in cardiac PET. *Phys Med Biol*. 2005;50(14):3313-3322.
136. Qiao F, Pan T, Clark JW, Mawlawi OR. A motion-incorporated reconstruction method for gated PET studies. *Phys Med Biol*. 2006;51(15):3769-3783. doi:10.1088/0031-9155/51/15/012
137. Matsuzaki Y, Fujii K, Kumagai M, Tsuruoka I, Mori S. Effective and organ doses using helical 4DCT for thoracic and abdominal therapies. *J Radiat Res*. 2013;54(5):962-970. doi:10.1093/jrr/rrt024
138. Jacobson MW, Fessler JA. Joint estimation of image and deformation parameters in motion-corrected PET. In: *IEEE Nuclear Science Symposium Conference Record*. Vol 5. ; 2003:3290-3294. doi:10.1109/nssmic.2003.1352599
139. Kalantari F, Li T, Jin M, Wang J. Respiratory motion correction in 4D-PET by simultaneous motion estimation and image reconstruction (SMEIR). *Phys Med Biol*. 2016;61(15):5639-5661. doi:10.1088/0031-9155/61/15/5639

140. Schleyer PJ, Thielemans K, Marsden PK. Extracting a respiratory signal from raw dynamic PET data that contain tracer kinetics. *Phys Med Biol.* 2014;59(15):4345-4356. doi:10.1088/0031-9155/59/15/4345
141. Gould KL, Pan T, Loghin C, Johnson NP, Guha A, Sdringola S. Frequent Diagnostic Errors in Cardiac PET/CT Due to Misregistration of CT Attenuation and Emission PET Images: A Definitive Analysis of Causes, Consequences, and Corrections. *J Nucl Med.* 2007;48(7):1112-1121. doi:10.2967/jnumed.107.039792
142. Memmott MJ, Tonge CM, Saint KJ, Arumugam P. Impact of pharmacological stress agent on patient motion during rubidium-82 myocardial perfusion PET/CT. *J Nucl Cardiol.* 2018;25(4):1286-1295. doi:10.1007/s12350-016-0767-x
143. Tomita Y, Ishida M, Ichikawa Y, et al. The Effect of Misregistration Between CT-Attenuation and PET-Emission Images in ¹³N-Ammonia Myocardial PET/CT. *J Nucl Med Technol.* 2016;44(2):73-77. doi:10.2967/jnmt.116.172742
144. Klingensmith WC, Noonan C, Goldberg JH, Buchwald D, Kimball JT, Manson SM. Decreased perfusion in the lateral wall of the left ventricle in PET/CT studies with ¹³N-ammonia: evaluation in healthy adults. *J Nucl Med Technol.* 2009;37(4):215-219. doi:10.2967/jnmt.109.062059
145. Koshino K, Watabe H, Enmi J, et al. Effects of patient movement on measurements of myocardial blood flow and viability in resting ¹⁵O-water PET studies. *J Nucl Cardiol.* 2012;19(3):524-533. doi:10.1007/s12350-012-9522-0
146. Nakazato R, Dey D, Alexánder E, et al. Automatic alignment of myocardial perfusion PET and 64-slice coronary CT angiography on hybrid PET/CT. *J Nucl Cardiol.* 2012;19(3):482-491. doi:10.1007/s12350-012-9528-7

147. Turkington TG, Degrado TR, Hanson MW, Edward Coleman R. Alignment of dynamic cardiac PET images for correction of motion. *IEEE Trans Nucl Sci.* 1997;44(2):235-242. doi:10.1109/23.568814
148. Naum A, Laaksonen MS, Tuunanen H, et al. Motion detection and correction for dynamic ¹⁵O-water myocardial perfusion PET studies. *Eur J Nucl Med Mol Imaging.* 2005;32(12):1378-1383. doi:10.1007/s00259-005-1846-4
149. Woo J, Tamarappoo B, Dey D, et al. Automatic 3D registration of dynamic stress and rest ⁸²Rb and flurpiridaz F ¹⁸ myocardial perfusion PET data for patient motion detection and correction. *Med Phys.* 2011;38(11):6313-6326. doi:10.1118/1.3656951
150. Lassen ML, Kwiecinski J, Cadet S, et al. Data-driven gross patient motion detection and compensation: Implications for coronary ¹⁸F-NaF PET imaging. *J Nucl Med.* 2018;60(6):830-836. doi:10.2967/jnumed.118.217877
151. Manwell S, Klein R, Xu T, DeKemp RA. Clinical comparison of the positron emission tracking (PeTrack) algorithm with the real-time position management system for respiratory gating in cardiac positron emission tomography. *Med Phys.* 2020;47(4):1713-1726. doi:10.1002/mp.14052
152. Slomka PJ, Pan T, Germano G. Imaging moving heart structures with PET. *J Nucl Cardiol.* 2016;23(3):486-490. doi:10.1007/s12350-015-0094-7
153. Arasaratnam P, Al-Zahrani A, R. Glenn Wells, Beanlands RSB, DeKemp RA. Respiratory motion resulting in a pseudo-ischemia pattern on stress PET-CT imaging. *J Nucl Cardiol.* 2016;23(1):159-160. doi:10.1007/s12350-015-0195-3
154. Pan T. Respiratory gating in PET/CT: A step in the right direction. *J Nucl Cardiol.*

- 2018;25(2):416-418. doi:10.1007/s12350-016-0647-4
155. Leys C, Ley C, Klein O, Bernard P, Licata L. Detecting outliers: Do not use standard deviation around the mean, use absolute deviation around the median. *J Exp Soc Psychol.* 2013;49(4):764-766. doi:10.1016/J.JESP.2013.03.013
156. Lu W, Nystrom MM, Parikh PJ, et al. A semi-automatic method for peak and valley detection in free-breathing respiratory waveforms. *Med Phys.* 2006;33(10):3634-3636. doi:10.1118/1.2348764
157. Manwell S, Chamberland MJP, Klein R, Xu T, Dekemp R. Evaluation of the clinical efficacy of the PeTrack motion tracking system for respiratory gating in cardiac PET imaging. *Proceedings of SPIE.* 10132. Medical Imaging 2017; Physics of Medical Imaging, 1013251 (9 March 2017); doi:10.1117/12.2255544
158. Dawood M, Büther F, Stegger L, et al. Optimal number of respiratory gates in positron emission tomography: A cardiac patient study. *Med Phys.* 2009;36(5):1775-1784. doi:10.1118/1.3112422
159. Klein R, Renaud JM, Ziadi MC, et al. Intra- and inter-operator repeatability of myocardial blood flow and myocardial flow reserve measurements using rubidium-82 PET and a highly automated analysis program. *J Nucl Cardiol.* 2010;17(4):600-616. doi:10.1007/s12350-010-9225-3
160. Dawood M, Büther F, Lang N, Schober O, Schäfers KP. Respiratory gating in positron emission tomography: A quantitative comparison of different gating schemes. *Med Phys.* 2007;34(7):3067-3076. doi:10.1118/1.2748104
161. Didierlaurent D, Ribes S, Batatia H, et al. The retrospective binning method improves the consistency of phase binning in respiratory-gated PET/CT. *Phys Med*

- Biol.* 2012;57(23):7829-7841. doi:10.1088/0031-9155/57/23/7829
162. Böning G, Todica A, Vai A, et al. Erroneous cardiac ECG-gated PET list-mode trigger events can be retrospectively identified and replaced by an offline reprocessing approach: First results in rodents. *Phys Med Biol.* 2013;58(22):7937-7959. doi:10.1088/0031-9155/58/22/7937
 163. Liu C, Pierce II LA, Alessio AM, Kinahan PE. The impact of respiratory motion on tumor quantification and delineation in static PET/CT imaging. *Phys Med Biol.* 2009;54(24):7345-7362. doi:10.1088/0031-9155/54/24/007
 164. Koch N, Liu HH, Starkschall G, et al. Evaluation of internal lung motion for respiratory-gated radiotherapy using MRI: Part I—correlating internal lung motion with skin fiducial motion. *Int J Radiat Oncol Biol Phys.* 2004;60(5):1459-1472. doi:10.1016/j.ijrobp.2004.05.055
 165. Renaud JM, Yip K, Guimond J, et al. Characterization of 3-Dimensional PET Systems for Accurate Quantification of Myocardial Blood Flow. *J Nucl Med.* 2017;58(1):103-109. doi:10.2967/jnumed.116.174565
 166. Chamberland M, DeKemp R, Xu T. List-mode motion tracking for positron emission tomography imaging using low-activity fiducial markers. In: *2014 IEEE Nuclear Science Symposium and Medical Imaging Conference (NSS/MIC)*. IEEE; 2014:1-3. doi:10.1109/NSSMIC.2014.7430809
 167. Manwell S, Klein R, deKemp R, Xu T. Whole-body motion correction in cardiac PET/CT using Positron Emission Tracking: A phantom validation study. In: *2018 IEEE Nuclear Science Symposium and Medical Imaging Conference Proceedings (NSS/MIC)*. IEEE; 2018:1-3. doi:10.1109/NSSMIC.2018.8824715

168. Manwell S, Klein R, deKemp R, Xu T. Whole-body motion correction in ¹³N-ammonia myocardial perfusion imaging using positron emission tracking. In: *2019 IEEE Nuclear Science Symposium and Medical Imaging Conference (NSS/MIC)*. ; 2019:1-5. doi:10.1109/NSS/MIC42101.2019.9059704
169. Memmott MJ, Tonge CM, Saint KJ, Arumugam P. Impact of pharmacological stress agent on patient motion during rubidium-82 myocardial perfusion PET/CT. *J Nucl Cardiol*. 2018;25(4):1286-1295. doi:10.1007/s12350-016-0767-x
170. Song C, Yang Y, Wernick MN, Pretorius PH, Slomka PJ, King MA. Cardiac motion correction for improving perfusion defect detection in cardiac SPECT at standard and reduced doses of activity. *Phys Med Biol*. 2019;64(5):055005. doi:10.1088/1361-6560/aafefe
171. Lassen ML, Kwiecinski J, Cadet S, et al. Data-Driven Gross Patient Motion Detection and Compensation: Implications for Coronary ¹⁸F-NaF PET Imaging. *J Nucl Med*. 2019;60(6):830-836. doi:10.2967/jnumed.118.217877
172. Gallezot J-D, Lu Y, Naganawa M, Carson RE. Parametric Imaging With PET and SPECT. *IEEE Trans Radiat Plasma Med Sci*. 2020;4(1):1-23. doi:10.1109/TRPMS.2019.2908633
173. Andersson JLR. How to obtain high-accuracy image registration: Application to movement correction of dynamic positron emission tomography data. *Eur J Nucl Med*. 1998;25(6):575-586. doi:10.1007/s002590050258
174. Klein S, Staring M, Murphy K, Viergever MA, Pluim JPW. Elastix: A toolbox for intensity-based medical image registration. *IEEE Trans Med Imaging*. 2010;29(1):196-205. doi:10.1109/TMI.2009.2035616

175. Viola P, Wells WM. Alignment by Maximization of Mutual Information. *Int J Comput Vis*. 1997;24(2):137-154. doi:10.1023/A:1007958904918
176. Thévenaz P, Unser M. Optimization of mutual information for multiresolution image registration. *IEEE Trans Image Process*. 2000;9(12):2083-2099. doi:10.1109/83.887976
177. Wells WM, Viola P, Atsumi H, Nakajima S, Kikinis R. Multi-modal volume registration by maximization of mutual information. *Med Image Anal*. 1996;1(1):35-51. doi:10.1016/S1361-8415(01)80004-9
178. Khalil A, Ng S-C, Liew YM, Lai KW. An Overview on Image Registration Techniques for Cardiac Diagnosis and Treatment. *Cardiol Res Pract*. 2018;2018:1-15. doi:10.1155/2018/1437125
179. Chen K, Smilovici Q, Lee W, et al. Inter-Frame Co-Registration of Dynamically Acquired Fluoro-Deoxyglucose Positron Emission Tomography Human Brain Data. In: *2007 IEEE/ICME International Conference on Complex Medical Engineering*. IEEE; 2007:901-906. doi:10.1109/ICCME.2007.4381871
180. Sun T, Petibon Y, Han PK, et al. Body motion detection and correction in cardiac PET: Phantom and human studies. *Med Phys*. 2019;46(11):4898-4906. doi:10.1002/mp.13815
181. Efseaff M, Klein R, Ziadi MC, Beanlands RS, DeKemp RA. Short-term repeatability of resting myocardial blood flow measurements using rubidium-82 PET imaging. *J Nucl Cardiol*. 2012;19(5):997-1006. doi:10.1007/s12350-012-9600-3
182. El Fakhri G, Kardan A, Sitek A, et al. Reproducibility and Accuracy of

Quantitative Myocardial Blood Flow Assessment with ^{82}Rb PET: Comparison with ^{13}N -Ammonia PET. *J Nucl Med.* 2009;50(7):1062-1071.

doi:10.2967/jnumed.104.007831

183. Saillant A, Armstrong I, Shah V, et al. Assessing Reliability of Myocardial Blood Flow After Motion Correction With Dynamic PET Using a Bayesian Framework. *IEEE Trans Med Imaging.* 2019;38(5):1216-1226. doi:10.1109/TMI.2018.2881992
184. Armstrong IS, Memmott MJ, Saint KJ, Saillant A, Hayden C, Arumugam P. Assessment of motion correction in dynamic rubidium-82 cardiac PET with and without frame-by-frame adjustment of attenuation maps for calculation of myocardial blood flow. *J Nucl Cardiol.* August 2019:1-13. doi:10.1007/s12350-019-01834-5
185. Hunter CRRN, Hill J, Ziadi MC, Beanlands RSB, DeKemp RA. Biodistribution and radiation dosimetry of ^{82}Rb at rest and during peak pharmacological stress in patients referred for myocardial perfusion imaging. *Eur J Nucl Med Mol Imaging.* 2015;42(7):1032-1042. doi:10.1007/s00259-015-3028-3
186. Orton E, Al-Harbi I, Klein R, Beanlands R, deKemp R, Wells RG. Prevalence of extra-cardiac interference in ^{82}Rb PET myocardial perfusion imaging. *J Nucl Med.* 2013;54(supplement 2):1689.
http://jnm.snmjournals.org/content/54/supplement_2/1689.abstract.
187. Yi C, Yu D, Shi X, He Q, Zhang X, Zhang X. Biodistribution and estimation of radiation-absorbed doses in humans for ^{13}N -ammonia PET. *Ann Nucl Med.* 2015;29(9):810-815. doi:10.1007/s12149-015-1012-4
188. Salient A. Estimation and reliability of myocardial blood flow with dynamic PET

[PhD Thesis]. University of Oxford. 2018.

<https://ora.ox.ac.uk/objects/uuid:4f81ddef-09ef-458c-9b5d-7c0a734dc559>.

Accessed February 19, 2020.

189. Ren S, Lu Y, Bertolli O, Thielemans K, Carson RE. Event-by-event non-rigid data-driven PET respiratory motion correction methods: comparison of principal component analysis and centroid of distribution. *Phys Med Biol*. 2019;64(16):165014. doi:10.1088/1361-6560/ab0bc9
190. Schleyer PJ, Dunn JT, Reeves S, Brownings S, Marsden PK, Thielemans K. Detecting and estimating head motion in brain PET acquisitions using raw time-of-flight PET data. *Phys Med Biol*. 2015;60(16). doi:10.1088/0031-9155/60/16/6441
191. Armstrong IS, Hayden C, Memmott MJ, Arumugam P. A preliminary evaluation of a high temporal resolution data-driven motion correction algorithm for rubidium-82 on a SiPM PET-CT system. *J Nucl Cardiol*. May 2020:1-13. doi:10.1007/s12350-020-02177-2
192. Badawi RD, Shi H, Hu P, et al. First Human Imaging Studies with the EXPLORER Total-Body PET Scanner. *J Nucl Med*. 2019;60(3):299-303. doi:10.2967/jnumed.119.226498
193. Karp JS, Viswanath V, Geagan MJ, et al. PennPET explorer: Design and preliminary performance of a whole-body imager. *J Nucl Med*. 2020;61(1):136-143. doi:10.2967/jnumed.119.229997